X-ray studies of ultraluminous X-ray sources

Wasutep Luangtip

A Thesis presented for the degree of
Doctor of Philosophy

Centre for Extragalactic Astronomy
Department of Physics
University of Durham
United Kingdom

September 2015

X-ray studies of ultraluminous X-ray sources

Wasutep Luangtip

Submitted for the degree of Doctor of Philosophy
September 2015

Abstract

Ultraluminous X-ray sources (ULXs) are extra-galactic, non-nuclear point sources, with X-ray luminosities brighter than 10^{39} erg s^{-1}, in excess of the Eddington limit for 10 $M_{\odot}$ black holes. Recent results indicate that the majority of ULXs are stellar remnant black holes accreting material at or above the Eddington rate, rather than sub-Eddington accretion onto intermediate mass black holes. However, precisely how these ULXs accrete material at a super-Eddington rate remains an open question. This thesis focuses on the nature of these system as well as their environments, and attempts to explain physically how the sources operate in this super-critical accretion regime.

This work begins with a study of the X-ray spectra of ULXs in very nearby galaxies ($D < 5$ Mpc). A range of physical models is used to explain the ULX spectra and to interpret the results physically. The outcomes consistently suggest that ULXs are stellar remnant black holes accreting material at or above the Eddington rate. It is demonstrated that the hard spectral component is consistent with emission from the inner radius of an advection-dominated slim accretion disc; the mass of black holes powering ULXs can be constrained from this hard emission, falling in the regime of stellar-mass black hole ($\sim$3 – 30 $M_{\odot}$). Assuming that the soft spectral component represents soft thermal emission from an optically-thick outflowing wind, the size of the wind is constrained to be between $\sim 10^4$ – 10^6 $R_{\rm g}$.

We further explore the nature of ULXs by studying the X-ray spectral evolution of the individual source Holmberg IX X-1 with observed source luminosity. We find that the spectra tend to evolve from relatively flat or two-component spectra in the

medium energy band, at lower luminosities, to a spectrum that is distinctly curved and disc-like at the highest luminosities. This spectral variability is consistent with the prediction of super-Eddington accretion models, in which the outflowing wind is expected to be launched from within the photospheric radius; the increase in accretion rate causes the more powerful wind to scatter a higher fraction of hard photons into the line of sight, while those that survive the passage through the wind will be Compton down-scattered to lower energies; these increase and soften the hard spectral component, resulting in a disc-like spectrum peaking at lower energy than the hard component seen at lower luminosity. Furthermore, we find observational evidence that the ULX might precess around its rotational axis, implied by a degree of degeneracy between different spectra observed at the same luminosity.

Finally, we study the population of ULXs present in a sample of 17 nearby luminous infrared galaxies (LIRGs). It is found that the LIRGs possess significantly fewer ULXs per unit star formation rate than nearby normal galaxies, by a factor of about 10. We argue that part of the deficit could be due to the high metallicity environment of the host galaxies suppressing the formation of ULXs, and the lag between star formation starting and the appearance of ULXs; however, the majority of the deficit of ULXs is likely to be due to the high amount of gas and dust in the LIRGs obscuring a large fraction of ULXs.

Declaration

The work in this thesis is based on research carried out at the Centre for Extra-galactic Astronomy, the Department of Physics, University of Durham,UK, under the supervision of Dr. Tim Roberts and Prof. Chris Done. No part of this thesis has been submitted elsewhere for any other degree or qualification and it is all my own work unless referenced to the contrary in the text.

Portions of this thesis have appeared in the following papers:

- Luangtip, W., Roberts, T. P., Mineo, S., Lehmer, B. D., Alexander, D. M., Jackson, F. E., Goulding, A. D., Fischer, J. L., 2015, MNRAS, 446, 470

Acknowledgements

First of all, I would like to thank my supervisors, Dr. Timothy Roberts and Prof. Christine Done, for their support, enthusiastic guidance and encouragement throughout the course of my PhD studies at Durham. I am also grateful to Dr. Andrew Sutton and Dr. Fabio Pintore, who took the time to answer a lot of questions about ULXs as well as X-ray astronomy, and taught me the basics of X-ray data analysis; Dr. Stefano Mineo, who spent a lot of time discussing in X-ray population and helping me to understand statistical methods for data fitting; and to the rest of the research group, who made this period of study so enjoyable.

Thanks must also be given to Ministry of Science and Technology of The Royal Thai Government for the financial support throughout my academic career.

Thank to my friends both in UK and Thailand who encouraged me and helped to create a fun when I was stressful. Finally, I am very grateful to my family; without their encouragement and support, I could not have got this far.

Contents

List of Figures

List of Tables

Chapter 1

Introduction

Ultraluminous X-ray sources (ULXs) are, as their name suggests, a class of very luminous celestial X-ray emitters. This thesis will focus on these sources. To begin with, in this chapter, a brief history of X-ray astronomy will be presented. Then the X-ray satellites and their instruments used to observe the ULXs in this thesis will be discussed. Finally, the astrophysics of black holes and ULXs will be explained.

1.1 A brief history of X-ray astronomy

Astronomy is the oldest field of the natural sciences. Studies of astronomy began in the optical waveband due to the visibility of the optical sky to the naked eye. Knowledge of astronomy has grown with time – from its earliest days in which ancient societies linked celestial objects with gods and spirits, to the era of modern astronomy, in which we can trace the observed expansion of the Universe back to the Big Bang. However, studies of multi-waveband astronomy did not begin until the 20th Century, when astronomers began to study the sky in forms of electromagnetic (EM) radiation that are invisible to the naked eye, such as X-rays, gamma rays, radio waves, and infrared radiation. This has opened up new windows to the Universe. One field spawned in this multi-wavelength revolution was X-ray astronomy.

The EM radiation we now call X-rays was discovered by Wilhelm Röntgen in 1895. He realised from his experiments that there was an invisible form of radiation (leading to the name 'X' as it was previously unknown) that was able to penetrate a

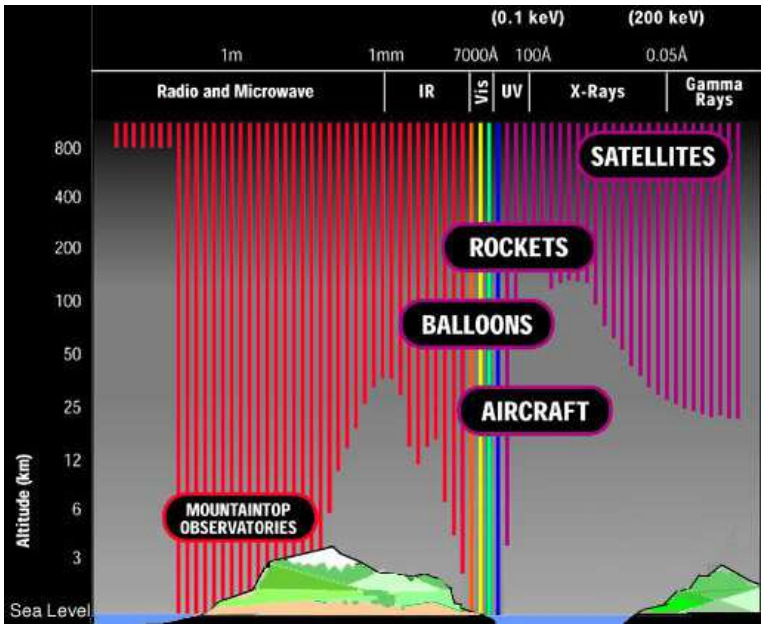

Figure 1.1: The penetration of extraterrestrial EM radiation through the Earth's atmosphere (image taken from `http://migall.fastmail.fm.user.fm/astronomy/telescopes_detectors/emr/page6.htm`). Obviously, X-rays are completely absorbed by the atmosphere well before arrival at the Earth's surface.

number of materials. Subsequently, in 1901, Röntgen received the first Nobel Prize in Physics for his discovery.[1] However, although X-rays had been discovered, studies in X-ray astronomy were not begun immediately after the detection. The X-ray sky cannot be observed directly from the Earth's surface due to atmospheric absorption. Fig. 1.1 illustrates the penetration of the Earth's atmosphere by various forms of EM radiation; it is clear that extraterrestrial X-rays are highly absorbed and so cannot reach the Earth's surface, even to the altitude of mountaintop observatories. Hence, observations of the X-ray sky are required to be carried out by high altitude instruments ($\gtrsim$ 100 km) such as balloons, rockets or satellites.

X-ray astronomy observations began five decades after the discovery of X-rays. Soon after the end of World War II, on August 5, 1948, a group of scientists at the US Naval Research Laboratories (NRL) led by Herbert Friedman started the first observations of the X-ray emission from the Sun. The experiment was launched on a US army V-2 rocket, captured from Germany after World War II; the rocket

[1] `http://www.nobelprize.org/nobel_prizes/themes/physics/karlsson/`

carried detectors consisting of a photographic plate behind a beryllium filter, with which the first extraterrestrial X-rays were detected and were interpreted as X-ray emission from the Sun (Burnight, 1949). This event marked the beginning of the X-ray astronomy era. Very early X-ray observations were carried on rockets and focused solely on the Sun as it was expected to be the only visible high X-ray intensity source.

The next turning point was the first detection of the extra-solar X-rays. In 1962, an Aerobee sounding rocket carrying a payload of three Geiger counters was launched, in order to search for fluorescent X-rays produced on the Lunar surface by X-rays from the Sun. It was expected that the X-ray intensity would peak when the detectors were pointed in the direction of the Moon. In fact, the mission failed to detect X-rays reflected from the Moon but, instead, they found two other surprising results (Giacconi et al., 1962): i) the first discovery of the cosmic X-ray background (a diffuse X-ray component seen over the whole sky) and ii) the first point-like X-ray source detection, located in the Scorpius constellation – known later as Sco X-1 – which is about million times brighter in X-rays than the Sun, but was not noticeable at other wavelengths. These discoveries led Riccardo Giacconi – the leader of the science team – to win the Nobel Prize for Physics in 2002 for his development of X-ray astronomy.[2] The Aerobee rocket missions continued to be launched by a team from NRL and led to the detections of many other bright X-ray sources, for example the Crab Nebula supernova remnant (Bowyer et al., 1964), Kepler's Supernova Remnant, Cygnus X-1 (Bowyer et al., 1965) and the first X-ray sources identified with extragalactic objects (Byram et al., 1966; Friedman & Byram, 1967). Another notable sounding rocket was the British Skylark, which was one of the most successful sounding rocket programmes, launched from 1957 – 2005. These missions provided the first good-quality X-ray images of the solar corona (Fig. 1.2). In addition, the first X-ray sky survey of the Southern Hemisphere was obtained from Skylark flights; nine individual X-ray sources were resolved and reported (Cooke & Pounds, 1971).

[2] `http://www.nobelprize.org/nobel_prizes/physics/laureates/2002/giacconi-facts.html`

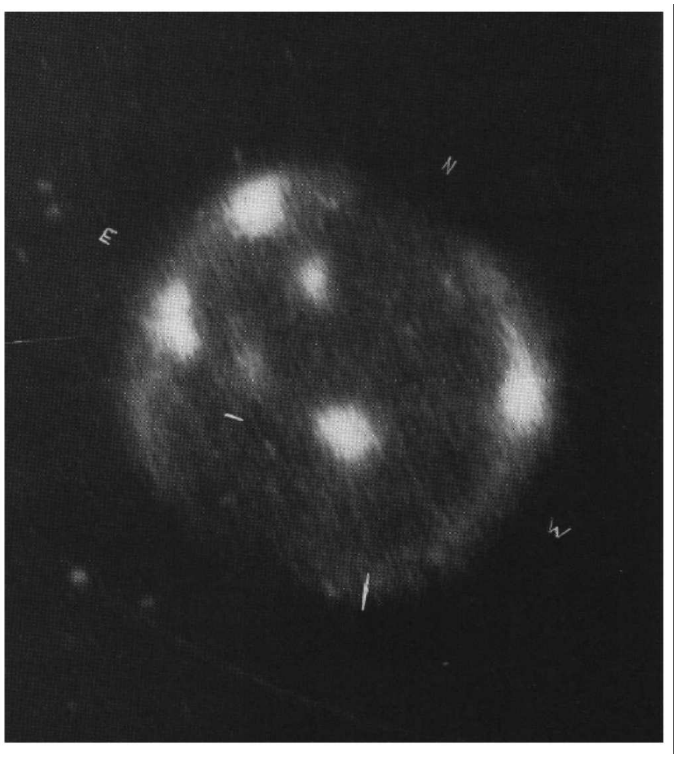

Figure 1.2: The first good-quality X-ray image of the Solar corona obtained from a Skylark rocket flight (image from Pounds 2002).

The early X-ray observations also relied on balloon flights. Such flights cannot reach high altitude (they reach only $\lesssim 50$ km), limiting the detection of low energy (soft) X-rays ($\lesssim 35$ keV; see Fig. 1.1), but the advantage of balloon missions over sounding rockets is the far longer observing time, as balloons are able to stay aloft for much longer. The first balloon-based detection of X-rays was the discovery of hard X-rays (15 - 60 keV) emitted from the Crab Nebula supernova remnant on July 21, 1964 (Clark, 1965). Both balloon and sounding rocket missions established a number of X-ray source detections during the early era of X-ray astronomy observations (1950s - 1960s); in 1969, a catalogue of discrete X-ray sources was reported with a total of 59 source detections (Dolan, 1970). In fact, the detection of discrete X-ray sources led to the first studies in a new area of astrophysics – accretion physics – from which, later, many of them were concluded to be powered by accretion onto a compact object such as a white dwarf, neutron star or black hole.

The next generation of X-ray observations began in 1970, when the first X-ray astronomy satellite was launched – *Uhuru* (Giacconi et al. 1971a), with an energy

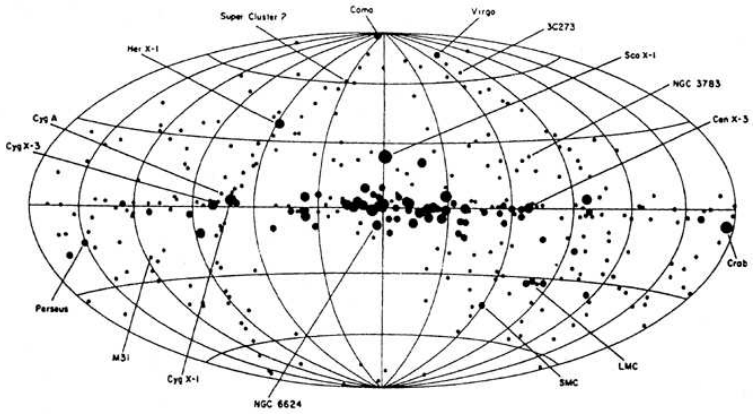

Figure 1.3: The X-ray sources detected in the *Uhuru* all-sky survey plotted in Galactic coordinates (image taken from `http://ned.ipac.caltech.edu/level5/Seitter/Seitter1_2.html`). The size of the filled circles is scaled with the logarithm of the source intensity.

bandpass of 2-20 keV and angular resolution of 0.52 degrees. Such orbiting satellites have many advantages over sounding rockets, not least that the possible observing time is improved substantially ($\sim 10^5$ times longer compared to the rockets). During the two year life time of *Uhuru*, the mission provided a comprehensive and uniform all-sky survey; 339 X-ray sources were detected and reported in the final *Uhuru* catalogue (Forman et al. 1978; Fig. 1.3); the majority of the population was identified as binary systems, supernova remnants, Seyfert galaxies and clusters of galaxies. The mission contributed to several important discoveries in X-ray astronomy, including the detection of diffuse X-ray emission from clusters of galaxies and the discovery of rapidly pulsing X-ray sources – e.g. Cen X-3 (Giacconi et al. 1971b) and Her X-1 (Tananbaum et al., 1972) – that were interpreted as the effect of a rotating neutron star (i.e. pulsar) accreting from another star.

Following the success of *Uhuru*, several X-ray satellites were launched during the 1970s and led to many key X-ray discoveries. For example, these included the discovery of the absorption dips in Cyg X-1 (Murdin, 1976) and the observation of rapid intensity variability from Cen A by the *Copernicus* satellite, the discovery of several long period (several minutes) X-ray pulsars and several bright X-ray transients by the *Ariel V* satellite, and the discovery of the first eclipse seen in a low-mass X-ray binary by *High Energy Astronomy Observatories-1 (HEAO-1)*. In

addition, another highlight from *HEAO-1* was a more comprehensive all sky X-ray survey catalogue (the *HEAO* A-1 catalogue) containing 842 X-ray sources detected in the 0.25-25 keV energy band (Wood et al. 1984, Fig. 1.4).

Following *HEAO-1*, the US National Aeronautics and Space Administration (NASA) launched the second *HEAO* (i.e. *HEAO-2*) in November 1978, later renamed as *Einstein* in order to honour Albert Einstein (Giacconi et al., 1979). It was the first X-ray satellite carrying an imaging X-ray telescope, resulting in a sensitivity several hundred times greater than any previous satellite missions, and so capable of imaging extended objects and diffuse emission, and of detecting faint X-ray sources. *Einstein* contributed to many important X-ray astronomy studies including the first discovery of X-ray emission from normal-hot (OB) stars (Harnden et al., 1979) and the detection of discrete X-ray sources in the Andromeda Galaxy (M31) and the Magellanic Clouds (Long et al., 1981).

In the 1980s & 1990s, many X-ray satellite missions continued to be launched and contributed significantly to X-ray astronomy studies. Among the several missions, one outstanding X-ray satellite was the *Röntgensatellit* (*ROSAT*; Truemper 1982) launched in June 1990. The mission dedicated its first six months to an all sky-survey of X-ray sources and UV sources, resulting in the first X-ray and XUV all-sky surveys. With an X-ray sensitivity of about a factor of 1000 better than that of *Uhuru*, the surveys yielded the largest X-ray catalogue at the time (Voges et al., 1999), ultimately resulting in ∼150000 object detections (Fig. 1.4) as well as the 479 sources detected in the XUV catalogue. Following the sky surveys, the mission was used to observe in a pointed phase, resulting in a catalogue containing a further ∼100000 serendipitous sources (Voges et al., 2000). Moreover, the mission also provided maps of the soft diffuse X-ray background with higher angular resolution and statistical significance than any previous missions (Snowden et al. 1995; Fig. 1.5); the extensive structure revealed in the maps helped in the understanding of energetic processes in the local interstellar medium and the Galactic halo. Another notable mission was the Japanese *Advanced Satellite for Cosmology and Astrophysics* (*ASCA*; Tanaka et al. 1994) launched in February 1993. It was the first X-ray satellite-based telescope using CCD detectors and combining imaging

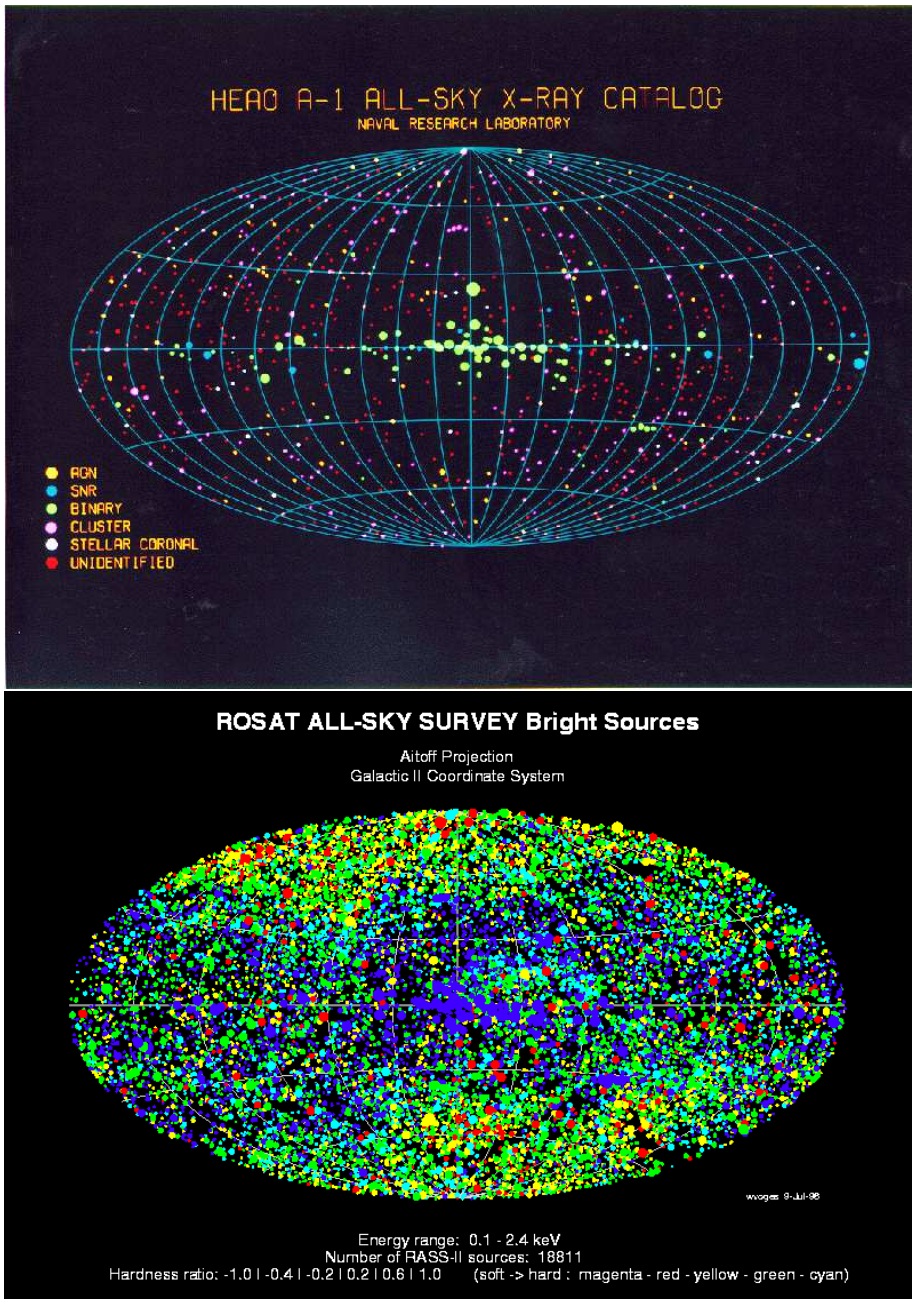

Figure 1.4: The X-ray sources detected by the *HEAO-1* (top panel) and *ROSAT* (bottom panel) all sky surveys plotted in Galactic coordinates. Images were taken from `http://chandra.harvard.edu/resources/illustrations/heaoA1.html` and `http://www.xray.mpe.mpg.de/rosat/survey/rass-bsc/sup/`, respectively.

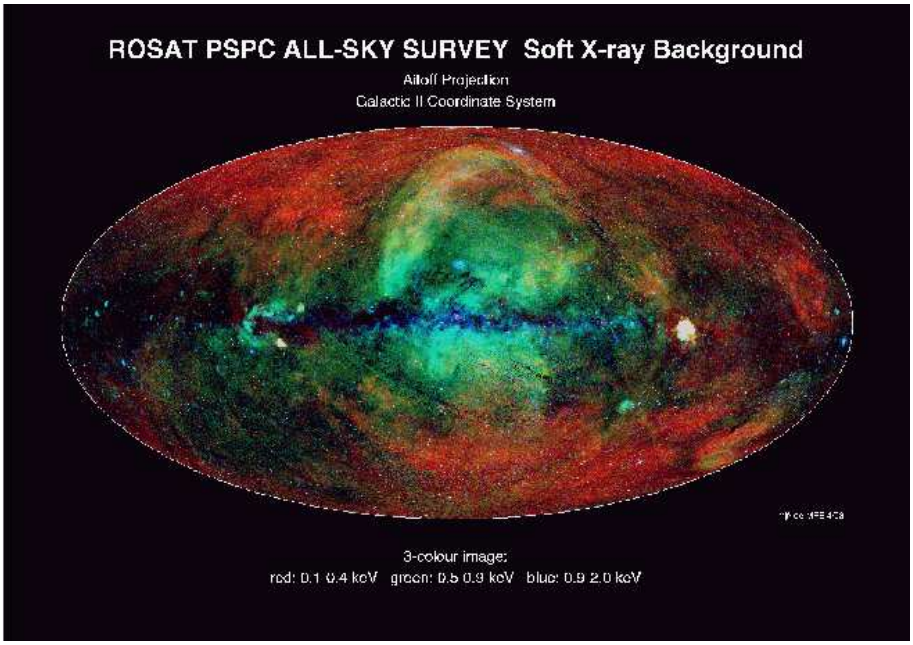

Figure 1.5: Map of the soft diffuse X-ray background from the *ROSAT* all-sky survey (taken from `http://www.xray.mpe.mpg.de/rosat/survey/sxrb/12/fits.html`).

capability with broad energy bandpass, good spectral resolution, and high effective area. With these properties, the most prominent capability of *ASCA* was in X-ray spectroscopy of astrophysical plasmas, especially the study of emission and absorption features, such as the spectroscopy of interacting binaries (e.g. Nousek et al. 1994; Vrtilek et al. 1994; Pravdo et al. 1995) and the study of broad Fe lines from active galactic nucleus (AGN; e.g. Bautz et al. 1994; Fabian et al. 1994; Guainazzi et al. 1996).

At the end of the 1990s, the current epoch of X-ray observations began with the launch of the first of the current fleet of X-ray observatories, the details of which will be given in Section 1.2. Over the last 60 years, from the first detection of the Solar X-rays, our knowledge of X-ray astronomy has increased immensely and it has become one of the most important fields of study in astronomy. We have learnt that X-ray emission is a phenomenon expected to be observed from many astronomical objects, including stars, supernovae, galaxies and binary systems. In this thesis, we will focus on the X-ray emission from a class of astronomical objects that are primarily observed in their dominant X-ray emission, called ultraluminous X-ray sources (see Section 1.5 for an introduction to ULXs).

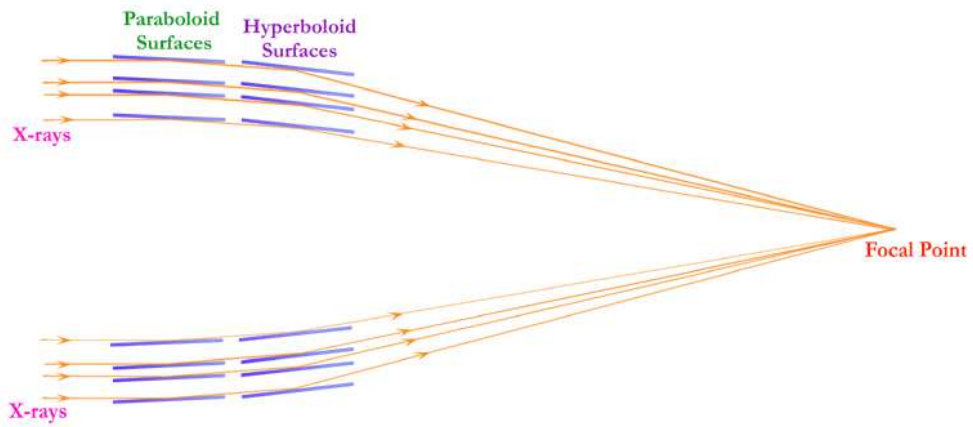

Figure 1.6: A schematic of the grazing incidence mirrors used in X-ray telescopes (image from `http://chandra.harvard.edu/xray_astro/history.html`).

1.2 Current X-ray observatories

Satellite X-ray observatories are the best means by which to observe X-rays emitted from astronomical objects. In this section, we will begin by briefly explaining the principle of X-ray telescope operation. Then, the X-ray satellite missions used in the context of this thesis will be discussed in the following sub-sections.

1.2.1 Principle of X-ray telescopes

The basic principles of X-ray telescopes are broadly similar to those of optical telescopes, in which the X-ray mirrors collect X-rays and focus them at a focal point where the X-ray detectors are installed. However, the X-ray telescope mirrors are completely different from those of optical telescopes. Whilst visible light can be reflected off mirrors, X-ray light cannot; indeed, X-rays can penetrate into the mirrors. Thus, to focus the X-ray photons to the focal point, a different, specific type of mirror is used, namely grazing incidence mirrors (Fig. 1.6). They are aligned nearly parallel to the incident X-ray direction (i.e. they have a very large incident angle), and induce the direction of the incident X-rays to change through small angles until they are directed to the detectors at the focal point where the characteristics of the X-rays are recorded. The photon collecting area (effective area) of the X-ray telescopes can be increased by nesting the mirrors inside one another (see Fig. 1.6).

The detectors installed in the focal plane record information relating to the incident photons such as their energy, spatial position and arrival time. For the current generation of X-ray telescopes, the key focal plane instruments are CCD detectors as the advantage of these devices is that they can do both imaging and spectroscopy simultaneously. CCDs (short for charge-coupled devices) are an array of vertical electrodes formed over a semiconductor substrate (usually silicon). The operation of CCD devices can be explained as the following. As an X-ray photon hits the CCD front surface, it is absorbed within the silicon of the CCD, resulting in the production of multiple electron-hole pairs in the underlying silicon substrate; the charges created (i.e the information of the incident photon) are then stored in the CCD for a short time (the frame time) until it is read-out.

To read X-ray information out from CCD detectors, the charges (data) are transferred to a neighbouring pixel. Rows of data are moved one-by-one in parallel to the output row; then data from each single CCD (pixel) in the output row are read-out at the output pixel (called output node) one-by-one until the data from all individual pixels in the output row are read-out. Then, the rows of data are moved to the adjacent rows and the one that is moved to the output row is read-out again. The steps are repeated until the data from the whole CCD detector are read-out.

The information that we hope to obtain from the CCDs relates to X-ray data from interesting sources. However, in practise, CCDs can respond to other unwanted data (i.e. backgrounds), including astrophysical background and non X-ray background photons, and charge particles.[3] One important background issue affecting the operation of CCD detectors in X-ray astronomy is particle flaring events; these are currently attributed to soft protons ($E_{proton} \lesssim$ 200-300 keV) which are presumably funnelled towards the detectors by the X-ray mirrors, resulting in a high background level likely to dominate the source data, especially if the interesting sources are faint. It is thought that these soft protons originate in the Earth's magnetosphere; the number of flares encountered by CCD detectors depends upon many factors, such as telescope position with respect to the magnetosphere and the

[3]The information on the background can be found on `http://xmm2.esac.esa.int/docs/documents/GEN-TN-0014.pdf`

amount of solar activity. However, as the soft proton flares are not persistent but are variable; one solution to correct for this background issue is by extracting only the data during the time intervals that the flare level is insignificant (i.e. during good time intervals).

In fact, some background events are able to be filtered out by the on-board processing unit. After the X-ray data are read-out from the CCD detectors, the processing examines every CCD pixel data in order to distinguish between a real photon and a background event. To do this, the pixel patterns of events incident upon the CCDs are considered; indeed, the background events are likely to create pixel patterns different from the real photon detections.[4] For example, *Chandra* (see Section 1.2.2) examines a 3×3 pixel island, centred on the local charge maximum, and then identifies event grades in that pixel island (Fig. 1.7). These grades are used as a basis to identify the useful data (real photons) and to remove background events from the telemetry.

Another issue that can occur when observing X-ray sources with CCD cameras, especially bright sources, is pile-up. Photon pile-up is a phenomenon in which two or more photons are detected as a single event – i.e. the arrival of more than one X-ray photon in one CCD pixel or in adjacent pixels before it is read out. The effect distorts the energy spectrum, as the observed photon energy is approximately the sum of multiple photons; the source count rate are also underestimated as two or more photons are counted as one. In the case of observations of extremely bright sources, the situation is worse; a hole is created at the centre of observed sources (see Fig. 1.8) since many photons are piled-up forming bad event grades, so most events at the centre are rejected. Moreover, as seen in Fig. 1.8, a trailed image (also called read-out streak, read-out artifact, transfer smear, and out-of-time image) is visible when observing a strong X-ray source. This effect happens since the CCD cameras still take data during the read-out process; as the data are moved from row to row, data is obtained in all pixels that the high intensity source passes over, resulting in the trail feature seen in the X-ray image. The effects of pile-up and trailed images

[4]See `http://cxc.harvard.edu/proposer/POG/html/chap6.html#subsec:acis_non_xrb`

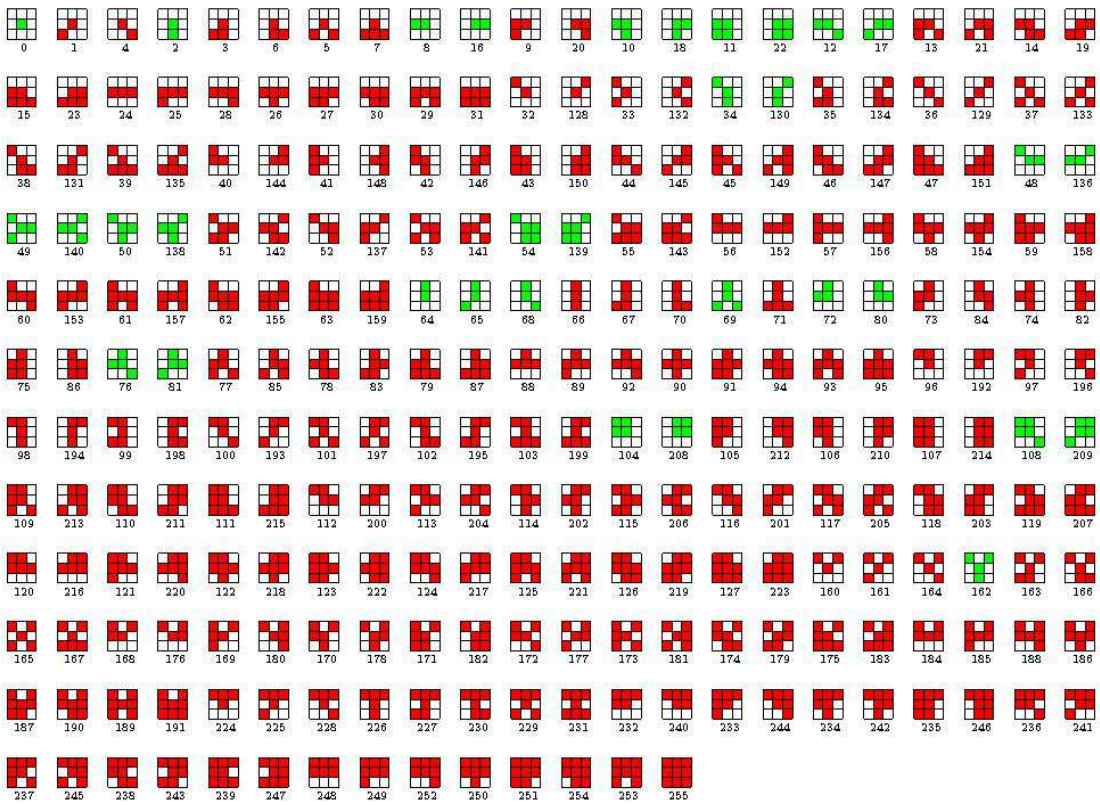

Figure 1.7: *Chandra* grades assigned on-board to detected events within 3×3 pixels (image from `http://cxc.harvard.edu/cal/projects/index.html`). The good event grades are shaded in green whilst the bad ones are shaded in red.

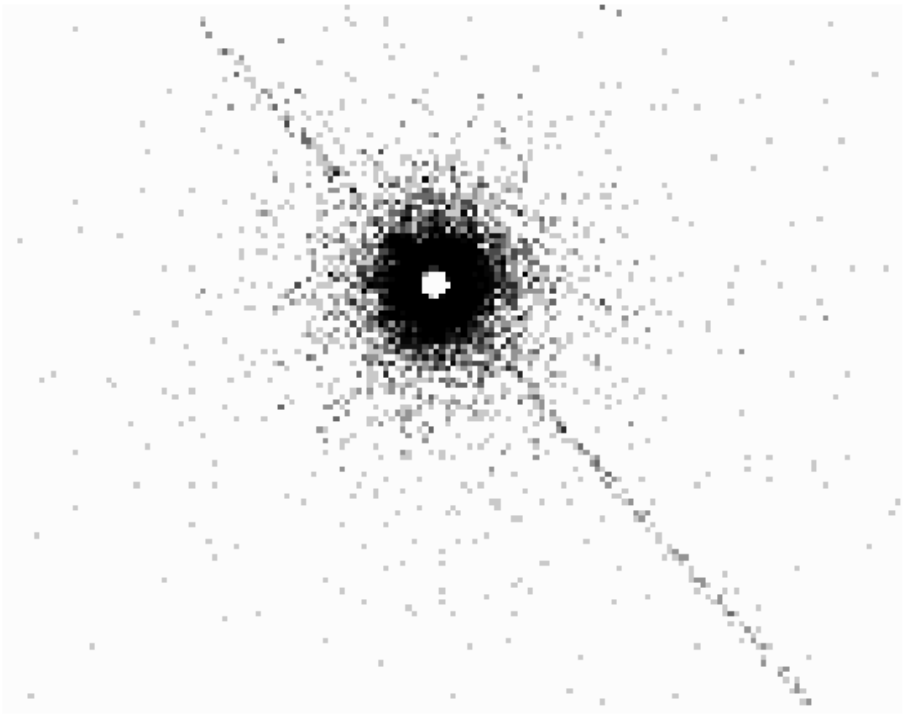

Figure 1.8: Trailed image of a strong X-ray source (taken from the *Chandra* Proposers' Observatory guide). The hole at the centre of source is created because most events are assigned bad grades due to pile-up and so are excluded.

can be reduced by decreasing the frame time and/or observing the source at off-axis positions with respect to the mirror focal point to reduce the mirror photon collecting area.

The current generation of X-ray telescopes are carried by satellites and are operated on-board. The satellite missions used in the context of this thesis are summarised in Table 1.1 and will be introduced in the following sub-sections. Information on all the other currently active X-ray missions can be found on the NASA high energy astrophysics science archive research center (HEASARC) web page.[5]

1.2.2 *Chandra*

The *Chandra* space telescope is one of NASA's Great Observatories – along with the active *Hubble* and *Spitzer* space telescopes and the retired *Compton Gamma Ray Observatory* – and is designed to observe the sky in the X-ray energy regime. It was

[5] `https://heasarc.gsfc.nasa.gov/docs/heasarc/missions/active.html`

Table 1.1: The summary of X-ray satellites contributing to this thesis

Mission	Ene. range[a] (keV)	Ene. res.[b] (eV)	PSF[c] (″)	Eff. area[d] (cm^2)	FOV[e] (′)	Vis.[f] (hr)
Chandra	0.1 – 10	100	0.5	555	30×30	44.4
XMM-Newton	0.15 – 12	55	6	4650	30	36.7
Suzaku (XIS)	0.2 – 12	50	120	1760	18×18	0.72
Swift (XRT)	0.2 – 10	70	8.8	133.5	23×23	∼0.8
NuSTAR	3 – 79	400	18	900	13×13	∼0.8

Note. The properties of the X-ray telescopes. For *Suzaku* and *Swift*, the properties of the soft X-ray instruments – XIS and XRT – are reported. [a]The telescope energy bandpass. [b]The instrument energy resolution at 1 keV, excepting for *NuSTAR* which is reported at 10 keV. [c]The full width at half maximum (FWHM) of the telescope point spread function (PSF). For *Suzaku*, the size of the half energy width (HEW) is reported. [d]The telescope effective area at 1 keV, excepting for *NuSTAR* which is reported at 10 keV. The quoted figures are for all detectors combined for *XMM-Newton, Suzaku* and *NuSTAR*, but only for the HRMA/ACIS-S combination for *Chandra*. [e]The diameter or square size of the telescope field of view (FOV). [f]The maximum target visibility per satellite orbit outside the particle-radiation dominated zone.

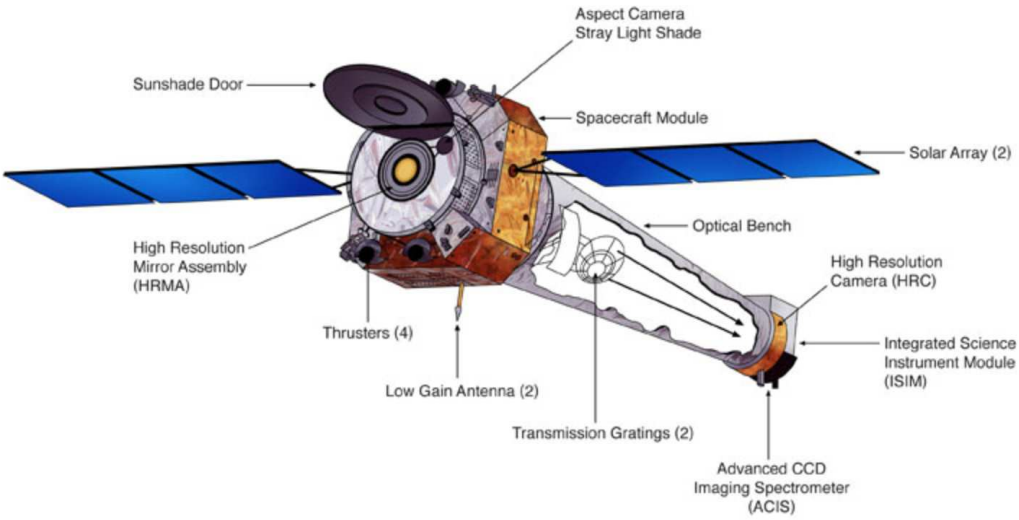

Figure 1.9: A sketch of the *Chandra* observatory (image from `http://spectrum.ieee.org/aerospace/astrophysics/the-rescue-of-the-chandra-xray-observatory`)

launched by NASA's Space Shuttle Columbia on July 23, 1999, from the Kennedy Space Center, Florida, USA. The spacecraft carries science instruments and an X-ray telescope which together consist of three main components (Fig. 1.9): i) the high resolution mirror assembly (HRMA), ii) two focal-plane instruments – the advanced CCD imaging Spectrometer (ACIS) and the high resolution camera (HRC) – and iii) two objective transmission gratings – the high and low energy transmission gratings (HETG and LETG respectively).

The HRMA consists of four nested sets of grazing-incidence X-ray mirrors with a diameter of 1.2 metres and a focal length of 10 metres. The *Chandra* mirrors are currently the largest, most precisely shaped and aligned, and smoothest X-ray mirrors in orbit, providing very high quality X-ray images with a spatial resolution of < 0.5 arcsec towards the centre of the 30×30 arcmin^2 field of view (FOV). The X-rays focussed by the HRMA are recorded by the one of the focal-plane instruments – either HRC or ACIS – dependent on operating mode since the two instruments cannot operate simultaneously. In fact, these two instruments are mounted in the focal plane such that their positions can be swapped in and out of the focal point of the HRMA. The imaging capability of the HRC is about similar to the focusing power of the HRMA, so it provides very high image resolution. However it provides little spectral resolution, although it can be used in conjunction with LETG to this end. In contrast, the ACIS detector is optimised to perform both imaging and spectroscopy. Here, we will focus on the operation of the ACIS detector as all *Chandra* data analysed in this thesis are obtained from ACIS observations. More detail of the HRC as well as the objective transmission gratings can be found on the *Chandra* Proposers' Observatory guide webpage.[6]

ACIS is an array of CCD detectors working as an X-ray imager. The instrument records the properties of individual X-ray photons hitting the detectors – position, energy and arrival time – providing high resolution imaging, moderate resolution spectroscopy and timing studies to an observer. Furthermore, the instrument can alternatively be used in conjunction with the transmission gratings (i.e. HETG or

[6] `http://cxc.harvard.edu/proposer/POG/html/index.html`

LETG) in order to obtain high resolution spectra. A schematic of the ACIS focal plane is given in Fig. 1.10. The ACIS contains 10 planar, 1024×1024 pixel CCDs which are divided into two sets: ACIS-I (2×2 array) and ACIS-S (1×6 array).[7] The array structure of the ACIS-I is optimised for imaging wide fields ($16' \times 16'$) whilst that of the ACIS-S is optimised as a readout for the HETG transmission grating. In fact, the chips ACIS-S3 (located at the focal point of the ACIS-S array) and ACIS-S1 are back-illuminated (BI) CCDs, which have a better quantum efficiency in the low energy band ($\lesssim 1$ keV) compared to the other chips which are front-illuminated (FI) CCDs. The ACIS-S3 BI chip provides the best ACIS spectral resolution without using the gratings. Thus for an observation over a small field (within $8' \times 8'$ FOV), the ACIS-S3 is appropriate to be used to obtain high quality images with reasonable spectral resolution.

The ACIS energy bandpass is between 0.1-10 keV with 100 eV energy resolution at 1 keV. In principle, any combination of the six ACIS chips can be operated simultaneously. One of two ACIS operating modes must be selected during an observation: timed exposure (TE) mode or continuous clocking (CC) mode. The TE mode collects the data from each preselected amount of time (the frame time; 3.2 seconds by default) and this mode provides a full two dimensional spatially resolved image; in contrast, the CC mode provides very fast collection of the data (every 3 milliseconds) with only one dimensional spatial resolution. In any observation of high intensity X-ray sources, the frame time needs to be optimised to avoid the effects of pile-up (see Section 1.2.1); reducing the frame time or using CC mode can help to avoid this issue.

Indeed, whilst the *Chandra* ACIS has excellent imaging resolution, permitting far superior spatial resolution of detected sources that any other current mission, its ability to collect X-ray photons (effective area) is less than that of other X-ray satellites such *XMM-Newton* and *Suzaku* (see Table 1.1). Thus long exposure times are required in order to obtain high quality spectra, especially for ULXs. This is aided by *Chandra* having a high altitude orbit; it provides good target visibility

[7] I and S stand for imaging and spectroscopy, respectively.

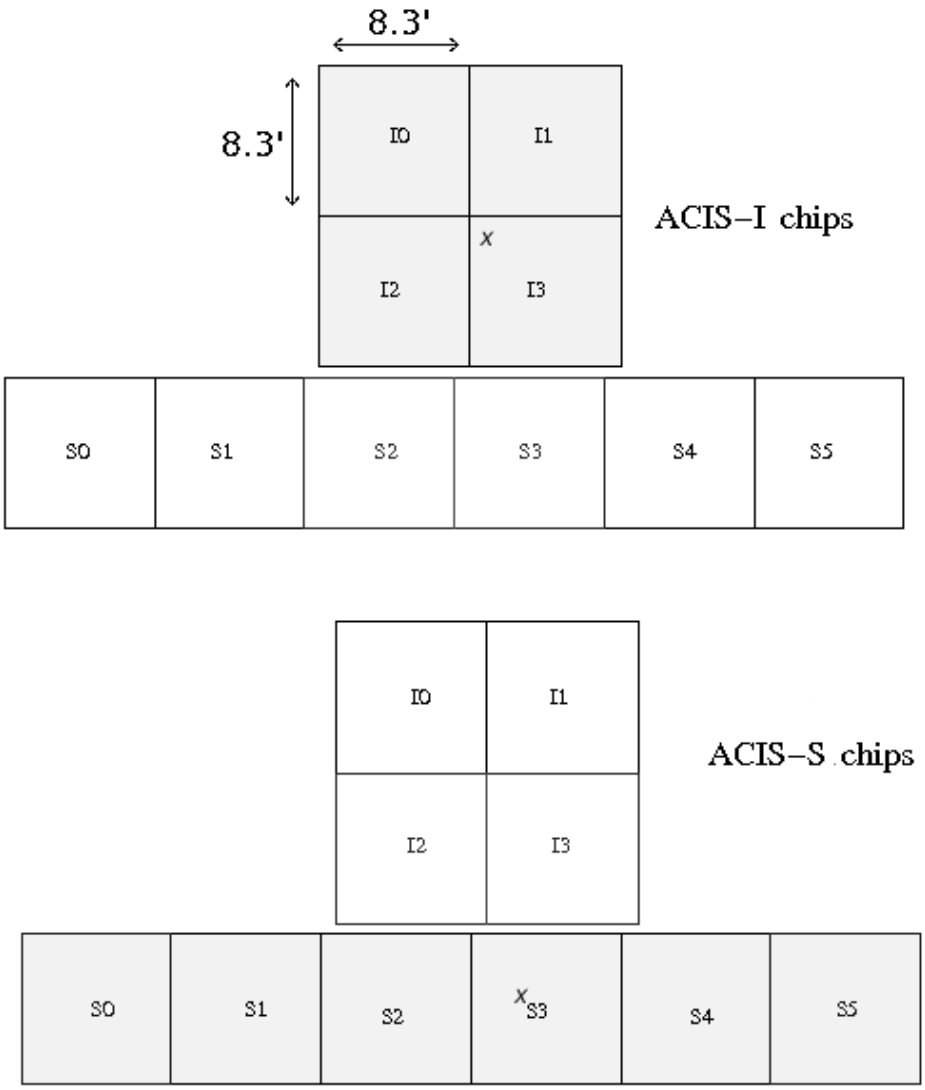

Figure 1.10: A schematic of the ACIS focal plane instrument (taken from *Chandra* Proposers' Observatory guide)

outside the particle-radiation dominated zone of ∼160 ks exposure time per orbit.

1.2.3 *XMM-Newton*

XMM-Newton – short for *X-ray Multi-Mirror Mission - Newton* – is the European Space Agency's (ESA) X-ray space observatory launched by an Ariane 504 rocket on December 10, 1999. It is ESA's second cornerstone of the Horizon 2000 Science Programme. The spacecraft carries three types of science instrument (Fig. 1.11): i) the European photon imaging cameras (EPIC) for X-ray imaging and X-ray spectroscopy, ii) the reflection grating spectrometers (RGS) for high resolution X-ray spectroscopy in the energy range of 0.33-2.5 keV and iii) an optical monitor (OM) for optical/UV imaging and grism spectroscopy (180-600 nm). The observatory provides simultaneous observations in the X-ray and optical/UV regime from a single platform. The data analysed in this thesis are obtained from EPIC and so the principals of this instrument will be discussed. More information on RGS and OM can be found on the XMM-Newton Users' Handbook webpage.[8]

XMM-Newton carries three X-ray telescopes, each of which is a grazing-incidence Wolter I telescope, consisting of 58 gold-coated nested mirrors, and has a focal length of 7500 mm and a circular FOV of 30 arcmin diameter. The combination of these telescopes provides a high collecting area for X-ray photons. They are co-aligned with a relative astrometry between the three EPIC cameras calibrated to be ∼1 – 2 arcsec across the full FOV. Three EPIC cameras, installed in the focal plane of each X-ray telescope, perform very sensitive X-ray imaging and X-ray spectroscopy with moderate spectral resolution ($E/dE \sim 20 - 50$ keV; although the RGS can be used in conjunction with EPIC to obtain high resolution spectra) over an energy bandpass of 0.15-12 keV, and with a spatial resolution of $\lesssim$6 arcsec FWHM. EPIC consists of one BI CCD camera, called EPIC pn, and two identical FI CCD type cameras called EPIC MOS (for metal oxide semi-conductor; these are EPIC MOS1 and EPIC MOS2), and each individual camera contains an array of CCD chips. The geometry of the MOS and pn detectors is shown in Fig. 1.12. The EPIC MOS consists of seven

[8] `http://xmm.esac.esa.int/external/xmm_user_support/documentation/uhb/XMM_UHB.html`

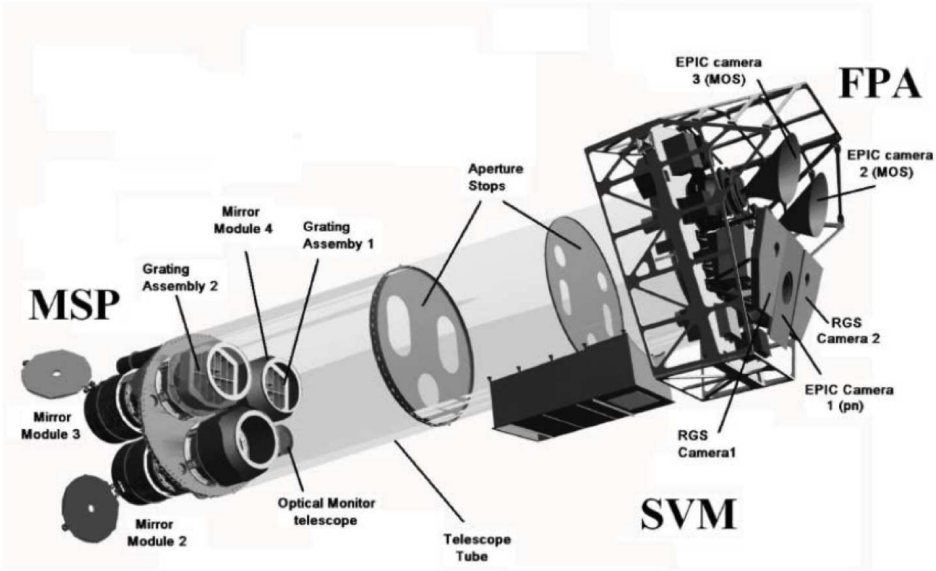

Figure 1.11: The *XMM-Newton* spacecraft and science instruments (image from Lumb et al. 2012)

individual identical chips; each individual CCD is not co-planar, but they are offset with respect to each other, following the slight curvature of the focal plane of the Wolter telescopes. For the EPIC pn, the camera is a single silicon wafer with 12 CCD chips integrated. These three EPIC cameras are operated simultaneously, providing three observational datasets from each individual observation. EPIC offers three main operating modes for an observation: full frame, partial window and timing modes. In the full frame mode, it provides full two dimensional imaging for the entire EPIC FOV with a time resolution of 2.6 sec for EPIC MOS and 73.4 msec for EPIC pn. The partial window mode allows two dimensional imaging, but only over a subset of the detector, with this compromise made to reduce the frame time if higher time resolution is required. Finally, the timing mode provides very high EPIC timing resolution; imaging is only in one dimension to allow high speed readout from the chips.

The major advantage of the EPIC cameras is that they provide a very large collecting area, compared to the other active X-ray telescopes (largest effective area; see Table 1.1). Combining the EPIC properties with the high altitude orbit of the satellite, the *XMM-Newton* observatory provides long uninterrupted observations

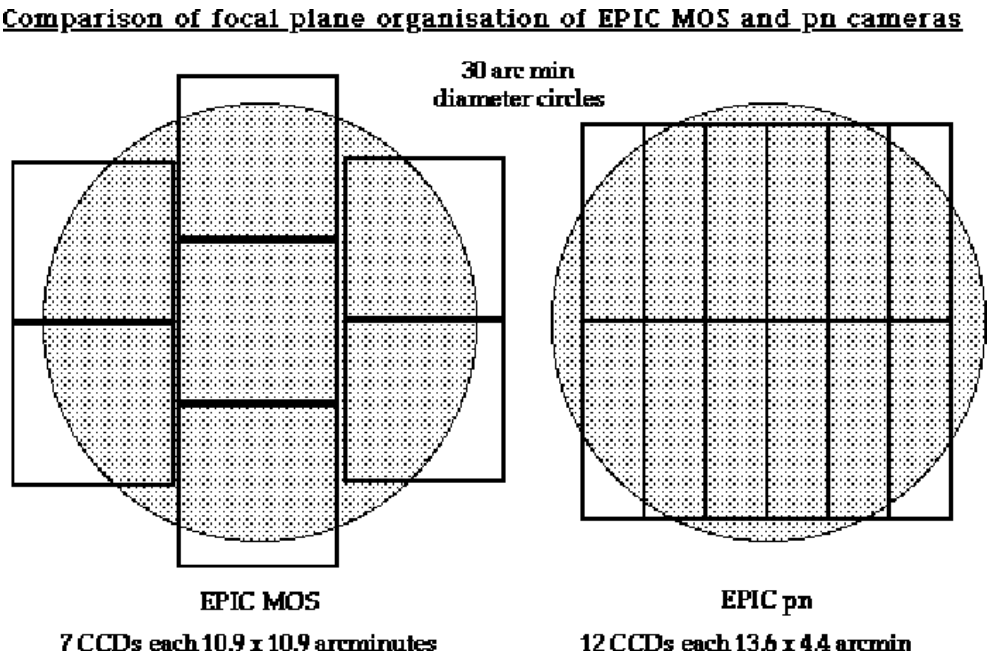

Figure 1.12: A sketch of the EPIC camera layouts – MOS (left) and pn (right) – over the 30 arcmin circular diameter FOV of *XMM-Newton* (taken from the XMM-Newton Users' Handbook)

(maximum exposure of 135 ks per orbit) with highly sensitive observations, making it the best of the current X-ray telescopes for characterising the X-ray properties of point sources such as ULXs.

1.2.4 *Suzaku*

Suzaku (formerly *ASTRO-EII*) is the fifth Japanese X-ray astronomy satellite, following after the highly successful ASCA satellite. It is a joint Japanese-US mission, developed by the Institute of Space and Astronautical Science of the Japan Aerospace Exploration Agency (ISAS/JAXA), in collaboration with the National Aeronautics and Space Administration's Goddard Space Flight Center (NASA/GSFC). The mission was launched by a Japanese M-V rocket on July 10, 2005 from the JAXA Uchinoura Space Center (USC). *Suzaku* is a low Earth orbit satellite with an apogee of 568 km and orbital period of about 96 minutes, providing ∼3 ks visibility per orbit for most targets. The spacecraft carries three types of science instrument (Fig. 1.13): an X-ray micro-calorimeter (X-ray Spectrometer; XRS), X-ray CCDs (the X-ray Imaging Spectrometers; XISs), and a hard X-ray detector (HXD); these

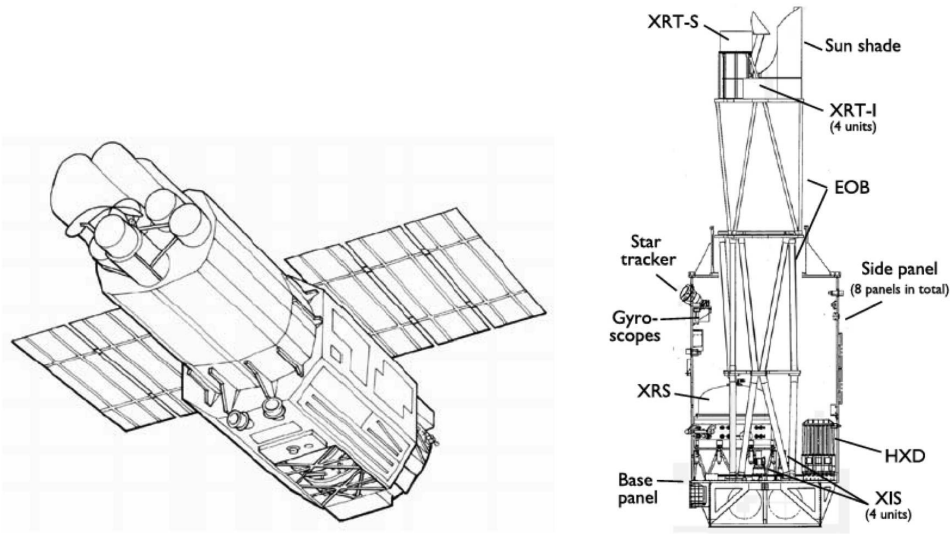

Figure 1.13: A schematic of the *Suzaku* spacecraft and science instruments (images from Mitsuda et al. 2007).

instruments can operate simultaneously. However, a month after launch, on August 8, 2005, a thermal short between the helium and neon tanks resulted in leaking of the liquid helium coolant of the XRS into space; so the XRS was no longer operative, leaving the observatory to function with just the XIS and HXD instruments.

The XISs are sensitive X-ray imaging CCD cameras placed in the focal plane of the individual X-ray telescopes. *Suzaku* contains four XIS cameras, of which three are front-illuminated detectors (FI; energy bandpass between 0.4-12 keV) and one is a back-illuminated detector (BI; energy bandpass between 0.2-12 keV); these provide X-ray imaging with 2 arcmin angular resolution and X-ray spectroscopy with moderate spectral resolution ($\sim$50 eV at 1 keV) across the FOV of 17.8$\times$17.8 arcmin^2. Similar to the *Chandra* and *XMM-Newton* BI chips, the benefit of the *Suzaku* BI detector over its FI detectors is the increased efficiency for collecting X-ray photons below 1 keV. *Suzaku* provides several modes of XIS operation including a normal mode (8 second frame time with two dimensional imaging), a partial window mode (data read out from a region of the CCD), partial timing mode (data read out with a reduced frame time) and P-sum mode (very fast timing, of the order of a few milliseconds, with one dimensional imaging). Unfortunately, in November 2006, one of the FI XIS camera was hit by a micro-meteorite and so the camera ceased

functioning. Another micro-meteorite hit in June 2009, resulting in the malfunction of 1/8 of the imaging area of another FI XIS.

In addition to the XIS detectors, the HXD helps to extend the *Suzaku* energy bandpass to over 10-600 keV. The HXD is a non-imaging instrument consisting of two types of sensor: PIN silicon diodes sensitive over 10 – 70 keV and GSO crystal scintillators covering 40 – 600 keV. HXD observations cover a FOV of 4.5×4.5 deg^2; however, at photon energy below ∼100 keV, an additional passive collimation can help to reduce the FOV to 34×34 arcmin^2. Although the HXD can permit the study of high energy X-ray emission, the large FOV of the HXD and its lack of imaging lead to a high instrument background and low sensitivity, particularly in the presence of bright nearby sources. In this thesis, we focus only on data obtained from the XIS observations.

1.2.5 *Swift*

Swift is a multi-wavelength observatory dedicated to the study of gamma-ray bursts (GRBs). It was developed as a collaboration between Italy, the United Kingdom and the USA, as a part of NASA's medium explorer (MIDEX) programme. *Swift* was launched into orbit on a Delta 7320 rocket on November 20, 2004. The spacecraft carries three science instruments (Fig. 1.14): a Burst Alert Telescope (BAT; 15-150 keV), the X-ray Telescope (XRT; 0.2-10 keV) and the UV/Optical Telescope (UVOT; 170-600 nm). These three telescopes work together to automatically detect GRBs and observe their afterglows in the gamma-ray, X-ray, ultraviolet, and optical wavebands.

The BAT is a highly sensitive instrument designed to search and provide a trigger for GRB events. It is a coded aperture imaging instrument with a large (1.4 steradian) FOV. The BAT extends over an energy bandpass from 15-150 keV with energy resolution of ∼5 keV at 60 keV and angular resolution of 22 arcmin FWHM for coded imaging. With these properties, the BAT can trigger for GRBs quickly and calculate an initial position of the burst within approximately 10 seconds of the detection.

The XRT was designed to follow up the initial burst of gamma-rays. A grazing

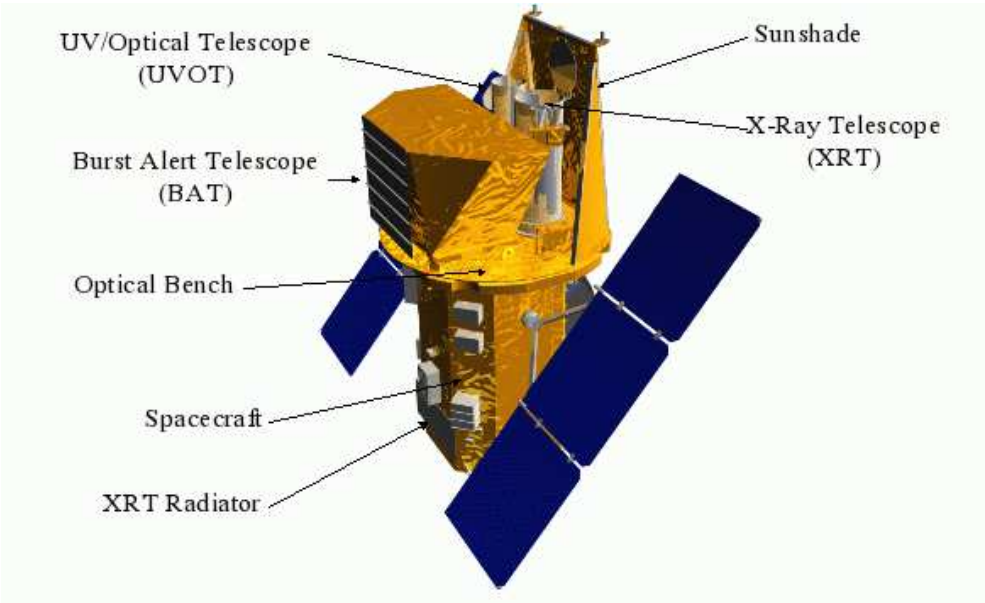

Figure 1.14: The *Swift* spacecraft and science instruments (image taken from `http://www.swift.ac.uk/about/instruments.php`).

incidence Wolter 1 telescope is used to focus X-rays onto a CCD detector placed at the focal plane. The XRT camera contains a single CCD-22 detector – very similar to that of the *XMM-Newton* MOS detector – and covers the energy range between 0.2-10 keV with energy resolution of 70 eV at 1 keV. It has a 23.6×23.6 arcmin^2 FOV with an angular resolution of ∼9 arcsec FWHM. With these properties, the XRT imaging locates the position of the burst with 5 arcsec accuracy within ten seconds of the target acquisition (for a typical GRB) and then continues to collect data, including fluxes, spectra, and light curves of the afterglow. The XRT currently provides three operating modes: i) imaging mode measuring the total energy deposited per pixel and so providing the GRB centroid position and estimated X-ray flux but no spectroscopy is obtained: ii) windowed timing mode used to obtain high resolution timing data (2.2 ms) with one-dimensional position information and spectroscopy: and iii) photon-counting mode permitting full spectral and spatial information within the FOV. *Swift* can change automatically between operating modes during a burst allowing observations of the GRB even if it shows high flux variability.

In addition to the XRT, the UVOT is also used to follow up the initial burst

in the UV and optical waveband regimes. The instrument design is based on the *XMM-Newton* OM telescope. The telescope is co-aligned with the XRT and covers the wavelength band from 170-600 nm within the 17×17 arcmin^2 FOV with an angular resolution of ∼2.5 arcsec FWHM. The UVOT provides optical and UV images through optical and UV filters; spectra can also be obtained through the use of optical and UV grisms.

Swift is a low Earth orbit satellite (∼600 km height) with an orbital period of ∼90 minutes; the satellite provides a fast slew rate of 50 degrees in < 75 seconds. Indeed, this is the origin of its name, as the Swift is a bird that can change direction very quickly in mid-flight, similar to *Swift*. This allows *Swift* to locate the positions of GRBs within 3 arcmin in ∼10-20 seconds after the initial burst detection using BAT, and an accurate position within 5 arcsec can be obtained after ∼90 seconds by XRT. Although *Swift* is dedicated to the observation of GRBs, it also continually performs an all sky hard X-ray survey and monitors for hard X-ray transients. Indeed, *Swift* also offers a guest investigator programme using the XRT, including monitoring programmes for interesting sources. In this thesis, we focus on *Swift* monitoring programmes of ULXs, and *Swift* pointed observations containing ULX data, obtained from by XRT. Note that *Swift* XRT has a very small effective area, compared to that of *Chandra* or *XMM-Newton*. Furthermore, as a *Swift* policy, the *Swift* guest observations are limited in exposure time per individual observation to be <40 ks. Thus most of individual ULX spectra obtained from the XRT have a very low number of photon counts.

1.2.6 *NuSTAR*

NuSTAR (short for *Nuclear Spectroscopic Telescope Array*) is a space-based X-ray telescope launched on a Pegasus XL rocket on 13 June 2012, as the eleventh mission of the NASA Small Explorer satellite program (SMEX-11). The mission is dedicated to the study of high energy X-ray emission, beyond the energy bandpass of the current low energy X-ray missions such as *Chandra* and *XMM-Newton* (Fig. 1.15). The spacecraft carries two major science components containing optics and detectors (Fig. 1.16). Two identical Wolter-I conical approximation X-ray optic

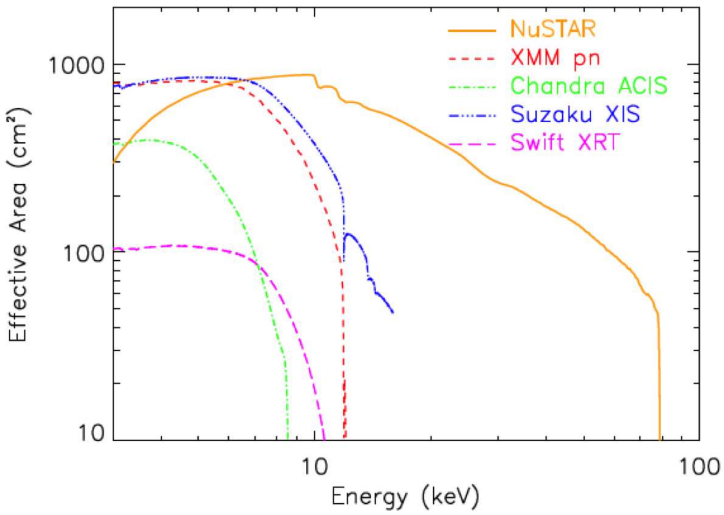

Figure 1.15: The effective area of *NuSTAR*, compared with that of the other, lower energy X-ray telescopes (image from Harrison et al. 2013).

modules are installed on the spacecraft; each individual telescope consists of 133 shells of multilayer-coated mirrors. Two identical, independent solid-state detectors are placed at the focal plane of each optics module – i.e. focal plane detector module A and B (called FPMA and FMPB)[9] – separated from the optics by the 10 metre focal length. Each detector contains a 2×2 array of 32 x 32 pixel chips. The combination of the new generation optics and detectors allows *NuSTAR* to observe X-ray emission in the 3-79 keV energy band with an energy resolution of 400 eV at 10 keV, across the 13×13 arcmin^2 FOV, with an angular resolution of 18 arcsec FWHM.

Before the launch of the *NuSTAR* satellite, observations of the high-energy X-ray sky were limited since previous high-energy X-ray orbiting telescopes did not provide true focusing optics; instead, they used collimated or coded mask instruments which lead to a high background level and low sensitivity in an observation. *NuSTAR* is the first true focusing high-energy X-ray telescope in orbit. The *NuSTAR* observatory provides a better sensitivity, spatial, and spectral resolutions by a factor of 10 – 100, compared to the previous X-ray telescopes operating in the same *NuSTAR* energy band pass. The low Earth orbit of the satellite ensures a low level of background in the observations; however, similar to other low Earth orbit X-ray satellites (i.e.

[9] `https://heasarc.gsfc.nasa.gov/docs/nustar/nustar_obsguide.pdf`

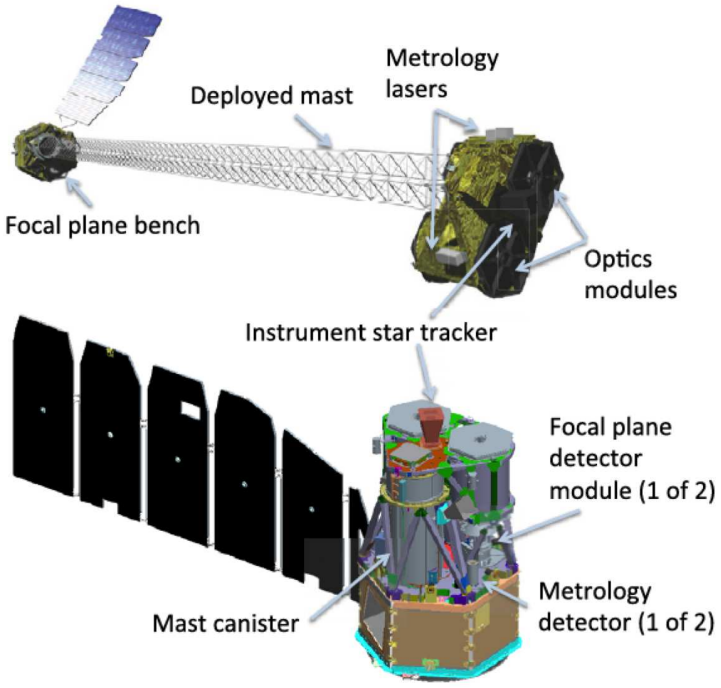

Figure 1.16: Diagram of the *NuSTAR* observatory in the stowed (bottom) and deployed (top) configurations (image from Harrison et al. 2013).

Suzaku and *Swift*), the visibility per orbit for most targets is low (∼3 ks per orbit).

1.3 Radiation processes in X-ray astronomy

We introduced in Section 1.1 that X-ray emission is a phenomenon that can be observed from many astronomical objects. However, there must be underlying physical processes producing this X-ray emission. In this section, we will explain the physics of the radiation processes generating the X-ray emission, in particular the emission observed from X-ray binary systems.

1.3.1 Blackbody radiation

A blackbody is a theoretical object that absorbs all incident EM radiation; so it appears perfectly black as it does not reflect any radiation. However, in thermal equilibrium, the black body emits EM radiation at the same rate as it absorbs; this process is known as blackbody radiation. Indeed, the EM radiation – i.e. the

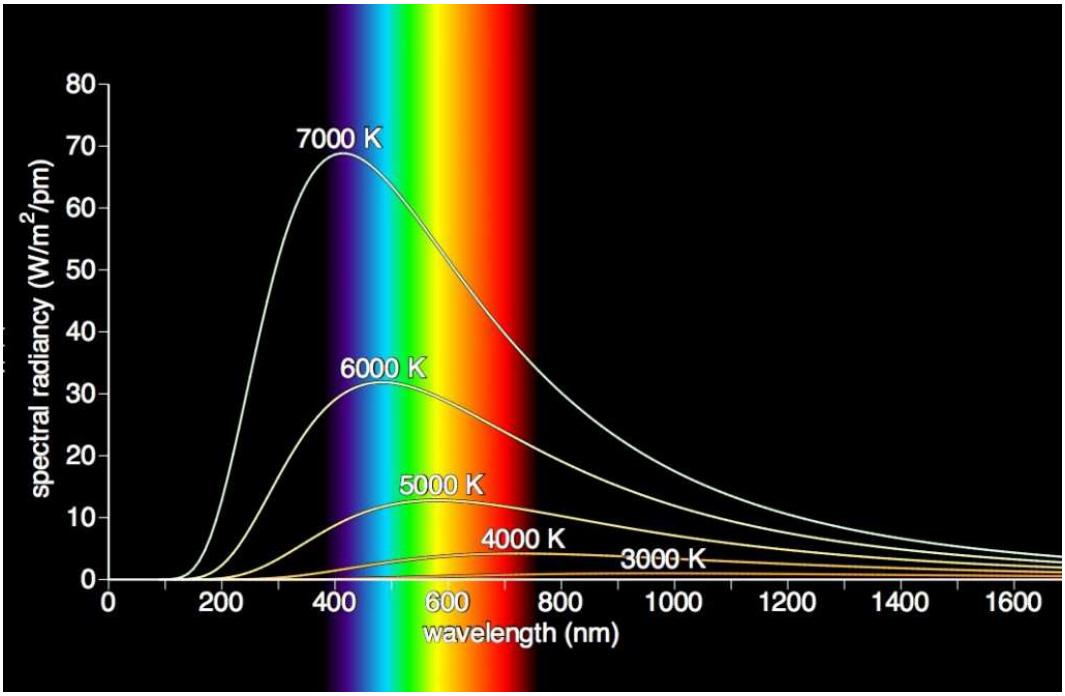

Figure 1.17: The spectra of blackbody radiation at different blackbody temperatures (image from `http://aetherforce.com/gestalt-theory-max-planck/`).

spectrum – of a blackbody can be described by Planck's law, saying that the EM emission can be determined by the temperature alone, and is not dependent on other factors such as the body's shape or composition. Fig. 1.17 illustrates the spectra of blackbody radiation at various temperatures. It is obvious that the observed peak of the spectra is shifted to shorter wavelength as the temperature of blackbody increases; in fact, this is known as Wien's displacement law stating that $\lambda_{\max} = b/T$ where b is Wien's displacement constant. The total flux F radiated from the blackbody at temperature T can be also determined by the Stefan-Boltzmann law $F = \sigma T^4$ where σ is the Stefan-Boltzmann constant.

Naturally, all matter that has temperature higher than absolute zero emits EM radiation, called thermal radiation. The thermal radiation from many ordinary objects can be approximated as blackbody radiation, including radiation from some astronomical objects such as stars or the accretion discs of compact objects. In the case of the thermal radiation from accretion discs of binary systems (see Section 1.4.2 and Section 1.4.3), as the material is highly optically thick, the photons are thermalised within the discs and so they are nearly in thermal equilibrium; the

photons that escape the disc are radiated approximately in the form of blackbody radiation, peaking in the X-ray regime.

1.3.2 Bremsstrahlung

Bremsstrahlung – a German term, from bremsen "to brake" and strahlung "radiation", meaning braking radiation or deceleration radiation – is an EM radiation process produced by the deceleration of charged particles when passing another charged particle (typically an interaction between an electron and an atomic nucleus, i.e. proton; Fig. 1.18). As an electron is decelerated, the lost kinetic energy is converted into a photon (primarily in the X-ray) due to law of energy conservation. Bremsstrahlung is also known as free-free emission since the initial free electron remains unbound after the interaction.

The thermal bremsstrahlung emission can occur in plasmas where electrons and atomic nuclei have sufficient interaction to exchange thermal energy and so are in thermal equilibrium. Such a plasma produces bremsstrahlung radiation due to the interaction between electrons and atomic nuclei within it; as the plasma particle velocity is dispersed continuously following Maxwell distribution, so the continuum emission is obtained from the thermal bremsstrahlung radiation. The phenomenon is often seen in astronomical plasma such as the emission from H II regions, intergalactic gas in clusters of galaxies, and accretion discs.

1.3.3 Synchrotron

Synchrotron radiation is produced when relativistic (or ultra-relativistic) charged particles – i.e. those moving at speeds close to the speed of light – are accelerated radially (i.e. moving in a curved path or orbit) in a magnetic field (Fig. 1.19). Theoretically, any charged particles which move in a curved path or are accelerated in a straight-line path will emit electromagnetic radiation; the term synchrotron refers to such an emission when the charged particles are accelerated to a speed that is close to the speed of light.

The process is responsible for non-thermal emission (i.e. emission from particles

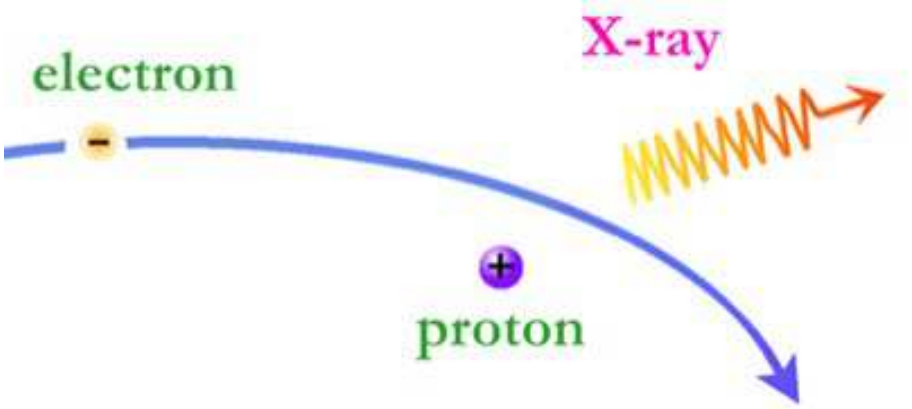

Figure 1.18: Bremsstrahlung radiation produced by the deceleration of an electron as it is deflected by the electric filed of proton (image from `http://www.astro.wisc.edu/~bank/`).

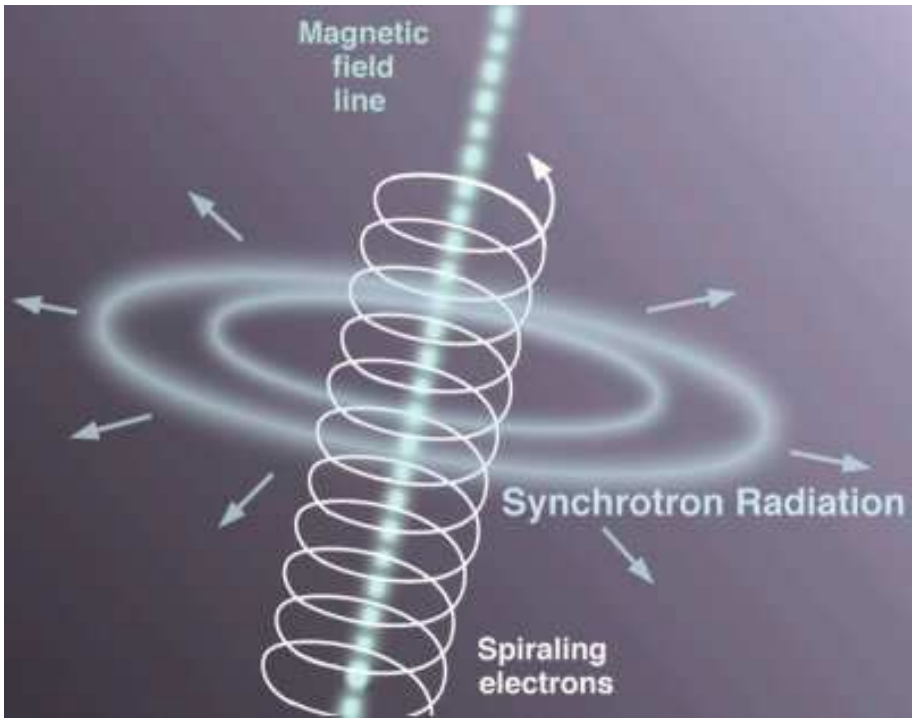

Figure 1.19: Synchrotron radiation produced by relativistic electrons gyrating in magnetic fields (image from `http://www.outerspacecentral.com/x_ray_page.html`).

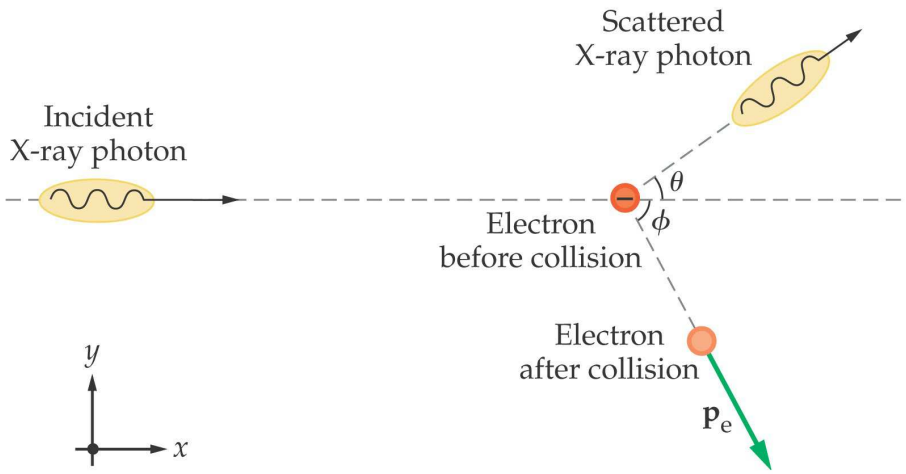

Figure 1.20: Compton scattering of a photon by an electron (image from Petrucci 2008).

not being in thermal equilibrium) from many kinds of astronomical objects, for example, radio emission from supernova remnants and extragalactic radio sources. Furthermore, it is thought that the process is also responsible for X-ray jet emission in AGN (Bai & Lee, 2001).

1.3.4 Comptonisation

Comptonisation is the inelastic scattering of a photon by a charged particle, usually an electron (Fig 1.20). The Compton effect was first observed by Arthur Compton in 1922, for which he earned the 1927 Nobel Prize in Physics.[10] Compton scattering is the energy exchange between a photon and an electron. When the incoming photon scatters with an electron, part of its energy is transferred to the electron. Since the photon loses its energy, the scattered photon has lower frequency (longer wavelength) according to the Planck-Einstein relation.

However, in case of that electron are relativistic, the process is inverse; since elec-

[10] http://www.nobelprize.org/nobel_prizes/physics/laureates/1927/compton-bio.html

trons have much more energy than photons, the scattered photons gain energy from electrons instead of losing their energy. This process is known as inverse Compton scattering since the photons are up-scattered by electrons. Inverse Compton scattering is an important phenomenon in X-ray astronomy since it is used to explained the non-thermal, high energy tail often seen in the X-ray spectra of binary systems which cannot be explained by thermal radiation such as blackbody (see Section 1.4.3).

1.3.5 Photoelectric effect

The photoelectric effect is a phenomenon in which a bound electron is released from an atom (i.e. become free electrons) when it absorbs an incoming photon (Fig. 1.21). This effect can be explained such that if the incoming photon which has energy $E = h\nu$ (where h is Planck's constant and ν is photon frequency) equal to or greater than the binding energy of the electron, it is absorbed by atom and the photon energy is transferred to the electron; part of the energy is used to free the electron from its atomic orbit – i.e. overcoming the binding energy – whilst the remaining energy is converted into kinetic energy allowing the electron to move with some velocity. In metallic material, a photoelectric current can be generated due to a number of free electrons being released within the material, leading to the name photoelectric since photons are converted into electrical current.

The photoelectric effect is important in X-ray astronomy because it works to distort the intrinsic X-ray emission from X-ray sources. Indeed, the intrinsic X-ray photons from the interesting sources can be absorbed by material along the line of sight – including interstellar medium in our Galaxy and the host galaxy of the X-ray sources, and the material associated with the sources – due to the photoelectric effect. An example of photoelectric absorption of intrinsic X-ray spectra is shown in Fig. 1.22; here the flat power-law continua with photon indexes of 2 are used to represent the intrinsic source spectra; it is clear that the effect can distort the intrinsic X-ray emission by absorbing X-ray photons, especially soft X-ray photons below 2 keV.

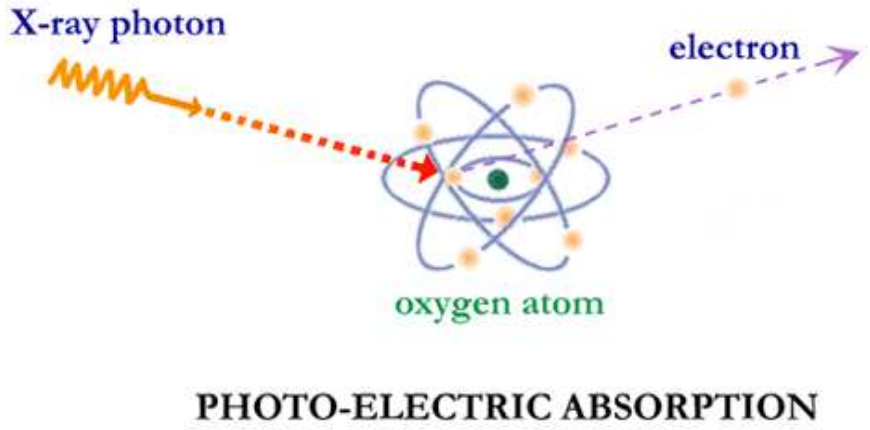

Figure 1.21: Photoelectric absorption (image from `http://chandra.harvard.edu/resources/illustrations/x-absorp.html`).

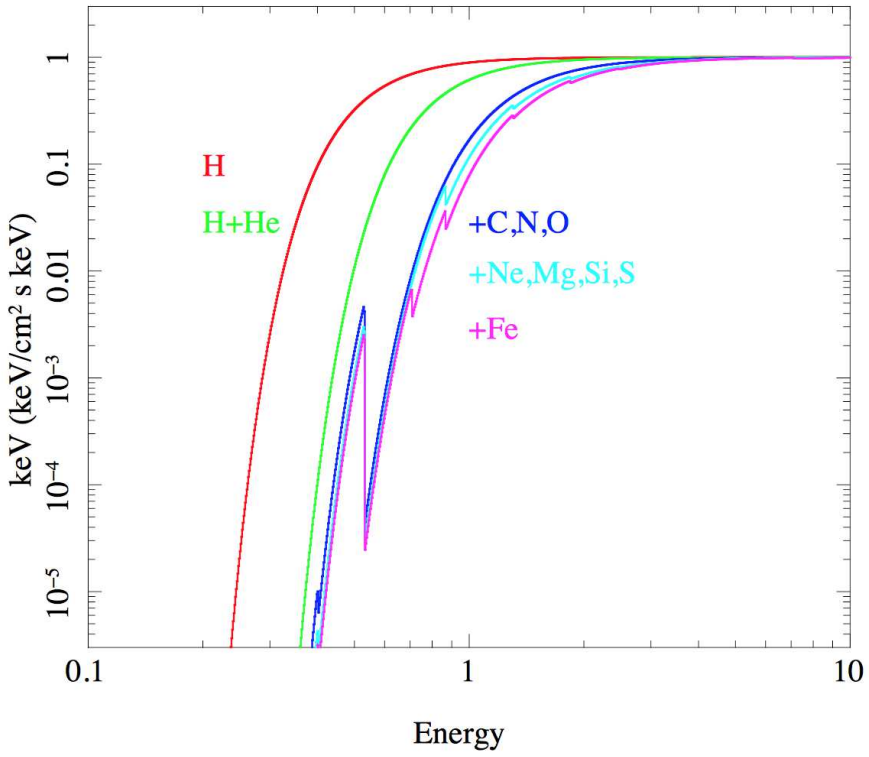

Figure 1.22: The effect of photoelectric absorption by various atomic elements on the typical power-law continua with the photon index of 2 (image from Done 2010).

1.4 Black holes

A black hole is a mathematically defined region of spacetime exhibiting such a strong gravitational pull that no particle or electromagnetic radiation can escape from it (Wald, 1984). The idea of a black hole began about a century after Sir Isaac Newton published the universal law of gravitation; in the 18th Century, two independent scientists, John Michell and Pierre-Simon Laplace, applied Newton's laws of gravity and proposed a similar idea, that some massive stars could have such strong gravity that their escape velocities are greater than the speed of light. Such an object was called a *dark star*. However, this idea was largely ignored at the time and in subsequent years as the effect of gravity on light was not understood yet.

In 1915, Albert Einstein published his theory of general relativity, showing how mass influences spacetime and the motion of light. Soon after, in 1916, Karl Schwarzschild applied Einstein's theory of general relativity and found a mathematical solution to the Einstein field equations that describes the gravitational field around a point mass; this solution defines the radius from the point mass M where the escape velocity from the surface of a sphere equals the speed of light, and is now named the Schwarzschild radius, $R_s = 2GM/c^2$ where G is the gravitational constant and c is the speed of light. Any object whose radius is smaller than its Schwarzschild radius will become a black hole. This was the first modern theoretical prediction of a black hole, and describes the simplest type of black hole system, a Schwarzschild black hole. This was later generalised based on the theory of general relativity to the 'no-hair' theorem, postulating that the black hole properties observed from outside the event horizon (Schwarzschild radius) can be described by only three parameters: mass, angular momentum and electrical charge. However, it seems that only first two parameters are important in astrophysical black holes since the charge of a black hole will be quickly neutralised by opposite charges.

A theory for the formation of astrophysical black holes had it origins in 1931, when Subrahmanyan Chandrasekhar derived the maximum mass limit for which collapsing stars can be halted by the balance between an outward force from electron degeneracy pressure and the inward crushing gravitational force, i.e. become white dwarfs; Chandrasekhar realised that above this limit, there is no stable solution

from electron degeneracy, and so the stars would continue to collapse. This implies further types of stellar remnant, which were later shown to be neutron stars or black holes (see detail in Section 1.4.1).

However, the direct observation of black holes is impossible since, by definition, no information from inside black holes can be observed outside the event horizon. However, we can detect black holes and study them indirectly by observing their effect on a nearby matter. If black holes reside in or pass through a region where there is matter in their close proximity – for example in the inter-stellar medium, or their companion stars in the case of binary systems – sometimes, the strong gravitational force is able to draw matter towards the black holes, in a process known as accretion (see Section 1.4.2 for details), in which the matter spirals inwards to the black hole through an accretion disc, and the gravitational potential energy is converted into electromagnetic radiation. This process allows astronomers to observe and study black holes.

The first confirmed black hole was Cygnus X-1. It was discovered in 1964 during the early X-ray rocket flights since it is one of the brightest X-ray sources in the sky. The source was observed later by the *Uhuru* satellite leading to the detection of X-ray intensity fluctuations on sub-second timescales; this was concluded as the discovery of a pulsating X-ray star at the time (Oda et al., 1971). Subsequently, in 1972, two independent measurements of the spectral Doppler shift of Cygnus X-1's optical counterpart allowed the first mass estimation of the primary accretor in the Cygnus X-1 system, and led to the conclusion that the mass of Cygnus X-1 could be $\gtrsim 2 - 3\ M_{\odot}$ (Webster & Murdin, 1972; Bolton, 1972), suggesting that Cygnus X-1 was likely to be a black hole rather than a neutron star. With further studies, soon after, it was concluded that Cygnus X-1 was most likely a black hole (Shipman, 1975).

In the following sub-sections, we will discuss the different types of black holes and their relative masses, the accretion process for matter near to black holes that produces the electromagnetic emission seen from around the black holes, and how the spectra of this emission appears in the X-ray energy regime.

1.4.1 Black hole types and masses

Based on observational evidence, astrophysical black holes can be broadly separated in two main classes – stellar-mass black holes and supermassive black holes – according to their mass. In fact, it is also a theoretical prediction that another type of black hole – miniature black holes – might have formed in the early Universe, shortly after the Big Bang, and have a mass much smaller than that of the Sun. However, astronomers do not have any observational evidence of their existence so, in this section, we will only discuss the other two types of black hole, which relate to the content of this thesis.

Stellar-mass black holes

Stellar-mass black holes can be formed as an endpoint of stellar evolution. Once stars finish burning their nuclear fuel, they can no longer be supported by the outward radiation pressure from the nuclear fusion, and so inward gravitational force starts to collapse the stars. The endpoint of this collapse can be determined by the stellar mass. For less massive stars, the gravitational collapse is halted and balanced by the degeneracy pressure of the star's electrons – as a result of the Pauli exclusion principle – and so these stars become white dwarfs. In the case of more massive stars (initial stellar mass $\gtrsim$6 $M_{\odot}$), the electron degeneracy pressure cannot resist the gravitational force and so they continue to collapse; the outer layer of the stars is blown out into space by an supernova explosion, leaving the stellar core, for which the mass is in excess of the Chandrasekhar limit – the maximum mass limit for which the electron degeneracy pressure can resist the gravitational force, which is 1.4 $M_{\odot}$. In this case, the gravitational energy combines electrons and photons together in the remaining stellar core via the inverse beta decay process, producing neutrons and neutrinos; thus they are called neutron stars as the gravitational collapse is stopped and balanced by neutron degeneracy pressure. However, in the case of the most massive stars (initial stellar mass of $\gtrsim$15 –20 $M_{\odot}$), the core is too massive to be supported by neutron degeneracy pressure (i.e. the mass is in excess of the Tolman-Oppenheimer-Volkoff limit); nothing can stop the gravitational collapse, so the matter is compressed into a gravitational singularity and the collapsing stars

become black holes.

The mass of black holes detected in our local Galaxy ranges between $\sim$3 – 20 $M_{\odot}$ (Remillard & McClintock, 2006), hence the name stellar-mass black holes (sMBHs). The mass of these stellar remnant black holes does not only depend on the initial stellar mass, but also depends on the amount of mass lost through both radiatively-driven winds during the stellar evolution and through the supernova explosion during the black hole formation. In a moderate metallicity environment, such as in our local Galaxy, these processes are efficient in expelling stellar matter and so limit the mass of black holes to be $\lesssim 20\ M_{\odot}$; however, in low metallicity environments, the processes are less efficient and so more mass remains to be collapsed into a black hole, of mass up to $\sim$80 $M_{\odot}$ (Belczynski et al., 2010), which we hereafter refer to as massive stellar black holes (MsBHs).

Supermassive black holes

Supermassive black holes are the most massive type of black hole, having masses between $\sim 10^5$ – $10^{10}\ M_{\odot}$. They are believed to reside in the centre of most galaxies (e.g. Magorrian et al. 1998), including our own Milky Way. In the cases in which they are accreting the mass around them, they result in AGN – an accretion disc around a supermassive black hole – emitting electromagnetic radiation at their galaxy centres in multiple-wavebands such as in the radio, microwaves, infrared, optical, ultra-violet, X-ray and gamma ray; the supermassive black holes can be detected from these emissions. However, in the case of normal galaxies such as the Milky Way, there is no AGN, but the existence of a supermassive black hole at our Galactic centre can be inferred from the path of material or objects such as stars moving around the invisible massive object (Fig. 1.23).

The origin of supermassive black holes still remains a puzzle. We don't know exactly how these extremely massive black holes form. One possible scenario is that the supermassive black holes start from *seed* black holes and grow by accreting matter and merging with other black holes. Alternatively, supermassive black holes might form together with their host galaxy by the collapse of supermassive objects

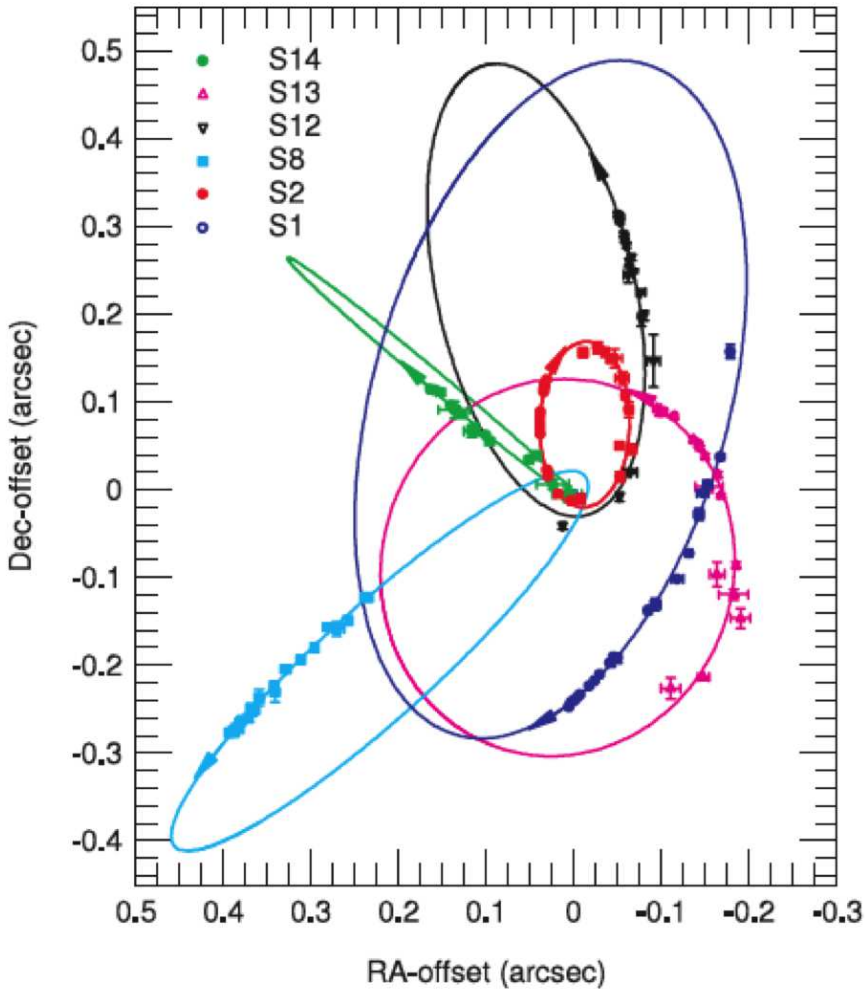

Figure 1.23: A projection of the stars orbiting around the Galactic centre, implying the existence of the Milky Way's supermassive black hole (image taken from Eisenhauer et al. 2005).

formed directly out of dense gas.[11]

The former scenario is interesting since the black holes' formation would require seed black holes; these seed black holes might form from the collapse of Population III stars in the low metallicity environment of the early Universe (Madau & Rees, 2001). The masses of these seed black holes are estimated to be $\gtrsim 100\ M_{\odot}$; indeed, these are another type of black hole called the intermediate mass black holes (IMBHs), the missing population potentially filling the gap in mass between sMBHs and supermassive black holes. The existence of IMBHs is still uncertain, although some observational evidence for an IMBH in the globular cluster G1 has been reported (Gebhardt et al., 2005). Indeed, it is thought that some extremely bright ULXs – the objects studied in this thesis – could be candidate IMBHs (see Section 1.5).

1.4.2 Black hole accretion

Black hole accretion can happen when there is matter near to black holes; due to the strong gravity of the black holes, in certain circumstances they are able to attract the matter to fall onto themselves. Accretion processes can occur in all types of black holes and the accretion mechanisms are broadly similar in principle. However, here we will focus particularly on the accretion processes in black hole binary (BHB) systems since they relate directly to the work presented in this thesis.

To explain physically how matter transfers into black holes, we may consider the concept of the Roche lobe, developed by a French astronomer named Edouard Roche. This is a region around a star in a binary system within which orbiting material is gravitationally bound to that star. Accounting for stellar gravity as well as the centrifugal force, the Roche lobe is the surface of critical gravitational isopotential, approximately tear-drop shaped for both objects, joining at the Lagrange point L1 where the gravity of both objects effectively cancels out (Fig. 1.24 top panel). Although the qualitative features of the Roche lobe are similar for all binary systems, the shape of the equipotentials is set by the mass ratio of the system whilst the overall

[11] See Volonteri (2010) for a review of supermassive black hole formation theory.

scale is set by the binary separation. Inside the Roche lobe, the matter is bound to each star by gravity; however, matter reaching outside the region can either escape the system, orbit both stars, or fall onto the binary companion.

In the top panel of Fig. 1.24, the material is bound inside the Roche lobe surface, so no matter transfers within the binary system. For some massive stars – usually O or B stars – the stellar wind is very strong and so energetic enough to escape the Roche lobe surface (see Fig. 1.24 middle panel); in this case, a fraction of the outflowing wind is captured by the compact object. The matter transferred to the compact object is accreted (called stellar wind accretion), and as it does so it emits electromagnetic radiation predominantly in the X-ray energy band; such an X-ray binary system is called a high mass X-ray binary (HMXB), which contains a companion star of mass $\geq 10\ M_{\odot}$. HMXBs tend to remain persistently bright on timescale of years and have a short life time ($\sim 10^5$ years); so they tend to associate with starburst galaxies (Tauris & van den Heuvel, 2006).

On the other hand, in cases in which the mass of the companion star is smaller than $\leq 1\ M_{\odot}$, the stellar wind is too weak to transfer matter to the compact object. However, in the course of the evolution of the binary system, if the binary separation decreases (case one) due to, for example, the loss of angular momentum via the stellar wind; or the donor star swells up (case two), for example, during the later stages of its stellar evolution as it becomes a giant or subgiant star, then mass may be transferred via the Lagrange point L1. Such a mass transfer is called Roche lobe overflow (Fig. 1.24 bottom panel). In case one, the mass transfer is driven by angular momentum loss and this results in short period binaries such as cataclysmic variables; on the other hand, the mass transfer in case two is driven by the expansion of the donor star – to giants or subgiants – and so the systems are confined to long period systems (Frank et al., 2002).

Roche lobe overflow will efficiently transfer mass from donor star to compact object as long as the donor star remains in contact with its Roche lobe. This type of X-ray binary system is defined as a low mass X-ray binary (LMXB). Such a system is likely to contain a companion star of type A or later (White et al., 1995). The lifetimes of these systems are long (10^7 – 10^9 years), compared to that of HMXBs.

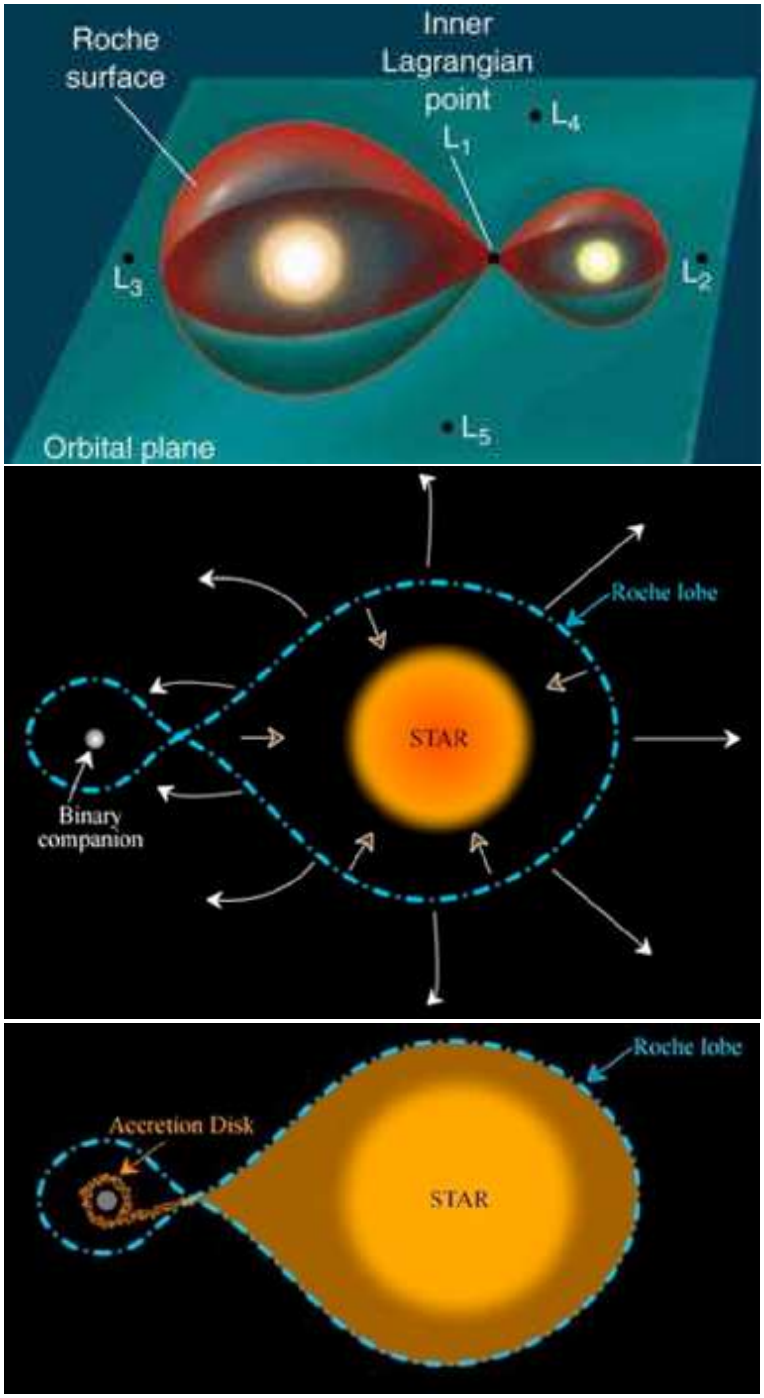

Figure 1.24: The Roche lobe surface of a binary system (Top panel; image from `http://www.daviddarling.info/encyclopedia/R/Roche_lobe.html`) and the mass transfer in a HMXB via stellar wind (middle panel) and in a LMXB via the Roche lobe surface (bottom panel; images from `http://astronomy.swin.edu.au/cosmos/R/Roche-lobe`). The sizes of Roche lobe surfaces in the X-ray binary systems are not to scale.

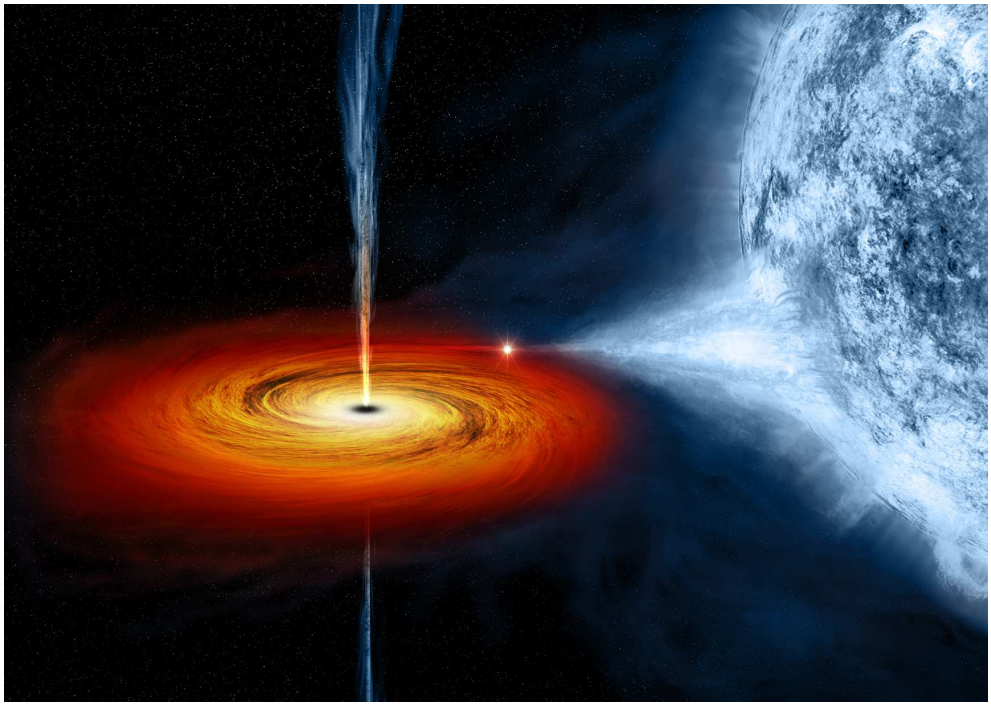

Figure 1.25: Artist's impression of an accretion disc around a black hole, formed by the matter transferring from the companion star (image from `https://www.nasa.gov/sites/default/files/cygx1_ill_0.jpg`).

Normally, LMXBs are very seldom X-ray emitting (i.e. they tend to exist in an inactive, quiescent state). However, LMXBs can often be triggered into activity by a process known as hydrogen ionisation instability – in which the gas temperature becomes hot enough to ionise hydrogen at some point in the accretion disc, leading to a higher mass accretion rate globally in the disc (see e.g. Done et al. 2007 for details of the process) – resulting in an X-ray outburst; these outbursts typically last for a month or more before the LMXB fades back into quiescence (Lewin et al. 1993; see Section 1.4.3 for the spectral transitions seen in X-ray outburst cycles).

The matter transferred to the black holes will also carry some angular momentum from the companion stars. This will prevent the matter from freefall onto the black holes; instead the matter conserves its angular momentum by spiralling towards the holes, forming a disc of material around the black holes known as an accretion disc (Fig. 1.25). The form of a standard accretion disc was derived by Shakura & Sunyaev (1973) and so is named a *Shakura-Sunyaev* disc. In such a disc it is assumed that the material spiralling around black holes is dense – i.e. optically

thick – and geometrically thin in the vertical direction. As the material moves circularly around black holes, at some distance from them, the outward centrifugal force is balanced by the inward gravitational force; thus the matter will spiral into the black holes only if it loses angular momentum via some mechanism. The main suggested means is due to friction with the matter moving in the adjacent layer. In addition, the matter can also lose angular momentum via turbulent motion and viscous stresses. As the matter spirals inward, gravitational energy is released; part of this energy is converted into the kinetic energy of the rotation whilst the remainder becomes electromagnetic radiation. Since the accretion disc is optically thick, the disc emission appears to be a summation of blackbody radiation from each accreting radius (See section 1.4.3). The total luminosity released from the disc can be approximated using Virial theorem: $L = GM\dot{m}/2R$. It is clear that the luminosity of the disc should increase proportionally with the mass accretion rate $\dot{m}$. However, the increase in the radiant flux of the disc also increases the outward radiation pressure. In fact, there is a critical luminosity where the inward gravitational force is equalled by the outward force from the radiation pressure, known as the Eddington limit

$$L_{\rm Edd} = \frac{4\pi GMm_p c}{\sigma_T} \simeq 1.3 \times 10^{38} \left(\frac{M}{M_\odot}\right) \ {\rm erg\ s^{-1}} \tag{1.4.1}$$

where G is the gravitational constant, M is mass of black hole, m_p is the mass of proton and σ_T Thomson scattering cross-section. Accretion above this limit could still be possible in some circumstances; we will discuss these in Section 1.5.1.

On the other hand, at very low accretion rates, the accretion mechanism does not seem to be similar to that described above. Indeed, observational data shows that a different accretion model is required. One strong possibility is an advection-dominated accretion flow (ADAF; Narayan & Yi 1995). According to the model, at low accretion rates the material density is also low and so the accretion flow is optically thin and geometrically thick. Thus the collisions between protons and elections are inefficient, leading to a two-temperature plasma of protons and electrons. This means that the major fraction of the gravitational energy gained by protons is

lost into the black hole, rather than transferred to electrons and radiated out from the flow.

1.4.3 X-ray spectra

We explain in Section 1.4.2 that black hole accretion processes can result in the emission of electromagnetic radiation. Depending on the mass of the black holes and their accretion mechanisms, their spectra could come out in different forms, across several electromagnetic wavebands. In BHB systems, the emission is predominantly in the X-ray energy band; and so in this section we will discuss the X-ray spectra of BHBs, given that they provide a basis for the X-ray spectral models of ULXs discussed in Section 1.5.1 and Section 1.5.2.

The typical components contributing to the X-ray spectra of BHBs are sketched in the top panel of Fig 1.26, whilst the bottom panel shows a plausible accretion geometry corresponding to the spectrum shown above. The X-ray spectra of BHBs are composed of multiple components (Gilfanov, 2010); the main ones are a disc component dominant in the softer energy band and a comptonised component dominant in the harder energy band; some spectra also require an additional reflection component. The soft spectral component is attributed to the emission from the optically thick and geometrically thin accretion disc (*Shakura-Sunyaev* disc). It can be explained physically by the multicolour disc blackbody (MCD) model. Such a model assumes that the thermal emission from the optically thick accretion disc is the summation of the blackbody emission from each accreting radius (Fig. 1.27); the blackbody temperature T at each individual radius R is different, with the inner radii hotter than the outer ones due to greater gravitational energy release, with the relationship between the two being $T(R) \propto R^{-3/4}$ for this type of disc. The comptonised component originates from soft disc photons comptonised in the geometrically thick, optically thin accretion flow located at the inner radius of the accretion disc (Fig 1.26 bottom panel), resulting in high energy photons. Finally, in cases where the comptonised photons illuminate the disc, these photons are reprocessed in the disc and contribute to a reflection component.

In general, the shape of a given BHB spectrum depends on the balance between

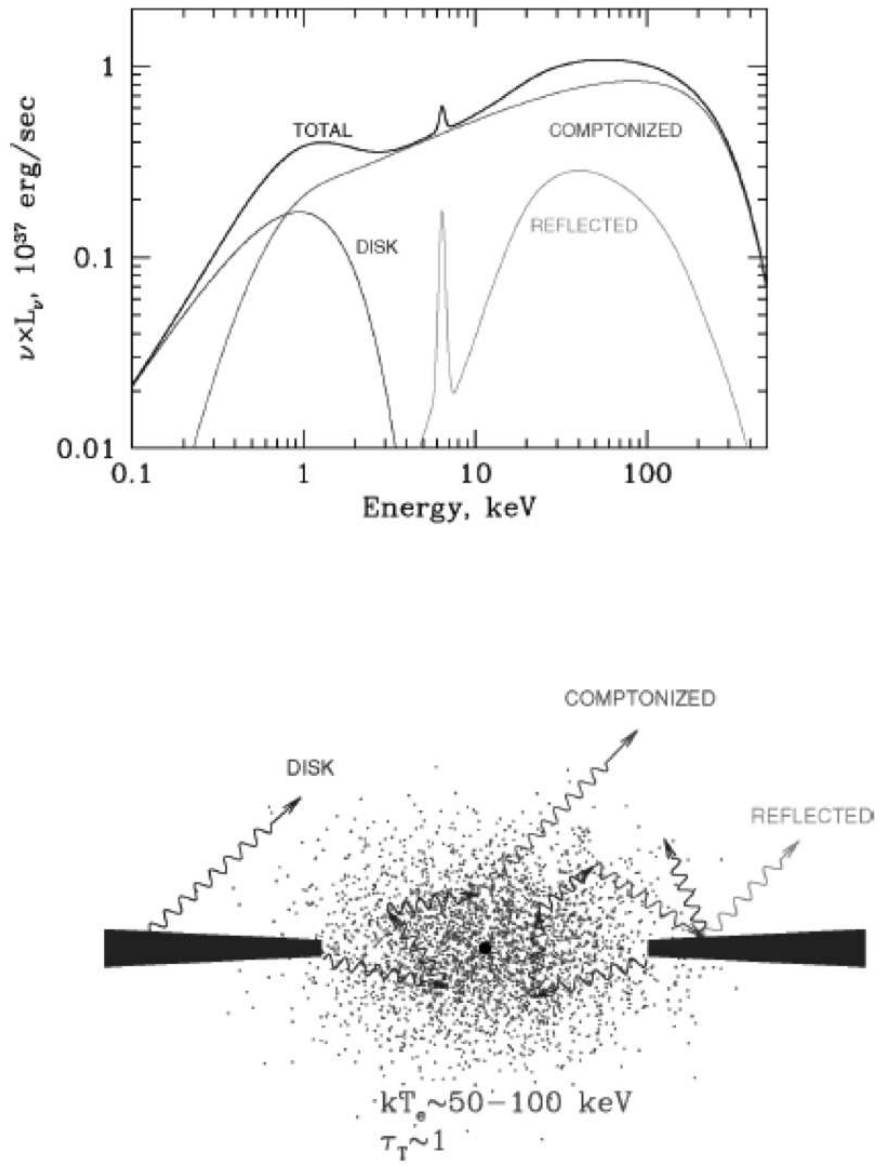

Figure 1.26: The main components of the X-ray spectra of BHBs (top) and a plausible geometry for the accretion, corresponding to the spectra above (bottom). Image credit: Gilfanov (2010).

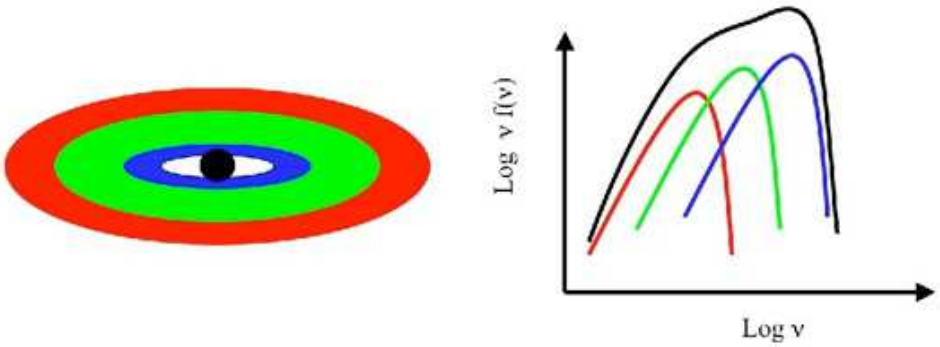

Figure 1.27: The thermal emission from a standard thin accretion disc. The spectrum of the disc can be explained as the summation of the blackbody emission from each accreting radius (image taken from `http://www.ualberta.ca/~jgladsto/Site/accretion.html`).

these three components. In fact, we find that the shape of an X-ray spectrum is to some extent a function of the X-ray luminosity; as demonstrated in the left panel of Fig. 1.28, the shape of the spectra change when the luminosity increases. The evolution of the X-ray spectra can be explained by the changes in the accretion geometry shown in the right panel of Fig. 1.28 (Done et al., 2007). At low accretion rates – low/hard state, $\dot{m} \sim 0.01$ – the spectra can be approximated by a power-law spectrum with $\Gamma \sim 1.4 - 2.1$ (Remillard & McClintock, 2006) up to ~ 100 keV, with a small contribution from a cool thermal component. In addition, a high fraction of flux variability (typical rms values of ∼30 %; Belloni 2010) and a persistent radio jet (Fender, 2006) can also be seen in this accretion state. We can interpret these spectra as the emission from an accretion geometry in which the optically thick disc is truncated at some large radius, whilst inside is an optically thin flow coupled to an inner disc corona. Indeed, a similar accretion geometry and mechanism is also thought to explain the faintest spectra seen at the lowest source accretion rates – known as the quiescent state – in which it is thought that the accretion is dominated by an optically thin and geometrically thick flow (Remillard & McClintock 2006, although see Corbel et al. 2006).

As the accretion rate increases to the thermal dominant state, the inner edge of the thermal disc moves inwards and is expected to reach the last stable orbit, which is the last orbiting radius before mass rapidly plunges to the black hole. This accretion state is also called the high/soft state since the spectra are seen

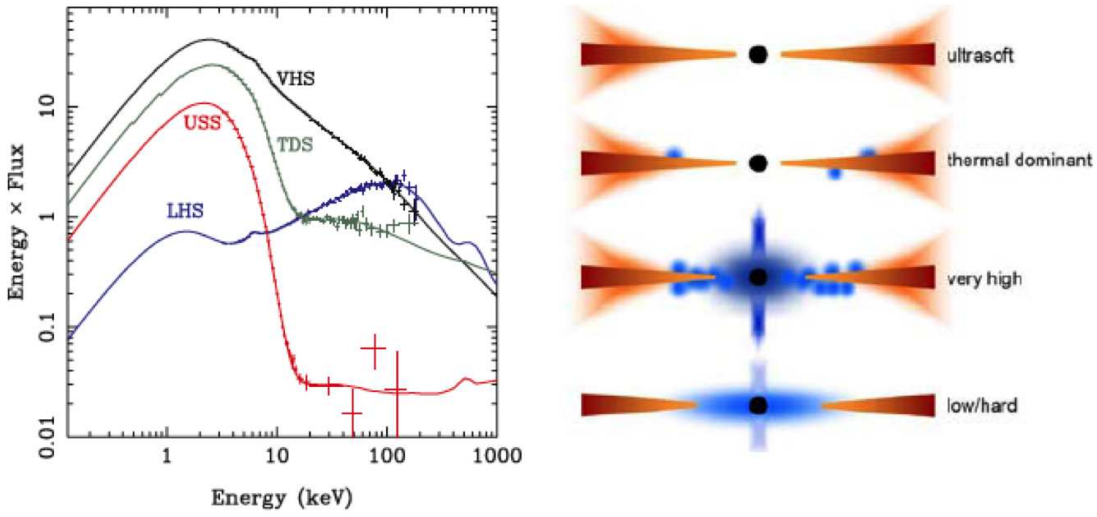

Figure 1.28: Left panel: the typical X-ray spectra of BHB systems at different accretion rates. Right panel: possible accretion geometries corresponding to the spectral states in the left panel. The optically thick and geometrically thin disc is shaded in red whilst the optically thin and geometrically thick accretion flow is coloured blue. Image credit: Done et al. 2007.

at high source luminosity and peak in the soft part of the spectrum, as the flux is dominated by thermal emission from the disc component ($\gtrsim$ 75%; Remillard & McClintock 2006), with only a small flux contribution from the high energy tail due to soft photons comptonised in a corona above the disc. The variability is in this state is very weak ($\sim$1% fractional rms; Belloni 2010). Finally, as the source accretion rate approaches the Eddington limit, the optically thick corona becomes denser and covers the inner part of the disc, resulting in a very high state. The spectra in this state are composed of a $\lesssim$ 50 per cent flux contribution from disc emission, with the remaining $\sim$40 – 90 per cent of the flux in a non-thermal high energy tail, approximated by a power-law spectrum with $\Gamma \gtrsim 2.4$ (Remillard & McClintock, 2006).

The transition between low/hard and high/soft spectral states is linked by intermediate states as shown in X-ray outburst cycle diagrams such as Fig. 1.29 (Belloni, 2010). From the quiescent state, as the outburst begins, the BHBs increase luminosity in the low/hard state, until they enter the hard-intermediate state, and the spectrum starts to become softer. The significant appearance of a thermal disc component can be seen in this intermediate state while the high energy spectral tail can

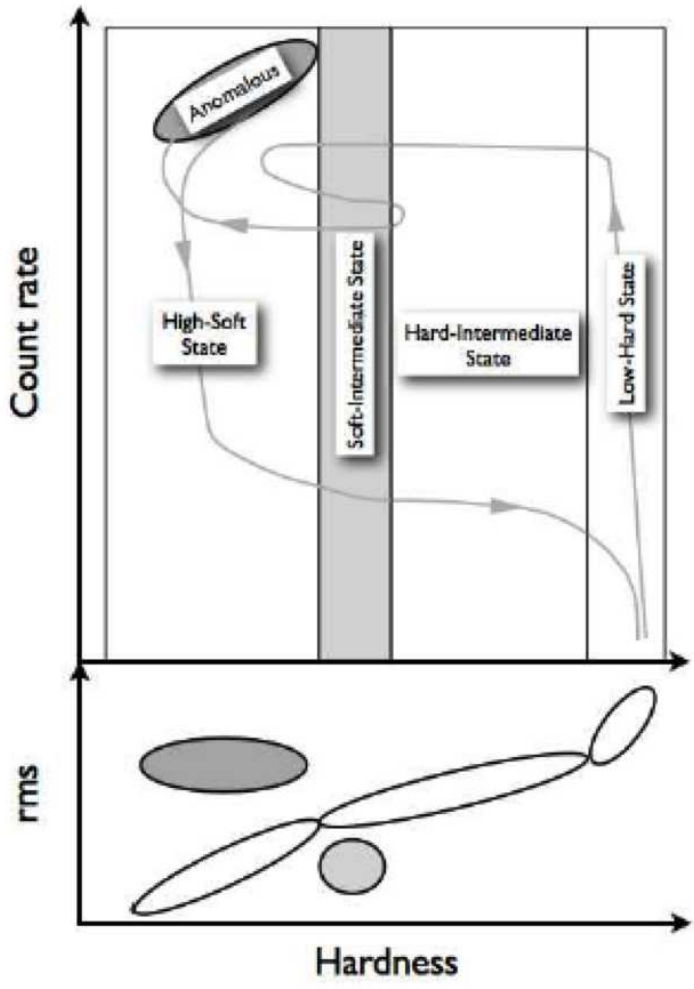

Figure 1.29: The X-ray outburst cycle of black hole transients, as seen in a hardness-intensity diagram (top) and hardness-rms diagram (bottom). Image credit: Belloni (2010)

be approximated by a power-law continuum with $\Gamma \sim 2.4 - 2.5$. The variability in this state is reduced from that in the low/hard state ($\sim 10 - 20\%$ fractional rms). Then, as the outburst continues, the black hole transients enter the soft-intermediate state – which has properties consistent with the very high state described above – in which the level of variability drops dramatically; it can be as low as a few per cent fractional rms. No significant change appears in the spectral hardness, it is only slightly softer than that of the hard-intermediate state; however at this point the jets are ejected in explosive events. After the soft-intermediate state, the black hole transients enter the high/soft state as described above. Finally at the end of the outburst cycle, the source luminosities drop and they move back to the quiescent state through the lower luminosity branches of the soft- and hard-intermediate states as shown in Fig. 1.29. More details on the definition of the spectral states and the outburst cycle are given by Belloni (2010).

1.5 Ultraluminous X-ray sources

Ultraluminous X-ray sources are defined as extragalactic X-ray point-like sources for which the observed luminosity in the 0.3 – 10 keV energy band reaches or exceeds the Eddington limit for a ~ 10 $M_{\odot}$ black hole (i.e. $\geq 10^{39}$ erg s^{-1}). Given that they are non-nuclear objects by definition, they cannot be powered by accretion onto the supermassive black holes at the centres of galaxies. Instead, their extreme luminosities argue for ULXs being powered by one of two possible classes of black holes. On the one hand, they could be powered by an exotic new class of black holes, the IMBHs ($10^2 M_{\odot} < M_{\rm BH} < 10^4 M_{\odot}$; Colbert & Mushotzky 1999), and if so then ULXs are accreting material at a sub-Eddington rate, similar to most known BHBs and AGN. Alternatively, ULXs could be powered by ordinary sMBHs in an exotic physical state in which they are somehow able to accrete material at a rate that exceeds the Eddington limit. A third possibility may also be on the table; ULXs may host MsBHs ($20 M_{\odot} < M_{\rm BH} < 100 M_{\odot}$) which possibly form in metal poor environments (e.g. Zampieri & Roberts 2009), and would be accreting matter at $\sim$ the Eddington rate.

ULXs were first discovered by the *Einstein* telescope (Fabbiano, 1988, 1989). At the time, the classification of the sources was still ambiguous; the lack of long term monitoring made it difficult to distinguish between persistently luminous sources (i.e. accretion onto compact objects) and transient events such as young supernovae. A decade later with the launch of a new generation of X-ray telescopes such as *ROSAT* and *ASCA*, astronomers were able to resolve some ULXs; the observational data indicated that the vast majority of these sources cannot be young supernovae. However, the interpretation of the nature of the sources remained unclear, with the most likely scenarios proposed to include super-Eddington accretion onto sMBHs, accretion onto massive black holes (M_{BH} ∼100 – 200 $M_{\odot}$, i.e. IMBHs) and beamed sources (e.g. Komossa & Schulz 1998; Okada et al. 1998).

In fact, a reasonable number of ULXs were first identified after the launch of *ROSAT* and *ASCA*. The *ROSAT* pointed phase led to the construction of several *ROSAT*/HRI catalogs of non-nuclear X-ray sources including ULXs (Colbert & Mushotzky, 1999; Roberts & Warwick, 2000; Colbert & Ptak, 2002), starting the study of ULXs as an active topic of research in X-ray astronomy. In the beginning, various names were used to identify this class of X-ray object in each individual ULX study, including extraluminous X-ray binaries (Colbert & Mushotzky, 1999), superluminous X-ray sources (Roberts & Warwick, 2000) and intermediate-luminosity X-ray objects (Colbert & Ptak, 2002). The term ULX was first used by the Japanese *ASCA* teams (Okada et al., 1998; Mizuno et al., 1999) and subsequently became the common name generally accepted for these objects.

The current detailed studies of ULXs were enabled by the launch of the present generation of X-ray satellites i.e. *Chandra*, *XMM-Newton*, *Suzaku* and *Swift*. The good quality data and large number of ULX detections they provide present an outstanding opportunity to investigate the nature of ULXs. The good sensitivity and large field-of-view of *XMM-Newton* has led to the identification of many ULXs which were not reported previously; indeed, the largest ULX catalogue was constructed based on the 2XMM Serendipitous Survey, and contains 470 ULX candidates (Walton et al., 2011). Further large numbers of ULXs residing in dense and/or spatially complex areas can be resolved by the high spatial resolution of the *Chandra* tele-

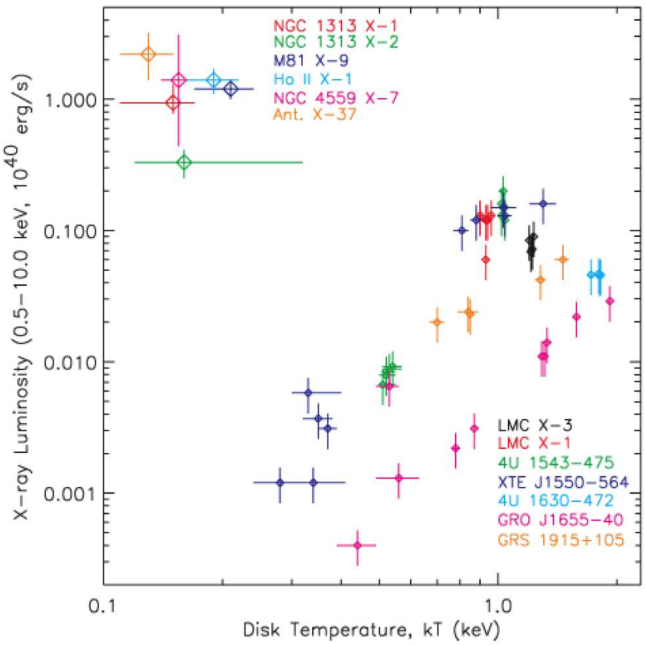

Figure 1.30: The disc temperatures of ULXs inferred from the softer component of their spectra (Miller et al. 2004b). The disc temperatures of BHBs are also plotted for comparison. It is obvious that the ULX disc temperatures are much cooler than those of the BHBs.

scope. Furthermore, good quality spectra of ULXs can be obtained from high sensitivity CCD cameras. These challenge astronomers to interpret the physical nature of ULXs. Indeed, a number of physical models and scenarios have been proposed to explain the nature of ULXs as a result of the modern X-ray observations. The key results can be summarised as the following.

At the beginning of the modern era of ULX studies, evidence seemed to point towards ULXs containing IMBHs. In particular, early studies of moderate quality ULX spectra found that they were composed of two components: a disc-like component and a power-law high energy tail (e.g. Miller et al. 2003, 2004a), similar to the components seen in BHB spectra. However, it was found that the disc temperatures of ULX spectra are much cooler (~ 0.2 keV) than the disc temperatures in the BHB spectra (Fig. 1.30; Miller et al. 2004b). Assuming that ULX spectra are directly analogous to BHB spectra, the disc component indicates the temperature of the innermost radius of the ULX accretion disc. According to the standard accretion disc model, the disc temperature kT is $\sim (M/10M_{\odot})^{-1/4}(L/L_{Edd})^{1/4}$ keV (Shakura

& Sunyaev, 1973). This equation implies that the disc temperature should be lower for more massive accreting objects at the same accretion rate. From these low disc temperatures a mass of $\sim$1000 $M_{\odot}$ was inferred, leading to the interpretation that ULXs host accreting IMBHs.

However, the IMBH interpretation struggles to explain the ULX populations found in galaxies. Firstly, observational data have shown that ULX populations have a close relationship with the star-forming regions in galaxies; this is best illustrated by the Cartwheel galaxy, in which the ULXs appear to reside in ongoing star-forming regions (see e.g. Gao et al. 2003). King (2004) showed that if all ULXs contain IMBHs, they would require a very large mass to have appeared in star clusters to explain the numbers of ULXs currently viewed in the Cartwheel, which is unlikely; in fact, his calculations were consistent with ULXs as a population of HMXBs – i.e. sMBHs with typical mass of $\gtrsim$10 $M_{\odot}$ – accreting matter at super-Eddington rates. Another inconsistency with IMBHs appears in the study of X-ray luminosity function (XLF). The appearance of a break at $\sim 2 \times 10^{40}$ erg s^{-1} in the XLFs of point-like X-ray sources detected in nearby galaxies (Grimm et al. 2003; Swartz et al. 2004, 2011; Mineo et al. 2012a) makes it difficult to reconcile that IMBHs dominate the population in the upper end of XLFs. According to Equation 1.4.1, the break luminosity is $\sim$Eddington for a 100 $M_{\odot}$ black hole; therefore if IMBHs do dominate this population at high luminosities, they rather inexplicably turn off below their Eddington limit. This appears very unlikely.

Furthermore, subsequent studies of ULXs focusing on high quality X-ray spectra have confirmed that ULX spectra are composed of two individual components: one dominating at energies below 1 keV (the soft excess) and another dominating at photon energies above 2 keV. However, it has been demonstrated that the hard component cannot be simply approximated by a flat continuum such as power-law model (see Fig. 1.31; Roberts et al. 2005; Stobbart et al. 2006; Gladstone et al. 2009), but is instead turned over at energies above 2 keV (hence we hereafter refer to it as the hard curvature component). In fact, the hard curvature detected in ULX spectra is unlike the behaviour of any of the common accretion states of BHBs (see Section 1.4.3), and so it is difficult to explain ULXs in the context of IMBH

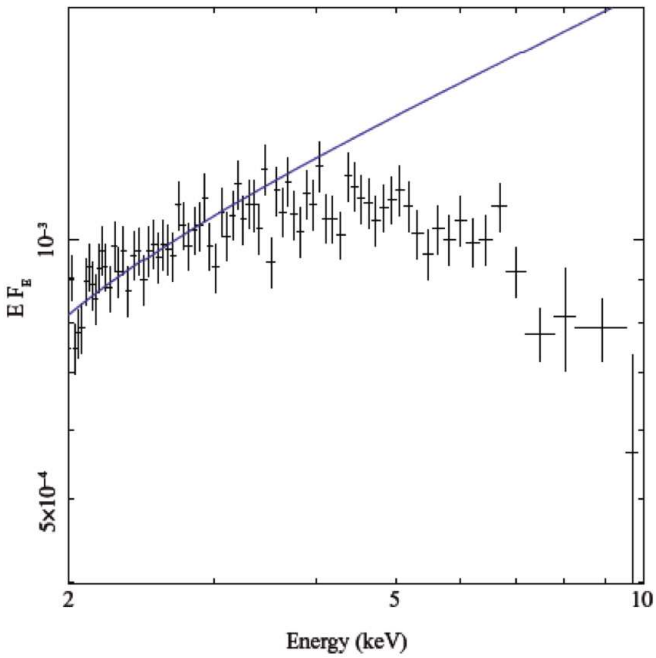

Figure 1.31: *XMM-Newton* EPIC pn spectrum of NGC 1313 X-2 in the 2-10 keV band. The spectrum has a pronounced high energy turnover and so cannot be approximated by the power-law continuum plotted as the blue solid line (Gladstone et al., 2009).

accretion, as we would expect the sub-Eddington accretion of IMBHs to lead to a common BHB spectral state (with some adjustments for mass scaling, e.g. a cooler accretion disc). In fact, the curvature suggests ULXs operate in a different spectral state; Gladstone et al. (2009) called this the *ultraluminous state*, and noted its differences from sub-Eddington states suggest that ULXs are powered by sMBHs accreting material at super-Eddington rates.

Recent studies of ULXs support this conclusion; they report the first direct mass constraints on the black holes powering ULXs, and find them to fall in the regime of sMBHs (Middleton et al., 2013; Liu et al., 2013). Most pertinently, an sMBH in NGC 7793 is seen to display the hallmarks of the ultraluminous state when accreting at a demonstrably super-Eddington rate (Motch et al., 2014). However, while studies suggest that the majority of the population of ULXs are sMBHs accreting material at super-Eddington rates, there is clear evidence that the population is heterogeneous. For example, a luminous ULX in M82 was recently shown to display rapid pulsations that can only be coming from a neutron star (Bachetti et al., 2014), and some of

the very brightest ULXs remain good candidates for sub-Eddington accretion onto IMBHs, for example HLX-1 in ESO 243-49 (Farrell et al., 2009) and a sample of the most extreme ULXs discussed by Sutton et al. (2012), including NGC 2276 3c (Mezcua et al., 2015). In this thesis, we will focus mainly on the super-Eddington accreting sMBHs; in the following subsections, we will discuss how ULX accrete material at rates that exceed the Eddington rate, and what their X-ray spectra look like in this accretion regime. The characteristics of the populations of ULXs found in the local Universe, most particularly their habitats, will also be discussed.

1.5.1 Accretion in the supercritical regime

We described in Section 1.4.3 how BHBs accrete material in a range from sub-Eddington to ∼Eddington rate. However, as discussed above, it is though that ULXs are super-Eddington accretors. In this section, we will review how black holes might accrete material at rates that exceed the Eddington limit.

Theoretical studies have suggested that ULXs could release excess energy via two different methods: using slim disc geometry, and the launch of an outflowing wind (Poutanen et al., 2007). In the slim disc model (Abramowicz et al., 1988), the disc scale height H/R is increased to ∼1, due to radiation pressure support inside the disc. Inside a trapping radius, the disc becomes advection dominated, in which the photon diffusion time from the interior to the surface of the disc is greater than the accretion time; so photons are advected into the black hole before they radiate out from the disc. This results in a change in the radial temperature profile from $T(R) \propto R^{-3/4}$ in case of the standard disc to $T(R) \propto R^{-1/2}$ in the slim disc model.

On the other hand, ULXs could also release excess energy by the launch of an outflowing wind. In this model, matter is blown away from the disc by radiation pressure, and a wind is launched from within the photospheric radius $R_{\rm sph} \approx \dot{m} R_{\rm in}$ with the local escape velocity $v_{\rm esc} \geq \sqrt{2GM/R}$, that forms a funnel-like structure around the rotation axis of the black hole. Here the mass is lost through all disc radii within the photospheric radius, maintaining the local Eddington accretion rate $\dot{m}$ to be ∼1. In fact, in recent models it is suggested that both methods can operate simultaneously (Poutanen et al., 2007). This has been supported by numerical

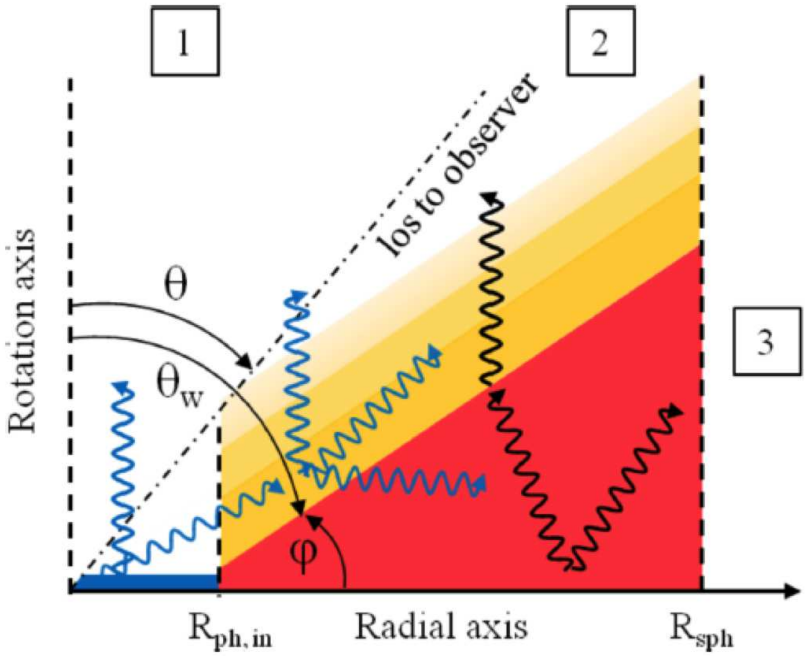

Figure 1.32: A schematic representation of a supercritical accretion model (Middleton et al., 2015). The innermost accretion disc is shaded in blue whilst the advection dominated disc and outflowing wind are shaded in red and yellow, respectively. The arrows indicate the photons emerging from each region. The numbers 1, 2 and 3 indicate the viewing angles associated with different ULX spectra as discussed in Section 1.5.2.

studies, including simulations of accretion flows at supercritical rates (e.g. Ohsuga 2007; Ohsuga & Mineshige 2011; Takeuchi et al. 2013), that show the disc is predicted to inflate to a large scale height and become advection dominated (i.e. slim disc), and to launch a massive outflowing wind from its surface.

A possible accretion geometry for a supercritical accretion regime has been described recently by Middleton et al. (2015; see also Poutanen et al. 2007), and is sketched in Fig. 1.32. According to the model, the supercritical inflow can be broadly defined by three different zones. The first zone is the innermost region where the radius is less than the inner photospheric radius ($R < R_{\rm ph,in}$). Within this zone, the wind is transparent ($\tau < 1$); the zone will appear as hot emission from the innermost disc, in which the peak temperature is distorted by some level of colour correction. Next, the second zone is where the radius is between the inner and outer photospheric radius ($R_{\rm ph,in} \leq R \leq R_{\rm ph}$). The accretion in this zone is locally Eddington

and so a huge amount of material is blown away from the underlying advection dominated disc. The wind in this zone is opaque and so the energy generated in the disc is thermalised in the wind and emerges at large radii ($\sim$ twice the radius at which it is generated). The result is smeared blackbody emission from $R_{\rm ph,in}$ to $R_{\rm ph}$ with a radial temperature profile $T(R) \propto R^{-1/2}$. Finally, the third zone is the outer photosphere where $R > R_{\rm ph}$. The wind becomes transparent again in this zone and so the radiation escapes at about the radius it is generated. The emission from this zone is a combination of the radiation from the outer disc and reprocessed X-ray photons downscattered through the optically-thick outflowing wind.

1.5.2 X-ray spectra

The characteristics of typical ULX X-ray spectra in the 0.3-10 keV energy band are summarised in Fig. 1.33. Overall, the spectra are composed of two components: the soft excess and the hard curvature (high energy turnover). A variety of empirical and physical models can be used to explain the spectra, leading to different interpretations of the nature of ULXs. For low and moderate quality spectra, a semi-empirical model of DISKBB + power-law is sufficient to approximate the ULX spectra, where the first component is an implementation of a multi-colour disc blackbody model (MCD; see Mitsuda et al. 1984). As the model describes the soft excess by the DISKBB component, and the high energy curvature can be approximated by the power-law component, these lead to a cool disc temperature, resulting in the past interpretation that ULXs contain IMBHs (e.g. Miller et al. 2003, 2004a,b; see above). Indeed, due to the simplicity of this model, it was later used to approximate ULX spectral shape in the classification of different ULX spectral regimes (Fig. 1.35; see Sutton et al. 2013b).

However, a focus on the highest quality spectra showed that the hard component displays a subtle but pronounced curvature that requires a curved component for adequate spectral fitting (Stobbart et al. 2006; Gladstone et al. 2009). This turnover has more recently been confirmed beyond all doubt by broadband *NuSTAR* observations, that show this break extends well above 10 keV (Fig. 1.34; Bachetti et al. 2013; Walton et al. 2014). Hence it has been shown that both hard and soft spectral

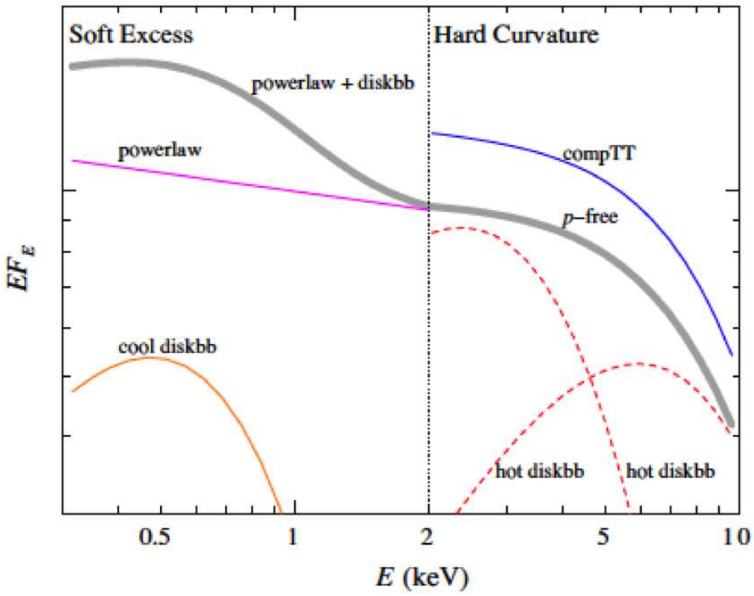

Figure 1.33: The typical shapes of ULX spectra in the 0.3-10 keV energy band (Feng & Soria, 2011). This shows that the spectrum is typically composed of two components. The models that successfully approximate the individual components of the spectrum are also highlighted.

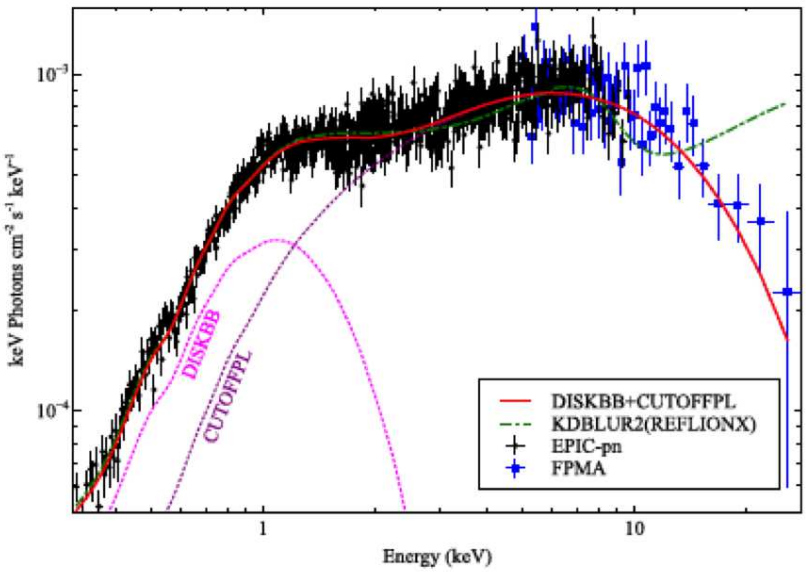

Figure 1.34: The spectrum of NGC 1313 X-1, observed simultaneously by *XMM-Newton* and *NuSTAR* (Bachetti et al., 2013). It is obvious that the high energy curvature is cut-off at energies below 30 keV.

components can be well represented by curved thermal-like models, such as DISKBB, DISKPBB or COMPTT models in XSPEC[12], depending on the assumed ULX geometry (e.g. Walton et al. 2014). Initially, the hard spectral component was explained as a comptonised component (e.g. COMPTT), a direct interpretation of which is that an optically cool and thick corona is present that obscures the innermost regions of the disc, whilst a standard disc model such as a MCD was used to describe the soft emission from the unobscured, outer part of the disc emission (Gladstone et al., 2009; Vierdayanti et al., 2010; Pintore & Zampieri, 2012). However, more recent works present an alternative interpretation. In this the hard spectral component can be physically attributed to the hot inner parts of the disc, that require a large colour correction (Middleton et al. 2011a; Kajava et al. 2012); on the other hand, the soft spectral component can be explained by attributing the cool disc component to an optically thick, massive outflowing wind that thermalises and downscatters much of the emission within it. It has been shown by Kajava & Poutanen (2009) that the temperature of the soft spectral component inferred from the MCD model relates to the soft component luminosity as $L_{\rm soft} \propto T_{\rm disc}^{-3.5}$, instead of the expected standard accretion disc correlation of $L_{\rm soft} \propto T_{\rm disc}^{4}$. This strongly implies that the soft spectral component could be the emission from an optically thick outflowing wind that cools as its luminosity increases (Poutanen et al., 2007). However, it has also been shown that a $L_{\rm soft} \propto T_{\rm disc}^{4}$ correlation can be obtained from the same dataset by excluding observations with large uncertainties and constraining the column density of each ULX to remain the same across different observations (Miller et al., 2013).

ULXs generally appear to exhibit the two component spectral characteristics described above at luminosities above 3×10^{39} erg s^{-1}. Below this luminosity, they appear to possess a broad disc-like spectrum. Sutton et al. (2013b) classified ULX spectra into three different regimes: broadened disc (BD), hard ultraluminous (HUL; hard component dominated spectrum) and soft ultraluminous (SUL; soft component dominated spectrum; Fig. 1.35). The evolution between these three spectral regimes can be explained as follows (Sutton et al. 2013b; Middleton et al. 2015).

[12] `https://heasarc.gsfc.nasa.gov/xanadu/xspec/`

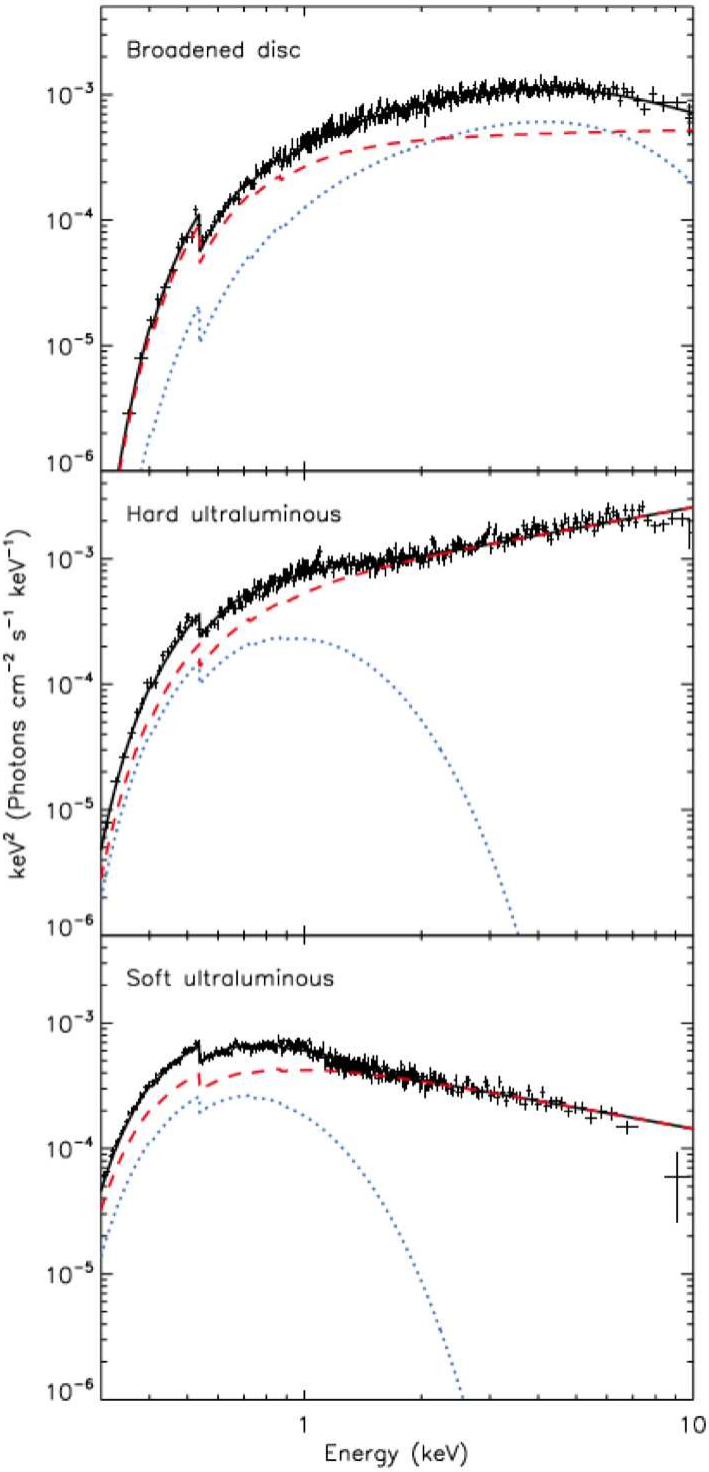

Figure 1.35: The three ULX spectral regimes, as classified by Sutton et al. (2013b).

At lower ULX luminosity ($\lesssim 3 \times 10^{39}$ erg s^{-1}), where sMBHs would be accreting material at ∼Eddington rate, the spectra are dominated by objects in the BD regime. These spectra are too broad to be approximated by a single disc component; instead, they require a double component model, and it has been suggested that this is an emergent form of the two component spectra seen in other ULXs (Middleton et al. 2011b). At higher luminosity ($\gtrsim 3 \times 10^{39}$ erg s^{-1}), ULXs accrete material at super-Eddington rates (again if they host sMBHs) and their spectra are predominantly two component in form, i.e. HUL or SUL. According to the super-Eddington accretion model described in Section 1.5.1, the balance between the soft and hard components is dependent on two factors – the mass accretion rate and viewing angle – which between them control the amount of wind emission and the view of the central disc emission that contribute the soft and hard components of the ULX spectra, respectively. Depending on the viewing angle of the observer, the observed ULX spectra can be divided into three cases – positions 1, 2 and 3 in Fig. 1.32. For a face-on or low inclination observer (position 1), the spectra appear HUL as the central hard emission can be seen directly. As the accretion rate increases, the wind increases and its funnel opening angle shrinks, and so there might be two possible changes: i) the wind enters the line of sight resulting in softer spectra since the central hard photons are either scattered out of the line of sight, or downscattered through the wind, or ii) the wind remains out of the line of sight and so the spectra get harder as the central hard photons are increasingly beamed up the funnel. Next, for the ULXs observed at larger inclination angle (position 2) where the wind intercepts the line of sight, the spectra appear SUL as hard photons are scattered away from this line of sight by the wind, whilst some that are downscattered through wind also increase the softness of the spectrum; such an effect becomes stronger with an increase in mass accretion rate, resulting in increasingly softer spectra. Finally, for an edge-on observer (position 3), the spectra are predicted to be extremely soft in X-rays, and possibly peak in the UV (ultraluminous UV sources; Kaaret et al. 2010). Note that within this thesis, we only consider the ULX X-ray spectra observed from positions 1 and 2.

This model is strongly supported by work considering the spectral and temporal

variability properties of ULXs, where very high levels of flux variability on timescales of $\lesssim$ 200s of seconds are associated with the hard spectral component when the spectrum is dominated by the soft component (i.e. the ULX is in a SUL regime; Sutton et al. 2013b). This can be explained by the wind being an inhomogeneous medium, where optically-thick clumps pass through the observer's line-of-sight to the central regions of the accretion flow and scatter away the hard photons (Middleton et al. 2011a; Middleton et al. 2015; Sutton et al. 2013b). That this variability is seen when the spectrum is in the SUL regime supports the notion that both accretion rate and viewing angle dictate the observational appearance of ULXs; in the SUL regime the line-of-sight intersects the wind, which diminishes the hard component, and adds extrinsic variability. In contrast, when viewed down the funnel, a HUL spectrum is observed, with little or no strong variability.

The major missing piece of the puzzle in this model is a direct detection of the wind material, from absorption or emission lines in the optically thin phase of the wind that must be present as the wind diffuses away from the disc. There have been attempts to search for direct evidence of an outflowing wind imprinting Fe-K absorption features on ULX X-ray spectra; however, no such feature was detected (Walton et al. 2012; Walton et al. 2013a), not least due to the observation target being a HUL object. However, it has been argued that evidence for a wind can be seen in residuals to SUL spectra seen at $\sim$ 1 keV, that can be modelled by broad absorption features, and could be the result of absorption in an optically thin plasma, part of the extended wind located at $\geq 1000\ R_{\rm g}$[13] (Middleton et al., 2014).

1.5.3 ULX populations

In general, ULXs are found in all types of galaxy. Given that the majority of the ULX population is likely to be accreting sMBHs, we can classify them into the same types of X-ray binaries as BHBs in our own Galaxy, depending on their secondary star. Statistically, the brighter ULXs are far more likely to be detected in spiral galaxies, rather than in elliptical galaxies. It was reported that about one third

[13]Where $R_{\rm g}$ is gravitational radius, equal to $R_{\rm s}/2$.

of the ULXs detected in spiral galaxies have luminosity $\gtrsim 4 - 5 \times 10^{39}$ erg s^{-1} and $\sim$10 per cent are brighter than 1×10^{40} erg s^{-1} (Feng & Soria 2011; see also Swartz et al. 2004; Walton et al. 2011); these ULXs are thought to associate with the HMXB population in thermal-timescale mass transfer episodes in which the donor stars evolve and expand to fill their Roche lobes, providing mass transfer at highly super-Eddington rates (King et al., 2001). In contrast, most ULXs detected in elliptical galaxies have luminosity $\lesssim 2 \times 10^{39}$ erg s^{-1} and only a small fraction of these ULXs are brighter than 2×10^{39} erg s^{-1} (Feng & Soria, 2011).

In terms of the numbers of ULXs detected in galaxies, in the local Universe (D < 14.5 Mpc) we detect one ULX per volume of 57 Mpc^3, one ULX per mass of 3.2×10^{10} $M_\odot$ and one ULX per star formation rate (SFR) of $\sim$0.5 $M_\odot$ yr^{-1}, on average (Swartz et al., 2011). Individually, the detection rate tends to increase in less massive galaxies, scaling as $M^{-0.6}$ (Feng & Soria, 2011). In elliptical galaxies, the average number of ULXs per unit mass is lower than the average value: just one ULX per 10^{11} $M_\odot$ (Feng & Soria, 2011; Plotkin et al., 2014). Hence more ULXs are found in low mass spiral and irregular galaxies; it has been suggested that this is because they have higher specific SFR and so more efficiently produce ULXs (Walton et al., 2011). Indeed, it has been suggested that the dominant population of ULXs is related to ongoing or recent star forming regions in younger systems. The surface density profile of ULX numbers with host galaxy radius is strongly peaked towards the centre of the host galaxies (Swartz et al., 2011), implying a connection between ULXs and stellar population. Indeed, it was found that ULXs are likely to reside in the bluer regions, indicative of recent star forming regions (e.g. Fig. 1.36; Gao et al. 2003; Swartz et al. 2009; Smith et al. 2012). It was also reported that high numbers of ULXs are detected in starburst galaxies (Fabbiano et al., 2001; Lira et al., 2002). In fact, it was found that the number of detected ULXs is directly proportional to the SFR of their host galaxies (e.g. Mineo et al. 2012a).

One method to analyse the ULX population is through the X-ray luminosity function (XLF). The XLFs of high SFR galaxies are dominated by HMXBs whilst those of elliptical galaxies are dominated by LMXBs; the ULX population contributes the high luminosity tail of the XLFs. With *Chandra* and *XMM-Newton*

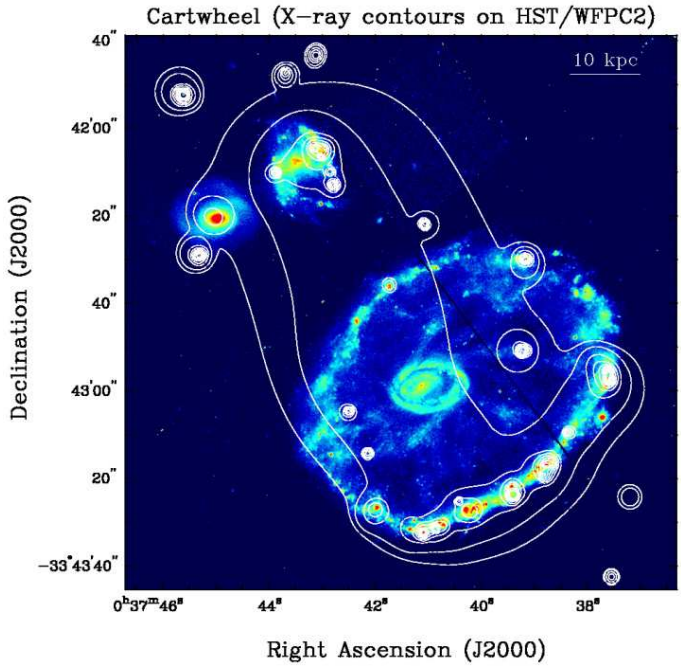

Figure 1.36: *Chandra* X-ray contours overlaid on the *HST*/WFPC2 optical image of the Cartwheel galaxy (Gao et al., 2003), demonstrating the connection between ULXs and recent star forming regions.

observations of galaxies (including serendipitous source detections), complete XLFs can be constructed (Grimm et al. 2003; Colbert et al. 2004; Swartz et al. 2004; Walton et al. 2011; Mineo et al. 2012a). Overall, the cumulative XLFs of the high SFR systems are approximately a simple power-law with a slope of $\sim$0.6 – 0.8 whilst those of elliptical galaxies are a simple power-law with a steeper slope of $\sim$1.5; the XLF normalisation of the high SFR galaxies is proportional to their SFR whilst that of the elliptical galaxies is proportional to the galaxy mass (Feng & Soria, 2011). This is consistent with the high luminosity end of the XLFs of highly star forming systems being dominated by short-lived HMXBs, whilst that of the elliptical galaxies is dominated by high-luminosity LMXBs.

However, the behaviour of the population above a luminosity of $\sim 10^{40}$ erg s^{-1} in XLFs remains uncertain; the XLFs appear cut-off at this luminosity (Fig. 1.37, Feng & Soria 2011), hence the population above the break is extremely rare. As discussed above, this implies that most ULXs might not contain IMBHs. However, this does not mean that IMBHs do not exist. Indeed, the detection of the very brightest ULXs with luminosity in excess of 10^{41} erg s^{-1}, as reported by Sutton et al. (2012), as well

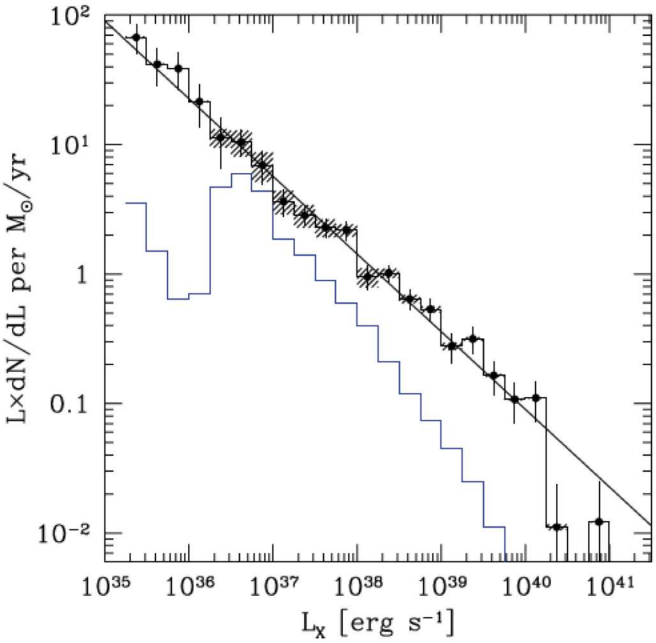

Figure 1.37: The differential XLF of high SFR galaxies, with cosmic X-ray background subtracted, normalised by star formation rate (Mineo et al. 2012a). The amount of cosmic X-ray background subtracted from the XLF is plotted in blue. The function shows a cut-off at a luminosity of $\sim 10^{40}$ erg s^{-1}.

as HLX-1 in ESO 243-49 (Farrell et al., 2009), seems to be inconsistent with the interpolation of the population above 10^{40} erg s^{-1} using the cut-off XLF model of Swartz et al. (2011). This may suggest the emergence of a small, physically different population above the cut-off luminosity.

1.6 Aims of this work

ULXs are an intriguing class of X-ray emitting object. Over three decades from the first discovery of ULXs, we have gained a lot of knowledge in the field of ULX astronomy. However, a complete understanding of the real nature of these systems remains elusive. In this thesis, we attempt to use X-ray data to constrain the nature of these systems and answer some of the remaining fundamental questions, including: i) if ULXs are sMBHs accreting material in a super-Eddington accretion regime, how do they do that?, and ii) what is the nature of ULXs in high SFR systems, in comparison to the nature of ULXs in normal star forming galaxies?

The thesis is laid out as follows. In Chapter 2, we investigate the properties of the X-ray spectra of ULXs in nearby galaxies observed by *Suzaku*. In Chapter 3, we focus on the X-ray spectral variability of the individual ULX Holmberg IX X-1 and examine how the source evolves from low to very high super-Eddington accretion rate. Then, the behaviour of the ULX population in high SFR galaxies and their X-ray spectral properties are investigated in Chapter 4. Finally, in Chapter 5, we summarise the key results found in the previous three chapters, and outline some methods for further progress in ULX studies.

Chapter 2

Suzaku observations of ultraluminous X-ray sources in very nearby galaxies

2.1 Introduction

As described in Section 1.5, previous work has suggested that ULXs could be powered by one of two possible classes of black holes. On the one hand, they might be powered by an exotic new class of black holes – IMBHs – accreting material at a sub-Eddington rate, similar to most known BHBs and active galactic nuclei (AGNs). Alternatively, ULXs could be powered by stellar remnant black holes (sMBHs or MsBHs) that are somehow able to accrete material at rates that exceed the Eddington limit.

The detailed study of the X-ray emission from ULXs, first enabled by the launch of the current generation of X-ray telescopes such as *Chandra*, *XMM-Newton* and (more lately) *Suzaku*, has strongly suggested that the majority of the ULX population are sMBHs accreting material at super-Eddington rates. However, the details of this process are still far from clear. In this chapter, we aim to improve our physical understanding of the X-ray spectra of ULXs using public data obtained from the *Suzaku* data archive. When chosen on the basis of proximity, i.e. only selecting the nearest ULXs ($d \lesssim 4.2$ Mpc), high quality ULX spectra can be obtained from *Suzaku* observations, providing the best possible constraints on the spectral modelling. In this chapter, we search through a range of empirical and physical models to help

explain ULX spectra, and attempt to interpret the results physically. The chapter is laid out as follows. In Section 2.2, we explain how we select the X-ray data from the *Suzaku* public archive, and how we reduce as well as create the ULX spectra. The spectral analyses are detailed in Section 2.3 and we discuss their results in Section 2.4. Our findings are summarised in Section 2.5.

2.2 Source selection and data reduction

2.2.1 Source selection and observations

In this chapter, we intend to study a sample of ULXs obtained from *Suzaku* observations. We selected only those observations that provide high quality ULX spectra, sufficient to allow the exploration of ULX spectral components (such as the soft excess and high energy curvature) by range of empirical and physical models. We began searching for *Suzaku* observations of ULXs by cross-matching the *Suzaku* data archive catalogue[1] with recent ULX catalogues, in particular all ULXs detected and reported in Walton et al. (2011); Sutton et al. (2012); Gladstone et al. (2009, 2013). Then each *Suzaku* observation matching to the position of one or more ULXs was examined to determine whether its observation time is sufficiently long to provide a high quality ULX spectrum. To do this, we calculated the number of photon counts expected for each ULX spectrum in the *Suzaku* observations. In brief, we converted the previous observed fluxes of ULXs[2] into *Suzaku* detector count rates in the 0.3-10 keV energy band, using the Portable, Interactive Multi-Mission Simulator (PIMMS).[3] Assuming that ULX spectra can be described by an absorbed power-law continuum with a spectral index (Γ) of 2 and total column density ($N_{\rm H}$) of $1.5{\times}10^{21}$ cm^{-2}, the detector count rates can be estimated and then converted into the expected number of photon counts in the ULX spectra, corresponding to the exposure time of the observations. Observations of ULXs that were estimated to contain $\gtrsim 3000$ total photon counts detected from across all *Suzaku* X-ray Imaging Spectrometers

[1] `http://www.darts.isas.jaxa.jp/astro/suzaku/`
[2] Using the ULX fluxes previously reported in Walton et al. (2011) or Gladstone et al. (2013).
[3] `http://heasarc.gsfc.nasa.gov/docs/software/tools/pimms.html`

(XISs) were included in the sample. Finally, we excluded any sources that cannot be spatially resolved (< 60 arcsecond separation) from their host galaxy AGN or any bright nearby point sources, to avoid contamination of the ULX spectra. We also excluded all ULXs in NGC 253 from our analysis due to a high level of diffuse emission from the host galaxy contaminating the ULX spectral extraction regions on the *Suzaku* XIS detectors.

Table 2.1 shows the basic properties of the ULX sample studied in this chapter. The sample comprises 10 ULXs residing in seven host galaxies, for which the distance ranges between 0.9 – 4.2 Mpc. Most of the sample ULXs – except for IC 342 X-1, IC 342 X-2 and Circinus XMM2 – have low Galactic column density ($N_{\rm H} \lesssim 5 \times 10^{20}$ cm^{-2}), beneficial in obtaining good spectral constraints, especially in the soft component of ULX spectra below 2 keV. The *Suzaku* observational data for the ULX sample are shown in Table 2.2. Here, we choose only to analyse the data obtained from the XIS detectors, excluding the data from the *Suzaku* hard X-ray detector (HXD) from the analysis due to the following reasons. Firstly, the sensitivity of the HXD detector is not optimal for the flux levels we find ULXs at, leading to (at best) low signal-to-noise (S/N) data above 10 keV. For example, a spectral study of NGC 1313 X-1 and NGC 1313 X-2 using the *Suzaku* HXD data reported a lack of hard X-ray emission above 10 keV in the ULX spectra (Mizuno et al., 2007), whereas a later study using the more sensitive imaging of the *NuSTAR* observatory showed a significant detection of the high energy tail above 10 keV in the spectrum of NGC 1313 X-1 (Bachetti et al., 2013). In fact, since NGC 1313 X-1 is one of the nearest and brightest ULX in our sample, we might not expect to detect a high energy spectral tail from the other dimmer and more distant ULXs when they were observed by the HXD instrument. In addition, due to the large field-of-view (FOV) of the HXD instrument (34 arcmin × 34 arcmin)[4], the hard X-ray spectra could easily be contaminated by the hard X-ray emission of nearby sources: for example, see Dewangan et al. (2013). So we exclude the HXD data to avoid uncertainty in the analysis.

[4]`https://heasarc.gsfc.nasa.gov/docs/astroe/prop_tools/suzaku_td/node12.html`

Table 2.1: The ULX sample and its properties

Source	RA (J2000)	Dec. (J2000)	d^a (Mpc)	$N_{\rm H}{}^b$ (10^{20} cm^{-2})	Luminosity^c (10^{39} erg s^{-1})
M33 X-8	01 33 50.9	+30 39 37	0.90	5.58	1.57
NGC 1313 X-1	03 18 20.0	−66 29 11	3.70	3.90	20.10
NGC 1313 X-2	03 18 22.3	−66 36 04	3.70	3.90	5.78
IC 342 X-1	03 45 55.1	+68 04 59	3.90	31.10	5.66
IC 342 X-2	03 46 15.0	+68 11 11	3.90	29.70	11.71
NGC 2403 X-1	07 36 25.5	+65 35 40	4.20	4.14	2.95
2XMM J073702.1+653935	07 37 02.1	+65 39 36	4.20	4.13	0.78
M81 X-6	09 55 33.0	+69 00 33	3.40	4.16	5.12
Holmberg IX X-1	09 57 54.1	+69 03 47	3.42	4.06	13.45
Circinus XMM2	14 12 39.2	−65 23 34	4.00	55.10	5.56

Note. Basic properties of the ULX sample, ordered by right ascension (RA). ^{a}Distance to the ULX host galaxy. ^{b}Galactic column density into the direction of the ULX obtained from Dickey & Lockman (1990). ^{c}The observed luminosity of the ULX in the 0.3-10.0 keV energy band calculated from the BB plus MCD with p free model (see Section 2.3.5). The maximum observed luminosity is reported for the ULXs that were observed in more than one epoch. The values in columns 2 – 4 are given in Gladstone et al. (2013) and references therein. In the case of the ULX 2XMM J073702.1+653935 – here after 2XMM J0737 – the values are obtained from Walton et al. (2011).

Table 2.2: *Suzaku* observational data

Source	Epoch[a]	Obs. ID	Obs. Date	Exposure time (ks)	Instruments[b]
M33 X-8		704016010	2010 January 11	106.10	XIS0, XIS1, XIS3
NGC 1313 X-1	a	100032010	2005 October 15	28.00	XIS0, XIS1, XIS2, XIS3
	b	703010010	2008 December 5	91.49	XIS0, XIS1, XIS3
NGC 1313 X-2	a	100032010	2005 October 15	28.00	XIS0, XIS1, XIS2, XIS3
	b	703010010	2008 December 5	91.49	XIS0, XIS1, XIS3
IC 342 X-1	a	705009010	2010 August 7	74.38	XIS0, XIS1, XIS3
	b	705009020	2011 March 20	75.45	XIS0, XIS1, XIS3
IC 342 X-2	a	705009010	2010 August 7	74.38	XIS0, XIS1, XIS3
	b	705009020	2011 March 20	75.45	XIS0, XIS1, XIS3
NGC 2403 X-1		800021010	2006 March 16	72.38	XIS0, XIS1, XIS2, XIS3
2XMM J0737		800021010	2006 March 16	72.38	XIS0, XIS1, XIS2, XIS3
M81 X-6	a	701022010	2006 May 8	103.53	XIS0, XIS1, XIS2, XIS3
	b	906004010	2011 September 15	45.92	XIS0, XIS1, XIS3
Holmberg IX X-1	a	707019010	2012 April 13	182.51	XIS0, XIS1, XIS3
	b1	707019020	2012 October 21	107.50	XIS0, XIS1, XIS3
	b2	707019030	2012 October 24	106.95	XIS0, XIS1, XIS3
	b3	707019040	2012 October 26	110.02	XIS0, XIS1, XIS3
Circinus XMM2		701036010	2006 July 21	108.04	XIS0, XIS1, XIS2, XIS3

Note. The *Suzaku* observational data for the sample of ULXs studied in this chapter. [a]Observational epoch of the ULX (hereafter obs). For the sources that are observed in more than one epoch, we indicate the epoch of observations alphabetically. [b]The *Suzaku* XIS CCD cameras operating during the observation. We note that the XIS2 suffered catastrophic damage in November 2006 and the *Suzaku* team decided to stop operating it, so no XIS2 data have been available since the damage (see Section 7.3.6 of `http://heasarc.gsfc.nasa.gov/docs/astroe/prop_tools/suzaku_td/node10.html`).

The list of XIS detectors operated in each observation is in column 5 of Table 2.2. Out of ten ULXs in the sample, six were observed in two separate epochs, thus providing useful information on the possible X-ray spectral variability of each source.

2.2.2 Data reduction

We reduced the observational data following the method suggested in the *Suzaku* data reduction guide version 4.0.[5] All scripts used to reduce the data are a part of the NASA HEASARC FTOOLS[6] package. We began by reprocessing the XIS data, using the script AEPIPELINE to perform data screening with the latest *Suzaku* pipeline, utilising the latest calibration data.

Next, we extracted the ULX spectra from all XIS detectors using a circular aperture centred on the position of each individual ULX. The size of the apertures varied from field to field (see column 2 of Table 2.3); in general cases, we applied the maximum circular radius of 260 arcseconds suggested by the *Suzaku* data reduction guide to gather as many of the source counts as possible; however, if the maximum extraction radius overlapped the equivalent area for any nearby sources or the host galaxy AGN, we reduced the size of the circular radius to avoid contamination of the extracted spectrum. A background extraction region for each spectrum was chosen from the entire area of the XIS detector, excluding the areas around all bright sources as well as the areas close to the *Suzaku* calibration sources located at the corners of the detector.[7]

The source and background spectra were extracted using the tool XSELECT. The instrumental response matrix file (RMF) and ancillary response file (ARF) file for each spectrum were generated using the scripts XISRMFGEN and XISSIMARFGEN, respectively. We then added the RMF and ARF files of each spectrum together to make a single instrumental response (RSP) file using the tool MARFRMF. To increase the spectral signal-to-noise, we stacked all front-illuminated (FI; XIS0, XIS2 and

[5] `http://heasarc.gsfc.nasa.gov/docs/suzaku/analysis/abc/`

[6] `https://heasarc.gsfc.nasa.gov/ftools/`

[7] See `http://heasarc.gsfc.nasa.gov/docs/astroe/prop_tools/suzaku_td/node10.html` Section 7.1.2.1.4

Table 2.3: Properties of the ULX spectra

Source	Ep.[a]	Extraction radius[b] (arcsec)	Net rate[c] (counts s^{-1})	Spectral bins[d]	Good energy range[e] (keV)	
					FI XIS	BI XIS
M33 X-8		260	1.39	2754	0.3 – 10.0[1,3,4]	0.3 – 8.2[1,3]
NGC 1313 X-1	a	229	1.24	1602	0.8 – 10.0[1]	0.8 – 9.0[1]
	b	229	0.32	1385	0.3 – 10.0[2,3]	0.3 – 7.0
NGC 1313 X-2	a	208	0.37	789	0.3 – 10.0[3]	0.3 – 8.0
	b	208	0.10	616	0.3 – 10.0[2,3]	0.3 – 7.0
IC 342 X-1	a	182	0.22	936	0.3 – 10.0[3,4]	0.3 – 8.5
	b	182	0.24	1019	0.3 – 10.0[3,4]	0.3 – 8.0
IC 342 X-2	a	203	0.45	1702	0.3 – 10.0[4]	0.3 – 8.4
	b	203	0.24	1077	0.3 – 10.0[4]	0.3 – 8.3
NGC 2403 X-1		188	0.18	930	0.3 – 10.0[2,3]	0.4 – 7.0
2XMM J0737		135	0.03	265	0.3 – 10.0 [2,3]	0.3 – 7.0
M81 X-6	a	83	0.25	1325	0.3 – 10.0	0.3 – 8.5
	b	94	0.22	527	0.8 – 10.0[1]	0.3 – 8.2[1]
Holmberg IX X-1	a	260	0.71	2643	0.3 – 10.0[1,4]	0.3 – 8.2[1]
	b1†	260	0.77	2475	0.3 – 10.0 [1,4]	0.3 – 8.2[1]
	b2†	260	0.83	2530	0.3 – 10.0[1,3,4]	0.3 – 8.3[1]
	b3†	260	0.83	2560	0.3 – 10.0[1,4]	0.3 – 8.0[1]
Circinus XMM2		85	0.18	1174	0.3 – 10.0	0.3 – 9.0

Note. [a]Observational epoch. [b]The radius of the circular area used to extract the source spectra. [c]The net, background-subtracted count rate of the source in the energy band shown in columns 6 and 7. [d]The number of bins available in the spectrum, after ensuring each bin has at least 25 counts (see text). [e]The energy band used in the analysis. The superscript numbers indicate the exclusion of bad spectral bins around the centres of emission lines originating in the *Suzaku* NXB (see text for detail): [1]Si-Kα (1.74 keV), [2]Mn-Kα (5.90 keV), [3]Ni-Kα (7.47 keV) and [4]Au-Lα (9.67 keV). †These spectra were modelled simultaneously – and are hereafter referred to as Holmberg IX X-1 obs b – since they were observed at roughly the same epoch (within one week).

XIS3) spectra together to make a single FI spectrum for each ULX, using the tool ADDASCASPEC. The FI and BI (back-illuminated; XIS1) spectra were then grouped to have a minimum of 25 counts per bin to utilise the χ^2 minimisation method during spectral modelling.

Finally, we inspected each ULX spectrum, searching for any poor quality spectral bins. We found that the *Suzaku* spectra show bad quality bins in both the low and high energy tails of the spectra, due to the relative drop in the effective area of the XIS detectors $\lesssim 0.3$ keV and $\gtrsim 8$ keV.[8] Hence we removed these bad quality bins from the analysis to leave only good quality data. In addition to this, we also removed the bad quality data around the instrumental emission lines of the *Suzaku* non-X-ray background (NXB), i.e. Si-Kα (1.74 keV), Mn-Kα (5.90 keV), Ni-Kα (7.47 keV) and Au-Lα (9.67 keV)[9]. As the NXB intensity is not uniform across the detectors (Yamaguchi et al., 2006) we cannot subtract this background emission from the source spectra perfectly; most of the ULX spectra show low S/N data around the central energy of NXB emission lines due to an inappropriate background subtraction. To solve this issue, we simply excluded the questionable data quality bins from the analysis. The good spectral energy ranges used in the analyses are shown in columns 6 and 7 of Table 2.3, and these spectra were used as the basis for further analysis.

2.3 Spectral analysis and results

Using the sample selection criteria described in Section 2.2, we derive a sample of 18 spectra from 10 ULXs; six ULXs are observed in two separate epochs, allowing us to track spectral variability in the each ULX between epochs. In this section, we utilise a range of empirical and physical models to analyse the ULX spectra and explain the results phenomenologically. The spectra were fitted using XSPEC[10] version 12.7.1, with those extracted from the FI and BI detectors in each observation fitted simultaneously over the energy ranges shown in columns 6 and 7 of Table 2.3

[8] `https://heasarc.gsfc.nasa.gov/docs/suzaku/gallery/performance/xis_area.html`
[9] For more on the origin and properties of the *Suzaku* NXB see Tawa et al. (2008)
[10] `http://heasarc.nasa.gov/xanadu/xspec/`

to optimise data quality during the modelling. In the case of Holmberg IX X-1 obs b, we fitted all six FI and BI spectra obtained from the observations b1, b2 and b3 simultaneously, as these spectra were observed within a short period (one week; see Table 2.2) and minimal spectral variability was seen between the different observations (see Walton et al. 2014).

In the following spectral fits, a constant multiplicative factor is added to all models to compensate for any calibration uncertainties between the FI and BI detectors. The constant is fixed at unity for the FI spectrum whilst that of the BI spectrum is allowed to be a free parameter; the fits show that there is less than 10 per cent difference between the FI and BI detectors across all ULXs. Interstellar absorption is modelled using a TBABS[11] model with the chemical abundance values from Wilms et al. (2000). We split the absorption into two components. The first component corresponds to the Galactic absorption along the line of sight to the ULXs, and its value is fixed to that measured by Dickey & Lockman (1990), calculated using the online NH FTOOL[12] and listed in column 5 of Table 2.1. The latter component stands for the absorption column external to our own Galaxy, which could be either along the line-of-sight through the host galaxy to the ULX, or intrinsic to the ULX itself, which is allowed to be a free parameter during the spectral fitting. Throughout this chapter all best-fitting parameter values are quoted with 90 per cent confidence intervals (Avni, 1976), and the luminosities are reported in the 0.3-10 keV energy band.

2.3.1 Single component models

We began by fitting simple single component models that are known to fit well to low and medium quality ULX data (e.g. Swartz et al. 2004). These provide an initial description of the *Suzaku* data, and an indication as to whether or not more complex models are required by the data.

Here, we used two single component models to fit the ULX spectra: an absorbed power-law model (TBABS*TBABS*POWERLAW in XSPEC) and an absorbed multi-

[11] https://heasarc.gsfc.nasa.gov/xanadu/xspec/manual/XSmodelTbabs.html
[12] http://heasarc.gsfc.nasa.gov/cgi-bin/Tools/w3nh/w3nh.pl

colour disc blackbody model (hereafter MCD, Mitsuda et al. 1984; TBABS*TBABS* DISKBB in XSPEC). The fitting results are shown in Table 2.4. Both absorbed power-law and absorbed MCD models yield unacceptable fitting results in most cases, with 24/36 fits rejected at 2σ significance or greater, i.e. with a null hypothesis probability[13] of $\lesssim 5$ per cent (although 4 of these are only marginally rejected, with null hypothesis probability between 1 and 5 per cent). Fig. 2.1 shows the spectrum of Holmberg IX X-1 obs a, fitted by an absorbed power-law model. Two sets of residuals are obvious, at around 1 keV (corresponding to the soft excess) and above 2 keV (the high energy turnover). These suggest that the *Suzaku* spectra are of sufficient quality to require an additive two component model to fit them, similar to previous *XMM-Newton* studies. Indeed, we found that the fitting of these ULXs can be improved significantly using a two component model to explain the spectra (see Section 2.3.2).

However, there are some spectra for which the absorbed power-law or absorbed MCD models (or both) provide an adequate fit. In general, these are the cases in which the spectra are only moderate quality ($\lesssim 1000$ spectral bins; i.e. NGC 1313 X-2 obs a, IC 342 X-1 obs a and b, IC 342 X-2 obs a, NGC 2403 X-1 and 2XMM J0737), excepting the case of Holmberg IX X-1 obs b in which the spectral quality is highest in the sample but the data can be fitted well by an absorbed power-law model. Interestingly, the preferred single component model for each spectrum (i.e. the one with the lowest value of χ^2) is consistent with the spectral regime classified in Section 2.3.2 (see also Table 2.5: BD regime for the MCD-preferring spectra and HUL regime for the power-law-like spectra). However, we note that even if the single component models seem to be sufficient to model some ULX spectra, we found that in all cases the fitting statistic can be improved by modelling these spectra with the double component models.

[13]The probability of the observed data being drawn from the model given the value of χ^2 and the number of degrees of freedom.

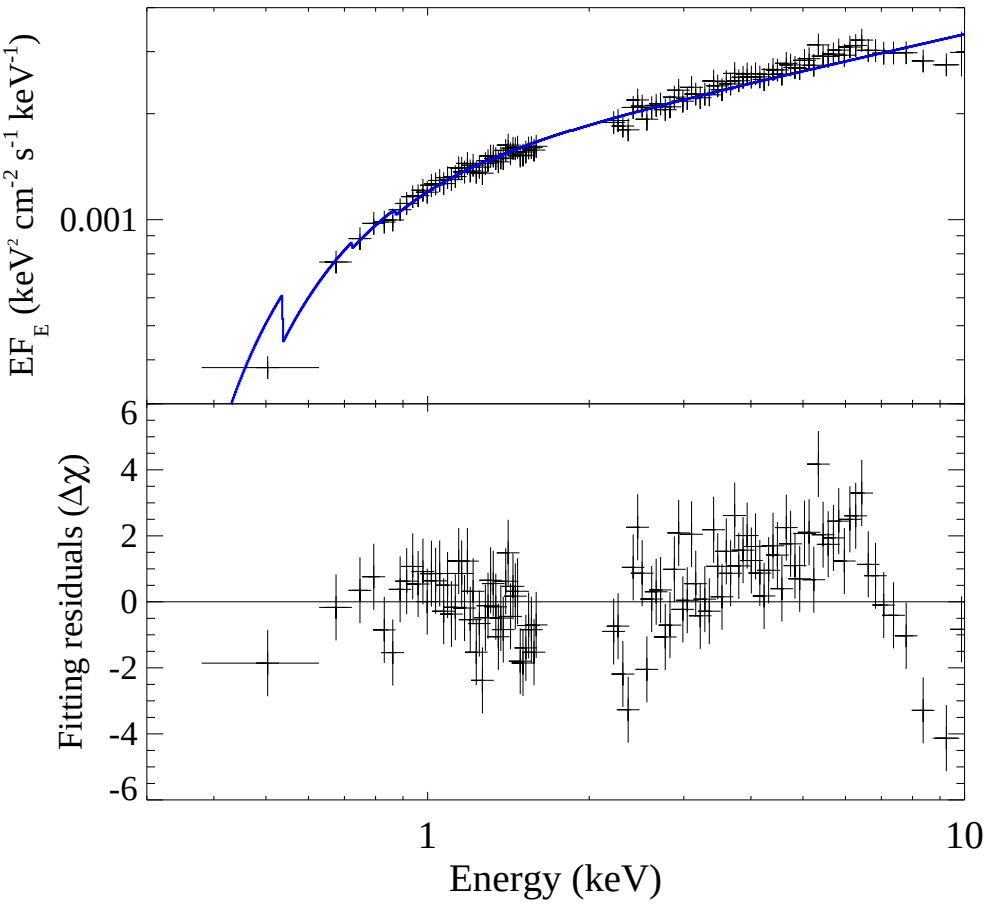

Figure 2.1: Top panel: *Suzaku* FI spectra of Holmberg IX X-1 obs a (black), rebinned to a minimum of 30σ statistical significance per data point. The data are unfolded from the detector response, using the best fitting absorbed power-law model that is over-plotted in blue. Bottom panel: the fitting residuals obtained from the model illustrated above. Obviously, the residuals suggest the presence of a soft excess and high energy turn-over in the ULX spectra as seen in previous studies using *XMM-Newton* data (e.g. Gladstone et al. 2009). Note that the apparent difference in significance between points in the top and bottom panels is an artefact of the rebinning; in the top panel the rebinning shows the average value of the bins that contribute to the rebinned point, whereas in the lower panel the summed significance of the datapoints (compared to the model) is shown.

Table 2.4: Single component models

Source	Ep.[a]	POWERLAW			DISKBB		
		$N_{\rm H}$[b] (10^{21} cm^{-2})	Γ[c]	χ^2/d.o.f.[d]	$N_{\rm H}$[b] (10^{21} cm^{-2})	$kT_{\rm in}$[e] (keV)	χ^2/d.o.f.[d]
M33 X-8		2.33 ± 0.07	2.14 ± 0.01	[4057/2750]	$< 1.15 \times 10^{-3}$	1.17 ± 0.01	[5604/2750]
NGC 1313 X-1	a	4.29 ± 0.20	1.98 ± 0.02	[2031/1598]	< 0.01	$1.53^{+0.02}_{-0.01}$	[1852/1598]
	b	$0.84^{+0.13}_{-0.12}$	1.79 ± 0.02	[1516/1381]	$< 9.38 \times 10^{-3}$	1.36 ± 0.02	[2925/1381]
NGC 1313 X-2	a	$4.13^{+0.30}_{-0.29}$	1.93 ± 0.04	[973/785]	$0.84^{+0.16}_{-0.15}$	1.47 ± 0.03	759/785
	b	$1.62^{+0.31}_{-0.30}$	2.05 ± 0.06	(676/612)	< 0.03	1.09 ± 0.04	[1030/612]
IC 342 X-1	a	$4.51^{+0.47}_{-0.45}$	1.75 ± 0.04	906/932	< 0.23	$1.89^{+0.04}_{-0.05}$	926/932
	b	$1.85^{+0.35}_{-0.34}$	1.61 ± 0.03	988/1015	< 0.02	1.88 ± 0.04	[1229/1015]
IC 342 X-2	a	$40.97^{+1.25}_{-1.21}$	2.23 ± 0.04	[2246/1698]	$23.61^{+0.71}_{-0.69}$	1.85 ± 0.03	1760/1698
	b	$20.31^{+1.33}_{-1.28}$	1.46 ± 0.05	[1272/1073]	$12.79^{+0.83}_{-0.80}$	$2.95^{+0.13}_{-0.12}$	(1160/1073)
NGC 2403 X-1		$3.21^{+0.27}_{-0.26}$	2.24 ± 0.04	[1382/926]	< 0.03	1.13 ± 0.02	964/926
2XMM J0737		< 0.30	1.54 ± 0.06	280/261	< 0.06	$1.61^{+0.11}_{-0.10}$	[328/261]
M81 X-6	a	3.66 ± 0.16	2.18 ± 0.02	[2028/1321]	< 0.03	1.31 ± 0.01	[1473/1321]
	b	$2.20^{+0.38}_{-0.36}$	1.79 ± 0.04	[664/523]	< 0.02	$1.59^{+0.04}_{-0.03}$	(579/523)
Holmberg IX X-1	a	0.95 ± 0.06	1.65 ± 0.01	[2841/2639]	$< 9.33 \times 10^{-4}$	1.62 ± 0.01	[8344/2639]
	b	1.33 ± 0.05	1.74 ± 0.01	7584/7557	$< 5.01 \times 10^{-4}$	1.53 ± 0.01	[17999/7557]
Circinus XMM2		$9.33^{+0.45}_{-0.44}$	2.46 ± 0.03	[1617/1170]	0.12 ± 0.25	1.3 ± 0.02	(1272/1170)

Note. [a]Observational epoch. [b]Absorption column external to our Galaxy. [c]Power-law photon index. [d]The minimum χ^2 for the given degrees of freedom, obtained from the best fit. The square brackets indicate the cases where the model can be rejected statistically (null hypothesis probability is < 1 %) whilst the rounded brackets indicate marginally rejected fits (null hypothesis probability is $\sim 1 - 5$ %). [e]Inner-disc temperature of DISKBB component.

2.3.2 Disc plus power-law model

As single component models cannot adequately describe the high quality *Suzaku* spectra, we require more complex models. In this section, we use a canonical model that has been extensively used to describe the spectra of both BHBs and ULXs (see e.g. Miller et al. 2004b; Stobbart et al. 2006 and references therein). As this model is also the basis of the spectral classification scheme for ULXs proposed by Sutton et al. (2013b) we also explore whether *Suzaku* spectra of ULXs are compatible with this scheme. Note that during the spectral modelling we attempt to fit the MCD component to both the soft or hard spectral components, in order to obtain the global minimum χ^2 value that we give here.

The fitting results tabulated in Table 2.5 show that the MCD plus power-law model provides a better description of the *Suzaku* spectra than the single component models. The additional two degrees of freedom yield an improvement in the fitting statistic in all cases, producing statistically acceptable fits (null hypothesis probability $\gtrsim$ 20 per cent for all spectra, excepting the Holmberg IX X-1 obs a spectrum which is marginally acceptable with a null hypothesis probability of $\sim$ 5 per cent). We note that the two component model also helps to improve the fitting statistic even in the spectra that can be well approximated by the single component models (see Section 2.3.1), with improvements to the fits of $\Delta\chi^2 \geq 13$ (and in some cases considerably more) for the two additional degrees of freedom. Hence these results imply that a double component model is a more appropriate choice than a single component model when describing the high quality ULX spectra obtained by *Suzaku*.

The stand-out result from this two-component model is the temperature of the MCD component. In all cases a best-fit was found with an inner disc temperature $kT_{\rm in} \gtrsim 1.2$ keV, although both NGC 1313 X-1 and X-2 have one observation where the ULX spectrum can be fitted equally well with a hot (> 2.5 keV) and a cool (< 0.3 keV) disc. This is in stark contrast to previous studies of ULXs using *XMM-Newton* data (e.g. Gladstone et al. 2009; Sutton et al. 2013b) where many of the MCD components are found to be cool discs ($kT_{\rm in} \lesssim 0.3$ keV). Some ULX discs are found to be relatively hot in *XMM-Newton* data ($1-2$ keV), but these are generally where

the spectrum is in the BD regime, where the curvature is pronounced but broader than a standard disc. However, in the *XMM-Newton* spectra that are resolved into two distinct components (SUL and HUL regimes), the disc component almost always fits to the soft end of the spectrum, resulting in a cool disc. This is not seen in the *Suzaku* data; in the distinctly two-component spectra the disc almost always fits to the hard end of the spectrum, with the power-law providing the soft excess (see Fig. 2.2).

This inversion of the spectral components suggests that the parameterisation of ULX spectra is mission-dependent. In this case, it appears as though the key driver of this difference could be the difference in soft effective area between the missions[14]; the very obvious soft excess detected in *XMM-Newton* data (that is preferentially fitted by the MCD) is not seen as well by *Suzaku* due to its significantly poorer response below 1 keV. Instead, the subtle curvature of the hard component drives the disc to fit to the hard part of the *Suzaku* spectra, with the power-law filling-in the moderate soft excess detection. However, this is an interesting result given the suggestion that the harder component may be direct emission from the central regions of the super-Eddington accretion flow (e.g. Kajava et al. 2012). We discuss the implications of this inversion of the components further in Section 2.4.

This spectral inversion produces an immediate problem if we wish to attempt to classify the ULX spectra into the same regimes as those proposed by Sutton et al. (2013b), as their method is primarily based on identifying the two-component soft and hard ultraluminous regimes by the detection of a cool MCD in the *XMM-Newton* fits. They do have one caveat in their classification scheme designed specifically for the case of NGC 55 ULX, where the disc does fit to the harder part of the spectrum, but the spectrum is distinctly two-component. In this, the ratio between the fluxes of the power-law and MCD components in the 0.3-1 keV band is used to distinguish SUL from BD spectra, where a dominant power-law implies a SUL spectrum. However, in the *Suzaku* fits the power-law dominates many spectra below 1 keV; but inspection of the spectra shows that they cannot be SUL as the harder

[14] `http://xmm.esac.esa.int/external/xmm_user_support/documentation/uhb/xmmcomp.html`

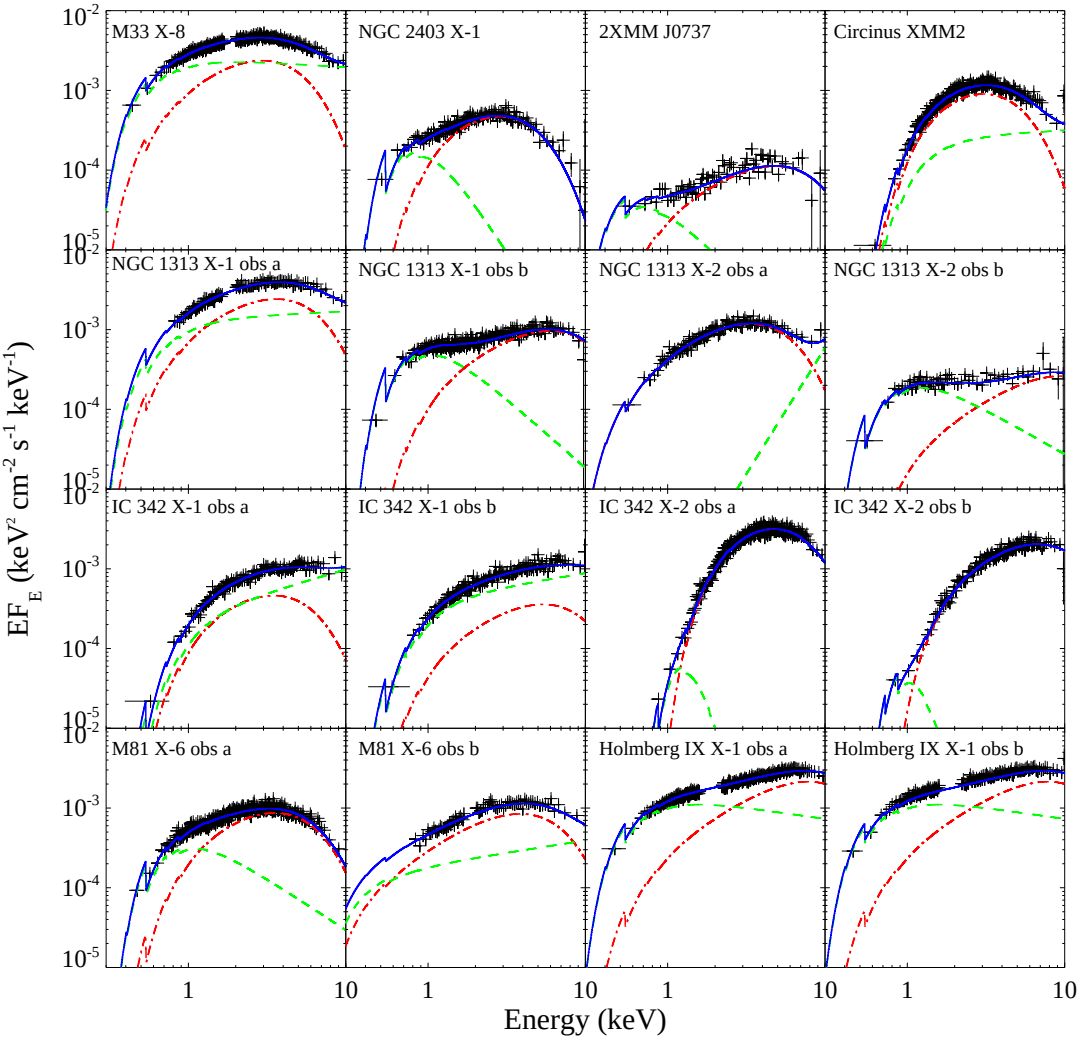

Figure 2.2: *Suzaku* FI spectra of the ULX sample. The spectra are rebinned to a minimum of either 20σ or 30σ statistical significant to clarify the plots. The ULX spectra (black data points) are plotted under the best fitting MCD plus power-law model (blue solid line). The individual MCD (red dash-dotted line) and power-law (green dashed line) components are also shown.

component dominates, as is very evident in Fig. 2.2. The mis-functioning of this classification is most obvious for NGC 1313 X-1 and X-2; both of their hot MCD spectra would be classified as SUL using the Sutton et al. (2013b) scheme, whereas the cool disc fits to both data are demonstrably HUL, and this is backed up by visual inspection of the spectra. We cannot therefore classify *Suzaku* spectra using the original Sutton et al. (2013b) scheme.

However, we are still able to classify sources into the three regimes suggested by Sutton et al. (2013b) by using a revised classification method suitable for *Suzaku* data, where detections of the soft excess are generally weak. Here we suggest the key driver of the classification is again the MCD temperature, but we distinguish BD spectra from SUL/HUL by defining a temperature range of 0.5 keV $< kT_{\rm in} <$ 2.0 keV for the MCD component in the BD regime. For spectra where the MCD temperature is outside these boundaries, we inspect the spectra by eye: they are classified to be in the HUL regime if the high energy component dominates the spectra, and SUL if the soft excess dominates. The ULX spectral classifications resulting from this new method are shown in column 8 of Table 2.5. In brief, eight spectra were classified as BD whilst four were classified as in the HUL regime. There are two cases – IC 342 X-1 obs b and 2XMM J0737 – that are ambiguous between the BD and HUL regimes since the uncertainty in MCD temperature overlaps the regime boundary at 2 keV. No spectra were classified as in the SUL regime here. We show a gallery of all the spectral shapes by plotting the spectra unfolded from the *Suzaku* detector response in Fig. 2.2. Furthermore, we also highlight that our revised classification method is broadly consistent with the *XMM-Newton* ULX regimes of Sutton et al. (2013b) for each object (see column column 9 of Table 2.5). Note that we did not attempt to classify the spectrum of IC 342 X-2 in either observation due to the high degree of absorption it experiences effectively masking any soft spectral component, thus leading to great uncertainty in its classification.

One interesting product of this classification is to highlight strong spectral variability, in particular where an object appears to transit between two regimes in different epochs. This happens in the cases of both NGC 1313 X-1 and X-2, that show HUL spectra at lower luminosities but become more disc-like when their lu-

Table 2.5: MCD plus power-law model

Source	Ep.[a]	$N_{\rm H}$[b] (10^{21} cm^{-2})	$kT_{\rm in}$[c] (keV)	Γ[d]	χ^2/d.o.f.	Luminosity[e] (10^{39} erg s^{-1})	Spectral regime[f] *Suzaku*	Spectral regime[f] *XMM-Newton*
M33 X-8		1.10 ± 0.15	1.22 ± 0.05	2.12 ± 0.06	2784/2748	1.57	D	D
NGC 1313 X-1	a	$1.78^{+0.60}_{-0.61}$	$1.50^{+0.14}_{-0.12}$	$1.91^{+0.22}_{-0.20}$	1631/1596	20.58	D	H
	b[§]	$3.96^{+0.60}_{-0.58}$	$2.51^{+0.2}_{-0.16}$	3.74 ± 0.30	1398/1379	5.64	H	H
	b[§]	$2.90^{+0.59}_{-0.54}$	0.18 ± 0.02	1.74 ± 0.04	1397/1379	5.84	H	H
NGC 1313 X-2	a	0.96 ± 0.18	$1.39^{+0.07}_{-0.12}$	< 1.86	744/783	5.84	D	D/H
	b[§]	$3.83^{+1.08}_{-0.93}$	$3.97^{+7.29}_{-1.17}$	$3.11^{+0.50}_{-0.43}$	642/610	1.66	H	D/H
	b[§]	$2.43^{+1.17}_{-0.83}$	$0.28^{+0.09}_{-0.07}$	$1.78^{+0.15}_{-0.18}$	642/610	1.66	H	D/H
IC 342 X-1	a	$1.86^{+1.12}_{-1.03}$	$1.41^{+0.42}_{-0.17}$	$1.42^{+0.32}_{-0.54}$	861/930	5.56	D	D/H
	b	$1.18^{+0.93}_{-0.78}$	$2.25^{+0.81}_{-0.85}$	$1.67^{+0.49}_{-0.23}$	969/1013	5.62	D/H	D/H
IC 342 X-2	a	$27.74^{+0.62}_{-0.81}$	1.77 ± 0.03	10.00*	1654/1696	11.72	–	D/H/S
	b	$15.55^{+1.17}_{-0.81}$	$2.80^{+0.09}_{-0.07}$	10.00*	1075/1071	7.66	–	D/H/S
NGC 2403 X-1		$4.81^{+1.25}_{-1.68}$	1.12 ± 0.04	$5.11^{+0.61}_{-0.87}$	951/924	2.92	D	D
2XMM J0737		< 4.60	$2.03^{+0.39}_{-0.26}$	$4.05^{+1.43}_{-1.65}$	262/259	0.78	D/H	–
M81 X-6	a	$3.34^{+1.11}_{-1.03}$	1.45 ± 0.03	$3.29^{+0.62}_{-0.65}$	1302/1319	4.20	D	D
	b	< 0.85	$1.63^{+0.22}_{-0.17}$	$1.69^{+0.84}_{-0.23}$	505/521	5.12	D	D
Holmberg IX X-1	a	$1.65^{+0.23}_{-0.22}$	$3.31^{+0.17}_{-0.14}$	$2.28^{+0.16}_{-0.15}$	2769/2637	12.90	H	H
	b	$1.57^{+0.14}_{-0.13}$	$3.11^{+0.14}_{-0.15}$	$2.01^{+0.10}_{-0.09}$	7516/7555	13.51	H	H
Circinus XMM2		$2.81^{+1.12}_{-0.92}$	$1.17^{+0.07}_{-0.05}$	$1.89^{+0.36}_{-0.61}$	1207/1168	5.57	D	–

Note. [a]Observational epoch. [b]Absorption column external to our Galaxy. [c]The inner-disc temperature of the DISKBB component. [d]Photon index of the power-law component. [e]The observed luminosity of the ULX in the 0.3-10 keV energy band. [f]ULX spectral regime as defined by Sutton et al. (2013b): broadened disc (D), hard ultraluminous (H) and soft ultraluminous (S). The classification method for the *Suzaku* spectra is described in Section 2.3.2, and the result is compared to the classification of the *XMM-Newton* spectra by Sutton et al. (2013b). [§]The data can be fitted equally well using both hot and cool MCD temperatures. *The parameter cannot be constrained.

minosity increases. However, none of the other objects that were observed in two distinct epochs transits between regimes (or, for that matter, shows very strong variation in the parameterisation of their components).

2.3.3 Disc plus Comptonisation model

We have demonstrated that a two-component model provides a better fit to the *Suzaku* ULX spectra than simple single component models. However, a MCD plus power-law model, where the power-law acts as the softer of the two components, does not make physical sense, given that the power-law is generally used as a proxy for Compton-upscattered disc photons. Hence, we turned our attention to more physically-motivated models. We began with one of the most successful models previously used to explain ULX spectra observed by *XMM-Newton*: a MCD plus Comptonisation model (DISKBB+COMPTT[15] in XSPEC; see e.g. Stobbart et al. 2006; Feng & Kaaret 2009; Gladstone et al. 2009). The origin of this model is in BHBs, where the hot corona is thought to sit above the inner part of the accretion disc, and to scatter disc photons to higher energies via inverse Compton processes, thus the disc should provide the softer spectral component, and the corona the hard component. Here we examine the *Suzaku* spectra using this model, and directly compare our results with those from *XMM-Newton*.

To begin with, we used the simplified version of the model where the seed photon temperature (Wien distribution temperature) of the Comptonisation component is tied to the temperature of the MCD component. The fitting results reported in Table 2.6 show that the model can describe the *Suzaku* spectra of the ULXs very well, with null hypothesis probability $\gtrsim 15$ per cent in all cases. Interestingly, similar results to previous studies using this model were found in our ULX sample (c.f. Gladstone et al. 2009; Vierdayanti et al. 2010; Pintore & Zampieri 2012); the curvature of the spectra drives fits that show the Comptonising coronae are cool ($kT_{\rm e} \sim 1 - 2$ keV) and optically thick ($\tau_{\rm e} \sim 10$), whilst the temperature of the MCD component is very cool ($kT_{in} \sim 0.1 - 0.2$ keV). We note that this behaviour is in con-

[15]The COMPTT model was developed by Titarchuk (1994)

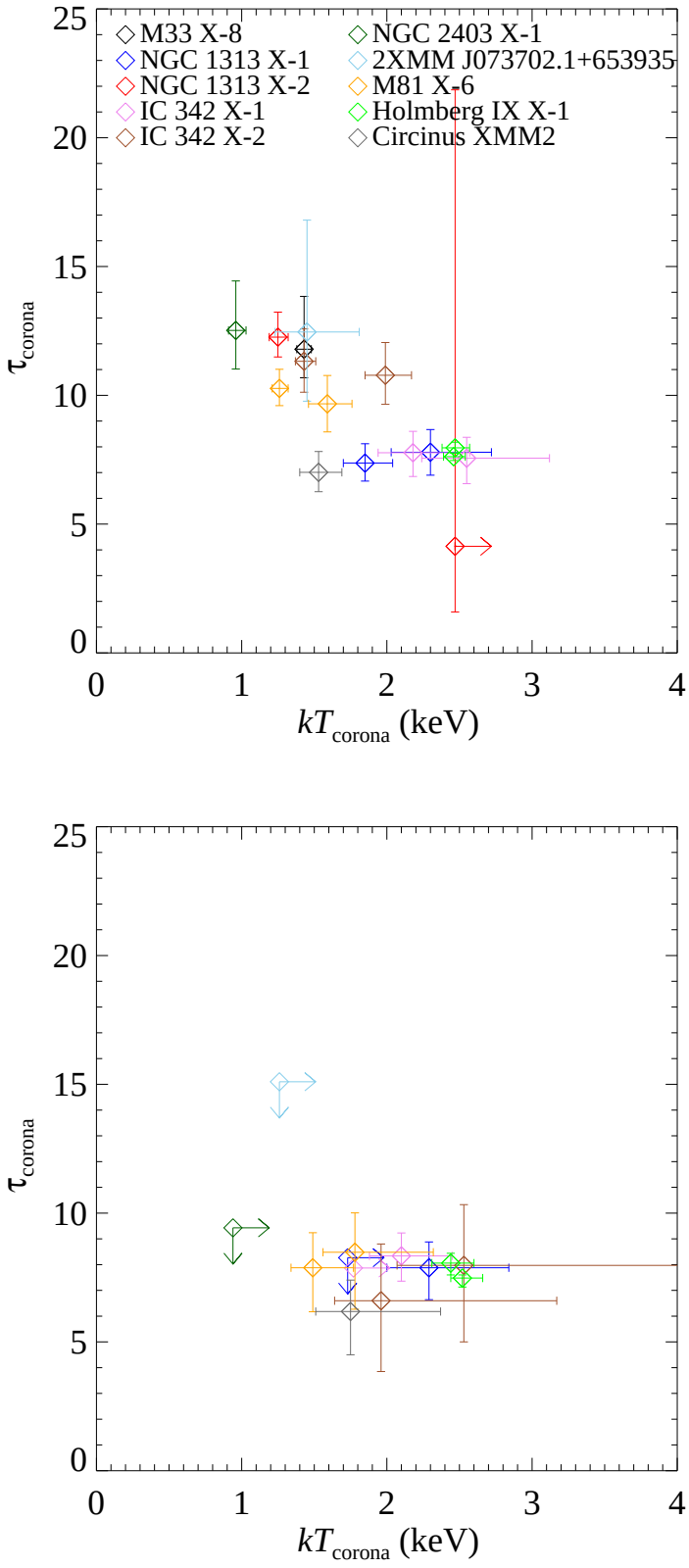

Figure 2.3: The coronal temperature versus its optical depth, obtained from the MCD plus Comptonisation model. The results from two different model configurations are shown: the coronal seed photon temperature (*top*) tied to and (*bottom*) untied from the inner-disc temperature of the MCD. The anti-correlation between the coronal temperature and optical depth found in the tied case disappears when the corona seed photon temperature is free.

trast to the nature of Galactic BHBs, where the Comptonising coronae are optically thin ($\tau \lesssim 1$) and hot ($kT_{\rm e} > 50$ keV). Moreover, an anti-correlation between the coronal temperatures and their optical depths was seen when we plotted these two parameters of the ULX sample together (see the top panel of Fig. 2.3), meaning the optical depth is likely to be higher as the corona temperature decreases. We tested the correlation statistically using Spearman's Rank Correlation Coefficient ($r_{\rm s}$); the two parameters show a significant anti-correlation of $r_{\rm s}$ = -0.75, corresponding to significance level of 99.9 per cent.

An interpretation of these optically thick, cool coronae in previous works on ULXs is that they occur as a result of super-Eddington accretion rates, in which excess mass is ejected into the corona, resulting in it thickening and so cooling (Gladstone et al., 2009). However, if this is true then the Comptonising medium should obscure the hot inner part of the accretion disc, and so tying the seed photon temperature to the cooler, visible parts of the disc beyond the corona is unrealistic; the seed photons should be originating in the hot disc under the corona. Hence, we re-modelled the ULX spectra by un-tying the coronal seed photon temperature from the MCD temperature.

The fitting results are shown in Table 2.7. Firstly, we examine whether adding an additional free parameter (the coronal seed photon temperature) can help to improve the fitting statistic using the F-test. As shown in column 9 of Table 2.7, the additional free parameter does help to improve the fitting statistic, at a significance of $\gtrsim$ 99 per cent in 11 spectral cases. Interestingly, most of these spectra are classified to be a BD state. On the other hand, the ULX spectra classified as HUL show a lesser improvement in their fitting statistic ($\sim$40 – 87 %). If we then examine the best fit parameters, compared to the case in which we tie the corona seed photon temperature, similar behaviours are found: the corona is cool ($kT_{\rm e}$ $\sim$1–3 keV) and optically thick ($\tau_{\rm e}$ $\sim$8) whilst the MCD temperature is cool (kT_{in} $\lesssim$0.5 keV). However, the new model showed subtle differences to the earlier version. Firstly, the seed photon temperature of the corona is hotter than that of the MCD component, consistent with the assumption that the coronae are seeded by the obscured hot inner part of the disc. In addition to this, we also found that the anti-correlation

Table 2.6: The MCD plus Comptonisation model: coronal seed photon temperature tied to the MCD temperature

Source	Ep.[a]	TBABS	DISKBB	COMPTT		χ^2/d.o.f.
		$N_{\rm H}$[b]	$kT_{\rm in}$[c]	$kT_{\rm corona}$[d]	$\tau_{\rm corona}$[e]	
M33 X-8		< 0.03	$0.60^{+0.06}_{-0.05}$	1.43 ± 0.05	$11.79^{+2.05}_{-1.11}$	2819/2747
NGC 1313 X-1	a	$7.54^{+1.59}_{-1.88}$	0.13 ± 0.01	$1.85^{+0.19}_{-0.15}$	$7.37^{+0.75}_{-0.70}$	1637/1595
	b	$2.24^{+0.62}_{-0.56}$	0.20 ± 0.02	$2.30^{+0.42}_{-0.27}$	$7.79^{+0.88}_{-0.89}$	1379/1378
NGC 1313 X-2	a	< 1.13	0.30^{*}	$1.25^{+0.07}_{-0.06}$	$12.26^{+0.97}_{-0.77}$	757/783
	b	$2.11^{+1.22}_{-0.86}$	$0.25^{+0.07}_{-0.05}$	> 2.47	$4.14^{+17.72}_{-2.55}$	642/609
IC 342 X-1	a	$4.52^{+0.91}_{-0.76}$	$0.06^{+0.02}_{-0.01}$	$2.18^{+0.39}_{-0.24}$	$7.77^{+0.83}_{-0.92}$	852/929
	b	$2.11^{+1.24}_{-0.75}$	< 0.13	$2.55^{+0.57}_{-0.31}$	$7.56^{+0.81}_{-0.99}$	968/1012
IC 342 X-2	a	$28.84^{+3.33}_{-2.71}$	0.07 ± 0.01	$1.43^{+0.08}_{-0.06}$	$11.32^{+1.26}_{-1.2}$	1669/1695
	b	18.22 ± 2.33	0.07 ± 0.01	$1.99^{+0.18}_{-0.14}$	$10.78^{+1.27}_{-1.13}$	1076/1070
NGC 2403 X-1		$3.31^{+1.40}_{-1.76}$	$0.12^{+0.03}_{-0.01}$	$0.96^{+0.07}_{-0.05}$	$12.52^{+1.92}_{-1.50}$	942/923
2XMM J0737		< 2.46	$0.16^{+0.09}_{-0.05}$	$1.45^{+0.36}_{-0.22}$	$12.46^{+4.34}_{-2.69}$	261/258
M81 X-6	a	$2.99^{+1.14}_{-1.45}$	0.15 ± 0.02	$1.26^{+0.06}_{-0.05}$	$10.27^{+0.74}_{-0.67}$	1301/1318
	b	$2.46^{+1.42}_{-1.22}$	$0.10^{+0.01}_{-0.02}$	$1.59^{+0.17}_{-0.13}$	$9.67^{+1.10}_{-1.09}$	508/520
Holmberg IX X-1	a	< 0.20	0.22 ± 0.02	$2.47^{+0.10}_{-0.09}$	$7.96^{+0.22}_{-0.21}$	2714/2636
	b	< 0.09	0.23 ± 0.01	$2.46^{+0.08}_{-0.07}$	$7.62^{+0.14}_{-0.15}$	7458/7554
Circinus XMM2		$12.22^{+2.01}_{-2.18}$	0.12 ± 0.01	$1.53^{+0.16}_{-0.13}$	$7.01^{+0.81}_{-0.75}$	1212/1167

Note. The best fitting result from the MCD plus Comptonisation model, in which the seed photon temperature of the Comptonisation model is tied to the temperature of the MCD component. [a]Observational epoch. [b]Absorption column external to our Galaxy ($\times 10^{21}$ cm^{-2}). [c]The inner-disc temperature of the DISKBB component (keV). [d]The coronal temperature (keV). [e]The coronal optical depth. *The parameter cannot be constrained.

Table 2.7: The MCD plus Comptonisation model: coronal seed photon temperature is free.

Source	Ep.[a]	TBABS	DISKBB	COMPTT			χ^2/d.o.f.	Prob.[g]
		$N_{\rm H}$[b]	$kT_{\rm in}$[c]	kT_0[d]	$kT_{\rm corona}$[e]	$\tau_{\rm corona}$[f]		(%)
M33 X-8		$0.31^{+0.14}_{-0.13}$	0.43 ± 0.05	$0.63^{+0.06}_{-0.07}$	> 51.57	< 5.66	2754/2746	100.00
NGC 1313 X-1	a	$1.98^{+1.90}_{-1.44}$	> 0.22	0.50 ± 0.10	> 1.73	< 8.27	1628/1594	99.75
	b	$2.15^{+0.67}_{-0.52}$	$0.24^{+0.04}_{-0.07}$	< 0.49	$2.29^{+0.55}_{-0.29}$	$7.88^{+1.00}_{-1.24}$	1378/1377	64.87
NGC 1313 X-2	a	$1.67^{+0.69}_{-0.30}$	$0.39^{+0.51}_{-0.08}$	$0.65^{+0.35}_{-0.05}$	3.48^{*}	3.57^{*}	742/783	100.00
	b	$2.25^{+0.71}_{-0.60}$	$0.33^{+0.02}_{-0.03}$	1.78 ± 0.16	$0.41^{+0.09}_{-0.04}$	$43.75^{+11.25}_{-10.15}$	640/608	87.63
IC 342 X-1	a	< 1.44	$0.08^{+0.05}_{-0.03}$	$0.36^{+0.02}_{-0.05}$	$2.1^{+0.35}_{-0.22}$	$8.34^{+0.89}_{-0.98}$	848/928	94.38
	b	< 3.61	$0.58^{+0.43}_{-0.49}$	< 2.50	> 1.77	7.87	967/1011	60.06
IC 342 X-2	a	$14.19^{+2.26}_{-1.83}$	$0.09^{+0.02}_{-0.01}$	$0.74^{+0.08}_{-0.09}$	$1.96^{+1.21}_{-0.32}$	$6.6^{+2.20}_{-2.75}$	1632/1694	100.00
	b	$4.87^{+2.65}_{-1.93}$	$0.08^{+0.02}_{-0.01}$	$0.72^{+0.11}_{-0.13}$	$2.53^{+1.94}_{-0.46}$	$7.97^{+2.36}_{-2.97}$	1059/1069	100.00
NGC 2403 X-1		$1.55^{+1.02}_{-0.80}$	$0.23^{+0.06}_{-0.05}$	$0.51^{+0.06}_{-0.11}$	> 0.94	< 9.43	927/922	99.99
2XMM J0737		< 1.70	$0.26^{+0.05}_{-0.13}$	< 0.77	> 1.26	< 15.10	259/257	71.53
M81 X-6	a	$2.35^{+0.70}_{-0.60}$	$0.26^{+0.05}_{-0.04}$	$0.48^{+0.09}_{-0.08}$	$1.49^{+0.28}_{-0.15}$	$7.88^{+1.36}_{-1.71}$	1283/1317	100.00
	b	< 1.59	$0.23^{+0.17}_{-0.08}$	$0.41^{+0.17}_{-0.10}$	$1.78^{+0.54}_{-0.22}$	$8.48^{+1.53}_{-2.21}$	501/519	99.11
Holmberg IX X-1	a	< 0.17	$0.24^{+0.04}_{-0.17}$	$0.22^{+0.02}_{-0.04}$	$2.44^{+0.16}_{-0.13}$	$8.06^{+0.38}_{-0.46}$	2714/2635	39.13
	b	< 0.61	$0.13^{+0.06}_{-0.07}$	$0.21^{+0.01}_{-0.04}$	$2.52^{+0.14}_{-0.08}$	$7.48^{+0.12}_{-0.35}$	7451/7553	99.37
Circinus XMM2		4.61 ± 2.60	$0.25^{+0.17}_{-0.06}$	$0.48^{+0.10}_{-0.07}$	$1.75^{+0.62}_{-0.24}$	$6.18^{+1.22}_{-1.68}$	1197/1166	99.99

Note. The best fitting result from the MCD plus Comptonisation model, in which the seed photon temperature of the Comptonisation model was allowed to be a free parameter. [a]Observational epoch. [b]Absorption column external to our Galaxy ($\times 10^{21}$ cm^{-2}). [c]Inner-disc temperature of the DISKBB component (keV). [d]The seed photon temperature of the Comptonisation component (keV). [e]The coronal temperature (keV). [f]The coronal optical depth. [g]Probability that the minimum χ^2 is improved by letting the seed photon temperature of the corona be a free parameter, defined as the value of 1− *Probability(F-test)*. *The parameter cannot be constrained.

between the coronal optical depth and temperature disappeared when we allowed the coronal seed photon temperature to be free from the MCD temperature. We measure a Spearman's Rank correlation coefficient r_s = -0.36, corresponding to the rejection of the hypothesis that these two parameters are correlated. This might imply that the anti-correlation reported in previous studies is an artificial relationship, a direct result of tying two physically-unrelated parameters together. We will discuss this further in Section 4.

2.3.4 Blackbody plus relativistic disc around spinning black hole model

Although the MCD plus Comptonisation model provides a very good fit to the data, the direct interpretation of the two components as an inner, thick corona and uncovered regions of the disc further from the black hole has recently been challenged. In particular, more recent works argue that the soft spectral component originates in a massive, optically thick, outflowing wind (Kajava & Poutanen 2009; Middleton et al. 2015; Sutton et al. 2013b), whereas the higher energy curved component could be physically attributed to the hot inner part of the disc, requiring a large colour correction compared to standard discs (Middleton et al. 2011a; Kajava et al. 2012). Hence, based on this alternative assumption of ULX geometry, we next examine our ULX sample using a double component model composed of a plain blackbody (hereafter BB; BBODY in XSPEC) plus a general relativistic accretion disk around a spinning black hole (in particular, an accretion disc around a Kerr black hole; KERRBB in XSPEC; Li et al. 2005); the BB continuum is used as the simplest representation of the blackbody emission from the optically thick outflowing wind, whilst the KERRBB model is used to represent the harder emission from the hot inner regions of an accretion disc. We note that the KERRBB model is the only currently available model taking into account full relativistic effects. Such effects are important and become significant when considering photon emission at very close to the black hole's last stable orbit. In addition, the model also provides a calculation of the mass and spin of the black hole that is powering the accretion flow.

During the spectral modelling, only three parameters of the KERRBB component – black hole mass, mass accretion rate and specific angular momentum (spin) of the black hole – are allowed to fit freely; the remainder of the KERRBB parameters are fixed at the default model value (including fixing the normalisation to unity). In addition, for the ULXs that are observed in two separate epochs, we modelled the spectra from both epochs simultaneously. This was so the black hole masses and spins could be set to the same value during both observations, as we do not expect them to vary between observations.

The best fitting results are reported in Table 2.8. Overall, the model yielded a worse fitting result than the MCD plus Comptonisation model. In particular, the data for NGC 1313 X-1 and IC 342 X-2 reject this model to a high statistical significance (null hypothesis probability of $\sim$0). For example, Fig. 2.4 plots the best fitting results of the NGC 1313 X-1 spectra modelled by the BB+KERRBB model. It is obvious that the KERRBB component struggles to explain the high energy tail of the spectra (> 5 keV), resulting in the poor fit. This might be due to the KERRBB model assuming a standard disc geometry and a constant mass accretion rate for all accreting radii, which may be an inappropriate assumption for ULXs accreting material at super-Eddington rates. We will discuss this further in Section 2.4. However, even though the model yielded worse fits than the previous two component models, we cannot completely reject the results obtained from this model as the best fitting statistic in 11 cases indicates an acceptable fit (null hypothesis probability of $\gtrsim 5\%$). So, the fitting results will be interpreted bearing this caveat in mind.

The most interesting result obtained from this model is that the masses of the black holes powering the ULXs are constrained in the range 4 – 30 $M_{\odot}$, within the regime of sMBHs. However, we note that the value of black hole mass obtained from the model correlates strongly with the spin parameter in our fits (see below). Fortunately, as the black hole spins are constrainable in the modelling of 11 spectra, the calculation of black hole mass can also be constrained in these cases. We found that the calculated values of the black hole spin are high (with the exception of IC 342 X-1, we see $a \gtrsim 0.8$, close to maximal spin values). Indeed, as the hard

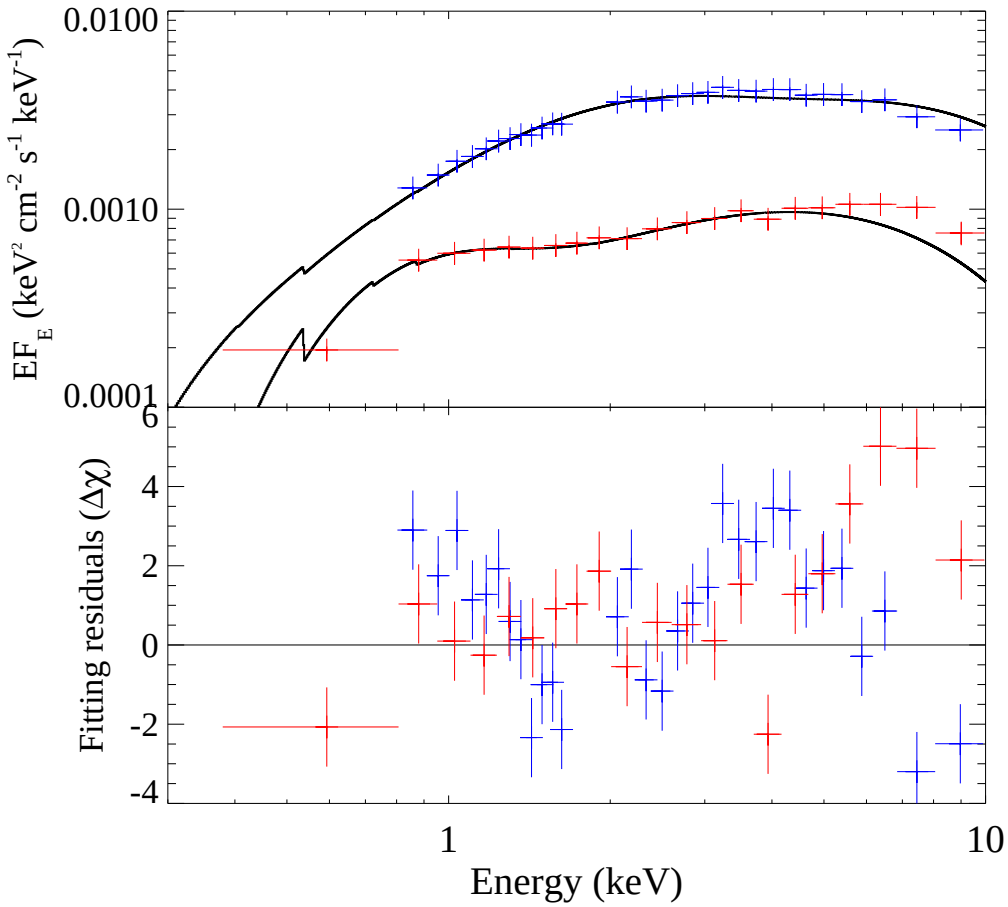

Figure 2.4: *Top panel:* The spectra of NGC 1313 X-1 obs a (blue plot) and NGC 1313 X-1 obs b (red plot) modelled by the BB plus KERRBB model (black line). *Bottom panel:* the fitting residuals corresponding to the modelling above. Note that both spectra are rebinned for display purposes, and similar caveats to Fig. 2.1 apply.

Table 2.8: The BB plus KERRBB model

Source	Ep.[a]	TBABS	BB	KERRBB			χ^2/d.o.f.[g]
		$N_{\rm H}$[b]	kT[c]	a[d]	$M_{\rm BH}$[e]	$\dot{m}$[f]	
M33 X-8		< 0.01	0.28 ± 0.01	>0.99	$11.55^{+0.33}_{-0.54}$	$1.02^{+0.18}_{-0.01}$	2877/2747
NGC 1313 X-1	a	< 0.02	$0.52^{+0.009}_{-0.011}$	>0.86	$13.55^{+0.85}_{-0.73}$	$12.01^{+9.99}_{-0.23}$	[3219/2975]
	b	$1.31^{+0.33}_{-0.38}$	$0.04^{+0.005}_{-0.009}$			$3.06^{+2.94}_{-0.05}$	[3219/2975]
NGC 1313 X-2	a	< 0.19	0.62 ± 0.02	0.99*	$5.82^{+1.20}_{-0.92}$	$7.85^{+0.49}_{-0.42}$	1447/1394
	b	$0.95^{+0.68}_{-0.55}$	0.25 ± 0.02			2.04 ± 0.09	1447/1394
IC 342 X-1	a	< 0.66	$0.56^{+0.04}_{-0.05}$	>0.54	$6.26^{+0.71}_{-0.68}$	$6.81^{+12.8}_{-0.27}$	1830/1943
	b	< 0.22	0.36 ± 0.03			$6.78^{+11.25}_{-0.18}$	1830/1943
IC 342 X-2	a	23.74 ± 0.68	0.71 ± 0.01	>0.99	$22.15^{+0.94}_{-1.58}$	$4.20^{+1.07}_{-0.05}$	[3299/2767]
	b	$49.61^{+3.04}_{-2.49}$	0.14 ± 0.01			$2.35^{+0.60}_{-0.05}$	[3299/2767]
NGC 2403 X-1		$2.38^{+0.76}_{-0.79}$	0.12 ± 0.01	0.99*	$28.54^{+2.05}_{-1.94}$	0.8 ± 0.02	932/924
2XMM J0737		< 1.37	0.15 ± 0.03	0.99*	$3.93^{+0.86}_{-0.68}$	$1.55^{+0.11}_{-0.05}$	260/259
M81 X-6	a	$0.95^{+0.38}_{-0.33}$	$0.24^{+0.04}_{-0.03}$	>0.79	$21.05^{+0.98}_{-11.07}$	$1.55^{+2.22}_{-0.03}$	1871/1863
	b	$1.39^{+0.69}_{-0.63}$	0.12 ± 0.01			$1.80^{+2.60}_{-0.04}$	1871/1863
Holmberg IX X-1	a	< 0.03	0.29 ± 0.01	>0.98	$12.27^{+0.25}_{-1.58}$	$7.99^{+2.28}_{-0.07}$	10384/10192
	b	< 0.02	0.31 ± 0.004			$8.35^{+2.38}_{-0.05}$	10384/10192
Circinus XMM2		1.15 ± 0.54	$0.56^{+0.04}_{-0.05}$	0.99*	$18.19^{+4.16}_{-3.78}$	$2.35^{+0.27}_{-0.26}$	1201/1168

Note. [a]Observational epoch. [b]Absorption column external to our Galaxy ($\times 10^{21}$ cm^{-2}). [c]Temperature of the BB component (keV). [d]The specific angular momentum (spin) of the black hole where -1 $\leq a <$ 1. *The spin is frozen at 0.99 (see text). [e]The mass of the black hole ($M_\odot$). [f]The mass accretion rate in units of Eddington mass accretion rate ($\dot{m}_{\rm Edd}$), assuming the black hole mass in column 6. It is defined as $\dot{m}_{\rm Edd} = L_{\rm edd}/\epsilon c^2$, where ϵ is the radiation efficiency of a standard accretion disk around a Kerr black hole. [g]The minimum χ^2 over degrees of freedom obtained from the best fit. The square brackets indicate the cases in which the model can be strongly rejected statistically (null hypothesis probability $\lesssim 0.001$).

component in the ULX spectra is very broad (see Fig. 2.4, obs b, for example), the model attempts to push the value of black hole spin to be very high, broadening the KERRBB spectra in order to obtain the best fitting result (although residuals remain, particularly to the high energy tail). On the one hand, this could imply that the black holes powering ULXs are truly high spin. However, optimising the spin parameter cannot completely explain the broadness of the hard energy component of the ULX spectra, suggesting that the spectra require an intrinsically broader spectrum to explain the hard component.

For the remaining five spectra in which the spin parameter is unconstrainable in the spectral modelling, we assume a black hole spin of 0.99. Note that by assuming the black hole spin value to take a maximal value of 0.99, we might overestimate the mass of black holes powering the ULXs. For example, in the case of the Circinus XMM2 spectral modelling, freezing the black hole spin at 0.99 and -1 (the maximum and minimum allowed values of black hole spin in the model) results in calculated black hole masses of $\sim$18 $M_{\odot}$ and $\sim$4 $M_{\odot}$, respectively.

2.3.5 Blackbody plus slim disc model

We showed above that, despite producing some interesting results, a model composed of a BB plus a KERRBB cannot always satisfactorily describe the *Suzaku* ULX spectra, especially in the high energy tail. In fact, it appears that ULXs require a very broad hard component to adequately describe their spectrum. Therefore, in this section, we modify the BB+KERRBB model by replacing the KERRBB component with a potentially broader hard component, a MCD in which the radial temperature profile of the disc (p) is allowed to be a free parameter (DISKPBB in XSPEC).

The fitting results show that this model can describe the ULX spectra equally as well as the MCD plus Comptonisation model, showing similar values of χ^2/d.o.f. (see Table 2.9). One peculiar result is that the best fitting result seems to be worse than that of the MCD plus Comptonisation model for one object, M33 X-8. In fact, we found that this spectrum prefers the BB component to explain its hard emission whilst the DISKPBB is used to approximate the soft excess. However, the other ULXs all show softer BB components. The value of the exponential parameter

p obtained from the DISKPBB component when it forms the harder component is $<$ 0.75 in most cases and, indeed, close to $\sim$0.5 in several cases. This is consistent with the prediction of slim accretion disc models (Watarai et al., 2000); we will discuss this further in Section 2.4.4.

Moreover, the good fit to this model enabled a first order calculation for the size of the putative outflowing wind, by assuming that the wind can be approximated by the BB spectral component. To begin the calculation, we calculated the intrinsic flux (i.e. that corrected for absorption) of the BB component by adding the multiplicative component CFLUX in front of the BB component, and then converted the flux into an intrinsic luminosity using the ULX distance listed in Table 2.1. Using the Stefan-Boltzmann law $L{=}\sigma AT^4$ where L, σ, A and T are the luminosity, the Stefan-Boltzmann constant, the blackbody surface area and the blackbody temperature, respectively, we estimated the surface area of the wind from the BB temperature and the BB intrinsic luminosity. Then, given that the wind has a spherical geometry with a covering fraction f (the fraction of the wind surface area covering the disc), the wind size R can be estimated as $R = (A/4\pi f)^{1/2}$. Here, we simplified the calculation by assuming a nominal covering fraction f of 0.8 throughout the calculation, although the real structure of the wind might be more complex (we will further discuss this point in Section 2.4.4). Note that we excluded both ULXs in IC 342 from the calculation due to the high absorption columns (both Galactic and extra-galactic) obscuring their BB components – in particular the high absorption column towards IC 342 X-2 of $N_{\rm H} \gtrsim 24 \times 10^{21}$ cm^{-2} beyond our own Galaxy – resulting in large uncertainties in the calculation of the BB temperature and intrinsic BB luminosity. We also excluded M33 X-8 from the calculation because its BB component fits to its hard emission, inconsistent with our assumption that the BB spectrum is the soft emission from the wind. The radial extents of the outflowing wind, plotted as a function of the total ULX intrinsic luminosities, are shown in Fig. 2.5. Here we report the wind sizes in units of gravitational radius, $R_{\rm g}{=}GM/c^2$, and we assume a $10M_{\odot}$ black hole. The size of the wind is then constrained to be between 10^4 – 10^6 $R_{\rm g}$ for the various ULXs.

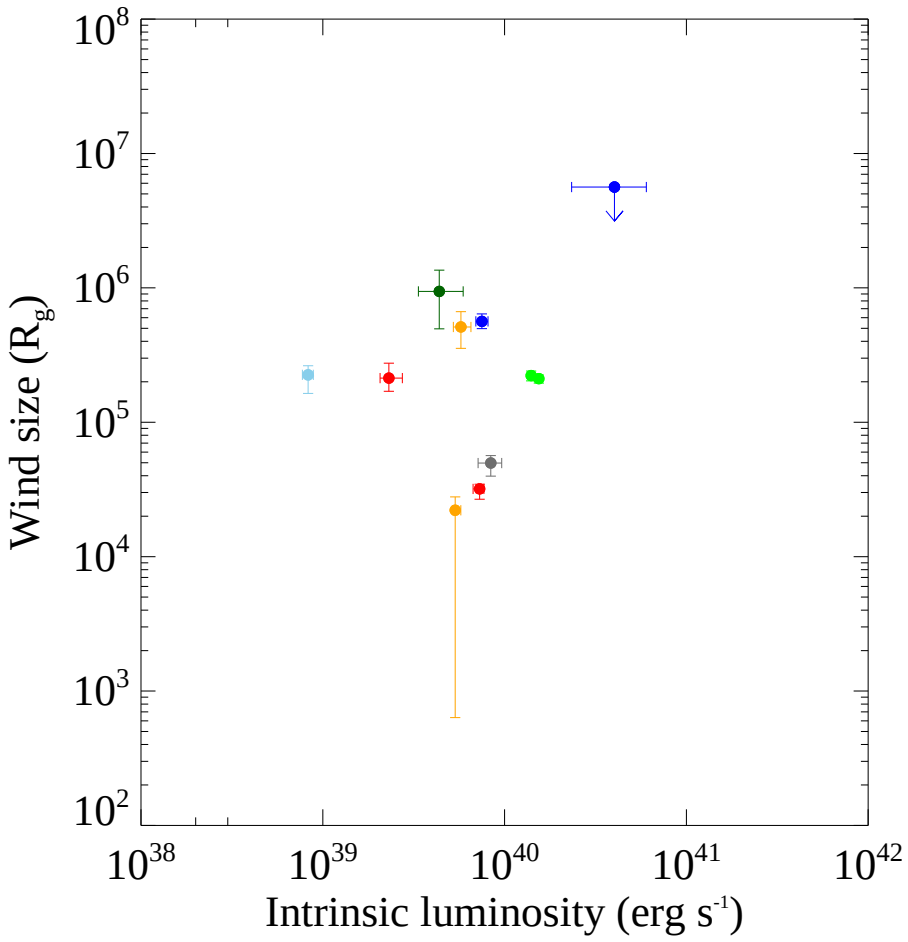

Figure 2.5: Outflowing wind radius as a function of the intrinsic ULX luminosity. The colour code is as per Fig. 2.3.

Table 2.9: The BB plus slim disc model

Source	Ep.[a]	TBABS	BB	DISKPBB		χ^2/d.o.f.
		$N_{\rm H}$[b]	kT[c]	$kT_{\rm in}$[d]	p[e]	
M33 X-8		$0.67^{+0.13}_{-0.15}$	$2.40^{+5.01}_{-0.73}$	$1.38^{+0.22}_{-0.23}$	$0.57^{+0.02}_{-0.01}$	2773/2747
NGC 1313 X-1	a	$5.18^{+2.28}_{-2.82}$	> 0.12	$2.24^{+0.25}_{-0.17}$	$0.55^{+0.16}_{-0.03}$	1632/1595
	b	$1.69^{+0.53}_{-0.46}$	$0.18^{+0.02}_{-0.017}$	$3.47^{+0.67}_{-0.53}$	$0.57^{+0.03}_{-0.02}$	1378/1378
NGC 1313 X-2	a	$2.16^{+0.50}_{-0.59}$	$0.82^{+0.07}_{-0.08}$	$3.34^{+0.77}_{-1.28}$	$0.53^{+0.07}_{-0.02}$	743/782
	b	$2.06^{+1.17}_{-0.80}$	$0.21^{+0.05}_{-0.05}$	> 4.37	0.53 ± 0.02	643/609
IC 342 X-1	a	$3.64^{+0.96}_{-0.88}$	$0.06^{+0.02}_{-0.01}$	$3.09^{+0.61}_{-0.41}$	0.57 ± 0.02	849/929
	b	$1.00^{+0.49}_{-0.42}$	< 0.03	$3.94^{+1.22}_{-0.55}$	$0.58^{+0.01}_{-0.02}$	965/1012
IC 342 X-2	a	$23.02^{+3.13}_{-2.57}$	0.07 ± 0.01	$1.72^{+0.09}_{-0.08}$	> 0.74	1653/1695
	b	$13.11^{+3.01}_{-3.15}$	0.07 ± 0.01	$2.68^{+0.36}_{-0.28}$	$0.8^{+0.16}_{-0.09}$	1069/1070
NGC 2403 X-1		$1.99^{+0.13}_{-1.28}$	$0.13^{+0.03}_{-0.02}$	$1.14^{+0.08}_{-0.07}$	$0.71^{+0.14}_{-0.08}$	934/923
2XMM J0737		< 1.60	0.15 ± 0.03	$1.99^{+0.68}_{-0.41}$	$0.72^{+0.28}_{-0.09}$	260/258
M81 X-6	a	$2.21^{+0.79}_{-0.64}$	$0.16^{+0.03}_{-0.02}$	$1.54^{+0.07}_{-0.06}$	0.62 ± 0.03	1289/1318
	b	< 0.48	$0.72^{+0.35}_{-0.22}$	< 4.36	< 0.65	504/520
Holmberg IX X-1	a	$0.43^{+0.18}_{-0.19}$	0.27 ± 0.02	$3.52^{+0.31}_{-0.27}$	$0.61^{+0.02}_{-0.01}$	2722/2636
	b	0.89 ± 0.12	0.26 ± 0.02	$3.71^{+0.20}_{-0.17}$	0.58 ± 0.01	7474/7554
Circinus XMM2		$2.55^{+1.28}_{-1.74}$	0.63 ± 0.09	$1.90^{+0.52}_{-0.27}$	$0.58^{+0.15}_{-0.06}$	1199/1167

Note. [a]Observational epoch. [b]Absorption column external to our Galaxy ($\times 10^{21}$ cm^{-2}). [c]Temperature of the BB component (keV). [d]Inner-disc temperature of the DISKPBB component (keV). [e]Exponent of the radial (r) dependence of the disk temperature (T), where $T(r) \propto r^{-p}$.

2.3.6 Blackbody plus cutoff power-law model

As demonstrated by the broadband spectral studies of NGC 1313 X-1 and Holmberg IX X-1 using a combination of *XMM-Newton* and *NuSTAR* data (Bachetti et al., 2013; Walton et al., 2014), a non-thermal high energy tail is suggested to be present in ULX spectra. Indeed, Bachetti et al. (2013) showed that the high energy tail is well-described by a cut-off power-law component. Thus, as a test, we modelled our *Suzaku* spectra using a BB plus cut-off power-law model. However, no statistical improvement is obtained from the model, when compared to the MCD plus Comptonisation model in Section 2.3.4 and the BB plus slim disc model in Section 2.3.5. So, a high energy non-thermal tail might be required by ULX spectra above 10 keV, outside the *Suzaku* observing bandpass; but a thermal component such as COMPTT or DISKPBB is sufficient to explain the hard component of the *Suzaku* ULX spectra. Therefore, we will not consider this model any further.

2.4 Discussion

We have analysed 18 good quality spectra of 10 ULXs located in very nearby galaxies ($d < 5$ Mpc) available in the public data archives of the *Suzaku* X-ray telescope. A range of empirical and physical models were fitted to the data in order to examine the X-ray spectral properties of the ULXs. In this section, the goodness of fit and the physical explanation obtained from each model will be discussed. Furthermore, we will compare and discuss whether the analysis results obtained from our *Suzaku* data are consistent with the results of *XMM-Newton* observations of very similar samples of ULXs.

2.4.1 The effect of telescope observational bandpass on spectral analyses

We have demonstrated that the *Suzaku* spectra cannot be well described by simple single component models – neither a MCD nor a power-law continuum – in most cases. This is consistent with the previous studies of ULX spectra using good quality

XMM-Newton data (Stobbart et al., 2006; Gladstone et al., 2009), which have shown that they instead required a two component model to achieve statistically acceptable fits. Indeed, we showed that the canonical two component model composed of a MCD and a power-law can describe the *Suzaku* ULX spectra; the fitting statistic is in most cases substantially improved using this model, compared to that of single component models.

However, there are seven spectra for which a single component model provides an acceptable fit. In six cases this is readily explicable as the limitations of moderate quality data. However, in the case of Holmberg IX X-1 obs b, which can be well-described by an absorbed power-law model, the spectra are very high quality ($\sim$7000 spectral bins). It appears that this result is because the spectrum of Holmberg IX X-1 obs b is relatively flat in the 1-6 keV energy band where the *Suzaku* area peaks (i.e. any strong curvature is at energies outside this range). Indeed, this spectral shape is consistent with other measurements of the spectral shape of Holmberg IX X-1 at low luminosity, as demonstrated by Vierdayanti et al. (2010); Walton et al. (2014); Luangtip et al. (in prep.). However we showed that the fitting statistics of all the spectra that can be well approximated by a single component model are improved when they are modelled by the two component model of a MCD plus a power-law. Thus we conclude that the *Suzaku* ULX spectra should preferentially be described by two component models.

Although the *Suzaku* ULX sample prefers two component models to describe their spectra, the spectral modelling results for MCD plus power-law models are somewhat different from previous ULX studies using *XMM-Newton* data (e.g. Stobbart et al. 2006; Gladstone et al. 2009). This is because the best fitting model yields a hot disc temperature in all objects, as the MCD component fits to the harder spectral component whilst the power-law component approximates the softer component of the spectra. This is interesting as the high disc temperature confirms the subtle high energy turnover (curvature) in ULX spectra, as was detected in the previous studies of high quality ULX spectra observed by *XMM-Newton* (and confirmed by *NuSTAR*, e.g. Bachetti et al. 2013). However, for this particular model, high disc temperatures ($\gtrsim$1 keV) were only found for BD spectra with *XMM-Newton*, and

two-component spectra (SUL/HUL) tended to yield low (cool, $\sim$ 0.2 keV) MCD temperatures, with the power-law comprising the hard component, in contrast to the *Suzaku* results. A stark example of the differences between *Suzaku* and *XMM-Newton* fits is Holmberg IX X-1. In *Suzaku* the MCD fits to the high energy curvature, which has an intrinsically hard spectrum with a turnover above 7 keV (cf. Fig. 1), and the power-law (with a soft photon index) "fills in" the soft excess. In contrast, the *XMM-Newton* spectra of this ULX (for example, see Fig. 8 of Gladstone et al. 2009) have a better defined and more pronounced soft excess feature, to which the MCD component fits whilst the hard component is instead approximated by the power-law continuum, resulting in a cool MCD temperature.

It is highly unlikely that the intrinsic spectra of the ULXs are varying uniformly between the *Suzaku* and *XMM-Newton* observations; the explanation for the differences in the spectral fits is therefore likely to be far more prosaic. In fact, it is likely that this is a direct consequence of the lower effective area of the *Suzaku* telescope and instruments than *XMM-Newton* below 1 keV.[16] This lack in area causes much sparser data in the regime crucial to the detection of soft excesses, below 1 keV, and so rather than fitting the curved MCD component to the obvious excess at these energies seen in *XMM-Newton* data, the subtle curvature seen at higher energies in *XMM-Newton* data forms a better driver for the MCD fit in the *Suzaku* data. In fact, this divergence in MCD plus power-law fits really serves to emphasise that, while this is a useful canonical model to use on ULX spectra, it is not a good description of the best data, for which two thermal (curved) components provide a better description (e.g. Stobbart et al. 2006; Walton et al. 2014).

A direct implication of the differences in fits between *XMM-Newton* and *Suzaku* data is that the classification scheme for different types of ULX spectra proposed by Sutton et al. (2013b), and based on MCD plus power-law model fits, does not work for the *Suzaku* data. In this chapter we have proposed amendments to the scheme that allow it to be applied successfully to *Suzaku* data, primarily by noting that the hottest MCD temperatures ($>$ 2 keV) appear when the spectrum is distinctly

[16] `http://astro-h.isas.jaxa.jp/researchers/sim_back_2010Feb10/sim/index_e.html`

two-component, and so can be used to differentiate SUL/HUL spectra from BD ones, although a visual inspection is required to distinguish between SUL and HUL regimes. The new scheme was successfully applied to our sample of ULXs, with the main result being that we do not see any SUL objects. However, given that the sample we look at contained no such objects in *XMM-Newton* observations, this should perhaps not be a surprise (and highlights the small number of objects we have in our sample). Most of the very nearby ULXs in our sample are observed in the BD regime; three of them are at slightly higher luminosities than the bulk of objects observed in this regime by *XMM-Newton* ($> 4 \times 10^{39}$ erg s^{-1}, compared to $< 3 \times 10^{39}$ erg s^{-1}; Sutton et al. 2013b), though two of these objects are also seen at similar luminosities with disc-like spectra by *XMM-Newton* (IC 342 X-1 and M81 X-6). Only Holmberg IX X-1 appears to be a clear HUL regime detection, and both objects in NGC 1313 appear to transit between a BD spectrum at high luminosity, and a HUL spectrum at lower luminosities. We discuss this last result further in Section 2.4.4.

2.4.2 The existence of a cool and optically thick corona?

In an attempt to improve our physical explanation of the ULX spectra, we then modelled them using a model composed of a MCD plus Comptonisation. We firstly use the popular, simplified version of the model where we tie the coronal seed photon temperature to the MCD temperature in order to get good constraints on the model-fitting parameters. Overall, the model fits well to the ULX spectra. Similar results to previous ULX spectral studies using *XMM-Newton* data (e.g. Gladstone et al. 2009) are obtained: low MCD temperatures and optically thick, cool coronae are observed. In addition, we also found an anti-correlation between the coronal temperatures and optical depths, similar to that found in previous studies (Vierdayanti et al., 2010; Pintore & Zampieri, 2012; Pintore et al., 2014). This behaviour was explained physically by the presence of the optically cool and thick corona, that obscures the inner part of the disc at super-Eddington accretion rates; as the accretion rate increases, more excess mass is ejected into the corona, resulting in a cooler and more opaque corona (Gladstone et al., 2009).

However, we have argued that tying the coronal seed photon temperature to the MCD temperature makes no sense since the inner disc is hidden by the opaque corona and so we are not using the true inner-disc temperature to seed the corona. To ensure the model is more consistent with a physical point of view, we freed the coronal seed photon temperature from the disc temperature. We demonstrated that the modified model helps to improve the goodness of fit, allowing for one more free parameter, in most cases (i.e. 11 spectra show $\gtrsim$ 95 per cent probability that the goodness of fit is improved), in contrast to the previous studies. For example, a broadband spectral study of Holmberg IX X-1 using *XMM-Newton* and *NuSTAR* data suggests that freeing the parameter does not help to improve the fitting statistic or significantly change the value of the model parameters (Walton et al., 2014). In addition, some *XMM-Newton* studies of ULXs also argue that freeing the parameter could lead to difficulty in finding a global minimum in the fitting (e.g. Feng & Kaaret 2009; Pintore & Zampieri 2012). However, we are able to find global minima, and constrain all parameters (in at least one direction) in almost all cases.

The fitting results are similar to those obtained with the seed photon temperature tied: a cool disc temperature, and an optically thick and cool corona. Interestingly, the model suggests that the temperature of the coronal seed photons is likely to be significantly higher than the MCD temperature, which is consistent with the obscuration of the inner disc by an opaque corona, or at least the hard component, if it is truly Comptonised, being seeded from a source distinct from the soft component. We also found that the largest improvements in fits ($\sim$100 per cent improvement in the goodness of fit according to the F-test) happen in the case of BD spectra (e.g. M33 X-8 and M81 X-6). This suggests that these spectra are too broad to be explained even by a coupled MCD and COMPTT spectrum; the seed photon temperature is needed to be uncoupled in order to reproduce the broadened spectra. In addition, the anti-correlation between the coronal temperature and optical depth seems to disappear when the seed photon temperature is free, with statistical tests showing no correlation between these two parameters. This suggests that the correlation seen in the case of the tied seed photon temperature is artificially induced by tying the parameters together.

In fact, recent work has shown that broadband ULX spectra can be explained equally well by several alternative models composed of two thermal (curved) components (Walton et al., 2014). Hence the MCD plus Comptonisation model is likely just one of several phenomenological models that describe the shape of ULX spectra very well, but may not describe their physics. In the remainder of the discussion we look at models that may better reproduce the physics of ULXs.

2.4.3 The mass of black holes powering ULXs

More recent studies of ULXs, including a number of hydrodynamical simulations, have favoured models that consider a super-critical accretion regime, where massive and optically thick outflowing winds are launched from within the photospheric radius of a disc accreting at substantially super-Eddington rates (e.g. Poutanen et al. 2007; Ohsuga 2007; Ohsuga & Mineshige 2011; Middleton et al. 2015). We therefore attempted to fit the data with models that approximated the two components in ULX spectra as the two main X-ray emitting regions predicted in this model: the cool and optically-thick wind, and the hot inner part of the disc. In the first case we did this using a BB plus relativistic disc model, BB + KERRBB.

In general this does not fit as well as the MCD plus Comptonisation model, with the fitting residuals suggesting in particular that the hard component is too broad to be approximated by a KERRBB spectrum. This drives the model best fitting results to take a value of black hole spin that is very high (close to the maximum Kerr black hole spin value) to reproduce the broad hard component. This may simply be informing us that the broad spectrum of the hard spectral component is evidence that ULXs are powered by rapidly spinning black holes. In fact, measurements for high spin black holes have been published for several BHB systems, for example GRS 1915+105 ($a > 0.98$; McClintock et al. 2006), LMC X-1 ($a = 0.92$; Gou et al. 2009) and M33 X-7 ($a = 0.84$; Liu et al. 2010). Furthermore, the spin of several supermassive black holes reported by previous studies could range from 0.6 to $>$ 0.98 (e.g. Brenneman & Reynolds 2006; Fabian et al. 2009; Schmoll et al. 2009). It is therefore possible that the black holes in ULXs possess similarly high values of spin.

However, even if the black hole spin is optimised to a near-maximal value, the model still cannot adequately reproduce the hard component of some ULX spectra. Thus it is likely that the black hole spin alone cannot completely explain the broadness of the hard component. Indeed, if this component does represent the emission from the hot inner parts of the accretion discs, the failure of the KERRBB model to fully explain the hard component might be due to the fact that the KERRBB model assumes a standard accretion disc geometry (Shakura & Sunyaev, 1973) and constant accretion rate for all disc radii. This is not the expected geometry for super-Eddington accretors. Theoretical works predict that at super-critical accretion rates, the disc should increase in scale height to about the order of unity ($H/R \sim 1$) as its interior becomes advection dominated, and it should lose a non-negligible fraction of the inflowing mass via the outflowing wind (Poutanen et al., 2007; Ohsuga, 2007; Ohsuga & Mineshige, 2011). A combination of these effects and, in particular, a large colour correction due to the high temperature of the inner disc (cf. Kajava et al. 2012) could lead to the broad hard component. Therefore, we suggest there are two possible origins for the breadth of the hard spectral component: either (i) it is solely the consequence of the conditions in the super-Eddington accretion disc, or (ii) it is a combination of the effects of super-Eddington accretion with the effect of a highly spinning black hole.

Nonetheless, despite the imperfect fits, an interesting result obtained from the KERRBB model is the mass of the black holes powering the ULXs. Assuming that to first order the effects of super-Eddington accretion can be ignored, we can constrain the mass of the black hole powering the ULXs via the KERRBB model. This shows that the ULXs are powered by sMBHs ($\sim$4 – 30 $M_{\odot}$). Indeed, these masses are consistent with the direct mass calculations by the other ULX studies, that also report that ULXs are powered by sMBHs (Middleton et al., 2013; Liu et al., 2013; Motch et al., 2014). However, we note that black hole masses calculated by the KERRBB model are strongly dependent on the black hole spin parameter and, as discussed above, a high spin is required to reproduce the broadened KERRBB spectrum, which may not be a real characteristic of the black holes. So, an overestimation of the black hole spin could lead to an overestimation of the black hole mass. Hence, a direct

implication is that some ULXs with a combination of a high spin estimate and a low black hole mass estimate might be powered by relatively low mass objects, perhaps below $3M_{\odot}$. In two particular cases, 2XMM J0737 and NGC 1313 X-2, this might imply the presence of a neutron star instead of a black hole. If so, these would join M82 X-2, that was shown to be a $1.4M_{\odot}$ neutron star accreting material at $\sim$100 times the Eddington limit by Bachetti et al. (2014), in the new class of neutron star ULXs.

2.4.4 Super-Eddington accretion models with an outflowing wind

We replaced the KERRBB component in the BB + KERRBB model with a DISKPBB component in an attempt to improve our description of the hard component of the ULX spectra; this worked, and interesting results are obtained from the model. Firstly, the exponent of the radial dependence of the disk temperature (p) is found to be $\lesssim$0.75 in most objects, consistent with theoretical predictions for advection-dominated accretion discs, where the disc has a large scale height due to support from radiation pressure in the disc interior, and where many photons are advected directly into the black hole before radiating out from the disc (e.g. Poutanen et al. 2007). Indeed, several ULXs prefer a temperature profile p $\sim$0.5, consistent with the value expected in the slim accretion disc model (Watarai et al., 2000).

The temperature of the DISKPBB component was found to be relatively lower for BD spectra ($\sim$1.5 – 2 keV) than for HUL spectra ($\sim$3 – 4 keV). If, as for sub-Eddington discs, the temperature of the disc scales in a positive sense with the accretion rate, then this suggests an increase in the mass accretion rate in the transition from a BD regime ($\sim$Eddington accretion) to a HUL regime (super-Eddington accretion; Gladstone et al. 2009; Sutton et al. 2013b). However, it is interesting to note that in case of NGC 1313 X-1 and NGC 1313 X-2, in contrast, their spectra appear to evolve from a HUL to BD regime as their luminosities increase. A similar pattern of spectral variability has also been found in the evolution of Holmberg IX X-1 spectra (see Chapter 3; also Walton et al. 2014). This evolution could be explained by a change in the wind power and geometry, due to an increase in the

accretion rate, in the context of the spectral-timing model for ULXs presented by Middleton et al. (2015). To see a HUL spectrum, then at lower luminosities we are observing the ULX at a relatively low inclination angle where the wind does not obscure the inner disc from our direct view. Hence we view a spectrum with two components, in which the thermalised emission from the optically thick wind and from the hot inner part of the disc contribute to the soft and hard spectral components, respectively. As the accretion rate increases, so does the luminosity, and the wind is more powerful and so the opening angle of the 'funnel' (a relatively evacuated region perpendicular to the disc, bounded by the inflated disc and wind) narrows. At this increased luminosity level, the wind may completely obscure the inner part of the disc from the observer's line of sight; hence a high fraction of the energetic photons emitted from the inner region of the disc are scattered away from the line of sight, resulting in a weaker hard spectral component. Photons that do arrive at the observer need to travel through the optically thick wind and so are down-scattered in the cool wind plasma. A combination of these down-scattered photons and an increase in the intensity of the soft emission from the wind could lead to a BD spectrum at the highest luminosities for NGC 1313 X-1 and NGC 1313 X-2. Interestingly, these observed spectra are consistent with simulations of Comptonised spectra from supercritical accretion regimes, in which the spectra become disc-like at the highest accretion rates (Kawashima et al., 2012).

Finally, we consider the fitting results obtained from the BB component of the BB plus DISKPBB model. Assuming that a photosphere at the base of the optically thick wind provides the soft component, and its spectrum can be approximated (to first order) by a BB spectrum, we calculated the size of the X-ray emission region of the outflowing wind. To simplify the calculation, the wind geometry is assumed to be spherical with an 80 per cent covering fraction. This demonstrates that the wind could extend up to $\sim 10^4 - 10^6$ $R_{\rm g}$ from the centre of the disc. Interestingly, this is consistent with the theoretical prediction of the size of the outer photospheric radius (the largest radius before the wind becomes optically thin) calculated by Poutanen et al. (2007). Indeed, Sutton et al. (2014) use an X-ray reprocessing model and a combination of *HST* and *XMM-Newton* data to show that ULX accretion discs (for

objects with disc-like spectra) extend to a radius of $\sim 10^6$ $R_{\rm g}$. This suggests that the optically thick wind should be truncated below $\sim 10^6$ $R_{\rm g}$, consistent with the calculated sizes of the wind from our simple BB component.

However, the recent simulations of Takeuchi et al. (2013) show that the typical size of the optically thick wind is of the order of $\sim 10^2$ $R_{\rm g}$, which is much smaller than that calculated in this chapter. Furthermore, X-ray spectral studies of possible broad absorption features in the wind (Middleton et al., 2014) suggest that the wind becomes optically thin at a disc radius $\gtrsim 10^3$ $R_{\rm g}$. Thus these studies may imply that we overestimate the size of the outflowing wind by a factor up to $\sim 10^3$. One cause could be an incorrect assumption of the wind geometry. Indeed, simulations have demonstrated that the wind is highly dynamical and its structure can be very complex (e.g. Ohsuga & Mineshige 2011; Takeuchi et al. 2013), which may also lead to temperature structure within the wind. So simply assuming a spherical geometry and single temperature may be inappropriate, and a more realistic geometric and/or temperature structure may be required in the calculation.

2.5 Conclusion

In the chapter, we have analysed high quality X-ray spectra of ULXs in very nearby galaxies, obtained from *Suzaku* observations. In particular, we attempted to describe the spectra using various empirical and physical models. The results can be summarised as follows.

Firstly, we compared the the results of fitting common, empirical models to the *Suzaku* data with results from previous ULX studies using *XMM-Newton* data. We demonstrated that the data quality of the ULX spectra in this chapter is sufficiently high as to require two component models, similar to *XMM-Newton* studies of the best quality ULX spectra. The canonical MCD plus power-law model provided acceptable fits to the data, but produced different fits to those commonly seen in *XMM-Newton* studies - the MCD tended to fit to the hard spectral component in all objects, and not the soft component as seen in *XMM-Newton* studies of objects in the SUL/HUL regimes. Whilst this does rather obviously confirm the spectral

turnover in the 2-10 keV regime characteristic of ULX spectra, it also highlights how the difference in effective area between *Suzaku* and *XMM-Newton* can drive different parameterisations of the same underlying models. In this case, it shows how the relative lack of soft response in the *Suzaku* detectors means that they do not detect the soft excess with the same definition as *XMM-Newton*, and so the MCD does not preferentially fit to the soft end. These differences in fits mean that the classification scheme for ULX spectra suggested by Sutton et al. (2013b) cannot be used for the *Suzaku* data. We therefore suggest amendments to the scheme, based on the MCD inner-disc temperature, that allow ULX spectra to be classified into the same BD/SUL/HUL regimes as previously.

We also fitted various different physical models to the data. The main results of these analyses can be summarised as:

(i) Models composed of a MCD plus a Comptonised spectrum produced very good fits to the data, as is seen for *XMM-Newton* data. However, we showed that the fits are improved if the coupling between the MCD temperature and the temperature of the seed photons for the corona is broken, particularly in the case of ULXs with BD spectra. This decoupling leads to the disappearance of an anti-correlation between the coronal temperature and optical depth of ULXs, found in previous *XMM-Newton* studies of ULXs, implying that result is a fitting artefact induced by directly linking the two components.

(ii) Assuming that the hard component of ULX spectra can be attributed to the hot emission from the inner disc, we attempted to constrain the mass of the black holes powering these ULXs using the KERRBB model. This does not produce good fits in all cases, as the hard components are somewhat too broad even for a relativistically-smeared disc model; this could be due to the limitations of the model, that assumes a geometrically-thin, sub-Eddington flow. The breadth of the hard component means that high spins are inferred for most ULXs. We are able to put constraints on the black hole masses, and find they all lie in the stellar-mass black hole range ($\sim$ 3-30 $M_{\odot}$); however if the high spins are overestimates, then the masses will be smaller and at least

two objects may have masses in the neutron star range.

(iii) Much improved fits to the hard component are found using the DISKPBB model. This suggests that the hard component could be emission from the hot inner part of a super-Eddington, geometrically thick disc (i.e. an advection-dominated slim disc). Furthermore, the innermost temperature of the disc inferred in this model seems to suggest a transition between the BD and HUL spectra; the disc temperatures of the BD spectra are lower than those of the HUL spectra, which is likely to imply a lower accretion rate.

(iv) Fitting a simple BB spectrum to the soft spectral component, representative of the soft thermal emission from the optically thick wind, we constrain the size of the outflowing wind to be between $\sim 10^4$ – 10^6 $R_{\rm g}$.

(v) The models that fit best to the data can be interpreted in terms of super-Eddington accretion models. This is in particular true of the spectral evolution of NGC 1313 X-1 and NGC 1313 X-2 with increasing luminosity. As the accretion rate increases, a more powerful wind will arise and enter the observer's line-of-sight. This will scatter many hard photons emitted from the central regions of the ULX out of the line of sight, while ones that survive the passage through the wind will be Compton down-scattered to lower energies. A combination of this reduction in and softening of the harder spectral component, and a rise in the emission of the wind itself, could result in the observed change of the spectra from the HUL to the BD regime as the luminosity increases.

The spectra observed by *Suzaku* appear qualitatively and quantitatively similar to ULX spectra observed by other missions, particularly *XMM-Newton*. We do however find several interesting new results. Chief amongst these are the constraints on the black hole mass that we get from a relativistic disc model (albeit that measurement is heavily caveated in the text); and the constraints on the radial extent of the optically thick wind that we obtain from modelling the soft excess as a simple blackbody. Both results appear to support scenarios we would expect to observe if the objects powering ULXs are stellar-mass black holes (or even neutron stars)

that accrete material at super-Eddington rates. This chapter therefore adds to the increasing body of evidence that points towards this interpretation for most ULXs.

Chapter 3

The X-ray spectral evolution of the ultraluminous X-ray source Holmberg IX X-1

3.1 Introduction

Holmberg IX X-1 is a nearby ULX (d = 3.42 Mpc; Liu & Bregman 2005) located close to the dwarf galaxy Holmberg IX. It is a persistent source with luminosity $\sim 10^{40}$ erg s^{-1} that displays variations in flux by a factor of 3 – 4 on timescales of days (Kaaret & Feng, 2009; Kong et al., 2010). The source was first discovered by the *Einstein* Observatory (Fabbiano, 1988) and has been well studied over the past thirty years due to its proximity and so high X-ray flux. Despite some initial uncertainty in its nature, with some discussion as to whether it was a background QSO or a supernova remnant, it was confirmed as a likely ULX at the start of the *XMM-Newton* and *Chandra* epoch (La Parola et al., 2001). Subsequent studies focusing on the high quality spectra obtained by *XMM-Newton* have shown that they are typical of a ULX in the HUL regime (e.g. Stobbart et al. 2006; Sutton et al. 2013b), and a study of its X-ray spectral variability by Vierdayanti et al. (2010) showed that the variability was not a simple function of luminosity, but that subtle variations occurred that appeared independent of accretion rate. A more recent study incorporating broad band (0.3-30 keV) spectra from *NuSTAR* demonstrated

that the spectra can be explained by two optically-thick thermal components, similar to the spectra seen in the 0.3-10 keV range; furthermore the spectral evolution was explored, with its characteristics hypothesised to be indicative of physical changes in the highly dynamical, outflowing wind or the evolution of the hot inner region of the disc itself (Walton et al., 2014). Given its high flux and hard spectrum, Holmberg IX X-1 was a natural choice to search for absorption/emission features in the Fe-K band that may be indicative of material in an outflowing wind. However, none were found to stringent limits by Walton et al. (2013a); this is perhaps unsurprising, though, given the HUL spectra that are indicative of Holmberg IX X-1 being viewed down the funnel in its disc/wind structure, rather than through its wind.

Although we now have a provisional working model for the super-Eddington processes that occur in ULXs, much of the detail remains to be determined. One obvious way of better assessing the physical mechanisms and/or geometry at play in ULXs is through the detailed study of bright, individual archetypes for the class. In this chapter, we analyse the variation in spectra of Holmberg IX X-1 using data obtained from the *Swift*, *XMM-Newton* and *NuSTAR* X-ray observatories, in order to constrain the spectral evolution of the ULX with increasing luminosity, and so better determine its physics. This chapter is laid out as follows. In Section 3.2, we explain how we select the X-ray data, how we reduce it and how we create the ULX spectra. The details of the spectral analysis are presented in Section 3.3 and we discuss what we learn from the variability of the spectra in Section 3.4. Our findings are concluded in Section 3.5.

3.2 Observations and data reduction

3.2.1 *Swift* data

The X-ray variability of Holmberg IX X-1 has been monitored intermittently by *Swift* during the last decade, some observations of which were part of a monitoring programme for bright ULXs (e.g. Kaaret & Feng 2009). We searched for useful

Swift observations of Holmberg IX X-1 in the *Swift* data archive catalogue[1], using a cone search with radius of 11 arcminutes such that the ULX position is located within the field of view of the *Swift* X-ray telescope (XRT). Only the data obtained in photon counting (PC) mode were selected in order to obtain 2D images of the observations. We also selected only those observations in which the XRT exposure time is > 40 seconds, in order to (typically) obtain at least 10 photon counts from the ULX in each observation. After this step, we ended up with 514 useful observations: 132 observations are ones in which the XRT points directly to the ULX – i.e. the ULX position lies within a circular region of 5 arcminute radius centred on the XRT detector aim point (hereafter on-axis observations) – whilst the other 382 observations are *Swift* monitoring observations of the nearby galaxy M81, where the ULX position is > 5 arcminutes from the XRT detector aim point (hereafter off-axis observations) but still lies with in the field of view of the XRT.

We reduced all selected observations of Holmberg IX X-1 following the *Swift* XRT Data Reduction Guide version 1.2.[2] In brief, the raw data were reduced using the script XRTPIPELINE. Using the default parameter values provided by the script, bad pixels were removed and clean event files were created from the good grade events (grade 0 – 12). Then, source and background spectra were extracted from the clean event files using the script XRTPRODUCTS, which also automatically created the appropriate auxiliary response files (ARFs) and response matrix files (RMFs). In all cases, the source spectra were extracted from a circular region of 47 arcseconds radius located at the source position, corresponding to the 90% encircled energy radius at 1.5 keV for the point spread function (PSF) of the *Swift* XRT.[3] For the background spectra, the extraction was divided into two cases; for the on-axis observations, the background spectra were extracted from an annular region (of inner and outer radii 75 and 150 arcseconds respectively) around the source extraction area; in the case of off-axis observations, we extracted the background spectra from a source free, circular region of radius 150 arcseconds next to the source extraction aperture. The

[1] `http://swift.gsfc.nasa.gov/archive/`
[2] `http://swift.gsfc.nasa.gov/analysis/xrt_swguide_v1_2.pdf`
[3] `http://swift.gsfc.nasa.gov/analysis/threads/uvot_thread_spectra.html`

properties of the spectra obtained from the *Swift* observations are listed in Table A.1.

3.2.2 *XMM-Newton* data

Holmberg IX X-1 has been observed several times over the last decade-and-a-half by *XMM-Newton*; these observations have been analysed by many authors, as shown in column 6 of Table 3.1. Here we include all these *XMM-Newton* data in our analysis. We began by searching for observations of the ULX in the *XMM-Newton* data archive;[4] all 15 observations of Holmberg IX X-1 that we found are tabulated in Table 3.1. We reduced the *XMM-Newton* data using *XMM-Newton* Science Analysis Software (SAS)[5] version 13.5.0 and following the instructions in the SAS thread web pages.[6] We reprocessed the observation data files (ODFs) to obtain new calibrated and reprocessed event files, using the scripts EPPROC and EMPROC for the pn and MOS data, respectively. Then, we filtered the event files for background particle flaring events using the SAS task ESPFILT, which generated the clean pn and MOS event files.

We extracted pn and MOS spectra from the good grade events suggested by the SAS thread, i.e. FLAG = 0 and PATTERN $\leq$ 4 for the pn and 12 for the MOS, respectively. The source spectra were extracted from a circular aperture of 50 arcsecond radius around the source position, corresponding to $\sim$90% encircled energy at 1.5 keV of the pn and MOS PSFs.[7] The background spectra were extracted from a source-free, circular area of 80 arcsecond radius near to the ULX, with the same off-axis angle to that of the source and, if possible, from the same CCD as the ULX. The corresponding RMFs and ARFs were generated with the SAS scripts RMFGEN and ARFGEN, respectively. The spectra were then grouped to have a minimum of 20 counts per bin to utilise the χ^2 optimisation method in the spectral modelling. The total number of the counts obtained from each *XMM-Newton* observation is shown in column 4 of Table 3.1.

[4] http://nxsa.esac.esa.int

[5] http://xmm.esac.esa.int/sas/

[6] http://xmm.esac.esa.int/sas/current/documentation/threads/

[7] http://xmm.esac.esa.int/external/xmm_user_support/documentation/uhb_2.1/node17.html

Table 3.1: *XMM-Newton* observations of Holmberg IX X-1

ObsID	Obs. Date	pn/M1/M2 Exp.[a] (ks)	Total Counts[b]	θ[c] (arcmin)	References[d]
0111800101[e]	2001-04-22	–/76.0/76.7	65072	10.70	1,2,3,4,5,6,7,8
0111800301[f]	2001-04-22	-	-	10.70	–
0112521001	2002-04-10	5.9/9.5/9.9	24138	2.09	1,2,3,6,8,9,10,11,12,13,16
0112521101	2002-04-16	7.2/8.6/8.5	29409	2.09	2,3,6,9,10,11,12,13,14,15,16
0200980101	2004-09-26	38.0/62.2/65.0	125946	2.18	1,2,3,4,5,6,7,9,10,11,12,16,17,18,19,20,21
0657801601[f]	2011-04-17	–	2634	4.50	11,22,23
0657801801	2011-09-26	3.6/10.8/13.3	28676	4.50	2,11,16,22,23
0657802001	2011-03-24	2.5/4.7/4.6	7154	4.50	2,11,16,22,23
0657802201	2011-11-23	11.7/15.3/15.2	60861	4.50	2,11,16,22
0693850801[ep1]	2012-10-23	5.7/7.8/8.0	24553	2.17	24
0693850901[ep1]	2012-10-25	4.9/8.3/11.1	28040	2.17	24
0693851001[ep1]	2012-10-27	3.9/5.3/6.5	21282	2.17	24
0693851101[ep2]	2012-11-16	2.5/4.4/4.4	24115	2.17	24
0693851701[ep2]	2012-11-12	6.1/9.3/9.0	50831	2.17	24
0693851801[ep2]	2012-11-14	6.6/8.5/8.5	51356	2.17	24

Note. [a]The good exposure times obtained from the pn, MOS1 and MOS2 detectors. [b]The total counts from the source from a combination of all three EPIC detectors. [c]The off-axis angle of the source (measured from the EPIC aim point). [d]References to previous studies of this ULX using the pertinent data. These are: (1) Winter et al. (2007); (2) Sutton et al. (2014); (3) Miller et al. (2013); (4) González-Martín et al. (2011); (5) Gladstone et al. (2009); (6) Sutton et al. (2013b); (7) Caballero-García & Fabian (2010); (8) Winter et al. (2006); (9) Walton et al. (2012); (10) Kajava & Poutanen (2009); (11) Pintore et al. (2014); (12) Vierdayanti et al. (2010); (13) Wang et al. (2004); (14) Poutanen et al. (2007); (15) Stobbart et al. (2006); (16) Middleton et al. (2015); (17) Heil et al. (2009); (18) Hui & Krolik (2008); (19) Grisé et al. (2011); (20) Dewangan et al. (2006); (21) Berghea et al. (2013); (22) Sazonov et al. (2014); (23) Dewangan et al. (2013); (24) Walton et al. (2014). [e]Only MOS spectra are extracted from the observation as the source position falls outside of the pn detector area. [f]We exclude the observation from the analysis as the good exposure time is too low to obtain good quality spectra. [ep1]The spectra extracted from these observations were stacked together and analysed as epoch 1 in the broadband spectral analysis. [ep2]The spectra extracted from these observations were stacked together and analysed as epoch 2 in the broadband spectral analysis.

In the broadband spectral analysis of the source (Section 3.3.3), we prepared the *XMM-Newton* spectra using the same method as that of the previous broadband study of the ULX (Walton et al., 2014). Hence we segregated the *XMM-Newton* spectra that were observed simultaneously with the *NuSTAR* observatory in October and November 2012 into epoch 1 and epoch 2 (See Table 3.1). The spectra obtained from the same detectors in each epoch were stacked together using the FTOOL ADDSPEC[8], in order to create a single spectrum of pn, MOS1 and MOS2 for each observational epoch. The spectra were then grouped to have a minimum of 50 counts per bin.

3.2.3 *NuSTAR* data

Holmberg IX X-1 was one of the ULX targets to be observed by *NuSTAR* during the primary mission phase; it was observed simultaneously with *XMM-Newton* in October and November 2012 (see Table 3.2; Walton et al. 2014). In this chapter, these public data are also included in our analysis. We reprocessed and reduced the data using the *NuSTAR* data analysis software (NUSTARDAS) version 1.4.1, which is part of the HEASOFT software version 6.16[9], using the *NuSTAR* instrument calibration files (*NuSTAR* CALDB) version 20140414. We extracted the spectra from these data using the wrapper task NUPIPELINE[10], which generated the filtered event files and then extracted the source and background spectra as well as appropriate RMFs and ARFs from the cleaned event and calibration files. The source spectra were extracted from a circular aperture of 101 arcsecond radius around the source position, corresponding to the 80% encircled energy radius of the *NuSTAR* detector PSF.[11] The background spectra were extracted from a source-free annulus (of inner and outer radius 170 and 270 arcseconds respectively) around the source extraction region.

Similarly to the *XMM-Newton* spectra, we divided the *NuSTAR* spectra into

[8] http://heasarc.gsfc.nasa.gov/ftools/caldb/help/addspec.txt
[9] http://heasarc.gsfc.nasa.gov/docs/software/lheasoft/
[10] https://heasarc.gsfc.nasa.gov/ftools/caldb/help/nupipeline.html
[11] http://www.nustar.caltech.edu/uploads/files/nustar_performance_v1.pdf

Table 3.2: *NuSTAR* observations of Holmberg IX X-1

ObsID	Obs. Date	Exp.[a] (ks)	Cnts[b]	Epoch[c]
30002033002	2012-10-26	31.2	13616	1
30002033003	2012-10-26	88.1	41967	1
30002033004[d]	2012-11-10	–	-	
30002033005	2012-11-11	40.8	31450	2
30002033006	2012-11-11	35.2	26399	2
30002033007[d]	2012-11-14	–	-	
30002033008	2012-11-14	14.5	11737	2
30002033009[d]	2012-11-15	–	-	
30002033010	2012-11-15	49.0	37202	2

Note. [a]The good exposure time obtained from each detector. [b]The total counts in each observation, from combining the FPMA and FPMB data. [c]The epoch of observation. The spectra within the same epoch are stacked together and analysed simultaneously (see Section 3.3.3 for the detail of analysis). [d]We excluded the observation from the analysis as the good exposure time is too low to obtain useful spectral data.

epoch 1 and epoch 2, segregating by the month in which they were observed (see column 5 of Table 3.2), following the method used in the previous broadband study of the ULX (Walton et al., 2014). The spectra obtained from the same *NuSTAR* detectors in each epoch were stacked together using the script ADDSPEC, in order to create a single spectrum from the FPMA and FPMB for each observational epoch. Finally, the spectra were grouped to have a minimum of 50 counts per bin.

3.3 Spectral analysis and results

The large number of X-ray spectra of Holmberg IX X-1, from multiple X-ray missions, provides us with an excellent opportunity to further examine the X-ray spectral evolution of this ULX with increasing luminosity. In this chapter, we constrain the shape and hence the evolution of the spectra primarily using a two component model composed of a multi-coloured disc blackbody model (MCD; Mitsuda et al. 1984) and a Comptonising corona (Titarchuk, 1994), i.e. DISKBB + COMPTT in XSPEC. We simplify the model by tying the seed photon temperature of the

COMPTT component to the temperature of the MCD component in order to get a better constraint on the model-fitting parameters.[12] It is noted elsewhere that this simplification may lead to unrealistic values of the seed photon temperature in ULX fits, as the measured MCD temperature might not reflect the true temperature of the seed photons from the inner disc due to the obscuration of this region by the putative optically thick corona (see e.g. Gladstone et al. 2009). However, in this chapter, we do not attempt to directly interpret the model parameters; instead, we use the model to evaluate the change in the spectral shape, and to attempt to track the relative contributions of the separate soft and hard components of the spectra. So, in our case, the simplification of the model should not overtly affect the interpretation of the spectral evolution. In fitting models to the spectral data, absorption along the line of sight to Holmberg IX X-1 is accounted for by adding two multiplicative absorption components (TBABS in XSPEC) into the model, using the interstellar abundances reported by Wilms et al. (2000). The first absorption component is fixed at 4.06×10^{20} cm^{-2}, and accounts for the Galactic column density along our line of sight (Dickey & Lockman, 1990), whilst the second component represents absorption external to our Galaxy, most likely in the immediate vicinity of the ULX and/or in its host galaxy. The spectra were modelled using XSPEC[13] version 12.8.2 over the energy band of 0.3-10 keV (unless otherwise specified). The best fitting parameters are derived using a χ^2 minimisation technique, and throughout this chapter their errors are quoted using the 90% confidence interval.

3.3.1 *Swift* spectral analysis

Individual spectral analysis

Unfortunately each individual *Swift* spectrum contains insufficient data for detailed spectral analysis ($\sim$10 – 1000 counts). If we are to obtain the S/N spectra required for this study, then we must stack *Swift* spectra with similar properties together. A previous spectral study of Holmberg IX X-1 using *Swift* data by Vierdayanti et al.

[12] Excepting the broadband spectral analysis, in which the parameter is required to be free to obtain a good fit (see Section 3.3.3).

[13] `http://heasarc.nasa.gov/xanadu/xspec/`

(2010) segregated the spectra into luminosity bins using the detector count rates of the ULX. However, this is not appropriate in this work, as we include off-axis *Swift* spectra, and the observed count rates for a source with a given flux are a function of the detector effective area which varies with off-axis angle (Tagliaferri et al., 2004). For example, the count rate of a source located at 10 arcminutes off-axis from the detector aim point is lower by ∼25 per cent than the count rate of the same source located at the detector aim point. Thus, to avoid this issue, we take into account the differences in the detector response by calculating the observed flux of Holmberg IX X-1 in each observation, instead of using the detector count rates. The fluxes were calculated by modelling the individual *Swift* spectra with an absorbed power-law (TBABS*TBABS*POWERLAW in XSPEC), with the absorption modelled as described above.

The 440 spectra in which ≥ 100 counts were detected were grouped to have a minimum of 10 counts per bin, and then each was fitted by the absorbed power-law model. In addition, to include more *Swift* data in the analysis, we also considered another 55 observations which have between 50 – 100 counts. We again grouped the low count spectra to have a minimum of 10 counts per bin, and the spectra were fitted by the absorbed power-law model. However, as these spectra cannot constrain all three model parameters, we froze two – the absorption column external to our Galaxy ($N_{\rm H}$) and the power-law photon index (Γ) – at the average value of the parameters obtained from the best fitting results of the higher count rate spectra, $\Gamma = 1.6$ and $N_{\rm H} = 3 \times 10^{21}$ cm^{-2}; we only allowed the normalisation to be a free parameter in the fitting. The fitting results of all the individual *Swift* spectra are reported in Table A.1 and these were then used as the basis for further spectral analysis.

The light curve of Holmberg IX X-1 obtained from the *Swift* monitoring observations is plotted in Fig. 3.1. It can be seen that the source flux varied by a factor of 4 – 5 over a period of eight years. As a first order analysis of the spectral evolution with time, we plot the photon index of the individual *Swift* spectra as a function of the observing time (bottom panel of Fig. 3.1); no obvious correlation between the photon index and observation time is evident. To further examine

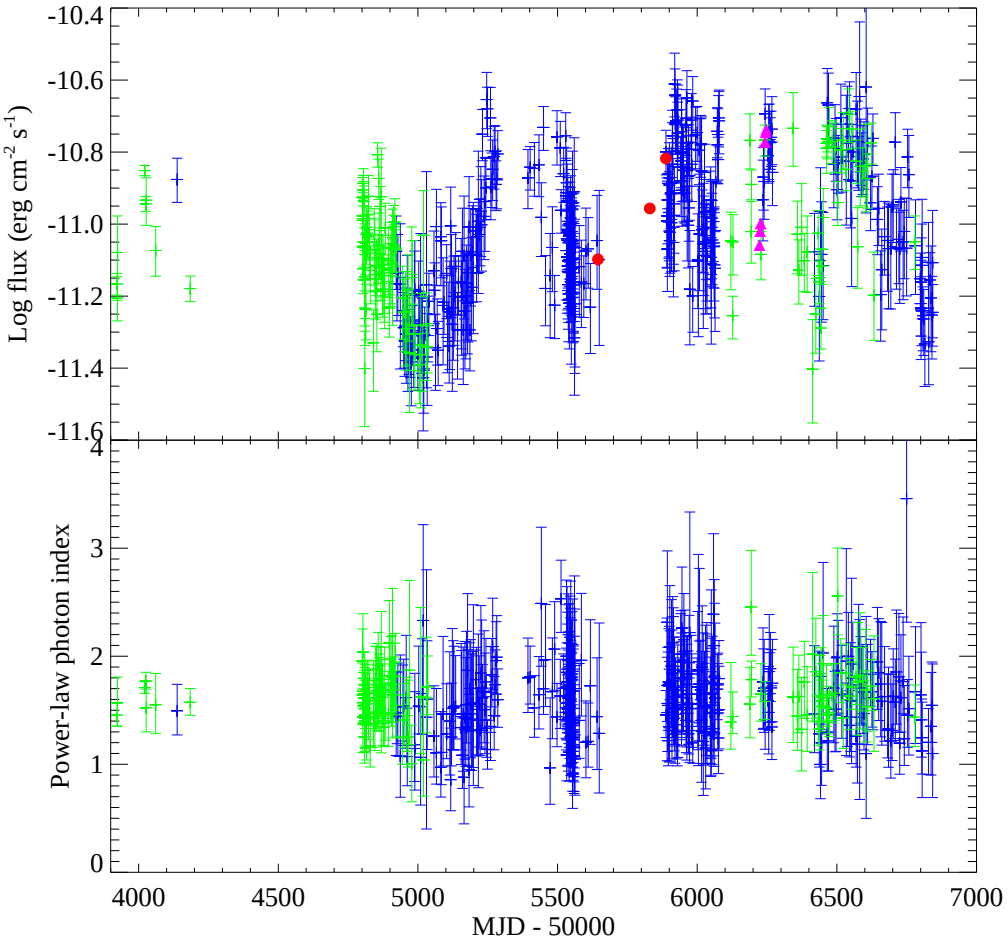

Figure 3.1: *Top panel*: the light curve of Holmberg IX X-1 , obtained from *Swift* on-axis (green) and off-axis (blue) observations. The time axis runs from June 2006 to August 2014. The solid red circles indicate the 2011 *XMM-Newton* observations, whilst the solid magenta triangles indicate the *XMM-Newton* observations taken contemporaneously with *NuSTAR* in 2012. *Bottom panel*: the photon index, plotted as a function of observing time, obtained by modelling the individual *Swift* spectra with an absorbed power-law model.

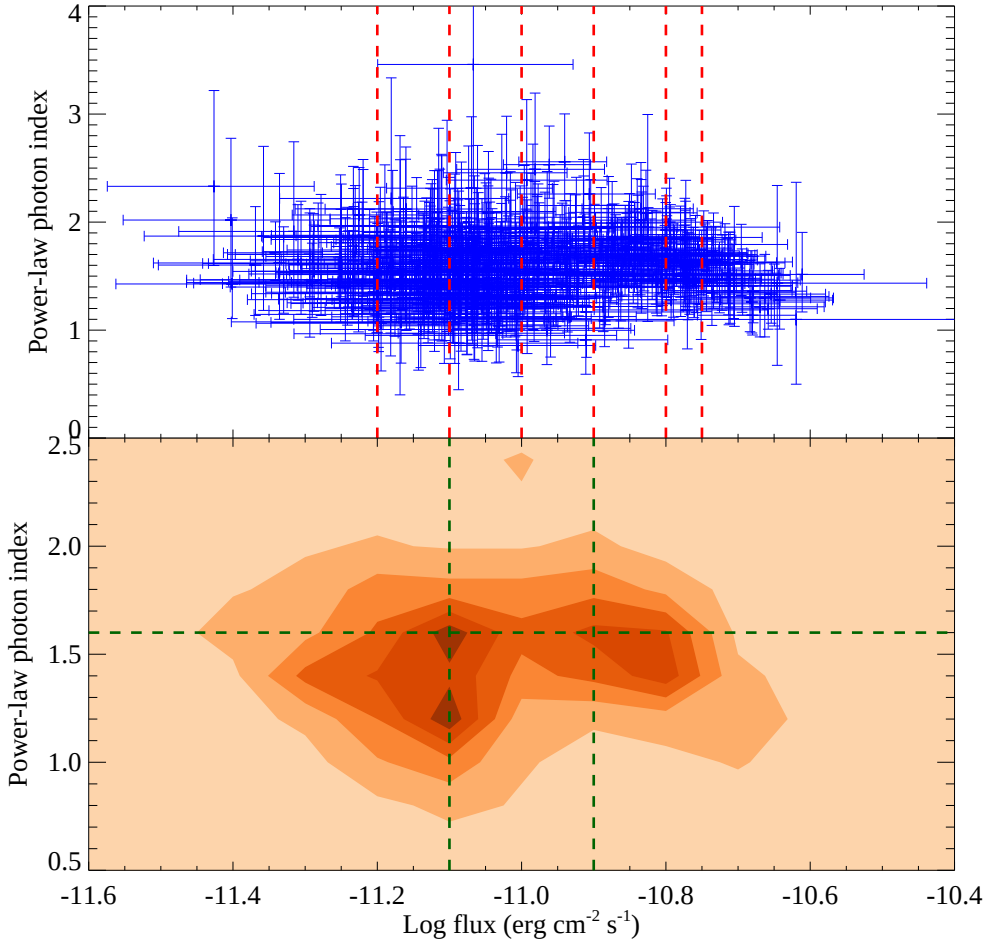

Figure 3.2: *Top panel*: the hardness-intensity diagram, obtained by fitting the individual *Swift* spectra with an absorbed power-law model. The boundaries used to segregate the *Swift* spectra into luminosity bins are plotted as red dashed lines. *Bottom panel*: the contour plot of the data density corresponding to the plot above. The boundaries used to segregate the *Swift* spectra into the spectral index-luminosity bins are plotted as green dashed lines (see Section 3.3.1).

the data, we plot the hardness-intensity diagram in Fig. 3.2 (where we use the observed 0.3-10 keV flux as a proxy for the intensity, and the photon index for the hardness). Interestingly, the spectra seem to have a bimodal distribution, with one peak at a flux of $\sim 8 \times 10^{-12}$ erg cm^{-2} s^{-1} and the other peak at double this flux ($\sim 1.6 \times 10^{-11}$ erg cm^{-2} s^{-1}). We will consider this further in next section.

Stacked spectral analysis: luminosity segregation

It has been shown in previous studies of ULX spectra (e.g. Stobbart et al. 2006; Gladstone et al. 2009) that their spectral features, particularly the high energy curvature, are subtle and can only be seen in high quality spectra. So, in order to obtain high S/N *Swift* spectra, we grouped the spectra into appropriate bins and stacked the spectra together to create a single spectrum for each bin, using the following criteria.

We began binning the individual *Swift* spectra using luminosity criteria. In particular, based on the bimodal distribution shown in Fig. 3.2, we divided the spectra in two main groups demarcated by an observed 0.3-10 keV flux of at log $f_{\rm X} = -10.9$ (in units of erg cm^{-2} s^{-1}), which we refer to hereafter as the low and high luminosity bins. Given the large number of counts available we were able to further sub-divide the low luminosity bin into four bins: low1 (log$f_{\rm X}$ < -11.2), low2 (-11.2 < log$f_{\rm X}$ < -11.1), low3 (-11.1 < log$f_{\rm X}$ < -11) and low4 (-11 < log$f_{\rm X}$ < -10.9). Similarly, the high luminosity bin was sub-divided into three bins: high1 (-10.9 < log$f_{\rm X}$ < -10.8), high2 (-10.8 < log$f_{\rm X}$ < -10.75) and high3 (log$f_{\rm X}$ > -10.75); see Fig. 3.2 (top panel) for the binning boundaries. We stacked the spectra in each bin together using the script ADDSPEC; the appropriate RMFs and ARFs were also combined by the script.

However, as the instrument response of the *Swift* XRT varies across the detector, combining responses with distinct differences – i.e. those of on-axis and off-axis spectra – may risk introducing uncertainties into a combined response file for the stacked spectra. To avoid this issue, we stacked the on- and off-axis spectra in each luminosity bin separately, such that we produced two spectra per bin. Finally, we grouped the stacked spectra to have a minimum of 20 counts per bin within

Table 3.3: The properties of the stacked *Swift* spectra

Spectral bin[a]	No. of spectra[b]		Total counts[c]	
	on-axis	off-axis	on-axis	off-axis
Luminosity binning				
Low1(Low)	23	60	4494	6374
Low2(Low)	29	58	10069	7764
Low3(Low)	36	89	11275	14318
Low4(Medium)	13	45	5804	8625
High1(High)	10	51	5372	13287
High2(High)	11	31	6587	8661
High3(High)	4	33	1574	9564
Photon index and luminosity binning				
Hard spectral bin				
Low	23	46	8202	6158
Medium	20	78	6372	12152
High	11	56	7704	15736
Soft spectral bin				
Low	23	31	5898	4549
Medium	26	55	10495	10704
High	14	55	5829	15480

Note. [a]The names of the stacked *Swift* spectral bins. Those in brackets indicate the new names after the spectra are re-binned to further improve S/N (see Section 3.3.1). [b]The number of *Swift* spectra contributing to each spectral bin. [c]The total number of photon counts from all spectra contributing to the spectral bin.

the spectra. We note that we excluded two *Swift* observations – observation IDs 00035335004 and 00035335005 – from the following analysis since they have a high number of counts ($\gtrsim$ 2900 counts) and so would potentially dominate the stacked spectrum they are each associated with (although they also have too few counts to be analysed separately). The properties of the stacked spectra in each luminosity bin are summarised in Table 3.3.

We began the analysis of the stacked spectra by modelling them with the absorbed MCD plus Comptonisation model. We modelled the on- and off-axis spectra of each luminosity bin simultaneously, adding a multiplicative constant to the model to allow for any calibration differences between the two spectra. The parameter was

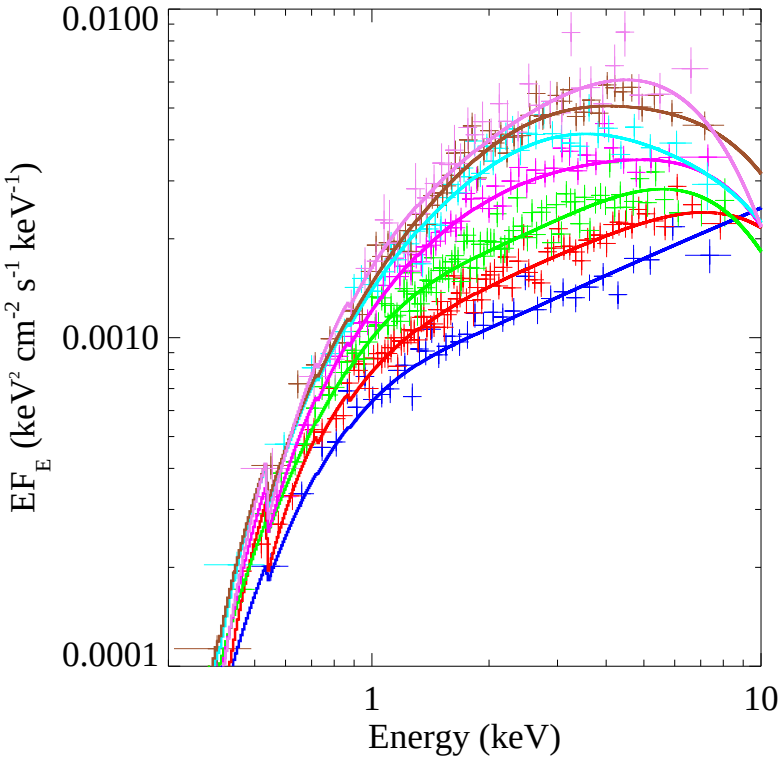

Figure 3.3: The stacked *Swift* spectra, showing the low1 (blue), low2 (red), low3 (green), low4 (magenta), high1 (cyan), high2 (brown) and high3 (violet) luminosity bins. Only on-axis spectra are shown, and they are re-binned to a minimum of 10σ statistical significance (5σ statistical significance for the high3 luminosity bin spectrum) per data point to clarify the plot. The best-fitting absorbed MCD plus COMPTT model for each spectrum is also shown by the solid lines.

frozen at unity for the on-axis spectra, whilst that of the off-axis spectra was allowed to be a free parameter; we found that the disagreement between the spectra was at no more than the $\lesssim$10% level.

The stacked spectra along with the best-fitting models are shown in Fig. 3.3. The plot reveals an interesting result; it is obvious that the spectra change shape as the luminosity increases – especially in the $\sim$1-6 keV energy band – from appearing as flat spectra at low luminosity to becoming more curved as the luminosity increases. This demonstrates clear evolution of the average ULX spectra with increasing luminosity. However, we found that the data were not sufficiently high quality to strongly constrain the model parameters with this choice of binning. So, in order to improve the constraints on the spectral fitting, we increased the S/N of

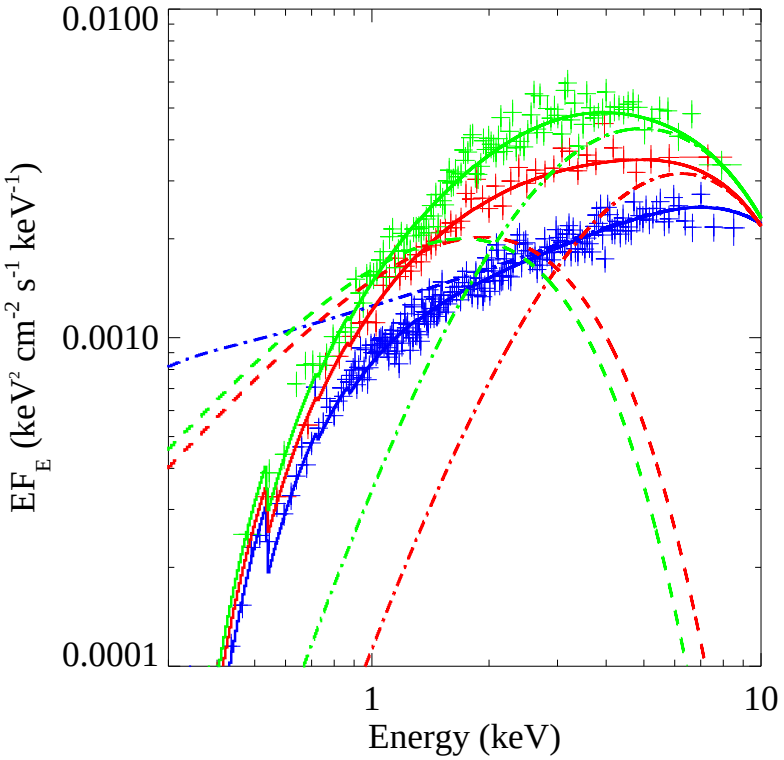

Figure 3.4: The stacked *Swift* spectra in the low (blue), medium (red) and high (green) luminosity bins. Only on-axis spectra are shown and they are re-binned to a minimum of 10σ statistical significance for clarity. The best-fitting absorbed MCD plus COMPTT models are shown as solid lines; the individual components, corrected for absorption, are also plotted as the dashed (MCD) and dash-dotted lines (Comptonisation).

the stacked spectra by combining those with similar characteristics in the ∼1-6 keV energy band; hence we stacked the spectra of the low1, low2 and low3 luminosity bins together as these spectra are similarly flat (hereafter the low luminosity bin; see Table 3.3). In contrast, the spectra of high1, high2 and high3 luminosity bins seem to be very curved and so were stacked together (hereafter the high luminosity bin). The spectra of the low4 luminosity bin was left to represent an intermediate spectral stage between the flat and curved spectra; hereafter we refer to it as the medium luminosity bin.

Again, we analysed the stacked spectra in the low, medium and high luminosity bins by modelling them with a MCD plus Comptonisation model; this produced statistically acceptable fits in all cases (null hypothesis probability > 0.05), and the best fitting results are reported in Table 3.4 and shown in Fig 3.4. Overall, similar

Table 3.4: The best fitting parameters for the stacked *Swift* spectra modelled by a MCD plus Comptonisation model

Spectral bin	$N_{\rm H}{}^{a}$ ($\times 10^{22}$ cm^{-2})	$kT_{\rm in}{}^{b}$ (keV)	$kT_{\rm e}{}^{c}$ (keV)	$\tau_{\rm e}{}^{d}$	χ^2/d.o.f.^{e}	$L_{\rm X}{}^{f}$ ($\times 10^{39}$ erg s^{-1})
Luminosity binning						
Low	$0.19^{+0.03}_{-0.01}$	< 0.11	$2.61^{+0.41}_{-0.28}$	$7.45^{+0.52}_{-0.59}$	1028.85/970	10.42
Medium	$0.12^{+0.02}_{-0.07}$	$0.81^{+0.41}_{-0.51}$	$1.89^{+1.04}_{-0.51}$	> 7.15	441.40/482	15.43
High	0.12 ± 0.01	$0.73^{+0.96}_{-0.15}$	$1.87^{+81.77}_{-0.30}$	> 1.57	819.04/849	20.19
Photon index and luminosity binning						
Hard spectral bin						
Low	$0.21^{+0.09}_{-0.05}$	$0.16^{+0.04}_{-0.02}$	$2.44^{+0.84}_{-0.39}$	$8.45^{+1.24}_{-1.41}$	496.78/501	9.19
Medium	0.20 ± 0.09	$0.14^{+0.04}_{-0.03}$	$1.96^{+0.29}_{-0.20}$	$9.53^{+1.02}_{-0.98}$	614.57/580	12.61
HIgh	$0.11^{+0.02}_{-0.01}$	$0.82^{+0.76}_{-0.28}$	> 1.03	> 0.97	706.40/665	20.47
Soft spectral bin						
Low	0.10 ± 0.02	$0.85^{+0.12}_{-0.39}$	> 1.89	> 3.43	312.87/391	9.78
Medium	0.13 ± 0.02	$0.78^{+0.31}_{-0.34}$	$2.24^{+3.46}_{-0.59}$	$9.56^{+67.50}_{-3.06}$	621.86/601	13.20
High	$0.13^{+0.02}_{-0.03}$	$0.68^{+0.37}_{-0.19}$	> 1.23	> 0.17	567.48/588	19.88

Note. [a]Absorption column external to our Galaxy. [b]The inner disc temperature of the MCD component. [c]The plasma temperature of the Comptonising corona. [d]The optical depth of the Comptonising corona. [e]Minimum χ^2 over degrees of freedom. [f]Observed X-ray luminosity in the 0.3-10 keV energy band.

spectral evolution to the previous, finer flux segregation is found; the average spectra are flat at low luminosity and become more curved at higher luminosity. They appear most curved at the highest ULX luminosity. Hence it appears that the two peaks in Fig. 3.2 occur where the spectra appear different; flat in the low luminosity bin, and curved in the medium and high luminosity bins.

We can further examine the changes in the average spectra by looking at what happens to the two components in the spectral fits. At low luminosity, the spectral fits are dominated by the COMPTT component; the MCD component makes a negligible contribution to the spectrum, resulting in the flat spectra. As the luminosity increases, the MCD component emerges to dominate the soft end of the medium and high luminosity spectra, whilst the COMPTT component dominates the hard end. However, this MCD appears very consistent between the medium and high bins, whereas the COMPTT continues to change, evolving towards a lower temperature as the luminosity increases in all 3 spectra. It is this apparent cooling of the corona, combined with the emergence of the MCD, that leads to the increasingly curved spectra at higher luminosities.

Stacked spectral analysis: photon index and luminosity segregation

The hardness-intensity diagram in Fig. 3.2 shows that the distribution of the data has definite structure. In the previous section, we examined the spectral evolution based on luminosity criteria alone. However, the hardness-intensity diagram also demonstrates that the photon indexes of individual *Swift* spectra vary widely for the same luminosity, between $\sim 1 - 2.5$. Indeed, there is even some evidence in the bottom panel of Fig. 3.2 for the low luminosity density peak having two distinct sub-peaks, either side of $\sim \Gamma = 1.4$. This strongly suggests that the average spectra are not a simple function of luminosity. Thus, in this section, we re-examine the *Swift* spectra using new binning criteria that combine the observed luminosities and spectral indexes of the individual observations. Firstly, we divided the spectra into hard ($\Gamma < 1.6$) and soft ($\Gamma > 1.6$) spectral bins. Then we further segregate the spectra in these bins into three luminosity bins: low ($\log f_{\rm X} <$ -11.1), medium (-11.1 $< \log f_{\rm X} <$ -10.9) and high ($\log f_{\rm X} >$ -10.9), whose boundaries are shown in the

bottom panel of Fig. 3.2. The criteria result in six spectral bins, the properties of which are summarised in Table 3.3.

We stacked the spectra in each bin together using the script ADDSPEC. Again, for each spectral bin, we stacked the on- and off-axis spectra separately. We note that, in this section, we do not include the low count *Swift* spectra in the analysis (the 55 observations that have no more than between 50 and 100 counts); as these spectra have an assumed spectral index of 1.6 (see above), they cannot be assimilated into either the hard or soft spectral bins. Finally, we grouped the stacked spectra to have a minimum of 20 counts per bin within each spectrum, and analysed the evolution of the spectra using the same model as in pure luminosity binning. The best fitting results are shown in the lower panel of Table 3.4. We illustrate the spectral evolution with increasing luminosity, for the soft and hard bins separately, in Fig 3.5.

The results obtained from this binning method are very interesting; the spectra in the hard and soft spectral bins show different evolution with increasing luminosity. For the hard spectra, the overall spectral evolution in shape is broadly consistent with that of the pure luminosity binning; the spectra seem to be flat in the $\sim 1-6$ keV range at low luminosity, and become curved at high luminosity. The detailed evolution of the two components is, however, somewhat different. The MCD component contributes at roughly the same, very marginal level to the total spectra at low and medium luminosity. However, at high luminosity, the component becomes hotter and dominates the soft end of the spectrum. In contrast, the COMPTT component is very dominant at low and medium luminosity; however at high luminosity, the component only dominates the hard band. We do, however, see the same gradual decrease in temperature in the hard component as the total luminosity decreases as for the pure luminosity binning.

In contrast, the evolution of the soft spectra with luminosity is somewhat different from that of the hard spectra, in particular at low and medium luminosity (see bottom panel of Fig. 3.5). Overall, the spectrum appears to be distinctly two component in the low luminosity bin; however, as the luminosity increases, the individual components of the MCD and COMPTT seem to merge together, resulting in a single-component-like curved spectrum. Furthermore, unlike the hard spectra, the

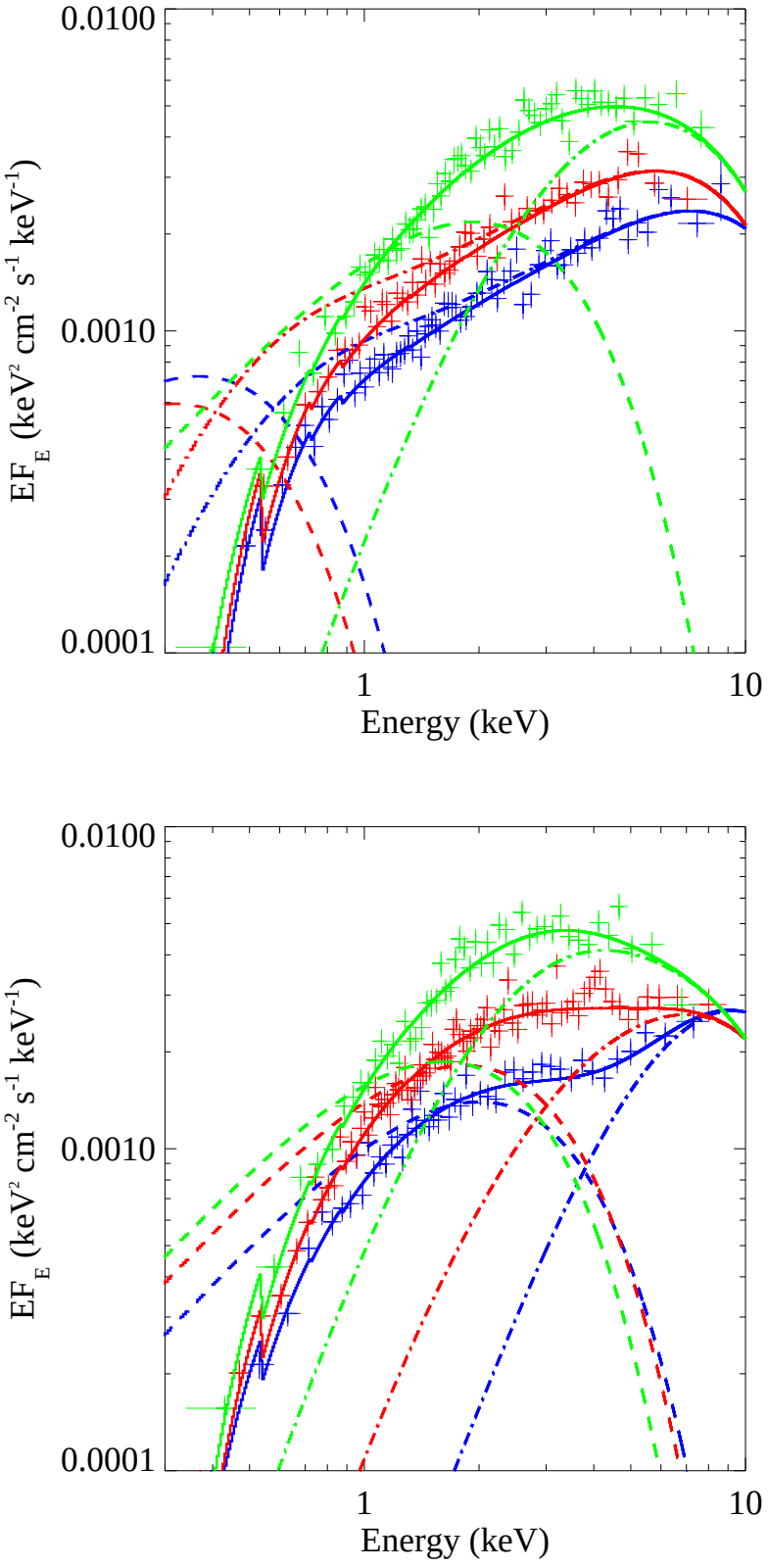

Figure 3.5: The stacked *Swift* spectra binned by a combination of spectral index and luminosity criteria. *Top panel*: the stacked hard spectra. *Bottom panel*: the stacked soft spectra. Only on-axis spectra are shown and they are re-binned to a minimum of 10σ statistical significance per data point to clarify the plot. The line styles and colours are as per Fig.3.4.

MCD component always appears to dominate the softer energy band of the spectra, and remains roughly constant as the luminosity increases (i.e. does not evolve very dramatically with increasing total luminosity). In contrast, the COMPTT component shows stronger evolution, showing the same pattern in decreasing peak energy as the luminosity increases as is seen in the other analyses. One interesting point to note from Table 3.4 is that the measured absorption appears lower in the soft spectra, although this difference is only significant above the 90 per cent level in the lowest luminosity bin.

3.3.2 *XMM-Newton* spectral analysis

Unlike the *Swift* spectra, the 13 *XMM-Newton* spectra were of sufficiently high quality to enable us to study Holmberg IX X-1 without stacking. We analysed these spectra using the same model as for the *Swift* stacked spectra in Section 3.3.1. For each individual observation, we model the pn, MOS1 and MOS2 spectra simultaneously, adding a multiplicative constant to the model to correct for any residual calibration differences between the *XMM-Newton* detectors; in practise this offset is at the $\lesssim 10$ per cent level. The best fitting results are tabulated in Table 3.5; to facilitate comparison with the other analyses, we sort the spectra in ascending order of their observed luminosities and also classify each *XMM-Newton* spectrum into an appropriate luminosity group, corresponding to the boundaries defined in the *Swift* pure luminosity binning in Section 3.3.1. Acceptable fits were found in all but 2 cases; observation ID 0200980101 is very marginally rejected (null hypothesis probability of 0.04), and 0111800101 was rejected with a null hypothesis of $\sim 5 \times 10^{-3}$, i.e. a $\sim 3\sigma$ confidence rejection. However, it is notable that these observations are the highest quality data for Holmberg IX X-1 and that there is a suggestion of residuals in the soft X-ray emission, in common with other ULXs, that may be causing this result (Middleton et al. submitted).

We show the spectral evolution of Holmberg IX X-1 with increasing luminosity, as seen by *XMM-Newton*, in Fig. 3.6. Overall, we see some broad consistencies with the *Swift* stacked spectra. There are some obvious degeneracies in spectral shape with luminosity, as suggested by splitting the stacked *Swift* spectra into hard

Table 3.5: The best fitting results for the *XMM-Newton* spectra modelled by a MCD plus Comptonisation model

Obs. ID	$N_{\rm H}{}^a$ ($\times 10^{22}$ cm^{-1})	$kT_{\rm in}{}^b$ (keV)	$kT_{\rm e}{}^c$ (keV)	$\tau_{\rm e}{}^d$	χ^2/d.o.f.^{e}	$L_{\rm X}{}^f$ ($\times 10^{39}$ erg s^{-1})	Spectral group^g
0200980101	0.11 ± 0.01	0.26 ± 0.02	$2.25^{+0.15}_{-0.13}$	$9.63^{+0.61}_{-0.54}$	(536.48/482)	8.50	Low
0112521001	0.11 ± 0.02	0.25 ± 0.05	$2.57^{+0.94}_{-0.45}$	$7.54^{+1.39}_{-1.40}$	324.22/336	9.83	Low
0657802001	$0.16^{+0.05}_{-0.04}$	$0.24^{+0.05}_{-0.04}$	> 2.41	$0.75^{+38.69}_{-0.61}$	200.62/205	11.17	Low
0112521101	$0.10^{+0.03}_{-0.06}$	$0.22^{+0.06}_{-0.04}$	$2.64^{+0.72}_{-0.42}$	$6.95^{+1.04}_{-0.95}$	368.12/350	11.27	Low
0693850801	$0.10^{+0.03}_{-0.06}$	0.22 ± 0.04	> 3.15	$1.07^{+4.88}_{-1.02}$	382.71/347	12.24	Low
0693850901	$0.11^{+0.03}_{-0.07}$	$0.26^{+0.10}_{-0.07}$	$2.46^{+0.67}_{-0.45}$	$7.61^{+1.86}_{-1.26}$	362.56/364	13.38	Low
0693851001	$0.10^{+0.02}_{-0.06}$	$0.30^{+0.20}_{-0.08}$	$2.16^{+0.52}_{-0.46}$	$8.27^{+4.61}_{-1.35}$	328.58/329	14.05	Medium
0657801801	$0.08^{+0.03}_{-0.07}$	$0.28^{+0.11}_{-0.04}$	$2.56^{+0.98}_{-0.43}$	$6.89^{+1.17}_{-1.23}$	331.12/354	15.47	Medium
0111800101	0.13 ± 0.01	$0.52^{+0.33}_{-0.18}$	$1.30^{+0.09}_{-0.11}$	> 11.39	(363.79/297)	19.20	High
0657802201	$0.10^{+0.03}_{-0.04}$	$0.28^{+0.07}_{-0.03}$	$1.97^{+0.16}_{-0.13}$	$8.38^{+0.61}_{-0.48}$	391.12/415	21.28	High
0693851701	$0.11^{+0.01}_{-0.02}$	0.71 ± 0.17	$1.76^{+0.17}_{-0.13}$	$11.77^{+3.83}_{-1.68}$	432.58/406	23.65	High
0693851801	$0.07^{+0.04}_{-0.06}$	$0.26^{+0.07}_{-0.03}$	$1.54^{+0.06}_{-0.05}$	$11.43^{+0.47}_{-0.41}$	428.36/407	25.17	High
0693851101	0.11 ± 0.02	$0.77^{+0.41}_{-0.24}$	$1.92^{+0.38}_{-0.22}$	> 8.57	384.06/355	25.62	High

Note.[a]Absorption column external to our Galaxy. [b]The inner disc temperature of the MCD component. [c]The plasma temperature of the Comptonising corona. [d]The optical depth of the Comptonising component. [e]Minimum χ^2 over degrees of freedom. Parentheses highlight fits for which the null hypothesis probability is < 0.05. [f]Observed X-ray luminosity in the 0.3-10 keV energy band. [g]The luminosity bin of the *XMM-Newton* spectra. We classify the spectra using the same luminosity boundaries used to create the *Swift* low, medium and high luminosity spectra in the pure luminosity binning in Section 3.3.1.

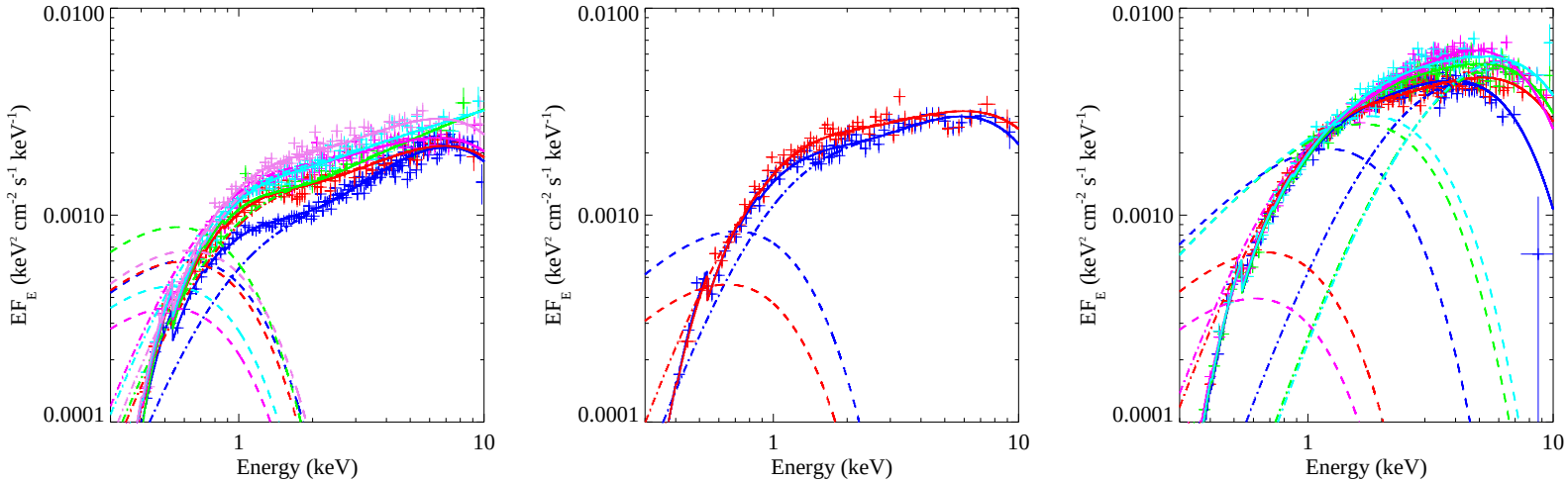

Figure 3.6: The *XMM-Newton* spectra, segregated into low (*left panel*), medium (*middle panel*) and high (*right panel*) luminosity groups using the same luminosity boundaries used to create the stacked *Swift* spectra. Only pn spectra (or MOS1 in case of ObsID. 0111800101) are shown and they are re-binned to a minimum of 10σ statistical significance for clarity. The best-fitting absorbed MCD plus COMPTT model is also shown as solid lines; the individual components of MCD and Comptonisation, corrected for absorption, are also plotted as dashed lines and dash-dotted lines, respectively. For each panel, the colour coding is used to indicate the relative luminosity of the source, ascending in order of increasing luminosity from blue to red, green, magenta, cyan and violet.

and soft bins, particularly in the low and high luminosity *XMM-Newton* groups. In the low luminosity group this manifests as both distinct two-component and flat spectral shapes (with the flat spectra apparently slightly more luminous); in the high luminosity group the differences are mainly in the turnover of the hard component. However, we again see the same trends in the data, with mostly flatter data (in the 1-6 keV range) giving way to much more pronounced curvature as the luminosity of Holmberg IX X-1 increases.

The evolution of the two individual components is also interesting. In the low and medium luminosity groups, only a small fraction of the total spectrum originates in the MCD component, and its properties remain approximately constant (e.g. $kT_{\rm in}$ is invariant within errors; see Table 3.5) as the luminosity increases from low to medium luminosity. However, in the high luminosity group, this component contributes significantly more to the spectrum in 3/5 cases, and in these cases is significantly warmer (~ 0.7 keV as opposed to ~ 0.25 keV). The COMPTT dominates the spectra in the low and medium luminosity groups, and remains dominant at the hard end of the spectrum in the high luminosity group. However, its temperature is demonstrably cooler as the luminosity increases, with $kT_{\rm e} > 2$ keV in the low and medium luminosity groups, but $kT_{\rm e} < 2$ keV in the high luminosity group, consistent with the trend noted qualitatively for the stacked *Swift* spectra.

3.3.3 Broadband spectral analysis

We have shown that the spectral evolution in the 0.3-10 keV range observed by *Swift* and *XMM-Newton* appears to follow a set pattern, albeit with some level of spectral degeneracy with luminosity. However, with *NuSTAR* we now have data that extend our bandpass for observing ULXs above 10 keV (e.g. Bachetti et al. 2013; Walton et al. 2013b). Therefore, in this section we extend our analysis to the 0.3-30 keV range[14] using two epochs of *XMM-Newton* and *NuSTAR* data taken contemporaneously in 2012 (see Section 3.2.2 and 3.2.3, also Walton et al. 2014). We model the *XMM-Newton* and *NuSTAR* spectra from each epoch together,

[14]The *NuSTAR* observing bandpass extends to $\sim$79 keV, however no significant detection of Holmberg IX X-1 is made above 30 keV (Walton et al., 2014).

Table 3.6: The results of joint *XMM-Newton* and *NuSTAR* spectral fits

Model	$N_{\rm H}$ [a] ($\times 10^{22}$ cm^{-1})	$kT_{\rm in}$ [b] (keV)	kT_0 or Γ [c]	$\%_{scat}$ [d]	kT_2 [e] (keV)	τ or p [f]	χ^2/d.o.f. [g]
Epoch 1: low/medium luminosity							
DISKBB+COMPTT (tied T_0)	$0.22^{+0.04}_{-0.02}$	$0.09^{+0.02}_{-0.04}$			3.22 ± 0.09	6.02 ± 0.16	(1625.53/1499)
DISKBB+COMPTT (free T_0)	0.12 ± 0.01	0.46 ± 0.05	0.73 ± 0.08		$3.69^{+0.21}_{-0.18}$	$5.13^{+0.30}_{-0.34}$	1561.90/1498
DISKBB+(SIMPL×COMPTT)	0.14 ± 0.02	$0.29^{+0.06}_{-0.02}$	$3.80^{+0.31}_{-0.10}$	> 70	$2.08^{+0.08}_{-0.12}$	7.47 ± 0.26	1558.54/1497
DISKBB+(SIMPL×DISKPBB)	$0.16^{+0.02}_{-0.03}$	$0.27^{+0.08}_{-0.06}$	$3.28^{+1.38}_{-1.35}$	27^{+47}_{-22}	$3.46^{+0.35}_{-0.42}$	$0.56^{+0.01}_{-0.01}$	1557.04/1497
Epoch 2: high luminosity							
DISKBB+COMPTT (tied T_0)	0.08 ± 0.004	$1.20^{+0.07}_{-0.06}$			$2.85^{+0.12}_{-0.11}$	$6.61^{+0.75}_{-0.53}$	(2082.89/1815)
DISKBB+COMPTT (free T_0)	0.13 ± 0.01	0.56 ± 0.05	0.88 ± 0.05		$4.16^{+0.63}_{-0.41}$	$3.19^{+0.37}_{-0.44}$	1872.29/1814
DISKBB+(SIMPL×COMPTT)[gb]	$0.15^{+0.02}_{-0.01}$	$0.32^{+0.07}_{-0.04}$	$3.59^{+0.08}_{-0.02}$	> 85	$1.06^{+0.02}_{-0.04}$	$11.67^{+0.06}_{-0.61}$	1869.45/1813
DISKBB+(SIMPL×COMPTT)[lc]	0.12 ± 0.003	0.58*	$3.56^{+0.08}_{-0.02}$	> 81	$1.01^{+0.01}_{-0.04}$	$11.92^{+0.08}_{-0.02}$	1886.80/1813
DISKBB+(SIMPL×DISKPBB)	$0.14^{+0.02}_{-0.01}$	1.63 ± 0.06	> 3.16	60^{+7}_{-39}	$3.19^{+0.72}_{-0.17}$	0.55 ± 0.01	1873.24/1813

Note. [a]Absorption column beyond our Galaxy. [b]The inner disc temperature of the MCD component. [c]The seed photon temperature of the COMPTT component (in units of keV) or the power-law photon index of the SIMPL component. [d]The scattered fraction of the SIMPL component. [e]The plasma temperature of the COMPTT component or the inner disc temperature of the DISKPBB component. [f]The optical depth of the COMPTT component or the value of the p parameter in the DISKPBB component. [g]Minimum χ^2 over degrees of freedom from the fit. [gb]The best fitting result obtained from the global minimum χ^2 statistic. [lc]The fitting result obtained from the local minimum statistic (see text). *We were unable to place constraints on this parameter.

adding a constant multiplicative factor into the model to correct for any calibration differences between all *XMM-Newton* and *NuSTAR* detectors; a $\lesssim 10\%$ difference in the constant parameter is required. We began by modelling the broadband spectra using the same MCD plus COMPTT model used successfully for the stacked *Swift* and the *XMM-Newton* spectra. However, the data reject the model for both epochs of spectral data (null hypothesis probability $\lesssim 0.01$; see Table 3.6).

It is no surprise that a simple MCD plus COMPTT model does not give a good fit, given that this has been demonstrated in several *NuSTAR* papers on different ULXs (e.g. Bachetti et al. 2013; Walton et al. 2014 etc.). In these papers it is demonstrated that an additional hard component may be present in the data above 10 keV. Here, we attempt 3 different model fits to account for this hard excess. Firstly, we use the same MCD plus COMPTT model, but this time allow the seed photon temperature (kT_0) of the COMPTT component to be a free parameter. The fitting result is improved significantly, compared to the previous model, and the fit is statistically acceptable. We plot the data and the best-fitting version of this model in Fig. 3.7. To directly compare these data with the evolution of the *XMM-Newton* and *Swift* spectra, we measured the flux of the broadband spectra in the 0.3 – 10 keV energy band and associated each epoch with the appropriate luminosity group in the previous analyses, corresponding to the luminosity boundaries defined in the *Swift* pure luminosity binning in Section 3.3.1. We find fluxes of $f_{\rm X} = 1.08 \times 10^{-11}$ erg cm^{-2} s^{-1} in epoch 1, at about the boundary luminosity between the low and medium luminosity groups, and $f_{\rm X} = 1.72 \times 10^{-11}$ erg cm^{-2} s^{-1} at epoch 2, consistent with the high luminosity group. These results are again unsurprising; the three *XMM-Newton* observations taken during epoch 1 were individually analysed in the previous section, and found to be in the low or medium luminosity groups, and the epoch 2 observations similarly found in the high luminosity group. What we do find here is that, despite the extension of the analysis to higher energies, the spectra are still qualitatively consistent with what was seen in the earlier sections, evolving from flat in the 1-6 keV band to curved as the luminosity increases. The two components also behave similarly – there is more change in the hard component as the luminosity increases, with an apparent cooling in its peak temperature

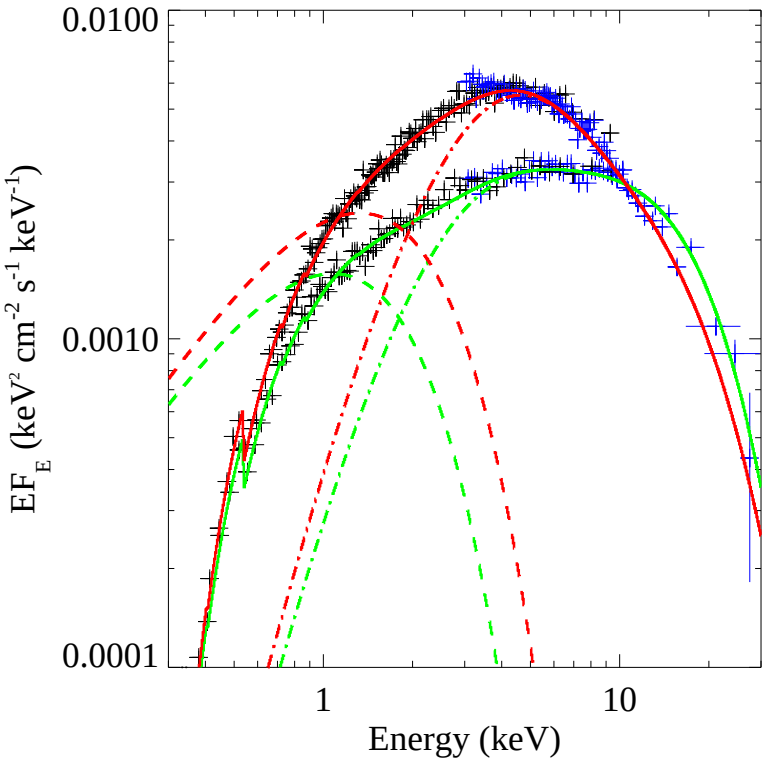

Figure 3.7: The broadband spectra of Holmberg IX X-1 observed by *XMM-Newton* (back) and *NuSTAR* (blue). Only *XMM-Newton* pn spectra and *NuSTAR* FPMA spectra are shown, and they are re-binned to a minimum of 20σ statistical significance to clarify the plot. The best-fitting absorbed MCD plus COMPTT models (with the seed photon temperature uncoupled from the disc temperature) for epoch 1 and epoch 2 are plotted as green and red solid lines, respectively. The individual MCD and COMPTT components, corrected for absorption, are also plotted as the dashed lines and dash-dotted lines, respectively.

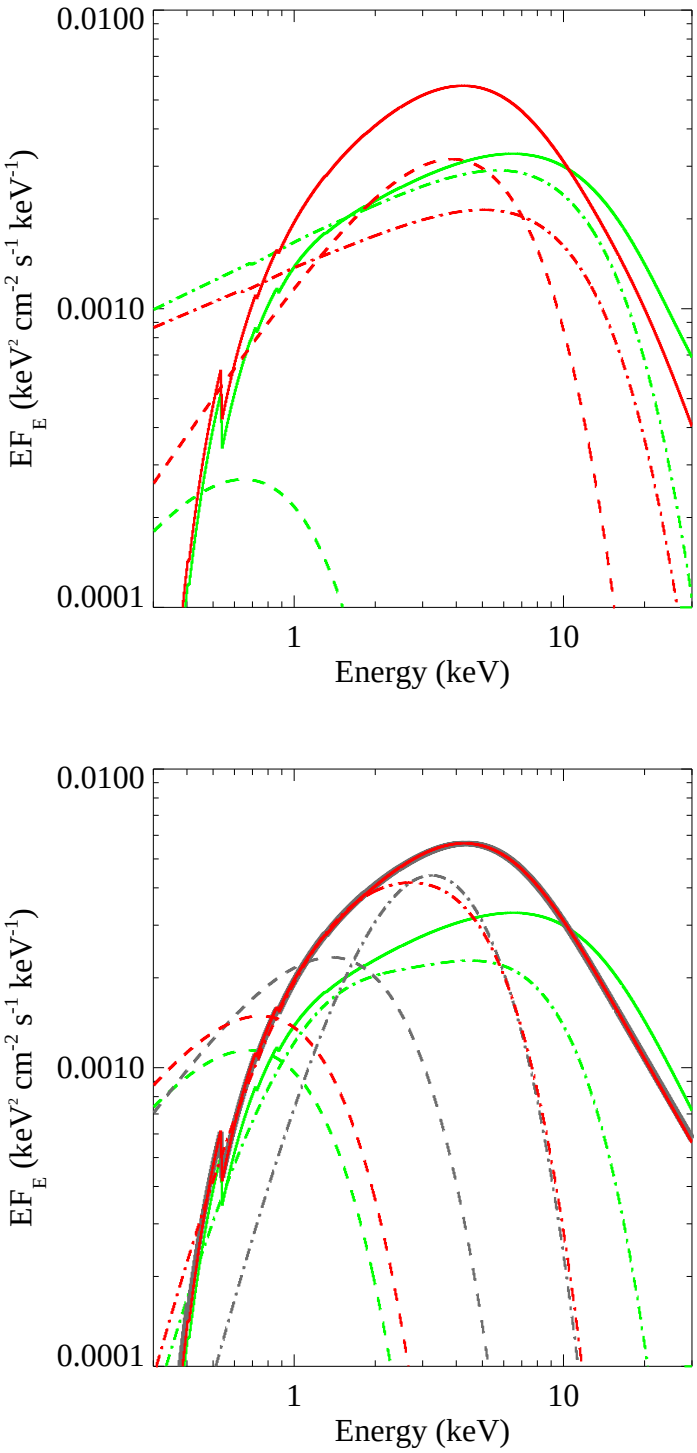

Figure 3.8: The DISKBB+SIMPL×DISKPBB model (*top panel*) and DISKBB+SIMPL×COMPTT model (*bottom panel*), best fitting to the broadband spectra of Holmberg IX X-1 for the epoch 1 (green) and epoch 2 (red) spectra. The best fitting models are plotted as solid lines. The MCD component, corrected for absorption, is plotted as dashed lines, whilst the DISKPBB or COMPTT component, corrected for absorption and modified by the SIMPL model, is plotted by the dash-dotted lines. The grey lines in the bottom panel are the fitting result for epoch 2 spectra obtained from the local model minimum (see text).

(although this is not demonstrated in the best fitting parameters, with the COMPTT temperatures consistent within errors) that appears better established in these data due to the longer tail to the data seen above 10 keV.

We have also attempted to account for the additional hard excess in the data by adding an additional component into the model, a SIMPL model that is an empirical approximation of Comptonisation in which an input seed spectrum is scattered into a power-law component (Steiner et al., 2009). In this we directly follow the models used in Walton et al. (2014), who model the same broadband dataset and propose two different spectral evolution scenarios. These are based on two models: DISKBB+SIMPL×DISKPBB and DISKBB+SIMPL×COMPTT. In the first case the hard component is modelled by an approximation for an advection-dominated 'slim' accretion disc in which the temperature profile of the disc is modelled as $T(r) \propto r^{-p}$ and values of $p \approx 0.5$ indicate a slim disc (e.g. Vierdayanti et al. 2006 and references therein); in the second it is modelled by the same COMPTT we have been using previously. We confirm that both models proposed by Walton et al. (2014) can fit to the broadband spectra equally well, with very similar fitting statistics to the uncoupled MCD plus COMPTT model.

The spectral evolution of both models with luminosity is similar to that is described in Walton et al. (2014). In brief, the evolution obtained from DISKBB+SIMPL ×DISKPBB suggests that evolution is mainly in the MCD component, that increases dramatically in both temperature and flux in the high luminosity epoch, whilst the DISKPBB component appears much closer to constant between the two epochs (see the top panel of Fig. 3.8). In contrast, the evolution obtained from DISKBB+SIMPL×COMPTT appears in the opposite sense. The MCD component seems to remain constant whilst the COMPTT component appears to play a much larger role in the evolution of the spectra when the luminosity increases (although in both cases very high scattered fractions for the SIMPL component are required, > 70 per cent), as is shown in the bottom panel of Fig. 3.8. However, we note that the spectral evolution obtained from the DISKBB+SIMPL×COMPTT model may not be unique; in fact, we found a local minimum in the χ^2 fitting of epoch 2 spectra where the $\Delta\chi^2$ between the global and local minimum is only $\sim$20 over 1813 degrees

of freedom, so we cannot reject the result obtained from the local minimum. Interestingly, the spectral evolution suggested by the local minimum is more consistent with the evolution obtained from the MCD plus COMPTT model, particularly for the *Swift* and *XMM-Newton* data, in which the MCD component gets stronger and warmer, and the COMPTT component peaks at lower energy when the luminosity increases. We will discuss this further in Section 3.4.

3.4 Discussion

Holmberg IX X-1 is a persistently luminous ULX, with a decade of monitoring by *Swift* showing a dynamical range of a factor $\lesssim 5$ and a typical luminosity of around $\sim 10^{40}$ erg s^{-1}. In this chapter we have examined the spectral evolution of this ULX with changes in luminosity, based on stacking *Swift* spectra in terms of their flux and as a combination of their flux and photon index (with the latter as a proxy for X-ray colour), on *XMM-Newton* pointed observations, and on combining contemporaneous *XMM-Newton* and *NuSTAR* data to provide a broader bandpass in which to study the variation of the ULX. Our main finding is that there appears to be a common trend in the changing morphology of the spectrum as the luminosity increases, albeit with evidence for some level of degeneracy with luminosity. At lower luminosities (around 10^{40} erg s^{-1}) we see the spectra as either a distinct, two component ULX spectrum with a dominant hard component, or as a hard, flat spectrum in the 1-6 keV range, with a turnover in the spectrum at higher energies. These spectra would classify Holmberg IX X-1 as in the *hard ultraluminous* regime of Sutton et al. (2013b). However, as the luminosity increases to $\sim 2 \times 10^{40}$ erg s^{-1}, its shape changes to become much more curved and disc-like, with a single peak at energies of $\sim$ 4-5 keV (indeed, it is likely that some of these spectra would be classified as *broadened disc* according to the Sutton et al. 2013b scheme).

The spectra in the 0.3-10 keV bandpass of *Swift* and *XMM-Newton* are all satisfactorily described by a model composed of two thermal components, a multi-colour disc blackbody model for the soft end of the spectrum, and an optically thick, cool Comptonising corona for the hard end, with the seed photon temperature of the

latter fixed at the temperature of the disc. Such a model has been found to be a good empirical description of ULX spectra in this bandpass, albeit with strong caveats against the direct physical interpretation of this model (e.g. Gladstone et al. 2009), and allows us to track the variation of the two components that make up the model. However, when the spectral bandpass is extended above 10 keV by the use of *NuSTAR* data, we find that this model no longer constitutes an acceptable fit to the data, as has been found for multiple *NuSTAR* observations of ULXs where additional hard flux is required (although this is somewhat model dependent in several ULXs; Walton et al. 2015 and references therein). Here, we have attempted to account for that in several ways. Firstly, we uncoupled the seed photon temperature of the corona from the disc. This method has been found to present difficulties in modelling ULXs below 10 keV, as it can lead to problems in minimising the χ^2 value and large uncertainties in the parameterisation of the model (Feng & Kaaret, 2009; Pintore & Zampieri, 2012). However, in this case we find that the broader bandpass does allow this model to be well constrained, with a statistically-acceptable fit that is the equal of other models. The disc temperatures are found to be relatively warm for a ULX (~ 0.5 keV), with the seed temperatures for the coronae, and the temperature of the corona itself, higher still (~ 0.8 and $\sim 3.5-4$ keV, respectively), which combine to give the spectrum the necessary breadth and hardness to model the increase in flux above 10 keV above the coupled model. Interestingly, in the previous broadband study of Holmberg IX X-1 by Walton et al. (2014), they find that freeing the coronal seed photon temperature does not improve the fit, or change the parameterisation of the model. We suggest that our different results may be an effect of our use of later versions of the *NuSTAR* calibration and/or software.

The behaviour of the individual MCD and COMPTT components again appear to follow general patterns in the 0.3-10 keV data, although this is somewhat confused by the degenerate behaviours. In most of the *Swift* and *XMM-Newton* data the variability is mainly in the Comptonised component, that brightens but appears to drop to a lower peak energy (i.e. cools down) as the total luminosity increases. The MCD component is mostly relatively stable, although it does appear to brighten and warm up in the most luminous datasets. However, the behaviour becomes much

less certain when the *NuSTAR* data are included. In the uncoupled version of the MCD plus COMPTT model similar behaviour is observed; however if the coupled version of the model is used with a SIMPL to represent the required hard excess, the evolution is a little less certain, with the COMPTT cooling but fits with the MCD both remaining the same, and increasing in temperature and flux, are permitted. The situation is confused even further by the use of a DISKPBB 'slim disc' model in place of the COMPTT , in which case the variability is dominated by the MCD and the slim disc remains relatively stable between the two epochs. The variability of the two components is therefore somewhat uncertain, and model-dependent.

Indeed, a remarkable feature of all the spectra is that *the data appear to show relatively little dynamical range below 1 keV*, particularly compared to the 1-6 keV regime. In fact, if we examine the range in spectral normalisation at both 0.5 keV and 3 keV in Figs. 3.4 & 3.6, we see that the 0.5 keV normalisation varies by factors $1.8 - 2$ in the two figures, compared to a variation of $4 - 4.3$ times at 3 keV. Hence the variation in relative normalisation is a factor $2 - 2.5$ smaller at the lower energy. This relative lack of variability in the lower energy range is strongly suggestive that any soft component in the spectrum is not varying strongly. Therefore, we can infer that the strong changes we do see in the modelled soft component may primarily be driven by the changes in the 1-6 keV band, with a hotter and brighter MCD required to help model the strongly curved spectrum seen at the highest luminosities. We therefore suspect that some of the changes in the parameterisation of the two component models may be more due to the limitations of the models in describing the spectrum, rather than representative of real underlying physical changes. Hence, we limit the remainder of our discussion to the implications of the change in the overall shape of the spectrum with luminosity for the underlying source physics, and do not discuss the two separate spectral components hereafter.

We will, however, start by discussing what the implication of our results are for two models discussed as viable possibilities for Holmberg IX X-1 by Walton et al. (2014), namely a slim accretion disc, and a wind-dominated model.

3.4.1 Slim accretion disc model

We first consider whether we could be observing the emission of an accretion disc. In a standard accretion disc we would expect to see that the peak temperature of the inner disc would scale with luminosity as $L \propto T^4$, with any changes being directly attributable to changes in the mass accretion rate. However, in Holmberg IX X-1 we see the peak in the spectrum, that is characteristic of the temperature of an optically-thick medium, decrease in energy as the luminosity increases. Interestingly, this could be consistent with the emission from a slim disc. At super-critical accretion rates we expect the disc to become geometrically thick as its interior becomes supported by radiation pressure from material advecting directly into the black hole (e.g. Poutanen et al. 2007). This means that in sources at high inclination angles, a slim disc can become self-obscuring and so if its scale height increases with luminosity it will appear to get softer as more of its harder central regions become self-obscured (Vierdayanti et al., 2013).

However, there are problems with this scenario for Holmberg IX X-1 . Firstly, the indications from both its optical spectra (lack of strong radial velocity variability in its broad emission lines; Roberts et al. 2011) and its X-ray behaviour (diagnosis as in the hard ultraluminous regime; Sutton et al. 2013b) are that it is viewed close to face-on, and not at a high inclination angle, so self-obscuration by the disc may be difficult to achieve in this object. Secondly, if the mass accretion rate is varying, then we would expect to see this reflected in variations of the soft part of the X-ray spectrum, as this part of the disc should remain visible, with a rising mass accretion rate leading to a rise in the soft X-ray flux that is particularly pronounced below 1 keV (see e.g. Fig. 1 of Vierdayanti et al. 2013). However, as noted above, the variations below 1 keV in the data we analyse are not particularly strong between different spectra, and less than those above 1 keV. Thus we do not regard this model as a particularly strong candidate for explaining the evolution of spectra with luminosity we see in this ULX.

3.4.2 The effect of a massive outflowing wind

It has been proposed that the soft component seen in the spectra of ULXs can be directly attributed to the presence of an optically thick, massive outflowing wind (e.g. Kajava & Poutanen 2009). Theoretically, such an outflowing wind should be launched from the disc at supercritical accretion rates (Poutanen et al., 2007; Ohsuga & Mineshige, 2011; Takeuchi et al., 2013). To explain the spectral variability in the context of an outflowing wind, we consider a spectral-timing model in the supercritical regime as recently described by Middleton et al. (2015). In this, as the accretion disc enters the supercritical regime its scale height H/R (where H is the height of the disc above its central plane at a radius R) increases such that $H/R \sim 1$, similarly to the slim disc model (i.e. the disc becomes geometrically-thick). However, in this model the intense radiation release from the disc drives its own loosely bound outer layers away, in the form of a massive, radiatively-driven wind, such that the accretion is always locally Eddington-limited. The disc and wind bound a funnel-shaped, low density region along the rotational axis of the black hole, into which the hard radiation of the inner disc can radiate freely, and/or is scattered along by the inner parts of the wind. The wind itself is an optically thick medium that emits thermally in soft X-rays. This geometry is summarised in Fig. 1 of Middleton et al. (2015; see also Fig. 2 of Poutanen et al. 2007), and it is inevitable that in this geometry the observed X-ray spectrum is primarily dependent upon viewing angle. It is also dependent upon accretion rate, as the opening angle of the funnel is predicted to close as the accretion rate increases, thus driving a more massive wind (King, 2009). This should mean, for a fixed line-of-sight, as the accretion rate increases the changes in spectrum should be predictable (c.f. Middleton et al. 2015): if viewed close to face-on, and the wind remains out of the line-of-sight, the spectrum should get harder as more of the hard flux is scattered over a smaller solid angle, up the line of sight towards the observer. If, however, the wind enters the line of sight then the spectrum should soften as the wind scatters some fraction of the hard photons out of the line-of-sight, and also Compton down-scatters some fraction of the hard photons that pass through it. In both cases the soft X-ray emission from the wind should increase, as the total outflow rate of the wind is proportional to the

mass accretion rate (Poutanen et al., 2007).

The latter scenario, in which the ULX is viewed close to face-on but some fraction of the wind starts to impinge on the line-of-sight as the mass accretion rate increases, would appear to be consistent with the evolution of the peak in the spectrum we see from Holmberg IX X-1. As the luminosity increases, this peak falls to lower energies, consistent with some fraction of the harder photons being scattered out of the line-of-sight and/or Compton down-scattered in the wind itself. Indeed, this spectral evolution is consistent with simulations of the Comptonised spectra of black holes at extreme supercritical accretion rates as described by Kawashima et al. (2012). They predict that at lower super-Eddington mass accretion rates, the spectra are harder than expected from a pure slim disc spectrum due to photon up-scattering in the shock-heated region near the black hole (a mechanism that we note may provide an explanation for the hard excess seen in *NuSTAR* spectra). However, at higher, extreme supercritical accretion rates, the simulated spectra are softer and become curved and disc-like as the outflow funnel opening angle becomes smaller, so decreasing the number of photons that escape without entering the cool dense outflow (the wind).

Thus this is a plausible scenario for the increased curvature, and falling peak temperature, that characterise the spectral evolution of Holmberg IX X-1. We note that a similar conclusion for the nature of this ULX was reached by Middleton et al. (2015), who also examined the variability data for this object, most notably in the form of a covariance spectrum that shows the variability is confined to a harder spectral component, consistent with extrinsic variability imprinted by a clumpy wind (Middleton et al. 2011a; Takeuchi et al. 2013; Sutton et al. 2013b).

Critically, this model also provides an explanation for the comparative lack of soft variability. King (2009) notes that the beaming factor b (i.e. the fraction of the sky that the funnel is open to) is related to the observed luminosity as $L \propto b^{-1}$, and is related to the mass accretion rate $\dot{m}$ as $b \propto \dot{m}^{-2}$. Thus, for the hard emission emanating from the central regions of the disc, we should see its luminosity increase as $L \propto \dot{m}^2$, which is faster than the luminosity of the isotropic wind emission increases ($\propto \dot{m}$). This relative hardening of the spectra is also discussed by Middleton et al.

(2015, e.g. their Eq. 10), and can both qualitatively and quantitatively explain how our spectra appear to vary more above 1 keV than below, including the dynamic ranges (factor ~ 2 difference between the faintest and brightest normalisations at 0.5 keV, compared to ~ 4 at 3 keV). Indeed, given that the luminosity of Holmberg IX X-1 is dominated by its hard X-ray emission, its dynamic luminosity range of ~ 4 in the reported observations imply that the underlying accretion rate probably varies by a factor of ~ 2 over the course of the decade of observations, making it a remarkably stable accretor.

3.4.3 Source precession

One feature of the spectra remains to be explained: the spectral degeneracy with luminosity. This has also previously been reported for this ULX by Vierdayanti et al. (2010), and differences in spectral shape at similar luminosities have also been reported for two other ULXs, IC 342 X-1(Marlowe et al., 2014) and Ho II X-1 (Grisé et al., 2010). These studies agree that the degeneracy demonstrates that the observed spectra of ULXs are not a function of accretion rate alone; Vierdayanti et al. (2010) suggest that changes in the structure of the outflowing wind may be culpable for the changes in spectral shape, whereas Marlowe et al. (2014) suggest changes in accretion state (possibly between broadened disc and hard ultraluminous regimes in the case of IC 342 X-1). It is also clear that this degeneracy is not a simple prediction of the wind model – assuming a fixed line-of-sight, the spectrum will change as described above according to the mass accretion rate, and so we do not expect any strong degeneracy in spectral shape with luminosity except perhaps when the wind comes into the line of sight and starts to diminish the hard flux. This should, however, only occur above a flux threshold, and not at all observed luminosities. Hence we need a further means of creating the degeneracy; and here we explore one, that the black hole rotation axis of Holmberg IX X-1 precesses with respect to our line-of-sight, and in doing so induces the degeneracy.

Precession is a known phenomenon of Galactic BHBs, most particularly in the case of SS433 (see Fabrika 2004 for a review). This is a very apposite example for Holmberg IX X-1 as SS433 has been suggested as a hyper-Eddington accretor that

would appear as a ULX if viewed face-on. The spectral variability we would expect from precession can be inferred from Kawashima et al. (2012) and Middleton et al. (2015). Essentially, for a fixed accretion rate, we would expect the spectra to be harder when the line-of-sight is closer to the axis, and softer when further away. This is again due to the effect of the funnel around the black hole rotation axis; closer to on-axis more hard photons from the inner disc are scattered towards the observer, whereas further from axis the edge of the funnel is reached and material in the wind starts to enter the line-of-sight, which both scatters away hard photons (again up the funnel) and Compton down-scatters other hard photons. Hence, for a fixed accretion rate, we would expect to see a constant soft component, but a hard component that diminishes and softens as the source precesses away from the black hole rotation axis. It is quite plausible that this can explain the differences between the soft and hard spectra we see in Fig. 3.5. For example, the peak energy in all the soft spectra is lower than in the hard spectra, consistent with down-scattering in the wind. Additionally, the soft spectra also appear brighter below 2 keV than the equivalent hard spectrum; this implies that their accretion rates are likely to be higher, but that hard flux is being lost to scattering in the wind. Hence the predicted changes from this physical process appear largely consistent with the degeneracy that we do see, so we infer that precession has an important role in the observed spectrum of this ULX.

3.5 Conclusion

In this chapter we have analysed *Swift*, *XMM-Newton* and *NuSTAR* spectra of the archetypal ULX Holmberg IX X-1. The wealth of data, particularly in the form of over 500 observations with *Swift*, has allowed us to study the evolution of the spectra with observed source luminosity. We find that the data tend to evolve from relatively flat spectra in the 1-6 keV range, or two-component spectra that have a classic hard ultraluminous form, at lower luminosities to a spectrum that is distinctly curved and disc-like at the highest luminosities, with the peak energy in the curved spectrum tending to decrease with increased luminosity. We study the spectra mainly in terms

of a two-component model consisting of a cool multi-colour disc blackbody and a hotter Comptonised medium (DISKBB + COMPTT in XSPEC), but the requirement for an additional component in *NuSTAR* data, the degeneracy in behaviour of the soft and hard components when other models are used, and the need for the MCD to become substantially brighter and warmer when the disc spectrum gets very curved, dissuades us from directly interpreting the changes in individual model components. Instead, we discuss the changes in the overall spectral shape in terms of physical models. We argue that a 'slim disc' model can produce the apparent cooling in the spectra at higher luminosities, if it is viewed at high inclination. However, other studies argue that Holmberg IX X-1 is viewed close to face on, and a relative lack of variability below 1 keV, compared to above, is not expected for a pure disc model. Instead, a super-critical accretion disc with a massive, radiatively driven wind appears likely to be able to explain the main characteristics of the spectral evolution, with the cooling occurring due to Compton down-scattering in the wind as it expands and starts to cross the line-of-sight at the highest accretion rates. The relatively higher increase in flux above 1 keV is then due to beaming of the hard emission from the inner disc up the 'funnel' structure bounded by the disc and the massive, optically-thick wind. The remaining characteristic of the data – a degree of degeneracy between different spectra observed at the same luminosity – can be explained if the ULX does not remain at a fixed inclination to the line-of-sight, but instead the black hole rotational axis precesses.

The analysis in this chapter adds to the growing body of evidence that many ULXs are likely to be sMBHs accreting at super-Eddington rates, where their observational properties can be explained by the distinct geometry produced by the combination of the large scale height disc, and the massive, outflowing wind. The supposition that this geometry changes in response to the accretion rate means that our view of this phenomenon is driven by two main factors: the accretion rate, and the inclination of the black hole axis to our line-of-sight. In the case of Holmberg IX X-1 we argue that the range of spectra seen, and particularly the degeneracy with luminosity, mean that both these parameters vary in the ULX; we see the ULX precess, as is seen in the Galactic black hole SS433. So, our understanding of the

ULX phenomenon continues to grow. However, many questions remain, not least the details of the exact geometry of the disc and outflowing wind (if this is indeed the correct model for ULXs), and the state of the material in it. The answers to some at least of these questions may be accessible in the immediate future with the launch of the *Astro-H* mission and its calorimeter, the high resolution and large collecting area of which will be ideal for detecting narrow emission and/or absorption feature in the ULX winds, if they are present.

Chapter 4

A deficit of ultraluminous X-ray sources in luminous infrared galaxies

4.1 Introduction

We introduced in Section 1.5.3 that ULXs are found in all types of galaxy. However, the number of ULXs per unit stellar mass in star forming galaxies is much higher than in elliptical galaxies, and this ratio tends to increase for the least massive galaxies (Feng & Soria 2011; also Swartz et al. 2008, Walton et al. 2011), suggesting that most ULXs are related to the ongoing star formation hosted in younger systems. Indeed a connection between ULXs and star formation is well established in the literature. Given this relationship we would therefore expect to detect relatively large numbers of ULXs in high SFR galaxies, and the number of ULXs in these systems should increase proportionally with the SFR. Luminous infrared galaxies (LIRGs) are one such very high star formation rate environment. LIRGs (see Sanders & Mirabel 1996 for a review) are defined as galaxies that emit more energy in the infrared (IR) than in all other wavelengths combined – $L_{\rm IR} > 10^{11} L_{\odot}$, where $L_{\odot}$ is the bolometric luminosity of the Sun. The trigger for the high infrared emission is thought to be the major effect of a strong interaction or the merger of molecular gas-rich galaxies, resulting in prodigious star formation; so the intense starbursts within giant molecular clouds heat the dust, resulting in a very high IR luminosity emitted from the LIRGs (Sanders & Mirabel, 1996).

However, another environmental factor might also affect the production efficiency of ULXs in galaxies: metallicity. It has been suggested that ULXs should be formed in higher numbers in low metallicity regions, as it is easier to evolve binaries to produce Roche lobe overflow onto a compact object in such environments (Linden et al., 2010). In addition, these environments should also lead to more efficient production of MsBHs via direct stellar collapse, due to reduced metal line-driven wind loss from massive stars (Zampieri & Roberts 2009; Mapelli & Bressan 2013; Fragos et al. 2013a, 2013b). Observational support for these hypotheses is beginning to emerge. For instance, *Chandra* observations of extremely metal poor galaxies (Prestwich et al., 2013) show that the number of ULXs normalised to SFR in these galaxies is high when compared to that of metal rich galaxies, although this is only at a formal significance of 2.3σ. Similarly, a marginally significant anticorrelation between the number of ULXs per unit SFR and metallicity was reported by Mapelli et al. (2011). In addition, Basu-Zych et al. 2013a demonstrated that the X-ray luminosity per unit SFR of Lyman break galaxies is elevated compared to local galaxies; in addition a study of a Lyman break galaxy analogue sample (Basu-Zych et al. 2013b) showed an anti-correlation between the X-ray luminosity per unit SFR and metallicity. They conclude that this is attributable to an enhanced population of X-ray binaries (XRBs) in the low metallicity environment of the galaxies, that must have a very strong ULX contribution.

Given the strong relationship between ULXs and star formation an obvious place to look for a large sample of ULXs is in the most active local star forming systems. In this chapter we study the population of ULXs in such an environment – a sample of the nearest LIRGs. Interestingly, such galaxies are typically relatively abundant in metals ($Z \gtrsim Z_{\odot}$), providing a sample of high-metallicity host environment ULXs to compare with other samples. This chapter is adapted from Luangtip et al. (2015) and is laid out as follows. In Section 4.2 we describe the sample of galaxies, and how the X-ray point source catalogue for these galaxies was constructed. We detail our analyses of the ULXs, in terms of their X-ray spectra, X-ray luminosity function and aggregated properties in Section 4.3, and discuss these in light of other results in Section 4.4. Our findings are summarised in Section 4.5.

4.2 Observations and data reduction

4.2.1 Observations and initial analyses

In this chapter we study the ULX population hosted by the sample of 17 LIRGs studied in Lehmer et al. (2010), using *Chandra* X-ray observations. In brief, this sample was selected as all LIRGs within a luminosity distance ($D_{\rm L}$) of 60 Mpc with a foreground Galactic column density ($N_{\rm H}$) $< 5\times10^{20}$ cm^{-2}. To qualify as LIRGs all galaxies have total infrared luminosity (8 – 1000 μm band; $L_{\rm IR}$) $> 1\times10^{11}L_{\odot}$, with the most luminous LIRG in the sample – Arp 299 – as bright as $\sim 8\times10^{11}L_{\odot}$. These luminosities correspond to SFRs $\gtrsim 7$ $M_{\odot}$ yr^{-1} for each galaxy in the sample (see Section 4.3.2 for the calculation of SFR). The general properties of each galaxy are shown in Table 4.1. For the purposes of this chapter we consider all galaxies for which Lehmer et al. (2010) present evidence of possessing an AGN in their Tables 1 and 3 (including the two objects classified as harbouring LINER/Sy 2 nuclei) as AGN hosts. The effect of an AGN contributing to the host galaxy IR emission and hence SFR will be taken into account in the following analyses.

For some LIRGs which their metallicities are available in literature, we reported the values in the form of the oxygen abundance 12+log(O/H) in column 9 of Table 4.1. The calculation of the 12+log(O/H) can be explained briefly as the following (Zaritsky et al., 1994). Firstly, the observed value called R_{23} index – defined as line flux ratio between [O II]$\lambda\lambda$3726,3729 + [O III]$\lambda\lambda$4959,5007 and Hβ – was measured from observations. Then the R_{23} was converted to the 12+log(O/H) using the selected calibration for R_{23} index; so different calibration could lead to different value of metallicity, although it was measured from the same observations (we will discuss this effect further in Section 4.4.2).

The observational data for these LIRGs were extracted from the *Chandra* data archive.[1] For the few galaxies that have multiple archival datasets, we selected the observation with the longest exposure time in order to obtain the most complete snapshot of the ULX population, and the best quality data for each individual

[1] `http://cxc.harvard.edu/cda/`

Table 4.1: Properties of the LIRG sample

Galaxy name	RA	Dec	R_{20} ellipse parameters			$D_{\rm L}$	SFR	Z	AGN?
			a (arcmin)	b (arcmin)	P.A. (deg)	(Mpc)	($M_\odot$ yr^{-1})		
(1)	(2)	(3)	(4)	(5)	(6)	(7)	(8)	(9)	(10)
NGC 1068	02 42 41	– 00 00 48	2.42	1.99	35	13.8	7.2	9.07[1]	Y
NGC 1365	03 33 36	– 36 08 25	4.60	3.45	50	18.0	9.1	9.01[1]	Y
NGC 7552	23 16 11	– 42 35 05	2.21	1.30	95	21.6	9.5	9.16[2]	N
NGC 4418	12 26 55	– 00 52 39	0.83	0.45	55	32.1	10.3	-	Y
NGC 4194	12 14 09	+54 31 37	0.64	0.44	170	40.7	10.9	-	Y
IC 5179	22 16 09	– 36 50 37	1.48	0.56	55	47.2	13.5	8.90[3]	N
ESO 420-G013	04 13 50	– 32 00 25	0.61	0.58	110	48.2	8.5	-	Y
Arp 299	11 28 30	+58 34 10	1.42	1.25	28	48.2	73.2	8.80[3]	Y
NGC 838	02 09 39	– 10 08 46	0.62	0.43	95	50.8	8.5	-	N
NGC 5135	13 25 44	– 29 50 01	1.75	0.86	125	52.9	14.5	8.70[3]	Y
NGC 5395	13 58 38	+37 25 28	1.53	0.80	5	54.0	11.3	-	Y
NGC 5653	14 30 10	+31 12 56	0.76	0.70	75	55.5	11.0	-	N
NGC 7771	23 51 25	+20 06 43	1.52	0.62	75	57.9	20.6	8.80[3]	Y
NGC 3221	10 22 20	+21 34 11	1.62	0.34	167	59.5	11.1	-	N
CGCG 049-057	15 13 13	+07 13 32	0.45	0.23	20	59.8	20.4	-	N
IC 860	13 15 03	+24 37 08	0.56	0.32	20	59.9	15.1	-	Y
NGC 23	00 09 53	+25 55 26	1.13	0.54	155	60.5	9.7	-	N

Notes. Basic properties of the LIRG sample, ordered by distance (based on table 1 of Lehmer et al. 2010). Column 1: common galaxy name. Columns 2 and 3: right ascension and declination, at epoch J2000, respectively. Columns 4–6: parameters of the R_{20} region for each galaxy: semi-major axis, semi-minor axis and position angle, respectively. Column 7: luminosity distance. The values in columns 1–7 were given in Lehmer et al. (2010). Column 8: star formation rate, corrected for an AGN contribution in the calculation (see Section 4.3.2). Column 9: metallicity, in the form of the oxygen abundance (i.e. 12+log(O/H)). The references are: [1]Zaritsky et al. (1994), [2]Moustakas et al. (2010) and [3]Relaño et al. (2007). Column 10: Indication of whether the galaxies possess an AGN (see text for details).

object. The exception to this was NGC 1365, for which we selected an observation with shorter exposure time as it covered a larger fraction of the galaxy's area, as defined by the R_{20} ellipse,[2] than the longest exposure, but still permitted us a statistically complete vista of the ULXs within its field-of-view (see Section 4.2.2). We decided not to merge the observations together to avoid an artificial boost in the number of ULXs compared to a single epoch observation, via the inclusion of multiple transient objects. Table 4.2 lists the observational datasets we selected for our analysis; more details on the instrument and set-up for each observation are provided in Table 2 of Lehmer et al. (2010).

The data were reduced using version 4.4 of the Chandra Interactive Analysis of Observation (CIAO)[3] tools. We first used the CHANDRA_REPRO script to create a new level 2 event file and a new bad pixel file, in order to utilise the latest calibration data. Then background flares were inspected and the exposure ranges that have a background level $> 3\sigma$ above the mean level were removed by the DEFLARE script. The level 2 event files created by these steps were then used as the basis for further analysis.

4.2.2 The source catalogue

Source detection

We began by searching for the X-ray point source candidates within the R_{20} ellipse region of each galaxy, using the CIAO WAVDETECT algorithm, that applies a Mexican Hat wavelet function with radii of 1, 2, 4, 8 and 16 pixels to images created from the level 2 data. A detection threshold level of 10^{-6} was used, corresponding approximately to a false detection probability of 1 per 10^6 spatial resolution elements. In addition, for the galaxies in which a part of the R_{20} ellipse was on (or near) the CCD edge, i.e. NGC 1365, NGC 7552 and Arp 299, we also supplied an exposure map at 1.5 keV to the WAVDETECT algorithm, created using the FLUXIMAGE tool, in order to increase the accuracy of the source detection in these regions. WAVDETECT

[2]The elliptical isophote equivalent to a level of 20 mag per arcsecond^2 in the K_s band, see Lehmer et al. (2010) and references therein.

[3]`http://cxc.harvard.edu/ciao/`

Table 4.2: *Chandra* observational data

Galaxy	Obs. ID[a]	Exp. time[b] (ks)	Refs.[c]
NGC 1068	344[d]	47.05	1,2,3,4,5,6
NGC 1365	3554[d]	13.42	7,8,9
NGC 7552	7848	5.08	10
NGC 4418	4060[d]	19.62	-
NGC 4194	7071	35.30	11,12
IC 5179	10392	11.96	-
ESO 420-G013	10393	12.42	-
Arp 299	1641	24.10	13,14,15,16
NGC 838	10394	13.79	-
NGC 5135	2187	26.41	-
NGC 5395	10395	15.65	17
NGC 5653	10396	16.52	-
NGC 7771	10397	16.71	-
NGC 3221	10398	18.96	-
CGCG 049-057	10399	19.06	-
IC 860	10400	19.15	-
NGC 23	10401	19.06	-

Notes. [a]The *Chandra* observation identifier. [b]The net exposure time after the removal of high background periods (see Section 4.2.1). [c]References to other analyses of the listed datasets, all of which were used by Lehmer et al. (2010). These are: (1) Smith & Wilson (2003); (2) Ptak et al. (2006); (3) Gültekin et al. (2009); (4) Swartz et al. (2004); (5) Swartz et al. (2011); (6) Peterson et al. (2006); (7) Strateva & Komossa (2009); (8) Wang et al. (2009); (9) Risaliti et al. (2005); (10) Grier et al. (2011); (11) Kaaret & Alonso-Herrero (2008); (12) Mineo et al. (2012a); (13) Huo et al. (2004); (14) Nelemans et al. (2010); (15) González-Martín et al. (2006); (16) Zezas et al. (2003); (17) Smith et al. (2012). [d]Galaxies with multiple observations; further details of these can be found in Lehmer et al. (2010).

was run over data segregated into images in three separate energy bands per observation: soft (0.3–2 keV), hard (2–10 keV) and full (0.3–10 keV). Subsequently, the sources detected in each energy band were cross-correlated with source lists from the other bands, with individual objects detected in multiple bands identified using a matching radius of 3 arcseconds. Each individual object was listed as one detection in the resulting combined source lists (one list per galaxy), with its position adopted from its full, soft or hard band detection, in that order of priority. There were a total of 214 candidate X-ray sources at this stage.

The ACIS EXTRACT package (Broos et al. 2010, 2012; hereafter AE)[4] was then used to finalise a catalogue composed of the most reliable point-like sources, and to characterise these objects. Firstly, we considered the statistical significance of the detected sources using the tool AE binomial no-source probability[5]; given that the observed source and background counts were obtained, the tool calculated the probability that the observed sources are background – i.e. the observed source counts are just a background fluctuation – assuming binomial statistic for the distribution of the detected source and background counts; two low-significance sources which have AE binomial no-source probability > 0.01 were removed in this step. After that, AE compared the source radial profile with the point spread function (PSF) for a point-like object at the source position and removed the sources that were not consistent with the PSF according to a Kolmogorov-Smirnov test (AE K-S probability < 0.01; i.e. extended sources). We also picked out any remaining objects by eye that might still be extended, and used the SRCEXTENT[6] script to test whether to reject them, excluding ones shown to be extended objects. Briefly, the tool derived the elliptical Gaussian parameters which are most strongly correlated with the source image. The same algorithm was also applied to derive the elliptical Gaussian parameters for the PSF of a point-like object at the source position. Then these two apparent ellipses were tested for consistency given the image statistics, and the algorithm reported whether the source was extended within 90% confidence inter-

[4] `http://www.astro.psu.edu/xray/acis/acis_analysis.html`

[5] See detail in `http://www2.astro.psu.edu/xray/docs/TARA/ae_users_guide.pdf` Section 5.10.3

[6] `http://cxc.harvard.edu/ciao/threads/srcextent/`

vals. In total, 61 extended sources ($\sim 30\%$ of all detected sources) were removed by the AE K-S test and SRCEXTENT tools. As the final step we compared our point source catalogue with NASA/IPAC Extragalactic Database (NED)[7] and SIMBAD astronomical database (hereafter SIMBAD)[8], and identified and removed the X-ray sources within 5 arcseconds of each galaxy centre, to exclude all possible AGN contamination from the host galaxy; eight sources were removed in this way. We also used these databases to search for foreground and/or background source contamination and four objects were identified, i.e. two stars, one QSO and one AGN, and removed. At the conclusion of these steps, we were left with the final catalogue of X-ray point sources for each galaxy, that we split into two source lists in Appendix B. Overall, 139 X-ray point sources were detected in 14 LIRGs; no point sources were detected in ESO 420-G013, CGCG 049-057 or IC 860. More than 50% of the point sources were detected in the two nearest galaxies, NGC 1068 and NGC 1365, due to a combination of their proximity and exposure times yielding far greater sensitivity to faint point sources than in the other galaxies in the sample.

Source photometry

The net photon count rate detected from each point source was calculated in the 0.3–10 keV band by AE, using a polygonal aperture set to the 90% encircled energy of the source PSF at 1.5 keV. The background level was set using an annulus around the source or, for the cases in which the source resided in densely populated regions or areas of heightened diffuse emission, we used a circular aperture located in a source-free region near to the source position, with a similar level of diffuse emission. The background area was set to be at least four times bigger than the source region and to encompass at least 100 counts. The web interface version of the Portable Interactive Multi-Mission Simulator (WEBPIMMS)[9] was applied to convert the calculated count rates into a 0.3–10 keV source flux, using an absorbed power-law continuum model.

[7] http://ned.ipac.caltech.edu
[8] http://simbad.u-strasbg.fr
[9] http://heasarc.nasa.gov/Tools/w3pimms.html

A typical value of ULX photon index (Γ) and column density ($N_{\rm H}$)[10] were used in the model: $\Gamma = 2$ and $N_{\rm H} = 1.5{\times}10^{21}$ cm^{-2} (see e.g. Swartz et al. 2004; Gladstone et al. 2009; Sutton et al. 2012). Finally, the luminosity of each source was calculated using the luminosity distance of its host galaxy. All source photometry is provided in Tables B.1 and B.2 in Appendix B, where we separate the detections into two lists according to whether their calculated luminosity is above or below the 0.3–10 keV luminosity threshold of 10^{39} erg s^{-1} used to demarcate a ULX.

ULX catalogue and completeness

The ULX candidates are tabulated in Table B.1. The number of ULXs detected in each galaxy is shown in Table 4.3, and the position of the ULXs within their host galaxies are shown in Fig. 4.1. In total, 53 ULXs were detected in 13 LIRGs; no ULXs were detected in NGC 4418, ESO 420-G013, CGCG 049-057 or IC 860.

A pertinent question is whether we have detected all of the ULXs in each galaxy? To address this question, we calculated a completeness function for each galaxy following the method of Voss & Gilfanov (2006). We first created sensitivity maps in the full band (0.3 – 10 keV) for each galaxy, assuming source spectra with power-law continuum forms (we still used typical ULX model parameters: $\Gamma = 2$ and $N_{\rm H} = 1.5 \times 10^{21}$ cm^{-2}, as this is appropriate for ULXs; cf. Gladstone et al. 2009; Sutton et al. 2012). We then computed the completeness function, $K(L)$, within the R_{20} region of each galaxy as per Voss & Gilfanov (2006), assuming that the fraction of cosmic X-ray background sources contributing to the sample is small and can be neglected (see below). Once the completeness functions were constructed, we defined the completeness luminosity ($L_{\rm comp}$) as the luminosity at which the completeness function, $K(L) = 0.9$; i.e. no more than 10 per cent of point sources are missing in the detection at this luminosity. We found that all galaxies have $L_{\rm comp} \lesssim 10^{39}$ erg s^{-1} (see the third column of Table 4.3). Indeed, as we are interested in the completeness of the ULX detection, we defined another parameter, $K(L_{\rm ULX})$, as the completeness of the point source detection at minimum ULX luminosity of 10^{39} erg

[10]Here this is a combination of both foreground Galactic and additional, extragalactic column density.

Table 4.3: ULX detections and completeness per galaxy

Galaxy	Number of ULXs[a]	log $L_{\rm comp}$[b]	$K(L_{\rm ULX})$[c]
NGC 1068	3 ± 0	37.53	1.00
NGC 1365	6^{+2}_{-1}	38.11	1.00
NGC 7552	2^{+3}_{-1}	38.47	1.00
NGC 4418	0 ± 0	38.31	1.00
NGC 4194	1 ± 1	38.55	1.00
IC 5179	8^{+0}_{-3}	38.88	0.98
ESO 420-G013	0 ± 0	38.87	0.96
Arp 299	8^{+1}_{-0}	38.96	0.93
NGC 838	2^{+1}_{-0}	39.01	0.89
NGC 5135	6^{+1}_{-2}	38.70	0.99
NGC 5395	4^{+1}_{-2}	38.85	1.00
NGC 5653	1 ± 1	38.90	0.95
NGC 7771	4^{+4}_{-0}	38.92	0.97
NGC 3221	6^{+0}_{-1}	38.90	0.99
CGCG 049-057	0 ± 0	38.87	1.00
IC 860	0 ± 0	38.86	1.00
NGC 23	2 ± 2	38.92	0.96
Total	53^{+16}_{-13}		

Notes. [a]The number of ULXs detected in each galaxy. The upper and lower limits were calculated from the number of sources whose 1σ luminosity upper limit lies within the ULX regime, and the number of ULXs with lower luminosity limit below the ULX regime, respectively. [b]The completeness luminosity in decimal logarithmic units, defined as the luminosity at which the completeness function, $K(L) = 0.9$. [c]The value of the completeness function at the minimum ULX luminosity of 10^{39} erg s^{-1}.

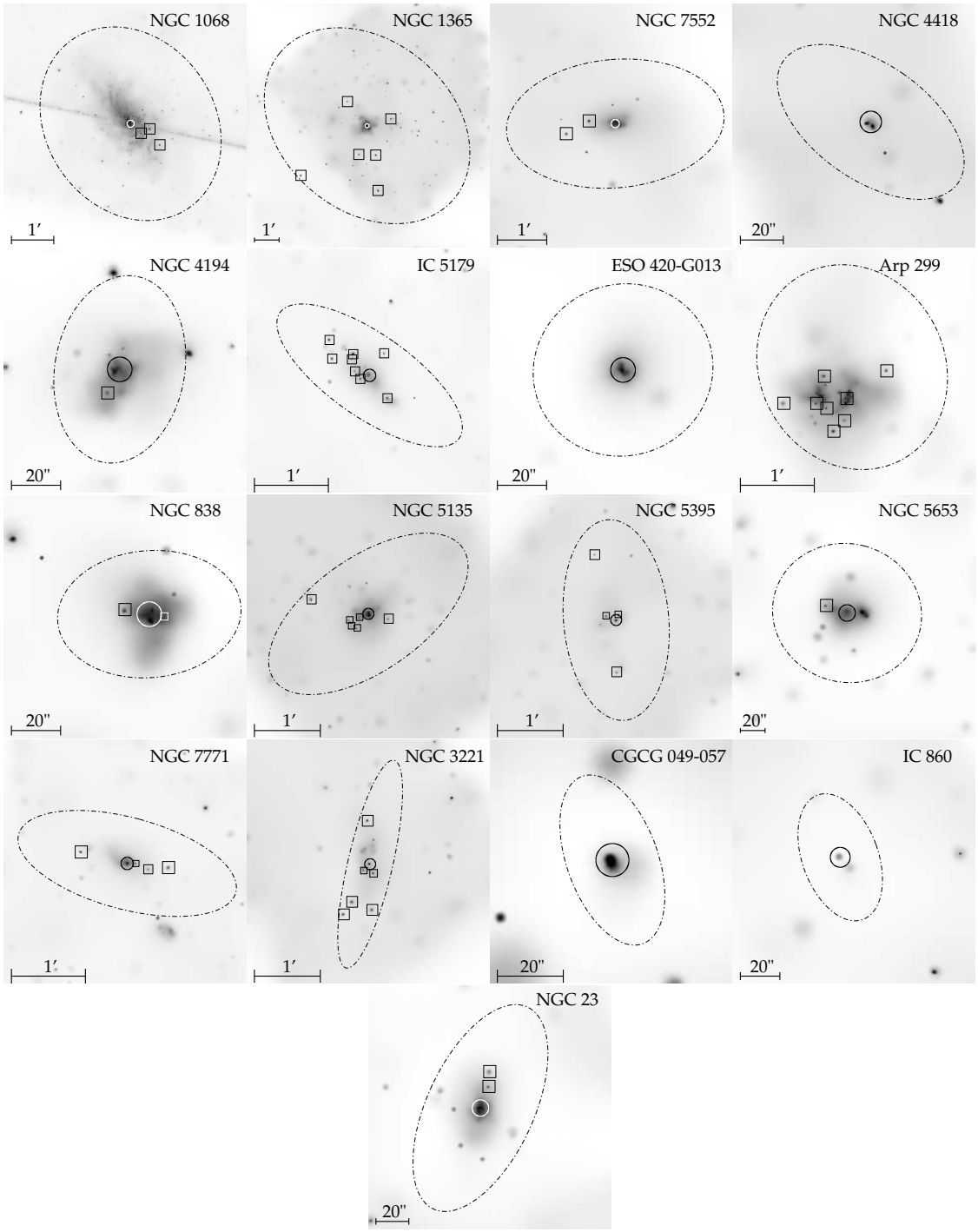

Figure 4.1: The ULX detections (boxes), presented on the 0.3–10 keV *Chandra* X-ray images of their host galaxies. The images were adaptively smoothed using the CSMOOTH algorithm with an S/N ratio set between 2 – 3 and a minimum smoothing scale of 0.5 pixels for a Gaussian kernel, and are displayed with arbitrary logarithmic scaling intended in each case to permit the ULXs to be visible. The dash-dot ellipses define the R_{20} region of each galaxy, and the circles indicate the 5 arcsecond radius regions excluded from the point source analysis due to their proximity to the nucleus. Note that no exclusion was made in the case of Arp 299 where the irregularity of this galaxy merger makes the definition of a single nuclear position difficult.

s^{-1} (the fourth column of Table 4.3). The analysis showed that the observations are sufficiently sensitive for 100 per cent of the ULXs to be detected in eight of the sample galaxies (i.e. $K(L_{\rm ULX}) = 1$). In addition, the remainder of the galaxies are complete to the $\gtrsim 90$ per cent level. Thus we are satisfied that the ULX catalogue is complete in terms of ULX detection.

Contamination from the cosmic X-ray background

An issue that must always be considered when examining source populations in external galaxies is the extent to which these populations are contaminated by foreground and/or background interlopers. While the majority of foreground objects, particularly at low Galactic latitudes, are bright stars that are readily identified in optical images, at the high Galactic latitudes of the LIRG sample the predominant contamination comes from the background QSOs that constitute the cosmic X-ray background (CXB). Fortunately, this contamination can be taken into account statistically from the known CXB source counts.

The number of CXB sources contributing to the ULX catalogue was estimated using the $logN-logS$ relationships of Georgakakis et al. (2008). We firstly calculated the flux in the 0.5–10 keV band of a source at the minimum ULX luminosity of 10^{39} erg s^{-1} at the distance of each galaxy. Then WEBPIMMS was used to divide this minimum ULX flux between the 0.5–2 keV and 2–10 keV bands, the soft and hard bands used in Georgakakis et al. (2008), respectively. In this calculation we used a CXB AGN-like power-law spectrum to convert the flux between energy bands; a Galactic column density of 5×10^{20} cm^{-2} (the upper limit on the foreground Galactic column density of the LIRGs) and a photon index of 1.7. We then converted these minimum fluxes to a maximum CXB contribution per unit area using Equation 2 of Georgakakis et al. (2008), before normalising the CXB contamination estimate to the R_{20} area of every LIRG in both the soft and hard bands. Finally, we summed these contamination estimates together to calculate a total contamination for the sample.

The calculation predicts a total of $\sim$ 10 soft band contaminants, and $\sim$ 14

contaminants in the hard band. This compares to 46 soft band detections[11], and 27 hard band detections, leading to contamination estimates of ~ 22 per cent and ~ 52 per cent respectively. However, we regard these numbers as upper limits, for the following reasons. Firstly, the soft band numbers do not account for the absorption of the background CXB source photons by the cold, neutral interstellar medium of the LIRGs. This will act to reduce the detectability of the background objects, and so diminish the numbers of contaminants. Secondly, the calculation is based on detectability in the full band; this does not guarantee a detection in the hard band. Indeed, in many galaxies a full band detection of a ULX is at the limit of the capabilities for the given exposure times (cf. the completeness analysis shown above). So, given that < 30 per cent of the photons detected by the *Chandra* ACIS-S detector for the AGN-like spectral model used here are above 2 keV, these would not result in hard band detections for the ULX flux limit (although, conversely, given that most of the photon flux is below 2 keV the situation is not as bad for that band – as is indeed shown by the relative soft/hard detection statistics given above). Indeed, a factor of ~ 4 increase in flux would be required to turn these full band detections into hard band detections; this means that the current estimate of contamination in this band is very likely a grossly inflated overestimation. We therefore disregard it, and quote only the soft band upper limit of $\lesssim 22$ per cent contamination for the sample. We note this is relatively low (thus permitting the completeness analysis shown above), so we are confident our sample is dominated by *bona fide* ULX detections. It is also consistent with the contamination fractions in previous similar ULX sample studies, with ~ 15 per cent of the ULXs detected in the spiral galaxy samples of Swartz et al. (2004) and Walton et al. (2011) estimated to be background objects via similar calculations.

[11] Given the low effective area of ACIS-S below 0.5 keV, we regard our 0.3–2 keV band as equivalent to the 0.5–2 keV band to first order.

4.3 Data analysis & results

4.3.1 Spectral analyses

The selection of a large sample of ULXs permits us to perform several experiments to investigate their properties, and how these properties relate to that of their host galaxies. One such experiment is to examine how their spectra evolve as a function of luminosity, where our sample can act as an independent control to investigate the suggested evolution from the study of the nearest and brightest objects, such as presented in Gladstone et al. (2009). However, given the low number of counts available for most of the ULX detections in our sample (cf. Table B.1) it is clear that we cannot do this for each individual ULX. Hence, we simply split the ULXs by luminosity, segregating into three equal logarithmical luminosity bins: low luminosity ($39 \leq \log L_{\rm X} < 39.33$, 25 sources); medium luminosity ($39.33 \leq \log L_{\rm X} < 39.67$, 21 sources); and high luminosity ($39.67 \leq \log L_{\rm X} < 40$, 6 sources), and proceeding to study their stacked spectra. These luminosity boundaries are broadly supported by evidence that ULXs do change in their spectral shape, from a disc-dominated to a two-component ultraluminous regime, at a luminosity $\sim 3 \times 10^{39}$ erg s^{-1} (cf. Gladstone et al. 2009; Sutton et al. 2013b). In one case – CXOU J024238.9-000055 – the high number of counts detected would have dominated the stacked spectrum of the high luminosity bin, and so we study it individually below.

We extracted the spectrum of each ULX using the CIAO SPECEXTRACT script. The same source and background regions as were used to extract source photometry in Section 4.2.2 were also used here as data extraction apertures. Once extracted, the spectra were stacked by the COMBINE_SPECTRA script using the *summation* method, to create a single spectrum for each luminosity bin, and grouped to a minimum of 25 counts per bin to permit χ^2 fitting. In the case of CXOU J024238.9-000055, the individual spectrum was also grouped to a minimum of 25 counts per bin. The spectra were then fitted in XSPEC[12] version 12 over the energy range 0.3–10 keV. In the following fits the absorption is modelled using the TBABS model with

[12] http://heasarc.gsfc.nasa.gov/xanadu/xspec/

interstellar abundances set to the values of Wilms et al. (2000); we do not explicitly account for foreground Galactic column in the fits as the stacked spectra will contain data from objects with differing values of this parameter, although we note that the initial selection criteria of the LIRG sample ($N_H < 5 \times 10^{20}$ cm^{-2}) ensures this is relatively low. All best fitting spectral parameter values are quoted with 90 per cent confidence intervals (Avni, 1976) unless otherwise specified.

Combined spectral fits

We began by fitting the stacked spectra with a simple empirical model, namely an absorbed power-law. The results are shown in Fig. 4.2 and the model fitting parameters are reported in Table 4.4. Two main results are apparent. Firstly, the absorption for this model is consistent between all three luminosity groups at $\sim 2 \times 10^{21}$ cm^{-2}; this is significantly ($\sim$4 times) higher than the foreground columns for any of the LIRGs, indicating that absorption from cold material is present in these galaxies. Secondly, a significant change in the stacked spectrum is seen between the low and medium luminosity groups, with the spectrum hardening from $\Gamma \sim 2.3$ to ~ 1.5 respectively. However, the spectrum then remains constant (within errors) between the medium and high spectra: there is no statistical distinction in power-law photon index between these two luminosity bins.

Similar results were seen when an absorbed multicolour disc blackbody model (MCD; DISKBB in XSPEC; Mitsuda et al. 1984) was used instead. In this case the absorption columns (N_H) of the three luminosity bins were also formally consistent with each other, and with no absorption, although the column for the low luminosity group had a much lower upper limit than the more luminous bins. But again, a significant hardening is seen between the low and medium luminosity bins, with the medium and high luminosity stacked spectra very consistent. While it would not be prudent to extract physical meaning from the results of this MCD fit given the likely wide differences in underlying spectra of the contributing sources, the similarity of the main results with the power-law fit – namely an apparent change in spectrum for objects at luminosities above and below $\sim 2 \times 10^{39}$ erg s^{-1} – points at a real change in underlying spectrum.

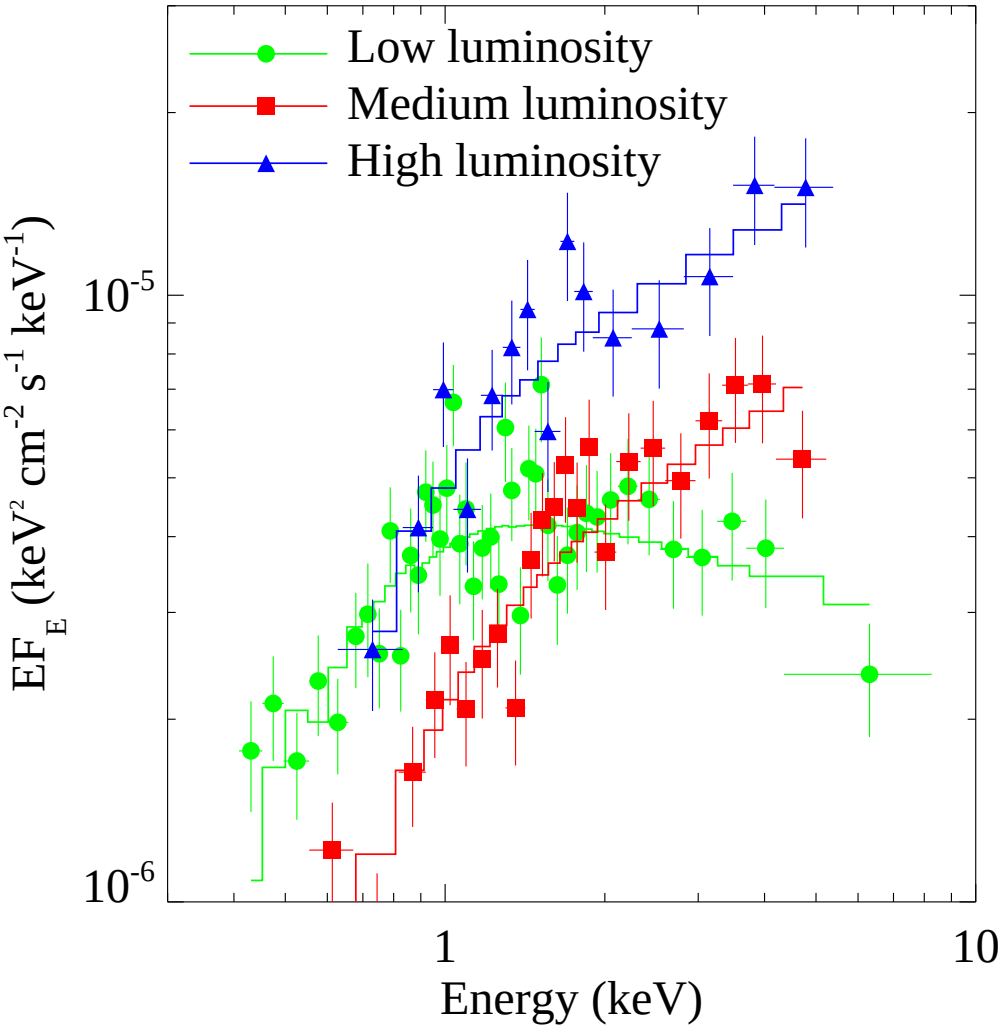

Figure 4.2: The stacked spectra of the low ($39 \leq \log L_{\rm X} < 39.33$, green circle), medium ($39.33 \leq \log L_{\rm X} < 39.67$, red square) and high ($39.67 \leq \log L_{\rm X} < 40$, blue triangle) luminosity groups, unfolded from the detector response. We also show the best-fitting power-law continuum model as the similarly-coloured solid line in each case.

Table 4.4: Combined spectral fitting

Luminosity bin	No. of sources[a]	Power-law			MCD		
		$N_{\rm H}$[b]	Γ[c]	$\chi^2/d.o.f.$[d]	$N_{\rm H}$[e]	$T_{\rm in}$[f]	$\chi^2/d.o.f.$[d]
Low ($39 \leq \log L_{\rm X} < 39.33$)	25	$0.19^{+0.04}_{-0.05}$	$2.31^{+0.11}_{-0.09}$	49.84/40	< 0.01	$0.84^{+0.08}_{-0.06}$	60.82/40
Medium ($39.33 \leq \log L_{\rm X} < 39.67$)	21	$0.25^{+0.15}_{-0.09}$	$1.48^{+0.21}_{-0.14}$	26.6/20	< 0.17	$1.59^{+0.44}_{-0.24}$	21.64/20
High ($39.67 \leq \log L_{\rm X} \leq 40$)	6	$0.23^{+0.20}_{-0.12}$	$1.57^{+0.21}_{-0.22}$	13.48/12	< 0.13	$1.59^{+0.63}_{-0.32}$	16.66/12

Notes. [a]the number of sources contributing to the luminosity bins. [b]Total absorption column measured from power-law model (10^{22} cm^{-2}). [c]Power-law photon index. [d]χ^2 fitting statistic, and number of degrees of freedom. [e]Total absorption column measured from MCD model (10^{22} cm^{-2}). [f]Inner-disc temperature (keV). All best fitting parameter values are reported with 90 per cent confidence intervals.

However, one must be extremely careful when stacking spectra not to induce any characteristics into the spectra by the choice of bins, or the relative contributions of sources to the bins. In this case, we note that all the source detections with very low total counts ($\lesssim 10$ counts) lie in the lowest luminosity bin; given the predominantly soft response of *Chandra* this raises the concern that these objects may not be contributing many counts above 2 keV, where the ACIS-S detector sensitivity falls off, thus artificially softening the stacked spectrum in this bin. However, we note two things: firstly, that sources would need to be very soft not to contribute counts above 2 keV in the ACIS-S – for example, an object with 10 detected counts and an intrinsic power-law slope of $\Gamma = 2.5$ and absorption $N_{\rm H} = 5 \times 10^{20}$ cm^{-2} would contribute 1–2 counts above 2 keV. Secondly, the 12 objects with low counts only contribute ~ 7 per cent of the total counts to this stacked spectrum. We confirm that this is not an issue by re-stacking the spectra in the low and medium luminosity bins to exclude all sources with more than 70 counts; this leaves spectra with 371 and 405 counts respectively. The power-law continuum fits to these spectra are consistent within errors with the full stacked spectrum fits to each bin, showing the same soft/hard spectral dichotomy (low luminosity bin: $N_{\rm H} = 0.3 \pm 0.2 \times 10^{22}$ cm^{-2}, $\Gamma = 2.1 \pm 0.4$; medium luminosity bin: $N_{\rm H} = 0.4^{+0.3}_{-0.2} \times 10^{22}$ cm^{-2}, $\Gamma = 1.4 \pm 0.4$). We therefore do not consider the low luminosity stacked spectrum to have been artificially softened by this effect.

There is one more concern about the low luminosity bin, though; two sources (CXOU J024238-000118 and CXOU J024240-000101, both in NGC 1068) contribute roughly one third of the counts to the bin each. We therefore examined their spectra (that were removed from the analysis reported in the above paragraph), and found that one object appears softer than the full stacked spectrum for this bin ($N_{\rm H} = 0.6 \pm 0.2 \times 10^{22}$ cm^{-2}, $\Gamma = 4.4 \pm 1.1$), and the other harder ($N_{\rm H} = 0.2 \pm 0.1 \times 10^{22}$ cm^{-2}, $\Gamma = 1.6 \pm 0.3$), cf. Table 4; hence their spectra average out across the bin. Considering that the other objects in this bin have a stacked spectrum that is consistent with the full stack, we confirm that the stacked spectra reflect the average of the underlying low luminosity ULX properties. The difference in spectra can therefore be regarded as a real effect, and we discuss it further in Section 4.4.1.

Finally, we attempted more complex spectral model fits, in particular an absorbed MCD plus power-law model. However, in large part due to the moderate quality of the stacked spectra (a few hundred to ~ 1000 counts per bin), no statistical improvements over the single component models could be discerned.

CXOU J024238.9-000055

CXOU J024238.9-000055 is one of the brightest ULXs in the entire sample, at $L_{\rm X} \sim 5 \times 10^{39}$ erg s^{-1}, and given its location in the nearest galaxy in the sample (NGC 1068) and the relatively high exposure for this galaxy (46.9 ks) we have accumulated sufficient counts from this object for an analysis of its spectrum. Previous work has shown it has a very hard spectrum: its power-law photon index is $\sim 0.8 - 1$ (Smith & Wilson, 2003; Swartz et al., 2004; Berghea et al., 2008). However, this is not due to excessive pile-up on the *Chandra* detectors; its observed count rate of ~ 0.03 count s^{-1} is no more than ~ 5 per cent piled-up.[13] It is not due to out-of-time events from the bright AGN in NGC 1068 either; although the source is located along the readout streak[14], we have verified using on- and off-streak backgrounds that the spectrum is not significantly affected by this detector effect (indeed, we note that the adaptive smoothing algorithm used to create Fig. 4.1 greatly exaggerates this effect compared to raw data). Hence the interpretation of the unusual hardness of this ULX is currently unclear. Here, we re-analyse the data to revisit this question.

We began by fitting the ULX spectrum with an absorbed power-law continuum model. A similar result to previous work was found: the power-law index was very hard, with $\Gamma = 0.75 \pm 0.1$ and $N_H = 0.67 \pm 0.2 \times 10^{22}$ cm^{-2}(see Table 4.5), and produced a statistically acceptable fit (null hypothesis probability of ~ 12 per cent). However, the spectrum of this source does show residuals compared to the data, with the largest feature falling below the model level at an energy of ~ 1.7 keV (cf. Fig. 4.3). We therefore attempted to improve the fit to the data by adding a Gaussian absorption component to the power-law model. This provided a reasonably significant improvement to the fit, with $\Delta\chi^2 = 18$ for 3 additional degrees of freedom

[13] http://cxc.harvard.edu/csc/memos/files/Davis_pileup.pdf
[14] http://cxc.harvard.edu/ciao/why/pileup_intro.html

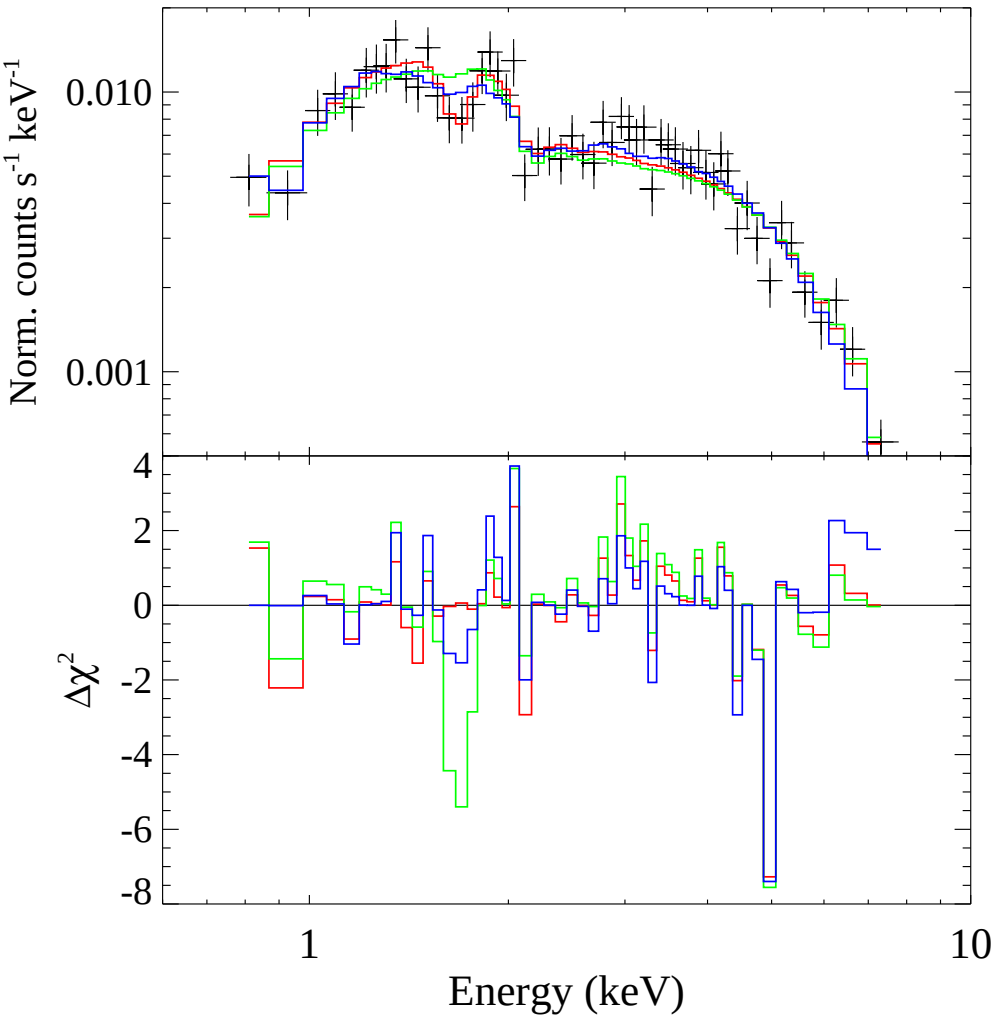

Figure 4.3: The spectrum of CXOU J024238.9-000055. *Top panel:* The spectral data (in black), with the best fitting power-law model (green line), power-law model with Gaussian absorption component (red line) and power-law model with partial covering absorber (blue line). *Bottom panel:* The residual differences between the data and the best fit, with the models plotted as above.

Table 4.5: Spectral fitting results for CXOU J024238.9-000055

Single power-law model	
$N_{\rm H}{}^{a}$	$0.67^{+0.17}_{-0.14}$
Γ^{b}	$0.75^{+0.12}_{-0.11}$
$\chi^2/d.o.f.$	$65.29/53$
Power-law model with Gaussian absorption	
$N_{\rm H}{}^{a}$	$0.75^{+0.12}_{-0.07}$
Γ^{b}	$0.88^{+0.16}_{-0.11}$
Line energy^{c}	$1.68^{+0.04}_{-0.08}$
Line width^{d}	$0.08^{+0.07}_{-0.04}$
$\chi^2/d.o.f.$	$47.13/50$
Power-law model with partial covering absorption	
$N_{\rm H}{}^{a}$	$0.68^{+0.30}_{-0.19}$
Γ^{b}	$1.65^{+0.77}_{-0.33}$
$N_{\rm H,pa}{}^{e}$	$7.95^{+6.08}_{-2.36}$
log ξ^{f}	$2.20^{+0.18}_{-0.19}$
Covering fraction^{g}	> 0.83
$\chi^2/d.o.f.$	$50.27/50$

Notes. A fixed Galactic column of 0.04×10^{22} cm^{-2} (the column density in the direction of NGC 1068) was added to each model. ^{a}Absorption column intrinsic to the ULX and/or its host galaxy (10^{22} cm^{-2}). ^{b}Power-law photon index. ^{c}Central energy of the Gaussian absorption line (keV). ^{d}Width of Gaussian absorption line (keV). ^{e}Column density of partial covering absorber (10^{22} cm^{-2}). ^{f}Logarithm of photo-ionisation parameter $\xi = L/(nR^2)$, where L is the total luminosity, n the density of the absorber and R the distance of the material from the ionising source. ^{g}Covering fraction of partial covering absorber (where 0 = totally uncovered and 1 = full covering). All best fitting parameter values are reported with 90 per cent confidence intervals.

for a broad absorption feature (width of $\sim$ 80 eV) at 1.68 keV. However, a single broad absorption feature at that energy is difficult to explain physically.

We therefore attempted a more physically meaningful fit to the data by modelling the residual using a partial covering, partially ionised absorption model, namely the ZXIPCF model in XSPEC, on top of an underlying power-law continuum model. This produced a very similar improvement in the fit to the single Gaussian absorption line ($\Delta\chi^2 = 15$ for 3 additional degrees of freedom), and also largely modelled the feature at $\sim$ 1.7 keV, using an absorber with a relatively high column of $\sim 8 \times 10^{22}$ cm^{-2} and high covering factor (> 0.83) of moderately ionised material ($\log \xi = 2.2$). Notably, the addition of the partial covering, partially ionised absorber led to a change in the slope of the underlying power-law continuum, with it increasing to a more typical value for a ULX of $\Gamma \sim 1.7$. This therefore appears to be a physically plausible interpretation of the spectral data for this ULX. We summarise the analysis of CXOU J024238.9-000055 in Table 4.5 and Fig. 4.3, and discuss it further in Section 4.4.

4.3.2 The correlation between ULXs and star formation in LIRGs

Whilst a relationship between the presence of ULXs and ongoing star formation is undisputed, the question of whether this relationship is universal, or whether it differs subtly in different environments is an open question, with evidence starting to suggest that differences may occur due to metallicity (see Section 4.1). Indeed, this sample itself presents an interesting puzzle – according to Swartz et al. (2011) we should see 2 ULXs per unit SFR; yet we only see 53 ULXs in a sample of galaxies with a summed SFR of $\sim 260\ M_\odot\ \mathrm{yr}^{-1}$, i.e. 0.2 ULXs per unit SFR, a factor of 10 lower than expected.[15] It is therefore of great interest to examine the relationship between ULXs and star formation in our sample in more detail, and to contrast it with other samples of galaxies.

[15]This is not the result of different SFR estimates – although we use a different method to calculate SFR than Swartz et al. (2011), the summed SFR for our sample calculated using both methods differs by < 2 per cent.

Table 4.6: Blue and FIR LIRG luminosities

Galaxy	$L_{\rm B}$ (10^{42} erg s^{-1})	$L_{\rm FIR}{}^{a}$ (10^{42} erg s^{-1})
NGC 1068	26.8 ± 2.5	159.8 ± 0.3
NGC 1365	30.1 ± 1.9	201.0 ± 1.2
NGC 7552	14.2 ± 1.7	207.7 ± 4.5
NGC 4418	3.3 ± 0.0	205.9 ± 7.3
NGC 4194	10.3 ± 1.2	217.7 ± 5.3
IC 5179	33.1 ± 4.0	302.6 ± 9.5
ESO 420-G013	9.7 ± 0.0	188.0 ± 4.4
Arp 299	36.8 ± 0.0	1436.3 ± 7.2
NGC 838	8.8 ± 0.3	190.7 ± 8.7
NGC 5135	27.4 ± 3.3	318.7 ± 17.7
NGC 5395	39.8 ± 7.3	202.9 ± 8.6^{b}
NGC 5653	23.1 ± 2.8	241.2 ± 12.4
NGC 7771	29.2 ± 1.3	450.4 ± 16.4
NGC 3221	24.4 ± 0.0	199.3 ± 11.1
CGCG 049-057	0.9 ± 0.0	452.5 ± 45.3
IC 860	3.1 ± 0.0	336.4 ± 33.6
NGC 23	39.3 ± 6.2	214.0 ± 12.3
TOTAL	360.4 ± 11.9	5525.2 ± 67.9

Notes. The luminosities are defined as per the text. ^{a}FIR luminosity, corrected for an AGN contribution to the total galaxy luminosity (see text). ^{b}The value may be overestimated for this galaxy because its FIR flux was not spatially resolved from its neighbouring galaxy NGC 5394.

Here two indicators are used to examine the relationship: the blue and far-infrared (FIR) luminosities of the host galaxies ($L_{\rm B}$ and $L_{\rm FIR}$). As reported by Swartz et al. (2009) ULXs tend to reside in regions that have a bluer optical colour than other parts of galaxies; and it was found that the number of ULX per unit blue luminosity is likely to be enhanced in the bluer galaxies (Smith et al., 2012), suggesting a connection between ULXs and recently formed, young stellar populations. Although the blue band luminosity is not a reliable indicator of star formation rate, here we derive it for direct comparison with previous work. The FIR luminosity was selected as a more accurate proxy of the SFR of the galaxies. We explain how we derived these luminosities below, and the values for each individual galaxy are given in Table 4.6.

• ***Host galaxy blue luminosity.*** Here we define $L_{\rm B}$ to be the luminosity of the galaxy in the B filter of the Johnson-Morgan UBV system (Johnson & Morgan, 1953). Most $L_{\rm B}$ values for the LIRGs were converted from B magnitudes corrected for extinction and redshift, which were reported in Third Reference Catalog of Bright Galaxies (RC3 catalogue; de Vaucouleurs et al. 1991). The standard photometric value for conversion was taken from Zombeck (1990). For ESO 420-G013, we calculated $L_{\rm B}$ from the photographic B magnitude reported in the RC3 catalogue. In the case of CGCG 049-057, we took the g-magnitude from SDSS DR9[16] and then converted it to a B magnitude using the method of Windhorst et al. (1991).

• ***Host galaxy FIR luminosity and SFR***. As 10 out of the 17 LIRGs host AGN (see Table 4.1), their total FIR luminosity $L_{\rm FIR}$ (defined as their luminosity between 42.4 and 122.5 μm) will be the summation of FIR luminosity emitted from both the host galaxy and the AGN. Thus simply using the total FIR luminosity risks overestimating the SFR of the galaxies. To correct this issue, we disentangle the FIR luminosity emitted by the AGN from the total FIR luminosity using the method of Mullaney et al. (2011). In brief, *IRAS* flux densities at four individual IR wavelengths (taken from Sanders et al. 2003) were fitted with five different host galaxy models (host galaxy IR emission templates) derived by Mullaney et al. (2011). The best fitting models were used to predict the fraction of AGN emission contributing to the total FIR luminosity, allowing a correction to be made that left the undiluted host galaxy luminosities. Overall, the model predicted a small contribution of AGN emission to the total FIR luminosity ($\sim$ 0 – 7%), except for NGC 1068 in which the AGN emission contributes $\sim$27 per cent of the total FIR luminosity. The FIR luminosities of the galaxies corrected for AGN contribution are shown in Table 4.6.

In addition, to calculate the SFRs, we firstly calculated the IR luminosities in the full 8 – 1000 μm regime ($L_{\rm IR}$), removing AGN contamination as described above. We then used the same calibration as in Lehmer et al. (2010, their Section 2.2) to convert the total $L_{\rm IR}$ to SFR as:

$$\mathrm{SFR}(M_{\odot}\mathrm{yr}^{-1}) = \gamma 9.8 \times 10^{-11} L_{\rm IR}, \tag{4.3.1}$$

[16] `http://skyserver.sdss3.org/dr9/`

where $L_{\rm IR}$ is the infrared luminosity in units of solar bolometric luminosity ($L_{\odot} = 3.9 \times 10^{33}$ erg s^{-1}) and γ is the correction factor accounting for UV emission emerging from unobscured star-forming regions. The value of the latter parameter for each galaxy was estimated following the method described in section 2.2 of Lehmer et al. (2010). The SFR of each galaxy is shown in column 8 of Table 4.1.

Global sample properties

A convenient and simple method to compare between our sample of galaxies and others is to work out the global properties, in terms of number of ULXs ($N_{\rm ULX}$) per unit luminosity in some relevant reference band. Here, we compute this quantity for the blue and FIR luminosities introduced above. In this calculation, we also separate our ULX sample into two sub-samples, those that were detected in the AGN host galaxies and those that were detected in the galaxies without AGN. This is predicated upon the assumption that AGN feedback can affect the SFR of galaxies (see Fabian 2012 and references therein).

The calculated values of the total number of ULXs per unit luminosity are shown in Table 4.7.[17] Firstly, we find no statistical distinction between the number of ULXs per unit luminosity in galaxies with and without AGN – so the incidence of ULXs appears independent of the presence of an AGN. We thus ignored this distinction, and proceeded to compare the global properties of our LIRG sample to other samples of galaxies observed by *Chandra*. These include the complete sample of 'normal' galaxies within 14.5 Mpc from Swartz et al. (2011); a sample of spiral galaxies from Swartz et al. (2004); and samples of both interacting and strongly interacting systems from Smith et al. (2012). We find that the number of ULXs per unit luminosity does depend on the host galaxy type. The ratio $N_{\rm ULX}/L_{\rm B}$ appears heightened in the LIRG sample; it is three times higher (at the $\sim 2.7\sigma$ significance level) in the full LIRG sample than the sample of normal galaxies, with smaller, marginal significance excesses also seen above the spiral ($\sim 1.5\sigma$)

[17] As Arp 299 contributes a significant fraction of the total $L_{\rm FIR}$ ($\sim$ 26 per cent), we have re-calculated these values after excluding this galaxy. We find that the values in Table 4.7 do not change significantly, so Arp 299 does not significantly bias our results.

Table 4.7: Number of ULXs per unit galaxy luminosity

Sample	$N_{\rm ULX}/L_{\rm B}$[a]	$N_{\rm ULX}/L_{\rm FIR}$[b]
All LIRGs	1471^{+447}_{-364}	959^{+290}_{-236}
LIRGs (AGN)	1478^{+420}_{-284}	861^{+242}_{-162}
LIRGs (no AGN)	1459 ± 493	1161 ± 389
Normal galaxies [1]	480 ± 50	5300 ± 500
Spiral galaxies[2]	770 ± 280	6467^{+726}_{-655}
Interacting galaxies[3]	990^{+194}_{-169}	7649^{+1315}_{-1147}
Strongly interacting galaxies[4]	1978^{+660}_{-520}	-

Notes. [a]Number of ULXs per unit galaxy blue luminosity (units of 10^{-46} (erg s^{-1})$^{-1}$). [b]Number of ULXs per unit galaxy FIR luminosity (10^{-47} (erg s^{-1})$^{-1}$). These numbers are reported with a 1σ error. The comparator samples are taken from: [1]Swartz et al. (2011); [2]Swartz et al. (2004); [3,4]Smith et al. (2012). All reference values were calculated and reported by Smith et al. (2012).

and interacting galaxy ($\sim 1.2\sigma$) samples. The differences in the $N_{\rm ULX}/L_{\rm FIR}$ ratio between the LIRGs and other samples are more dramatic, with the LIRGs showing significantly suppressed ULX numbers per unit luminosity, by factors $\sim 5-8$ (all significant at a $> 5.6\sigma$ level). Given that both luminosities are, to first order, related to recent star formation, the fact that the ratios go in different directions compared to the other galaxy samples (i.e. an excess of ULXs compared to blue luminosity; a large deficit compared to FIR) again appears puzzling. We will discuss this further in Section 4.4.

Correlation between ULXs and their host galaxy luminosities

We also investigated whether there was any relationship between $N_{\rm ULX}$ or the cumulative luminosity of the ULXs in each individual galaxy, $L_{\rm ULX}$, and the luminosity of that galaxy in both blue and FIR light. We show scatterplots for all four possible relationships in Fig. 4.4, with the best fitting linear relationship shown. Clearly, a possible relationship exists between $L_{\rm B}$ and both $N_{\rm ULX}$ and $L_{\rm ULX}$, albeit with large scatter; however the ULX population appears not to scale with $L_{\rm FIR}$. We tested this statistically using the Pearson correlation coefficient (r), and find evidence of a pos-

itive correlation for both $N_{\rm ULX}$ and $L_{\rm ULX}$ with $L_{\rm B}$ ($r = 0.74$ and 0.65, respectively – corresponding to significance level of $\gtrsim 99.5\%$); however no evidence for a linear relationship is forthcoming for the possible relationships with $L_{\rm FIR}$ ($r \sim 0$ in both cases).[18]

4.3.3 X-ray luminosity functions

A further means of examining the ULX population of the LIRGs is by constructing their X-ray luminosity function (XLF). We constructed the XLF in both cumulative and differential form for the full sample of 53 ULXs, combining the data for all galaxies.

To obtain the XLF in differential form, we binned the sources into logarithmically spaced luminosity bins, taking into account the correction for incompleteness. Since we use only sources with luminosity above $10^{39}\,{\rm erg\,s^{-1}}$, the latter correction is small (see Table 4.3). We subtracted the expected contribution of background AGNs from each bin, using the $\log N - \log S$ from Georgakakis et al. (2008), based on the sum of the areas within the R_{20} of all the LIRGs.[19] The number of background AGNs in each luminosity bin was computed after having converted the luminosity at the distance of each galaxy into flux. The resulting incompleteness-corrected, AGN-subtracted number of sources was normalised by the sum of the SFR of all the LIRGs.[20] The differential XLF is shown in the top panel of Fig. 4.5. The error bars correspond to 1σ uncertainty using Poisson statistics and accounting for the uncertainty in the number of both ULXs and background AGNs. The combined XLF in cumulative form was constructed by integrating the un-binned differential XLF and is shown in the bottom panel of Fig. 4.5. Interestingly, this highlights that there are no ULXs with luminosities above 10^{40} erg s^{-1} in our sample (see

[18] We confirmed that the result was not biased by the selected range of IR luminosity we used by examining the relationship between the $N_{\rm ULX}$, $L_{\rm ULX}$ and IR luminosity in the full band (8 – 1000 μm). The same result was found: no correlation between $N_{\rm ULX}$, $L_{\rm ULX}$ and the IR luminosity.

[19] In fact, only LIRGs in which the observations are sensitive enough to detected all ULXs in the given luminosity bin should be included in the calculation (see Mineo et al. 2012a); however, the entire sample were included in the calculation since we showed in Table 4.3 that all LIRG observations are very sensitive and so are able to detect more than 90% of ULXs residing in the LIRGs.

[20] See footnote 19.

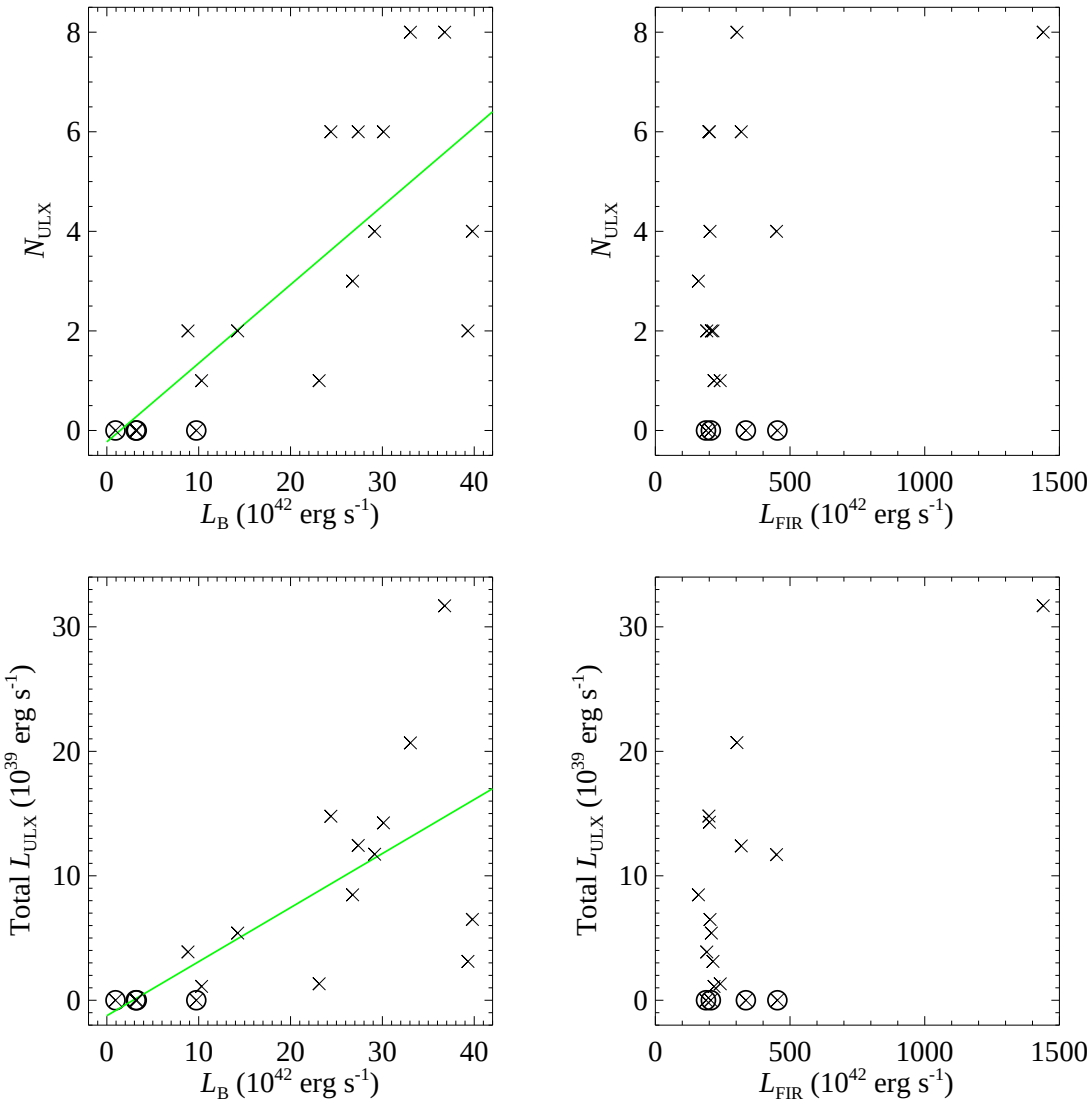

Figure 4.4: Scatterplots showing the ULX population properties against the host galaxy luminosities for the LIRG sample. The panels show: *top left* – number of detected ULXs versus host galaxy blue luminosity; *top right* – number of detected ULXs versus host galaxy FIR luminosity; *bottom left* – summed ULX luminosity versus host galaxy blue luminosity; *bottom right* – summed ULX luminosity versus host galaxy FIR luminosity. The linear best fit is also shown as a solid straight line in the plots in which we found a correlation (see text). The circles highlight the four galaxies in which no ULXs were detected: NGC 4418, ESO 420-G013, CGCG 049-057 and IC 860.

Section 4.4 for further discussion).

Following Mineo et al. (2012a), the fit of the XLF was performed on un-binned data using a maximum-likelihood (ML) method. The predicted contribution of resolved CXB sources was included in the model as described above. We began by fitting the XLF with a pure power-law model, defined as follows:

$$\frac{\mathrm{d}N}{\mathrm{d}L_{39}} = A \times \mathrm{SFR} \times L_{39}^{-\gamma}, \qquad L_{39} \leq L_{cut} \tag{4.3.2}$$

where $L_{39} = L_{\mathrm{X}}/10^{39}$ erg s^{-1}, $L_{\mathrm{cut}} = 10^{42}\,\mathrm{erg\,s^{-1}}$, A is the normalisation. Using this model, we obtained the best-fitting values for the XLF parameters: $\gamma = 1.75 \pm 0.25$ and $A = 0.11 \pm 0.02$ (see Table 4.8). The slope is in agreement with the typical value for star forming galaxies (Grimm et al. 2003; Swartz et al. 2011; Mineo et al. 2012a). However, its normalisation at 10^{39} erg s^{-1} is substantially lower than for these other XLFs, for example it is a factor ~ 5 below the normalisation found by Mineo et al. (2012a).[21] This again points to a relative deficit of ULXs in the LIRG sample.

Next, We fitted the cumulative XLF with a pure power-law model (Equation 4.3.2) using the ML method described above (see Table 4.8 for the fitting result). However, the shape of the cumulative XLF (bottom panel of Fig. 4.5), induced us to search for a possible break by repeating the ML fit, using a broken power-law model:

$$\frac{\mathrm{d}N}{\mathrm{d}L_{39}} = A \times \mathrm{SFR} \times \begin{cases} L_{39}^{-\gamma_1}, & L_{39} < L_b \\ \\ L_b^{\gamma_2-\gamma_1}\, L_{39}^{-\gamma_2}, & L_b \leq L_{39} \leq L_{\mathrm{cut}} \end{cases} \tag{4.3.3}$$

where L_b is the break luminosity. We did not find convergence for a break luminosity, although we explored a very broad range of parameters searching for the ML.

We repeated the fitting procedure described above using alternative statistical

[21] Our SFR estimator assumes a Kroupa (2001) initial mass function (IMF) whereas a Salpeter IMF was used by Mineo et al. (2012a). Using this form of the IMF leads to a corrected value of the normalisation of the Mineo et al. (2012a) XLF of 0.59.

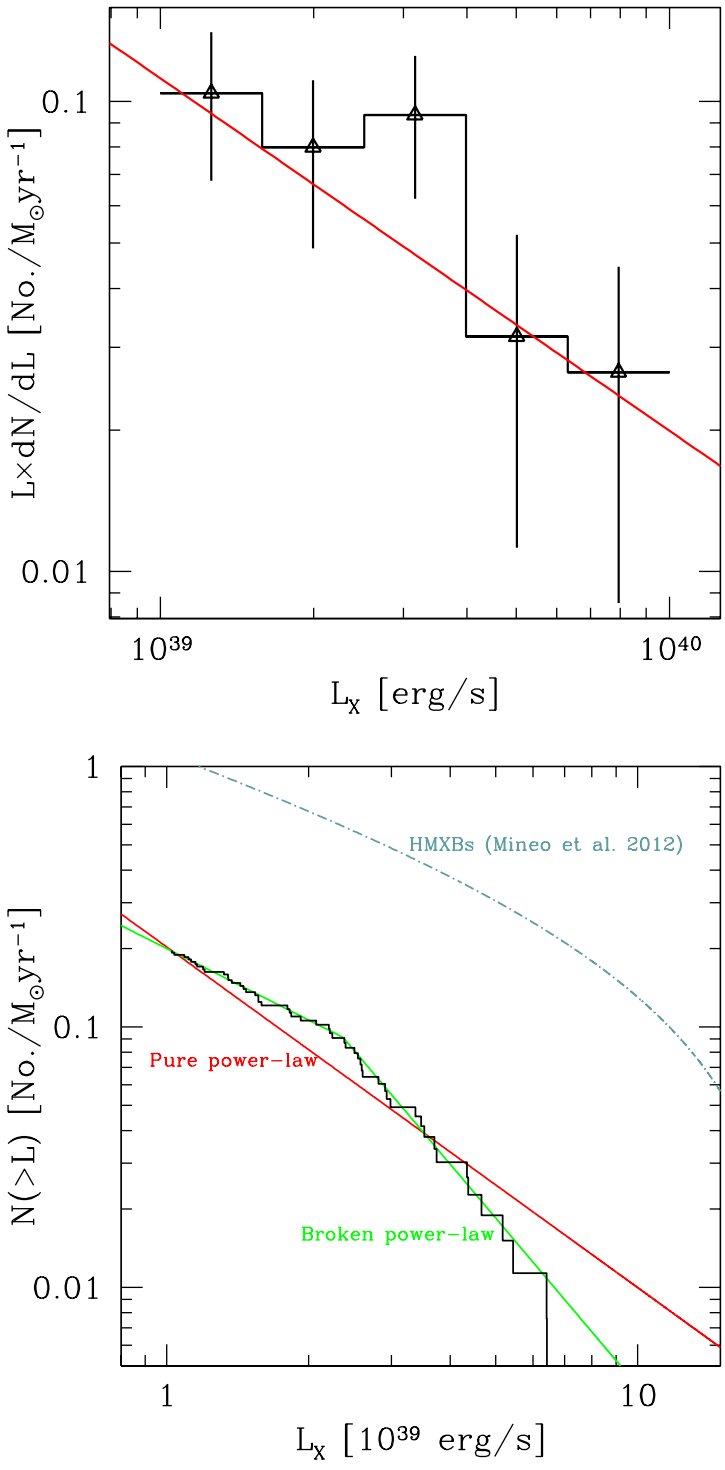

Figure 4.5: SFR normalised XLFs for the 53 ULXs in our sample of LIRGs. *Top panel*: differential XLF. We plot 1σ errors on each data point. The best-fitting pure power-law model obtained from the ML by is overlaid in red. *Bottom panel*: cumulative XLF. The best fitting pure power-law model (similar for ML and C-stat) is plotted in red, while the broken power-law model is in green. For comparison, Mineo et al. (2012a) HMXB XLF is plotted in blue. All luminosities are in the 0.3–10 keV band. See Section 4.3.3 for details.

Table 4.8: X-ray luminosity function: fitting results from maximum likelihood method

XLF form	Pure power-law model	
	γ	A
Differential	1.75 ± 0.25	0.11 ± 0.02
Cumulative	$1.31^{+0.19}_{-0.17}$	0.20

Notes. The best fitting results from the maximum likelihood method. The definitions of the models and their parameters are given in Equations 4.3.2 and 4.3.3, and the text. All best fitting parameter values are reported with 1σ errors.

Table 4.9: X-ray luminosity function: fitting results from Sherpa

XLF form	Pure power-law model			Broken power-law model				
	γ	A	Stat./$d.o.f.^a$	γ_1	γ_2	A	$L_{\rm b}$	Stat./$d.o.f.^a$
Differential	$1.84^{+0.31}_{-0.27}$	$0.15^{+0.05}_{-0.04}$	1.64/3	-	-	-	-	-
Cumulative	1.29 ± 0.06	0.20	25.05/50	$0.91^{+0.13}_{-0.14}$	$2.14^{+0.29}_{-0.24}$	0.28	$2.37^{+0.36}_{-0.23}$	3.38/48

Notes. The best fitting results from SHERPA. The definitions of the models and their parameters are given in Equations 4.3.2 and 4.3.3, and the text. The broken power-law model was fitted to the cumulative XLF only. [a]Value of minimised statistic/degrees of freedom; we use the χ^2 statistic (*chi2gehrels*) to fit the differential XLF, and the Cash statistic (*cstat*: Cash 1979) to fit the cumulative XLF. All best fitting parameter values are reported with 1σ errors.

methods provided by SHERPA package version 4.4.[22] We first analysed the cumulative XLF. Given the un-binned nature of the cumulative data, we assumed that the distribution of the data are consistent with Poisson statistics. Then a ML analysis was performed on these Poisson data to optimise the goodness of fit and find the best model fitting parameters; this used the *cstat* function (Cash, 1979) in SHERPA. We note that *cstat* is different from the ML method described above in that the *cstat* performed the ML analysis using a Poisson distribution function and assuming Poisson statistics for the data, whilst the earlier analysis performed the ML method on the XLF distribution functions (i.e. pure power-law and broken power-law functions). The fitting results are shown in Table 4.9. In this case, the broken power-law model provided an estimate for the break luminosity, $L_{\rm b} = 2.37 \times 10^{39}$ erg s^{-1}, with a substantial improvement to the fit compared to the pure power-law model (ΔC-stat of 22 for 2 additional degrees of freedom). It also appears to better describe the data by eye. However, the pure power-law model provided a statistically good fit to the data too, therefore we cannot reject one model in favour of the other.

The apparent statistical improvement of the broken power-law model over the pure power-law model might imply that the broken power-law model was substantially over-fitting the function, with this plausibly being due the low number of ULXs in the sample leading to large uncertainty in each data point. This is the likely explanation for the ML procedure for a broken power-law model not converging as the large uncertainty would lead to an insignificant statistical difference between the two models. Moreover, none of the more extensive population studies of the last decade (Grimm et al. 2003; Swartz et al. 2011; Mineo et al. 2012a) reported on features at a similar luminosity. Even if the break is present, another possibility is that a feature resembling a break may be artificially caused by the considerable ($\sigma/\langle N(>L)\rangle \sim 1.7$) dispersion in the normalisation of the individual XLFs, which is comparable with that observed by Mineo et al. (2012a) at the same luminosity threshold ($\sigma/\langle N(>L)\rangle \sim 1.5$, see discussion in Section 7.1 of Mineo et al. 2012a).

[22] `http://cxc.harvard.edu/sherpa4.4/`

A second means of artificially inducing a break could be by over-estimating the completeness of the sample, i.e. incompleteness could act to turn down the XLF slope at lower luminosities if we have not accounted for it properly (see the discussion in Section 3 of Fabbiano 2006). However, this is eminently testable in our data as several of our galaxies are complete well below the putative break (cf. Table 4.3); hence the number of sources above and below the break in these galaxies can be compared to the numbers in the galaxies with sensitivity limits closer to the break luminosity. We find that 6/11 ULXs are below the putative break in the five nearest host galaxies (NGC 1068, NGC 1365, NGC 7552, NGC 4418 & NGC 4194); this compares to 21/42 in the more distant LIRGs. Given the small numbers of objects involved these numbers appear consistent, hence there is no reason to suspect that incompleteness is inducing the putative break feature. If the break is a real feature intrinsic to the ULX population, it immediately becomes very interesting as the steepening of the XLF slope above L_b may suggest that much of the deficit in ULXs is originating above this putative break. We will further discuss the possible physical explanation of the very putative break in Section 4.4.2.

As a check, we also used SHERPA to fit the differential XLF. In this case we had to assume χ^2 statistics (*chi2gehrels*) and fit the binned differential XLF. This is, strictly speaking, not appropriate for the number of sources per luminosity bin. The reduced fitting statistic is substantially below unity, primarily as a consequence of the small number of bins. However, we note that the best-fitting parameters for the two forms of the XLF obtained with the procedure described above for a pure power-law model (Table 4.9), are in full agreement with those provided by the ML fitting (Table 4.8).

4.4 Discussion

4.4.1 X-ray spectral results

In Section 4.3.1, we presented an analysis of the stacked spectra for three groups of ULXs, segregated by their observed luminosity. The analysis of stacked spectra is notoriously difficult to interpret, as summing spectra that may have a variety

of underlying levels of absorption and intrinsic forms may not necessarily reveal anything about the population of sources contributing to the stack. However, in the case of the stacked spectra we create, we see one remarkable result; the stacked spectrum of the sources below $\sim 2 \times 10^{39}$ erg s^{-1} appears markedly different to the stacked spectra of the two more luminous groups. Both the power-law continuum fit and MCD model fit show that the lowest luminosity spectrum is significantly softer than that in the two more luminous groups, which are statistically indistinguishable from each other.

Further interpretation is difficult due to the uncertainty in the absorption column, which may vary substantially for the individual ULXs given that LIRGs are known to contain substantial quantities of cold, neutral gas (Mirabel & Sanders, 1988). This would work to distort any underlying spectrum – for example, if the average spectrum was heavily absorbed, just a handful of non-representative, low absorption sources would 'fill-in' the soft end of the spectrum and lead to a relatively low column being measured. Indeed, this may be part of the reason for the columns on the MCD fits being consistent with zero, although they are substantially higher than the enforced Galactic foreground upper limit for the sample of $< 5 \times 10^{20}$ cm^{-2} in the power-law fit. We therefore do not directly interpret the power-law slopes or disc temperatures in light of Galactic binaries and/or other ULXs. We do note, however, that previous analyses have suggested transitions in ULX spectra at similar luminosities. Both Gladstone & Roberts (2009) and Yoshida et al. (2010) examine ULXs in the interacting galaxies NGC 4485/90 (and also M51 in the latter paper), and note a change from power-law-like spectra dominating, to more disc-like spectra at $\sim 2 - 3 \times 10^{39}$ erg s^{-1}, that they also reconcile with the objects becoming substantially super-Eddington beyond that luminosity. Furthermore, the detailed ULX spectroscopy of Gladstone et al. (2009) and follow-up work by Sutton et al. (2013b) show that below $\sim 3 \times 10^{39}$ erg s^{-1} most ULXs have disc-like spectra in the wider *XMM-Newton* bandpass; above this luminosity their spectra resolve into two components, with roughly equal numbers dominated by either the hard or soft component. This is again interpreted as a transition from an $\sim$ Eddington rate phase, to a super-Eddington state. Based on their work we can speculate why our

stacked spectra may harden at higher luminosities – if there is substantial absorption present in the LIRGs, it will act to extinguish the signal from the soft ULXs more efficiently than the harder objects. A salient example of this effect is the extreme ULX in NGC 5907, where a high foreground column may hide a large soft contribution to its spectrum (Sutton et al. 2013a). This would therefore preferentially hide the softer ULXs at high luminosities, leaving only the hard spectrum objects to contribute to the stacked spectrum.

One object in our sample had sufficient counts in its *Chandra* X-ray spectrum for us to analyse it separately. We found the spectrum of CXOU J024238.9-000055 to be very hard, with a power-law of photon index $\Gamma = 0.75 \pm 0.1$ providing an acceptable fit to the data. This result is consistent with previous studies, which also found that the photon index is very hard (Smith & Wilson, 2003; Swartz et al., 2004; Berghea et al., 2008). Indeed, the photon index seems to be extremely hard for ULX spectra (Swartz et al., 2004), but instead may be consistent with the X-ray spectral properties of background AGN. Obviously, in order to distinguish between these two possibilities, the optical counterpart to the X-ray source needs to be identified by further optical observations. However, if the source is a genuine ULX residing in the host galaxy NGC 1068, an interesting interpretation is obtained. Smith & Wilson (2003) interpret the hard spectrum of this ULX as inverse Compton scattering of synchrotron emission in a jet. However, they also noted the presence of a broad feature that dips below the continuum level at ~ 1.7 keV, and suggest that this may be a spurious feature resulting from an artefact in the gain table of the *Chandra* ACIS-S instrument. We have re-analysed the data with the latest *Chandra* calibration database that includes corrections for such features[23], but still find the feature to be present. We therefore characterised it using a single Gaussian absorption line; this produced a good fit to the data, but produced a broad (~ 80 eV width) line centred at 1.68 keV, that we struggle to attribute to any single physical absorption feature.

We therefore considered an alternative solution – that the feature is the result

[23]In a correspondence with the *Chandra* X-ray centre help desk we were informed that this issue was corrected for in calibration database (CALDB) versions 3.0.0 and later.

of absorption in a range of partially covering, partly-ionised material (a 'warm' absorber model). Interestingly, a similar model was suggested as a way of producing the apparent two-component *XMM-Newton* spectra of ULXs by Gonçalves & Soria (2006), and was also used to describe the spectrum of a ULX in NGC 1365 by Soria et al. (2007). In the latter paper they propose that the ionising material may be in an outflow, with its origins in the formation and subsequent ejection of a Comptonising region above the inner accretion disc. Interestingly, the best fitting parameters from Soria et al. (2007) – $N_{\rm H}, \Gamma, \xi$ – broadly agree with our best fitting parameters. Our value of ionisation parameter $\xi \approx 158 \pm 87$ for CXOU J024238.9-000055 corresponds to the ionised material being located at a distance $R < L/(\xi N_{\rm H})$, which for the ionising luminosity (i.e. intrinsic $L_{\rm X}$ extrapolated from the model fit between 13.6 eV and 20 keV) gives a maximum radius for the material of 3.5×10^{15} cm ($= 2.3 \times 10^{9} R_{\rm g}$ where the gravitational radius $R_{\rm g} = GM_{\rm BH}/c^2 = 15$ km for a $10 M_{\odot}$ black hole). Clearly this is located in the proximity of the ULX, but not close to the inner regions of the disc, consistent with material that has been ejected from the system in some sort of outflow. We note that a massive, likely highly ionised outflow is a prediction of super-Eddington models (e.g. Poutanen et al. 2007); evidence has recently been sought for it by looking for partially ionised Fe-K lines in spectrally hard ULXs (e.g. Walton et al. 2012, 2013a), with little success. However, signatures of partial ionisation may be preferentially located in the softer part of the X-ray spectrum (Middleton et al., 2014), that is easier to see in objects that are wind-dominated – here we may be seeing precisely that.

4.4.2 Why is there a deficit of ULXs in LIRGs?

In this chapter we have presented evidence for a significant deficit in the number of ULXs detected in this sample of LIRGs, compared to the expectation based on the relationship between the number of ULXs and the SFR in nearby galaxies. This manifests itself both in the raw numbers – we expect to detect ~ 500 ULXs in this sample if it follows the number of ULXs per unit SFR relation of Swartz et al. (2011), compared to just 53 detections – and in the characteristics of the XLFs we construct from our detections. In the latter, the normalisation of the differential XLF is a

factor of ~ 5 lower at 10^{39} erg s^{-1} than the most complete previous analysis of the HMXB XLF (Mineo et al. 2012a), and although the differential slope is consistent within errors with previous work the cumulative form has a slope that is steeper than that found for most star forming systems (c.f. Fabbiano 2006 and references therein), implying fewer sources are present at high luminosities. This steep slope may be the result of a break in the XLF at $\sim 2 \times 10^{39}$ erg s^{-1}; at energies below the break we see a slope similar to that in star forming galaxies ($\gamma_1 \approx 0.9$). If this shallow slope were extrapolated to luminosities above 10^{40} erg s^{-1} we would expect to see ~ 7 ULXs in that regime; instead we see none. In this section, the possible explanations for the deficit will be discussed.

A real deficit or observational effects?

A pertinent question we must therefore ask about the presence of this deficit is simply: why? A first consideration is whether we really detect all the ULXs that are bright in the 0.3–10 keV regime in the host galaxies. In this regard we are certainly using the best instrument available for this study; the exquisite sub-arcsecond spatial resolution of *Chandra* is unparalleled in this respect, allowing us by far the clearest X-ray view of these regions, and minimising any source confusion. We cannot completely avoid this - for example, the nucleus of M82 hosts at least two extreme ULXs (e.g. Feng & Kaaret 2007), that we would not resolve if placed at the distance of our furthest LIRGs. However, we will miss very few ULXs ($\lesssim$10%) due to sensitivity issues in these galaxies (see the completeness analysis in Section 4.2.2), with the sample essentially complete in terms of sensitivity to ULX detection.

But while we may have sufficient sensitivity to detect ULXs over the projected area of the galaxies, this could be compromised locally by extended diffuse X-ray emission. In particular, the extended source detections that we reject from our point source detection analysis might physically comprise a mixture of extended and faint point-like X-ray emitters, and so could hide ULXs that otherwise would have been detected. To determine whether this has a large influence on our sample we consider that the diffuse emission is likely to be spectrally soft in star formation (SF)-dominated galaxies, and so dominant only below 2 keV (cf. Pietsch et al.

2001; Franceschini et al. 2003; Jenkins et al. 2004; Mineo et al. 2012b); hence the hidden ULXs would be visible as point-like sources at higher energies (above 2 keV). However, we face the problem that we do not have high photon statistics in this regime, and our sensitivity is relatively poor. In fact, the best way to proceed is to re-visit our initial source lists for each galaxy where we already have a complete record of the detectable objects above 2 keV as our hard band detections. We therefore determined which of the hard band detections did not make it into our final source catalogue, and investigated why.

In total, there are 17 objects that have full band luminosities in excess of the ULX threshold of 10^{39} erg s^{-1} which are detected as hard band sources but do not make the final source list. For each of these objects we revisited their hard band data and ran the SRCEXTENT algorithm to determine whether they appeared point-like or extended, although we caution that in several cases the photon statistics were limited and so the results may not be conclusive. We found that a total of four sources were spatially extended above 2 keV; the remaining 13 were consistent with point-like objects. However, nine of these point-like objects were located with 5 arcseconds of the nuclear position of their host galaxy and so are rejected from consideration. Of the four remaining objects, two that lie in Arp 299 are questionable ULX detections as they are coincident with plausible contaminants in the host galaxy (a supernova remnant, and the secondary nucleus in this merging system). Hence only two plausible ULX candidates remain, one each in NGC 1068 and Arp 299. Both objects were originally rejected as extended full band sources, but are resolved to be point-like sources in the hard band. Given that we can only do this for two objects, this indicates that we are not missing a significant population of ULXs by rejecting extended sources.

Although the nuclei of the galaxies cover a relatively small region of their surface area, we may miss a proportion of the ULX population by excluding this region – see Lehmer et al. (2013) for an example that would be excluded from the nearby starburst galaxy NGC 253. This is particularly pertinent as the star formation in LIRGs can be very centrally peaked, so by excluding the nucleus we may be rejecting a region containing a large fraction of the galaxy's star formation, and so

a proportional number of ULXs. There will, however, be observational difficulties with detecting such a population – as Fig. 4.1 shows, the central regions tend to have far higher surface brightness in X-rays and possible spatial complexity compared to the outer regions. But, given the high spatial resolution of the *Chandra* telescope mirrors (0.5 arcsecond on-axis resolution), we should have the imaging power to resolve the nuclear region of each galaxy, and detect the brightest point-like sources if they are abundant in that region. Yet, we only find three examples of galaxies with more than a single source detection in the nuclear region, and in one of these objects (in NGC 1365) the source furthest from the nuclear position is relatively faint ($\sim 10^{38}$ erg s^{-1}). Conversely, 15 out of 17 galaxies have at least one source detection (in two cases – NGC 4418 and NGC 5653 – there are two detections) in the nuclear region with a luminosity in the ULX regime, although seven of these are spatially extended sources in the full band (of which five are resolved to point sources above 2 keV). Eight of these are galaxies with a suspected/confirmed AGN[24]; and although we detect a source in each galaxy that we regard as lacking an AGN based on previous evidence, we cannot reject an AGN nature for any of these objects without further observations and detailed analyses that are beyond the scope of this chapter. Thus, the situation is unclear on how many of these detections could be *bona fide* ULXs in the nuclear region. However, the total number of detected ULXs in the nuclear regions appears significantly smaller (< 17, likely half that amount given the evidence for AGN) than the numbers of ULXs detected outside the nuclei. So the deficit of ULXs seems to appear significantly worse in the central regions of the galaxies, albeit with some caveats about the difficulty of observing in that region.

To investigate this further we examined the total flux within each 5 arcsecond radius nuclear region, excluding the flux from the detected point sources, in order to place an upper limit on the possible residual flux from ULXs hidden within the diffuse emission. This analysis was only performed for the seven galaxies in which

[24]Interestingly, the two galaxies without a point source detection in their nucleus – ESO 420-G013 and IC 860 – have some evidence for the presence of an AGN; looking at Fig. 4.1 they do have X-ray emission in their nucleus that presumably was too extended for the WAVDETECT algorithm.

we have no multi-wavelength evidence for the presence of an AGN, to avoid any complex spatially extended emission that could be related to such an object. For three galaxies – NGC 7552, NGC 838 and NGC 23 – there are a sufficient number of counts ($\gtrsim 300$) to extract a spectrum of the emission within the 5 arcsecond nuclear region. The spectra were fitted with a two component model comprising an optically thin thermal plasma (MEKAL in XSPEC) plus a power-law continuum, both subject to the same absorption column. The first component can be used to represent the diffuse emission from the active star forming region, whilst the latter represents the integrated emission from X-ray binary systems in the region. Both NGC 7552 and NGC 23 displayed similar residual nuclear spectra, with moderate absorption ($5-20\times10^{20}$ cm^{-2}) and similar plasma temperatures and power-law photon indexes ($kT \sim 0.6-0.7$ keV; $\Gamma \sim 2$), whereas NGC 838 appeared somewhat more absorbed, with a cooler diffuse component ($N_{\rm H} \sim 7\times10^{21}$ cm^{-2}; $kT \sim 0.15$ keV; $\Gamma \sim 2.5$). We estimated the observed flux from X-ray binaries in each galaxy nucleus from the power-law component in each object. In order to do the same for the galaxies with too few counts for spectral analysis, we extracted the total residual count rates in the nuclear region of each galaxy, and then applied a factor of 0.5 multiplier to each total to account for only $\sim$ 50 per cent of counts originating in the X-ray binary population of each galaxy (which was estimated from the fitted spectra). We then converted these counts to fluxes using a typical ULX-like spectrum, consistent with the power-law continua seen in the three bright galactic nuclei ($N_{\rm H} \sim 1.5\times10^{21}$ cm^{-2}, $\Gamma \sim 2$). The estimated observed luminosities in the power-law component for each galaxy are shown in Table 10.

Assuming that the luminosity distribution of X-ray binary systems in the nuclear region of the LIRGs follows the Mineo et al. (2012a) XLF, we converted the power-law luminosity into a number of ULXs using that XLF. In each case we worked out the normalisation required to give the integrated luminosity by integrating under the XLF in the 10^{37} – 10^{40} erg s^{-1} range, and then using this to calculate the number of ULXs present, that we show in Table 10. A strict upper limit would simply assume that each ULX has a luminosity of 10^{39} erg s^{-1}; however a population of ULXs should have a range of luminosities, and integrating under the XLF accounts for

Table 4.10: Upper limits on the number of ULXs hidden within the diffuse component of each galaxy nucleus without evidence for an AGN

Galaxy	$L_{\rm PL}$ [a] (10^{39} erg s^{-1})	$N_{\rm ULX,hid}$ [b]	$(f_{\rm nuc}/f_{\rm gal})_{\rm IR}$ [c]
NGC 7552	18	3.8	0.2
IC 5179	7.1	1.5	0.17
NGC 838	30	6.5	0.49
NGC 5653	7.9	1.7	0.2
NGC 3221	2.2	< 1	0.08
CGCG 049-057	1.3	< 1	0.81
NGC 23	33	7.2	0.45

Notes. [a] Total observed luminosity estimate for the hard power-law component in each galaxy nucleus. [b] Estimated upper limit on the number of ULXs hidden within the diffuse emission in this region (see text for details). [c] Fraction of the total 8 μm flux from each galaxy residing in the nucleus.

this. What this method does not account for is that the brightest objects should still be detected as point sources, even within bright diffuse emission, by *Chandra*; but as we saw above the number of such objects detected within the nuclear regions is small. Given that these nuclei are likely to be far more complex than our simple modelling allows for, and may contain additional components that contaminate the hard band (e.g. hard diffuse emission, extended reflection nebulae from an unseen AGN), we consider our $N_{\rm ULX,hid}$ estimate as a reasonable upper limit on the number of ULXs that may be hidden within these nuclei. In total we may have up to ~ 21 ULXs hidden within these galaxies, or ~ 3 per nucleus. Over the whole sample this would extrapolate to ~ 50 ULXs, or a rough doubling of our ULX numbers, and hence an increase in ULX incidence to 0.4 ULX per unit SFR.

As an independent check of the effect of excluding the nuclear region, we estimated the fraction of the global star formation we are excluding for each galaxy. We used the FIR emission as mapped by 8 μm *Spitzer* images[25] as a proxy for the SFR, and in each case we corrected for the contribution of an old stellar population to the 8 μm flux using the 3.6 μm images and Equation 1 of Calzetti et al. (2007). Then, we took the ratio between the SFR in the central 5 arcsecond nuclear region and

[25] `http://sha.ipac.caltech.edu/applications/Spitzer/SHA/`

that of the rest of the galaxy (out to the R_{20} ellipse), again for the seven galaxies with no evidence for an AGN. We found that the nuclear region contribution to the total SFR, $(f_{\rm nuc}/f_{\rm gal})_{\rm IR}$, varied widely, between $\sim 8-80$ per cent in the AGN-less galaxies (see Table 10). However, there was only one case in which it exceeded 50 per cent, so if we take this as the upper limit on the coarse average contribution from the nuclear region and apply that as a correction to the regions outside the nucleus across the whole sample, then we can set an upper limit on our global incidence of ULXs in the LIRG sample of 0.4 ULXs per unit SFR. Interestingly this upper limit coincidences with the result from the flux analysis demonstrated above.

However, despite the suggested rise in ULX numbers from the upper limits place on the nuclear regions, if we combine the observational effects described above, it is very implausible that they will result in a factor of 10 increase in ULX detections. We therefore regard the deficit as a real effect, and consider physical origins for it.

Possible explanations for the deficit

So, what is the physical origin of the deficit of ULXs in the LIRGs? Firstly, we would not expect that all ULXs come from young stellar populations. There are ULXs seen in elliptical galaxies that must be related to their LMXB populations, and we should expect all galaxies with old stellar populations to possess a similar underlying population of LMXBs that scales with the mass of the system (Colbert et al., 2004; Lehmer et al., 2010). This is not accounted for by Swartz et al. (2011); their number of ULXs per SFR that we base our deficit deduction on will contain ULXs from both populations. However, this cannot lead to the deficit of ULXs in the LIRGs, for the simple reason that our LIRG sample contains $\sim$ 4 times more mass than the combined mass of the nearby galaxies in Swartz et al. (2011), at $\sim 1.3\times10^{13}M_{\odot}$ versus $\sim 3.5\times10^{12}M_{\odot}$[26]; thus we would expect our sample to possess more LMXB ULXs, that would act to increase the number of ULXs per SFR. In fact, using the estimate of Feng & Soria (2011) and making a conservative (factor 2) correction for the high background contamination in the elliptical sample of Walton

[26]The total mass of the LIRGs was taken from table 1 of Lehmer et al. (2010).

et al. (2011) we might expect 0.5 LMXB ULXs per $10^{11} M_{\odot}$ of galaxy mass. We would then expect that less than one fifth of the Swartz et al. (2011) ULXs (~ 17) are LMXBs; however we would expect more LMXB ULXs in our sample (~ 65) than we observe ULXs in total. Given the high SFR that accompanies the high mass of our sample systems, this serves to emphasise that a real deficit in ULXs is present in the LIRG sample.

Could this deficit be due to some factor inhibiting the formation of ULXs in the environment of the LIRGs? An obvious property that might suppress the formation of ULXs, given recent studies (e.g. Mapelli et al. 2011; Prestwich et al. 2013; Basu-Zych et al. 2013a, 2013b; Brorby et al. 2014), could be the relatively high metallicity of the LIRGs. A good comparator sample for the LIRGs in this respect is the high metallicity galaxies sample of Prestwich et al. (2013), that was demonstrated to show a much lower incidence of ULXs per unit SFR than a sample of extremely metal poor galaxies. A comparison of our Table 4.1 and table 9 of that paper shows that (where available) both samples have a very similar spread of metallicity; and indeed Table 10 of Prestwich et al. (2013) quotes a $N_{\rm ULX}$ per SFR of 0.17 ± 0.042 per $M_{\odot}$ yr^{-1}, identical within errors to our value of 0.2 ± 0.05 per $M_{\odot}$ yr^{-1}. However, Prestwich et al. (2013) used a different method to calculate SFR (Calzetti et al. 2010, based on the Hα and 24 μm fluxes); when we use our SFR calculation method on their sample of galaxies we find that the SFR drops by a factor ~ 6 to a total of 16.77 $M_{\odot}$ yr^{-1} across the whole sample.[27] Hence the number of ULXs per SFR for this sample increases dramatically, up to 1.04 ± 0.26 per $M_{\odot}$ yr^{-1}; notably this is lower than the average relation in nearby galaxies, but it is again significantly higher than the number of ULXs per SFR in the LIRGs (and is also significantly higher than the upper limits accounting for the excluded nuclear regions derived above). Given that our LIRGs have high metallicity similar to that of the high metallicity galaxies sample of Prestwich et al. (2013), we might presume the same level of ULX suppression by metallicity effect in our LIRG sam-

[27]There were no *IRAS* data available for NGC 4625 in the high metallicity sample; we retained the estimate used by Prestwich et al. (2013), but note that this will not adversely affect the results as it had the smallest estimate of SFR in the sample at 0.22 $M_{\odot}$ yr^{-1}.

ple. However, we caution that one caveat here is that the metallicities reported in Table 4.1 were calculated from different calibrations (see references in the table); it was demonstrated by Kewley & Ellison (2008) that the systematic difference in the value of metallicity (i.e. $\Delta[\log(\mathrm{O/H})]$) due to the choices of calibration can be up to 0.7 dex; indeed, further systematic measurements of metallicity, that supersede the current disparate methods, are required to confirm that the samples do overlap in metallicity. However, although, we take this uncertainty into the account, it is unlikely that our LIRG sample will turn out to be metal poor galaxies; in fact, the values still lie within the regime of metal rich galaxies (with some marginally high metallicity galaxies). Hence, given that the LIRG have high metallicity similar to that of Prestwich et al. (2013) sample, we conclude that the relatively high metallicity of the LIRGs appears insufficient reason on its own to explain their deficit in ULXs.

One reason for suspecting that metallicity affects the incidence of ULXs is the possibility that larger black holes (the MsBH class, with masses between 20 and $100 M_{\odot}$) might form in low metallicity regions. Conversely, very few such objects should be seen in higher metallicity regions. If such objects, accreting at $\sim$ Eddington, constitute a large proportion of ULXs up to the HMXB XLF break, then an interesting consequence should be that the XLF break shifts to lower luminosities in high metallicity environments. This is precisely what is suggested by the very putative break in the cumulative XLF, with the break apparently shifting down by a decade in luminosity to the Eddington limit for an $\sim$16 $M_{\odot}$ black hole, compared to the break found in the Mineo et al. (2012a) XLF. The lack of ULXs with luminosities above 10^{40} erg s^{-1} certainly appears consistent with this scenario. In addition, this result is supported by the spectral changes seen in this sample, with the change in spectral form either side of the same luminosity as the putative XLF break suggesting the transition between stellar-mass black holes accreting at $\sim$ Eddington, and those at super-Eddington rates. However, this is not supported by wider spectral studies that see a similar pattern in ULXs located in all galaxy types (Gladstone et al. 2009; Sutton et al. 2013b) – if a large proportion of ULXs were $\sim$ Eddington accretion onto MsBHs, we would see the disc-like spectra reported

by Gladstone et al. (2009) extend up to the XLF break in many sources, but they instead are mainly seen below 3×10^{39} erg s^{-1}, seemingly ruling this out. One interesting scenario remains, though – the factor of 10 drop in the XLF break luminosity could still be due to a drop in the mass of the compact objects, if the objects below the break are predominantly super-Eddington neutron stars, that reach maximal super-Eddington luminosities at the putative XLF break. This might be the case if the high metallicities impede the formation of all black holes, not just MsBHs, and the change in spectrum might then be the difference between the super-Eddington neutron stars and an underlying population of black holes. Clearly this is highly speculative, and requires a great deal of improvement in data quality in order to investigate this hypothesis. Firstly, we need to confirm the presence of the break; then we need to identify the source populations either side of it. This will almost certainly require next generation X-ray observatories that can begin to disentangle black holes and neutron stars at large distances based on their observational characteristics.

The next possibility we consider that might cause the deficit of ULXs is whether the stellar populations of the LIRGs are too young to allow a population of ULXs to form. As ULXs are composed of a compact object accreting material from a stellar companion, they will require time to evolve from an initial massive stellar binary system. This inevitably introduces a lag between the start of star formation in a system, and the appearance of ULXs. According to Linden et al. (2010), the number of ULXs formed in solar metallicity environments peaks at $\sim$4 – 5 Myr after the beginning of star formation, and a lag of up to $\sim$ 10 Myr is required to see the peak for ULX populations formed in a sub-solar metallicity medium. These ages are consistent with the resolved stellar population ages around two nearby ULXs, that are of the order of $\lesssim$ 20 Myr (Grisé et al. 2008; Grisé et al. 2011). So the critical question is: how long is it since the star formation began in the LIRGs? Older studies, based on the correlation between the Bracket-γ and far-infrared emission, estimates star formation ages in LIRGs at between 10 – 1000 Myr (Goldader et al., 1997). However, later work based on the spectral energy distributions of LIRGs and ULIRGs (ultraluminous infrared galaxies) from near IR to radio wavelengths

suggests star formation timescale of $\sim$5 – 100 Myr (Vega et al. 2008; see also Clemens et al. 2010). In fact, the star formation ages of a few individual LIRGs have been reported in previous works: for example, 57 Myr for Arp 299 (Vega et al., 2008; Clemens et al., 2010), and 30 Myr for both NGC 7552 and NGC 4194 (Takagi et al., 1999). Thus it seems unlikely that the LIRGs are too young for their populations of ULXs to switch on.

However, the age calculations above assume a single age for the newly-formed stellar population. This might not be a good assumption because the star formation activity is unlikely to be uniform throughout the galaxies (see e.g. Mineo et al. 2013); it is possible that star formation may have begun more recently in some regions in the galaxies than in other areas. For example, the spatial study of NGC 5135 by Bedregal et al. (2009) suggests that the most recent star forming areas in the galaxy could be $\sim$0.5 – 1 Myr younger than other regions. Moreover, they also suggest that NGC 5135 might host two recently-formed stellar populations with different ages: a new population that formed $\sim$6 – 8 Myr ago, and a second, older stellar population of $\gtrsim$200 Myr age. Thus simply assuming the same stellar age along the whole galaxy might not reflect the real history of star formation in LIRGs. However, even bearing these caveats in mind, we would realistically require the vast majority of the star formation in the LIRGs to have started within the last 5 Myr for the populations of ULXs to be significantly suppressed; given the ages quoted above this is very unlikely. Therefore, while this effect may have some influence in the LIRG sample, we regard it as unlikely to be the major factor in the ULX deficit.

So, if the deficit of ULXs in LIRGs is unlikely to be caused by metallicity effects or a very young stellar population, then is there another possibility that may act to reduce the number of detected ULXs? The answer is potentially revealed in the global $N_{\rm ULX}$ - luminosity relations discussed in Section 4.3.2. In particular, Smith et al. (2012) find similar ratios in a sample of interacting galaxies taken from the Arp catalogue – they find an enhancement in the $N_{\rm ULX}/L_{\rm B}$ compared to normal galaxy samples, but in their most IR luminous objects they find the $N_{\rm ULX}/L_{\rm FIR}$ ratio significantly suppressed. They suggest two reasons for this: either the FIR luminosity is significantly enhanced by nuclear activity; or the large columns of gas

and dust in these objects are obscuring a large fraction of the ULX population. In this chapter we have explicitly removed possible AGN contamination from the FIR fluxes using the method of Mullaney et al. (2011), and then shown that these ratios are the same for LIRGs that both host and do not host AGN; hence we rule out the first scenario. We therefore favour the second explanation – that the suppressed $N_{\rm ULX}/L_{\rm FIR}$ ratio in LIRGs could be a result of missing many ULXs due to their signal being extinguished by the high absorption columns in these galaxies due to dust attenuation. Indeed, Lehmer et al. (2010) suggested that an apparent lack of luminosity in X-rays present in the LIRGs, compared to expectation, might be due to dust obscuration. Furthermore, such an effect is seen also in normal star-forming galaxies (Fig. 11 of Mineo et al. 2012a) as well as in the sample of Local Lyman Break Galaxy Analogues which is shown in the left panel of Fig. 7 of Basu-Zych et al. (2013b). Indeed, that is also consistent with the other relationships we see – both X-rays and blue light relate to young stellar populations, so explaining the proportionality relationship between the two; but the unusually high number of ULXs per blue luminosity in these galaxies is plausibly due to a faster loss of blue light than X-rays in the absorbing material.

Hence we have a plausible explanation for the overall deficit of ULXs per SFR in the LIRG sample; we do not see most of them because they are hidden behind the material fuelling the high SFR in these objects. But is this consistent with the columns of material we expect in LIRGs? We can quantify the column densities required to support this scenario by examining how the detectability of sources with *Chandra* depends on their intrinsic spectrum, their observed luminosity, their distance and the intervening columns. If we assume 20 ks exposures (typical for our sample), and a power-law form for our spectra, then we can use WEBPIMMS to calculate the dependence of the detected counts on absorption column and distance to the ULXs, which we show in Fig. 4.6. Taking a minimum detectability threshold of six counts (cf. Table B.1) demonstrates that the effective extinction of the ULXs strongly depends on distance to the host galaxies. In the nearest system (NGC 1068, at 14 Mpc) a faint ULX (at 10^{39} erg s^{-1}) would be fully extinguished by a column of $\sim 10^{23}$ cm^{-2}, whilst a brighter object (with luminosity 10^{40} erg s^{-1}) requires

a higher column of $\sim 10^{24}$ cm^{-2} to be obscured from our view. These columns reduce with distance – at 30 Mpc the equivalent columns are $\sim 10^{22}$ and a few times 10^{23} cm^{-2} respectively, while at 60 Mpc even minimal column ($\sim 10^{20}$ cm^{-2}) will cause a faint ULX to be missed, and $\lesssim 10^{23}$ cm^{-2} is required to obscure a bright ULX. Crucially, these columns are consistent with those seen in LIRGs. For example, Genzel et al. (1998) reported that some ULIRGs have high optical extinctions, $A_{\rm V} \sim$ 1000, corresponding to a column density of $\sim 2 \times 10^{24}$ cm^{-2} (using the conversion of Güver & Özel 2009 where $N_{\rm H} = 2.21 \times 20^{21}$ cm^{-2} $A_{\rm V}$). Indeed, a FIR spectral study of NGC 4418 by *Herschel*/PACS revealed a very high value of column density in the nuclear region of the galaxy, $N_{\rm H} \sim 10^{25}$ cm^{-2} (González-Alfonso et al., 2012). Clearly, these high columns are commensurate with completely obscuring ULXs from our view.

One caveat of this conclusion is that it appears unlikely that there is a steady gradation of column as one enters the LIRGs. In such a situation one might expect to see a range of obscuring columns building up to the high central values, and this would lead to a population of absorbed, and so spectrally hard, but not completely obscured ULXs. We see no such population in the LIRGs, with just one ULX being a hard band only detection, arguing that the absorbing material is a relatively dense medium enshrouding the ULX population. We speculate that such a medium might produce the very putative break in the XLF, but only if the brighter ULXs are preferentially buried behind the screen of material.[28] Interestingly, this is also entirely consistent with the acute lack of ULX detections in the nuclear regions discussed in the previous section; we would expect the innermost regions of each LIRG to be the most deeply enshrouded in dust and gas, and so the most difficult to observe ULXs in.

Indeed, this argument is well supported by the degree of obscuration of the central AGNs by X-ray absorbers in the line of sight. Table 4.11 summarises the measured column density of the AGN absorbers for the LIRGs possessing AGNs,

[28]There is perhaps a hint of the more luminous ULXs being more absorbed in the harder stacked spectra of these objects, although the measured absorption columns do not significantly vary between the three luminosity bins.

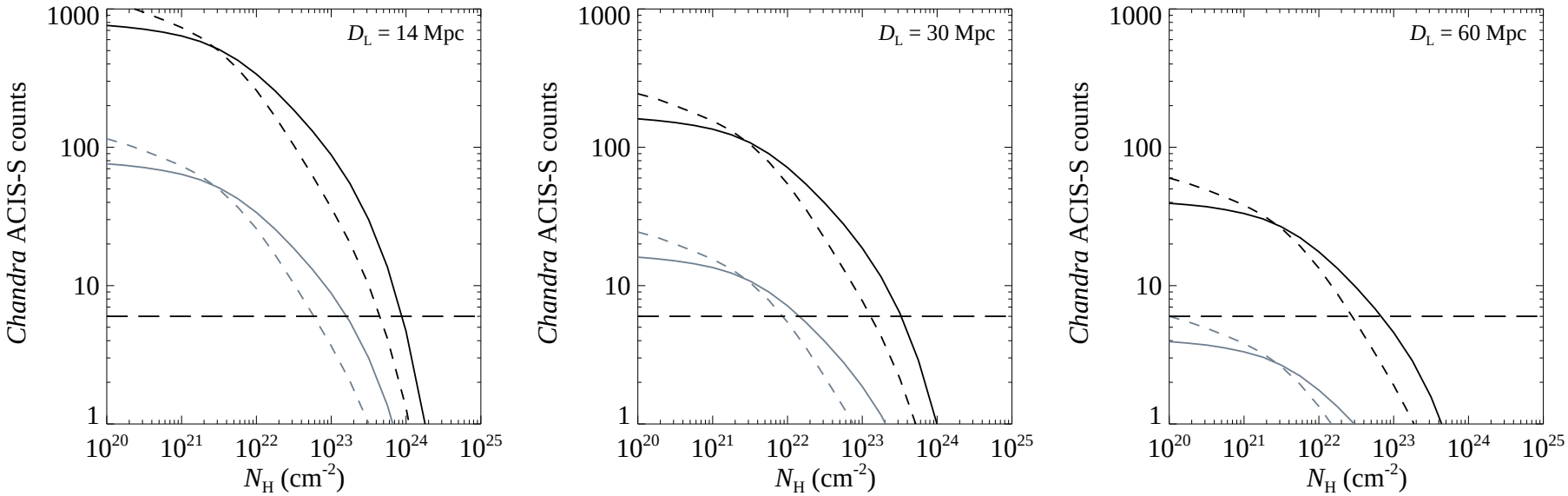

Figure 4.6: Simulated *Chandra* ACIS-S counts detected from ULXs as a function of column density ($N_{\rm H}$), calculated at luminosity distances of 14 (left), 30 (middle) and 60 (right) Mpc. Assuming 20 ks observations, WEBPIMMS was used to simulate the number of counts detected from ULXs with photon indexes of 1.5 (solid line) and 2.5 (dashed line). Both calculated values for faint (10^{39} erg s^{-1}; grey lines) and bright (10^{40} erg s^{-1}; black) ULXs are plotted here. The horizontal dashed line indicates the detection limit – the minimum number of counts where ULXs are detected as point sources in our observational data by the WAVDETECT algorithm.

obtained from the literature. In most galaxies, the absorber column density is $\gtrsim 10^{24}$ cm^{-2} – i.e. the AGNs are Compton thick; although this column density could be intrinsic to the AGNs (e.g. as tori), in very high star forming environments such as in LIRGs this gas could also be the highly dense interstellar medium in the central regions of those galaxies, along the line of sight to the AGNs. The latter possibility is interesting since the high degree of X-ray absorption, if from the interstellar medium, explains the lack of ULXs in the central regions. Indeed, this absorber column density is consistent with the expected absorption values discussed above, even with NGC 7771 in which only a low absorption column is required to hide all ULXs from our view. However, there are a few AGNs in which the absorber column density might be too low to completely obscure the ULXs. In case of NGC 1365, the AGN appears to change between Compton thin and thick due to the variation of its absorber (Risaliti et al., 2005); thus the question is did we observed the AGN during the Compton thin or Compton thick epochs? Fortunately, due to the proximity of NGC 1365, the observation provided the sufficient spectral quality (∼800 counts) to perform the spectral analysis of the central AGN. Interestingly, the spectrum can be explained well by the single component reflection model (PEXMON in XSPEC) with power-law photon index of 2.23, suggesting that the AGN spectrum is reflection-dominated; this implies that the AGN is highly obscured during the epoch that we observed NGC 1365. Alternatively, using the model of two partial covering fraction absorption components (PCFABS×PCFABS×POWERLAW in XSPEC), we can constraint the column density of the absorber to be $0.8^{+0.3}_{-0.2} \times 10^{24}$ cm^{-2} with the covering fraction of $0.9^{+0.02}_{-0.03}$. However, given this variability, the absorber must be associated with the AGN; this puts an upper limit on the interstellar medium towards the centre of this galaxy, which must be the lowest measured absorption towards the AGN. In this case at least it appears that it is not Compton thick.

Finally, interesting supporting evidence for the obscuration scenario is provided by another exotic phenomenon that appears to be under-represented in LIRGs – core-collapse supernovae (CCSNe). Optical surveys for these explosive transients reveal that up to 83 per cent of the expected CCSNe (given the calculated SFR) are missing (e.g. Horiuchi et al. 2011; Mattila et al. 2012). Again, this is directly

Table 4.11: The column density of X-ray absorber in AGNs of the LIRGs

Galaxy	$N_{\rm H}{}^a$	Refs.^{b}
NGC 1068	>10	1,2
NGC 1365	0.5-1^c	3
NGC 4418	>1	4
Arp 299 (NGC 3690)^d	2.5	5
Arp 299 (IC 694)^d	<0.01	5
NGC 5135	1	6
NGC 7771	∼0.005-0.01	7

Note. The column density of the X-ray absorber in AGNs reported for the LIRGs which possess an AGN, with values that are available in literature. ^{a}Column density of the absorber (10^{24} cm^{-2}). ^{b}References to the works reporting the values of the absorber column density. These are: (1) Bauer et al. (2014); (2) Matt et al. (1997); (3) Risaliti et al. (2005); (4) Maiolino et al. (2003); (5) Ballo et al. (2004); (6) Bassani et al. (1999); (7) Jenkins et al. (2005). ^{c}The absorption column density is reported to be variable. ^{d}Arp 299 is merging galaxy consisting of two nuclei: NGC 3690 and IC 694.

attributable to the very dusty environments of the LIRGs, which obscure and so extinguish the emission from these objects.

4.5 Conclusion

In this chapter we have studied the population of ULXs present in a sample of 17 nearby, low foreground absorption LIRGs, based on *Chandra* observations. We detect a total of 53^{+16}_{-13} ULXs in the galaxies, among a total of 139 point X-ray sources, of which we expect less than one fifth to be background objects. We consider the sample to be essentially complete in ULX detection. Our main results can be summarised as follows:

- The source spectra were stacked into three groups as a function of source luminosity. The stacked spectrum of the lowest luminosity sources ($L_{\rm X} < 2 \times 10^{39}$ erg s^{-1}) is significantly softer than the two more luminous stacks, that are indistinguishable from one another. This is consistent with a change in accretion state for $10M_{\odot}$ black holes as they progress from $\sim$ Eddington rate accretion into a super-Eddington, ultraluminous state.

- In one object (CXOU J024238.9-000055 in NGC 1068) we have sufficient statistics to study its spectrum individually. Although its spectrum can be acceptably fitted with a power-law continuum with a hard photon index, making it is consistent with a background AGN spectrum, the fitting still leaves a large residual at ~ 1.7 keV. We find that this can be modelled by the presence of a partially ionised partial covering medium, located within $10^9 R_{\rm g}$ of the ULX, which might be material expelled from the system in a radiatively-driven outflow, as expected for super-Eddington accretion.

- The LIRGs possess significantly fewer ULXs per unit SFR than nearby 'normal' galaxies, by a factor of ~ 10. This deficit also manifests itself as a lower normalisation of the differential XLF than for nearby HMXB samples, and a steeper slope to the cumulative XLF than nearby star forming galaxies. This is very unlikely to be the result of more LMXB ULXs in the normal galaxy

sample; nor is it likely to be due to observational effects such as source confusion, or ULXs missed by the detection code due to being embedded in diffuse emission. Very few of the missing ULXs are detected in the nuclear regions we initially exclude from our analysis; however correcting for those ULXs that may be present based on sources hidden within a diffuse nuclear component, or the SFR of the nuclear region, still presents upper limits significantly below the number of ULXs expected from normal galaxies.

- Metallicity may have some influence on ULX numbers. It might suppress the formation of massive stellar remnants, which may be consistent with a very putative break found in the cumulative XLF and the total absence of ULXs above 10^{40} erg s^{-1}. However, we regard this effect as unlikely to explain the whole deficit.

- A second factor that may have some impact on the deficit is the lag between star formation starting and the appearance of ULXs. However, given the stellar ages of newly formed populations in LIRGs are typically estimated to be older than 5 Myr, this provides sufficient time to turn ULX populations on, so we are disinclined to regard this as a major contributor to the deficit.

- The relatively high ratio of $N_{\rm ULX}/L_{\rm B}$, and very low ratio in $N_{\rm ULX}/L_{\rm FIR}$, of the LIRGs compared to normal galaxy samples point to a very plausible explanation for the main cause of the deficit – a large part of the ULX population is hidden behind the high columns of gas and dust present in these systems. We show that the columns of absorbing material present within LIRGs are sufficient to fully obscure a population of ULXs. This is supported by the the detection of far fewer ULXs per unit SFR in the nuclear regions of the LIRGs where we expect the obscuration to be greatest, and by a similar observational deficit in core-collapse supernovae, that should also be more numerous in LIRGs than is observed.

If there are large hidden populations of ULXs in the most massive star forming galaxies in the Universe, as is suggested by this sample of LIRGs, then this has

interesting implications. Firstly, given the flat XLFs of star forming systems, it can be shown that ULXs dominate their hard X-ray luminosity. However, if these objects are hidden from view, then the observed hard X-ray luminosity of these systems will be largely suppressed below its intrinsic value; it cannot then provide a good measure of the star formation rate of the galaxy, invalidating relations derived from lower SFR systems. This hidden population may also contribute to feedback processes in the galaxies – a factor of 10 more ULXs would boost the radiative feedback by a factor of 10, and a similar level of mechanical feedback would also be expected for these systems. Given that the numbers of massive star forming systems similar to LIRGs increase to peak at redshifts ~ 1, this implies that understanding the concealment of X-ray source populations is important for understanding the intrinsic X-ray emission of the galaxies now being picked up in deep surveys, and how the sources that contribute to this emission help shape their host galaxies. Further work that builds on this study and permits a deeper understanding the X-ray populations of nearby LIRGs is therefore key to understanding our X-ray view of galaxies at the peak of cosmic star formation.

Chapter 5

Conclusion

Throughout this thesis we have attempted to investigate the X-ray behaviours of ULXs, in order to better understand the nature of these sources. In this chapter we will summarise the key results found in this thesis; a number of possible future studies, based on the results in this thesis, will also be suggested at the end of this chapter, that will facilitate further exploration of the nature of ULXs.

5.1 The X-ray spectral properties of ULXs

The X-ray spectral properties of various samples of ULXs were investigated in this thesis and can be summarised as follows. In Chapter 2, we studied the X-ray spectra of ULXs in very nearby galaxies ($\lesssim$ 5 Mpc) observed by *Suzaku*. Given that they are so nearby (in relative terms), we demonstrated that the data quality of the ULX spectra in this chapter is sufficiently high as to require two component models, similar to *XMM-Newton* studies of the best quality ULX spectra. Indeed, the ULX spectra could be explained equally well by several alternative models composed of two thermal (curved) components: one fitted to the soft excess and another one fitted to the high energy turn-over. We suggested that a two component model composed of a MCD plus a Comptonisation model, which was successful in explaining the spectra in previous ULX studies, is likely just one of several phenomenological models that describe the shape of ULX spectra very well, but may not describe their physics.

We showed that the canonical MCD plus power-law model provided acceptable fits to the data and produced two main results; firstly, the spectral turnover in the 2-10 keV regime characteristic of ULX spectra is confirmed, as the MCD tended to fit to the hard spectral component in all objects; however, these MCD fits are different to those commonly seen in *XMM-Newton* studies in which, normally, the MCD fits to the soft spectral component for objects in the SUL/HUL regimes. This highlights the relative lack of soft response in the *Suzaku* detectors – compared to those of *XMM-Newton* – meaning that they do not detect the soft excess with the same definition, and so the MCD preferentially fits to the hard end of the spectrum.

We suggest a new, amended version of the Sutton et al. (2013b) scheme to classify *Suzaku* ULX spectra based on the MCD inner-disc temperature, that allows these spectra to be classified into the BD/SUL/HUL regimes. The classification scheme helps us to track the spectral evolution of ULXs with increasing luminosity. The spectral transition from the BD to UL regimes (HUL or SUL) when the luminosity is in excess of $\sim 3 \times 10^{39}$ erg s^{-1} can be argued to originate in a change in the mass accretion from ∼Eddington to super-Eddington states (Gladstone et al. 2009; Sutton et al. 2013b); this is consistent with the spectral transition from BD to HUL with increasing luminosity seen in the stacked spectra of the LIRG sample in Chapter 4. However, in this thesis, the key detection is a change in the opposite sense; the transition from a HUL spectrum at lower luminosities to a BD spectrum at higher luminosity is seen in the two ULXs in NGC 1313 (Chapter 2) and Holmberg IX X-1 (Chapter 3). We argued that this could be the transition from a lower/moderate super-Eddington rate to an extremely super-Eddington mass accretion rate. We also demonstrated that the mass of black holes powering the ULXs could be constrained from the hard components of the observed X-ray spectra (with some caveats) and found that they all lie in the stellar-mass black hole range ($M_{\rm BH}$ ∼3-30 $M_{\odot}$), or, in a few cases, possibly in the neutron star range (i.e. $M_{\rm BH} \lesssim 3\ M_{\odot}$). All our spectral analysis results are consistent with ULXs as sMBHs (or neutron stars) accreting matter at super-Eddington accretion rates.

At super-critical accretion rates, the disc should increase in scale height to about the order of unity ($H/R \sim 1$) as its interior becomes advection dominated, and it

should lose a non-negligible fraction of the inflowing mass via an outflowing wind. Our results are consistent with the suggestion that the hard spectral component could be emission from the hot inner part of a super-Eddington, geometrically thick disc (i.e. an advection-dominated slim disc) whilst the soft spectral component could be physically attributed to the soft thermal emission from the optically thick wind. In particular, in Chapter 2 we demonstrated that the hard component of ULX spectra is consistent with emission from an advection-dominated slim accretion disc. Furthermore, we performed a very simple calculation of the size of the outflowing wind from the soft emission, which could be constrained to be between $\sim 10^4 - 10^6\ R_{\rm g}$. In addition, a direct detection of the outflowing wind might be seen in the individual object e.g. CXOU J024238.9-000055 discussed in Chapter 4. As its spectrum can be modelled by including a partially ionized partial covering medium, located within $10^9\ R_{\rm g}$ of the ULX, this might indicate the presence of material expelled from the system in a radiatively driven outflow, as expected for a super-Eddington accretion model.

Furthermore, we also highlight that the transition between a HUL spectrum at lower luminosities and a BD spectrum at high luminosity can be interpreted in terms of super-Eddington accretion models, where we observe ULXs at a very low inclination angle. As the accretion rate increases, a more powerful wind will arise and start to enter the observer's line-of-sight. This will scatter many hard photons emitted from the central regions of the ULX into the line of sight, while ones that survive the passage through the wind will be Compton down-scattered to lower energies. A combination of this increase in and softening of the harder spectral component, and a rise in the emission of the wind itself, could result in the observed change of the spectra from the HUL to the BD regime as the luminosity increases. In addition, we also suggest that we might see precession in the super-Eddington accretor Holmberg IX X-1; a degree of degeneracy between different spectra observed at the same luminosity can be explained if the ULX does not remain at a fixed inclination to the line-of-sight, but instead the black hole rotational axis precesses.

5.2 The population of ULXs in LIRGs

In Chapter 4, we studied the population of ULXs present in a sample of 17 nearby LIRGs. We demonstrated that the LIRGs possess significantly fewer ULXs per unit SFR than nearby 'normal' galaxies, by a factor of $\sim$10. This deficit also manifests itself as a lower normalisation of the differential XLF than for nearby HMXB samples. We argued that this deficit of ULXs is unlikely to be due to observational effects including source confusion, or ULXs missed by the detection code due to being embedded in diffuse emission. We also showed that although we correct for those ULXs that may be present based on sources hidden within a diffuse nuclear component, or the SFR of the nuclear region, it still presents upper limits significantly below the number of ULXs expected from normal galaxies.

Thus we suggested that the deficit of ULXs in the LIRGs could be due to some physical mechanisms affecting the number of ULXs in the galaxies. Part of the deficit could be due to the high metallicity environment of the host galaxies suppressing the formation of ULXs. In addition, another factor that may have some impact on the deficit is the lag between SF starting and the appearance of ULXs. However, we argued that these effects are unlikely to explain the whole deficit; we suggested that the majority of the deficit of ULXs could be due to the high volume of gas and dust in the LIRGs obscuring the ULXs from our view. This would imply that a large part of the ULX population is hidden behind the high columns of gas and dust present in these systems. We also show that the columns of absorbing material present within LIRGs are sufficient to fully obscure a population of ULXs.

If this interpretation is correct, it could have implications for X-ray studies of the early Universe. If a large fraction of the X-ray population is obscured in that era due to being embedded in environments similar to those of the LIRGs, then surveys will miss that population, and so may underestimate the X-ray contribution to feedback processes. This means that understanding the concealment of X-ray source populations is important for understanding the intrinsic X-ray emission of sources within galaxies, and how this emission contributes to feedback mechanisms in the early Universe.

5.3 Future work

In this thesis, we have worked within the framework of super-Eddington accretion models in order to explain the X-ray behaviours of ULXs. Although we have shown that these are well supported by current X-ray data, we do not pretend that the debate over the nature of ULXs has concluded, and other possible explanations for the properties of at least some ULXs remain. Further experimental data can help to test the validity of all these arguments. In this section, we will suggest some other ways to examine the proposed arguments and further explore the nature of ULXs.

5.3.1 Probing deeper into the nature of ULXs and their outflowing wind

In this thesis, we suggested that the shapes and variations of observed ULX spectra could be explained by super-Eddington accretion, including the effects of a massive outflowing wind. Although the X-ray data are well consistent with such a model, no strong evidence of the direct detection of a ULX wind has been reported. Indeed, it is still far from clear what the structure and composition of the wind are (if it exists). Here we will suggest a few ways to investigate the nature of the wind.

Walton et al. (2013a) attempted to search for narrow absorption features in the X-ray spectra of Holmberg IX X-1 imprinted by the outflowing wind; they reported no significant features in the Fe-K band down to an equivalent width of $\sim$20 eV. However, it has been shown that spectral residuals in the Fe-L bandpass, detected in the spectra of NGC 5408 X-1 and NGC 6946 X-1, can be explained as broad absorption features associated with a partially ionised, optically thin phase of an outflowing wind (Middleton et al., 2014). Thus, if such a wind is present, we can determine whether atomic features associated with material in this wind would be detected by current and near-future X-ray instruments. To do this, we chose to use a continuum model composed of a MCD plus a Comptonisation component, that provided the best fit to epoch 2 of the broadband spectra of Holmberg IX X-1 in Chapter 3, as this spectral model should represent the highest mass accretion rate of the source and so a massive outflowing wind is expected to be present close to or

Table 5.1: An examination of the weak absorption features in the simulated ULX spectra

Spectrum	χ^2/d.o.f.	
	Power-law[a]	Power-law+Gaussian[b]
XMM-Newton + RGS	54.45/58	49.58/55
Astro-H + SXS	251.47/197	209.64/194
Althena + X-IFU	3201.93/497	1348.18/494

Notes. The best fitting results for the weak absorption feature at ∼1.3 keV imprinted by the outflowing wind in the simulated ULX spectra. The spectra were fitted over the energy range from 1.2-1.4 keV. [a]Minimum χ^2 over degrees of freedom obtained from the single power-law model. [b]Minimum χ^2 over degrees of freedom obtained from the power-law model with a Gaussian absorption line.

within the line-of-sight. Then the partially ionised absorption component was added to the continuum model to represent absorption from the optically thin phase of the wind; the same wind absorption component developed by Middleton et al. (2014) and fitted to the putative wind absorption in the NGC 5408 X-1 spectra were used here. In brief, the model assumed that this optically thin wind is located at >1000 $R_{\rm g}$ and has outflow velocity of $0.12c$; the properties of the wind material are defined by the following parameters: metallicity $Z = Z_{\odot}$, column $N_{\rm H} = 6.4 \times 10^{22}$ cm^{-2} and ionisation parameter $\log \xi = 3.18$.

Using this wind model, we simulated spectra for three current and near future X-ray instruments – *XMM-Newton*, *Astro-H* and the *Advanced Telescope for High-ENergy Astrophysics* (*Athena*) – and tested whether these instruments would be capable of detecting absorption features in this wind. In brief, we simulated a 100 ks spectrum for each X-ray instrument, using the main high resolution spectrometer of each telescope – thus we simulated data from *XMM-Newton* + RGS, *Astro-H* + SXS and *Athena* + X-IFU. We then fitted each simulated spectrum with the wind absorption model used to generate the spectra. The simulated spectra and modelling results are shown in Fig. 5.1, Fig. 5.2 and Fig. 5.3.

It is obvious that all three X-ray instruments should be capable of detecting the strong O-K edge absorption feature imprinted on the spectra at energy ∼0.62 keV (if present), including the current *XMM-Newton* RGS instrument. However, we note that no strong evidence of the detection of any such absorption feature – especially

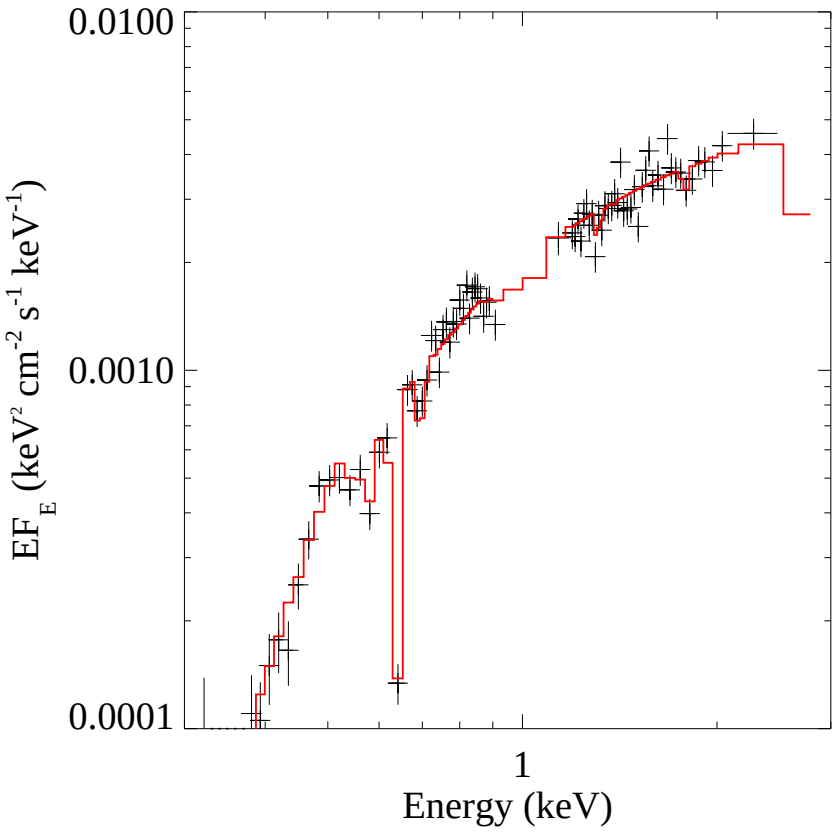

Figure 5.1: Simulated *XMM-Newton* + RGS spectrum from a 100 ks observation of Holmberg IX X-1 at its highest source accretion rate, with absorption by an outflowing, optically thin phase of a super-critical wind imprinted on the spectrum. The data are binned to 5σ significance for clarity. The the best-fitting continuum spectrum plus wind absorption model is overlaid in red.

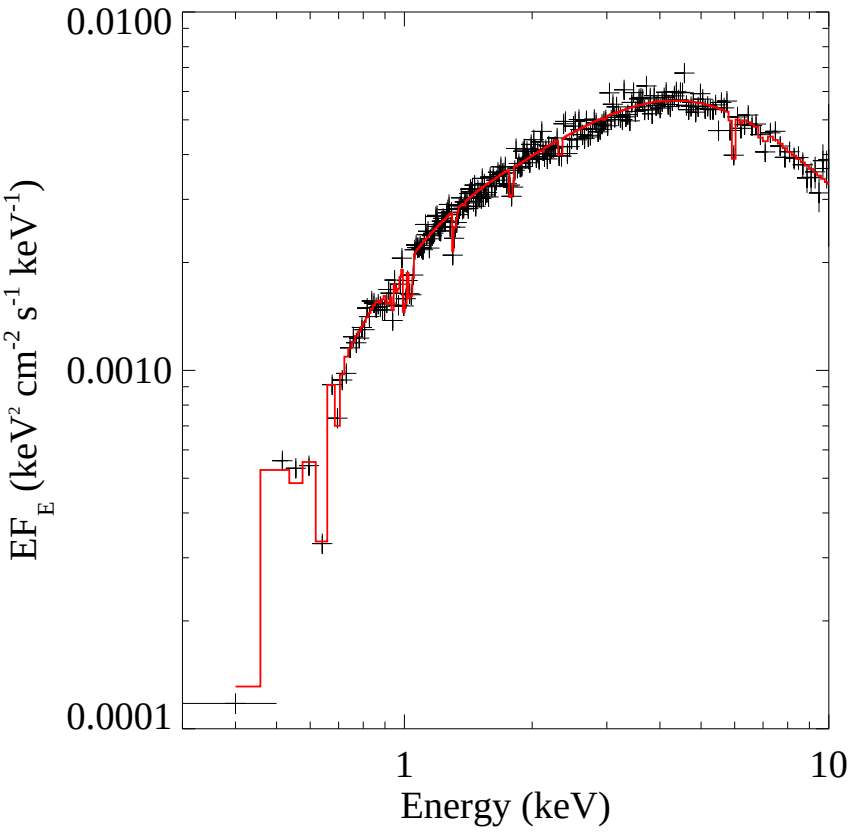

Figure 5.2: Simulated *Astro-H* + SXS spectrum as per Fig. 5.1. The data are binned to 20σ significance for clarity.

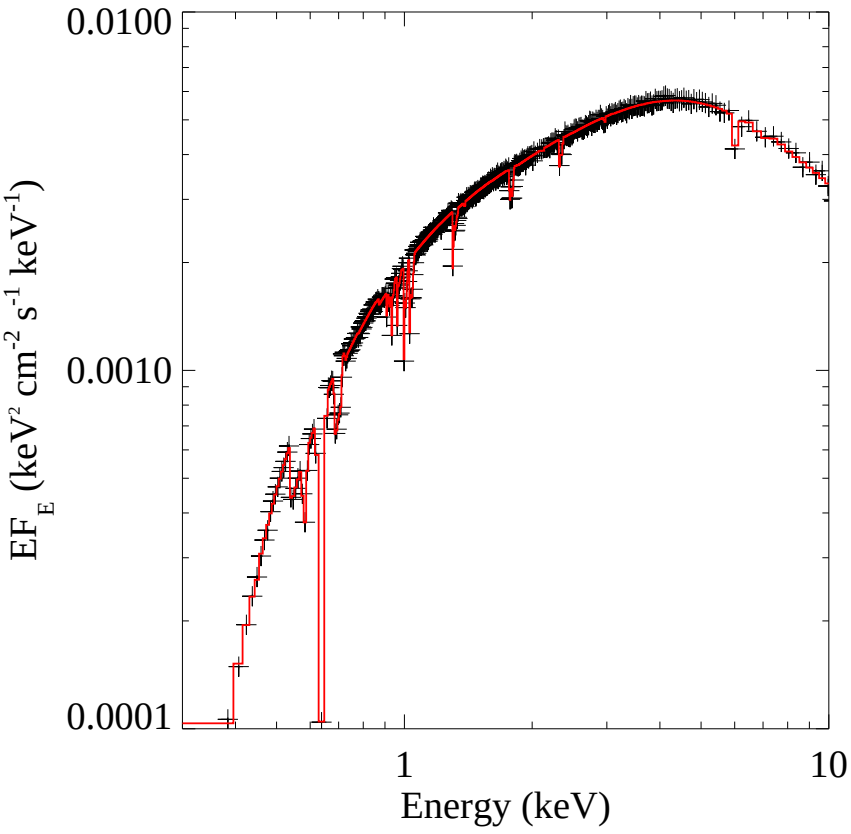

Figure 5.3: Simulated *Athena* + X-IFU spectrum as per Fig. 5.1. The data are binned to 80σ significance for clarity.

by *XMM-Newton* RGS instrument – has been reported so far (although see Goad et al. 2006). Indeed, most of the Holmberg IX X-1 spectra observed to date are in the HUL regime, implying that the source was observed nearly face-on and so the wind was unlikely to intercept the line of sight (see Section 1.5.2), resulting in a lack of, or weakness in, any wind absorption features. It was suggested by Middleton et al. (2014) that the absorption would be seen in SUL spectra – in which ULXs are observed at high inclination and so the wind intercepts the line of sight – and it is likely to be a broad feature; however high S/N data are still required in order to identify such a feature.

However, assuming that such a wind model represents the crude properties of the ULX wind, the interesting point is whether we can detect weak absorption features imprinted on the spectra, which definitely cannot be detected by the current X-ray instruments such as *XMM-Newton* RGS. Excitingly, if the weak wind absorption features exist, such features could be detected by the near-future missions *Astro-H* and *Athena*. We confirmed that these weak absorption features will be detected by considering one narrow absorption feature at ∼1.3 keV; we fit the spectra over the narrow energy range of 1.2-1.4 keV using a pure power-law continuum model, and compare this to a power-law plus Gaussian absorption line model, as shown in Table 5.1. For the RGS spectrum, no statistical improvement was found when adding the Gaussian absorption component to the model ($\Delta\chi^2$ ∼5 for three additional degrees of freedom); however, the model with the absorption component yielded a significant statistical improvement over the single power-law model when fitted to the *Astro-H* + SXS spectrum ($\Delta\chi^2$ ∼40, corresponding to an improvement in null hypothesis probability of ∼20%) and the *Athena* + X-IFU spectrum ($\Delta\chi^2$ ∼1800). This was despite the equivalent width of the absorption feature being as small as ∼2 eV. This indicates that *Astro-H* and *Athena* will be capable of observing very shallow and narrow wind absorption features that are currently undetectable by the available X-ray instruments. The detection of absorption features will not only provide unambiguous evidence of the presence of wind material in the line-of-sight to the ULX, but will also help us to understand more about the structure and the atomic composition of the wind plasma. If we are able to compare the observational

constraints on the wind to new theoretical simulations by the current or near-future generations of high performance computers, we should gain a great deal of insight into the ULX wind.

In addition, it is possible that the Russian *Spectrum-Roentgen-Gamma* (*SRG*) satellite will be launched in the near future. With eROSITA – the primary instrument on-board – it will perform the first imaging all-sky survey in the medium energy X-ray band (up to 10 keV) with an unprecedented spectral and angular resolution. More ULX candidates should be identified, potentially producing the largest available catalogue of ULXs, and providing a new and large sample of ULXs for study. Also, with the excellent effective area of the *Astro-H* hard X-ray telescope, the study of high energy spectra (e.g. non-thermal high energy tail) of ULXs will be enhanced.

5.3.2 The obscuration of ULXs by gas and dust in LIRGs?

In Chapter 4, we suggested that the major factor in the deficit of ULXs in LIRGs could be the high columns of gas and dust in the LIRGs, which obscure the ULXs. Here we will suggest a few ready ways to confirm this scenario, based on the current generation of X-ray telescopes, in particular the *Chandra* observatory. The first method is by directly measuring an absorption column in the host galaxies through the X-ray spectra of ULXs located in the LIRGs. Deep *Chandra* observations of the LIRG sample would provide moderate quality spectra of ULXs residing in the systems. For example, a 200 ks *Chandra* ACIS-S observation of the LIRG NGC 1365 ($D_{\rm L}$ = 18 Mpc) will provide at least 400 spectral counts for each individual ULX residing in the galaxy. Such moderate quality spectra of individual sources will be sufficient to carry out simple spectral modelling; using an absorbed power-law model, the measurement of column density ($N_{\rm H}$) can be constrained to better than $\pm 3 \times 10^{21}$ cm^{-2}, providing an absorption column along the line-of-sight to the ULXs. Assuming that ULXs have intrinsic absorption columns of $N_{\rm H}$ $\sim$1.5 $\times$ 10^{21} cm^{-2} (including any contribution from the outflowing wind), any extra absorption can be attributed to the host galaxies. Indeed, for nearby LIRGs such as NGC 1068 and NGC 1365, the large X-ray population distributed around the galaxies will provide

a rough map of the absorption column of their hosts, useful in identifying high obscuration regions. However, a large caveat of this method is that we can only measure the absorption from partially absorbed ULXs, most likely located on the near side of the LIRGs; most ULXs are completely absorbed and obscured in the LIRGs, meaning they cannot contribute to the measurements.

Another method is by expanding the range of the LIRG sample. If the dearth of ULXs is related to the high column of gas and dust in the host galaxies, the effect should be strongest in the highest column density environments, i.e. in the highest SFR galaxies. Indeed, we found that the LIRG with the highest SFR in the sample – Arp 299 – has a relatively low number of ULXs per unit SFR, compared to the other LIRGs. This suggests that a larger fraction of ULXs are obscured in the higher SFR environment due to a higher amount of gas and dust. Thus, to further test this scenario, we could examine the number of ULXs per unit SFR in even higher SFR galaxies, such as in the highest SFR LIRG and ULIRG system using the same method as in Chapter 4. Given the very high spatial resolution of *Chandra* telescope, we should be able to resolve the number of ULXs even if we include galaxies at larger distances than the current LIRG sample.

We have performed a preliminary analysis on a new sample of LIRGs and ULIRGs that are located slightly beyond the original LIRG sample in Chapter 4 (60 Mpc $\leq D_{\rm L} \leq$ 80 Mpc), and that have observational data available in the *Chandra* data archive. In brief, the sample contains five LIRGs and one ULIRG; three out of six galaxies, including the ULIRG, already have a sufficient exposure time to detect all ULXs whilst the exposure time of the other three galaxies is below the sensitivity limit for detecting all their ULXs. The analysis results are shown in Fig. 5.4. For the new LIRG sample, the calculation provides a lower limit given that the exposure times for some galaxies are not sensitive enough to detect all ULXs. Interestingly, it is found that the number of ULX per unit SFR appears to decrease as the SFR increases, consistent with the assumption that a larger number of ULXs might be obscured by the higher gas and dust content in the highest SFR ULIRG/LIRGs. However, given the small sample sizes, newer and deeper *Chandra* observations of a further expanded sample would be useful to confirm this.

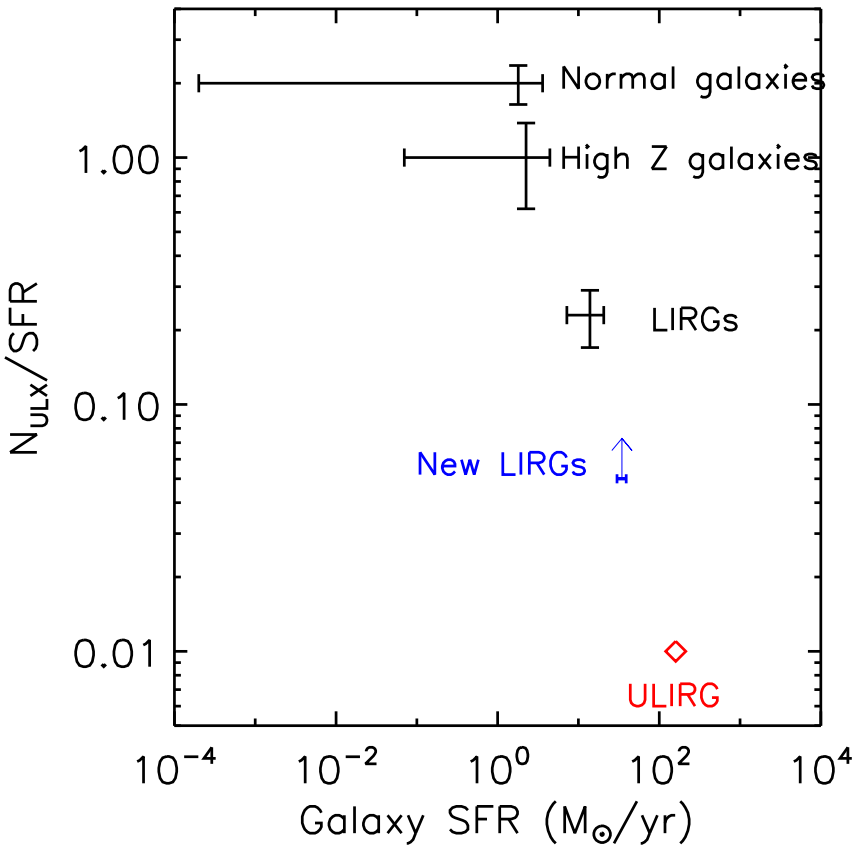

Figure 5.4: The number of ULXs per unit SFR plotted as a function of SFR. The data plotted in blue and red are the preliminary results from an analysis of LIRG and ULIRG data available in the *Chandra* data archive. The comparator samples plotted in black are taken from the sample in Chapter 4 (LIRGs), Swartz et al. (2004; normal galaxies) and Prestwich et al. (2013; high metallicity galaxies).

5.4 Concluding remarks

In this chapter, we have summarised the major results found in this thesis. A number of further studies, which can build on the work presented herein are also suggested, in order to further investigate the physics underlying ULXs. Over 30 years from the first detection of ULXs, the field of ULX astronomy has come a long way and the understanding for this sub-class of X-ray source has been enhanced substantially, including the contributions presented in this thesis. Although it is currently believed that the majority of the ULX population are accreting sMBHs, the physics of super-Eddington accretion is still an open topic for debate. Using observational data obtained from near-future missions, and theoretical simulations by high performance computing machines, studies in the field of ULX astronomy should have a very exciting future.

Appendix A

The *Swift* monitoring observations of Holmberg IX X-1: spectral analysis of individual observations

Here, we present the spectral fitting results from all *Swift* monitoring observations of Holmberg IX X-1 with sufficient photon statistics to permit the analysis. The individual spectra extracted from the observations are modelled by an absorbed power-law model; the best fitting results are reported in the following Table A.1 (see Section 3.3.1 from more details).

Table A.1: The absorbed power-law fits to the individual *Swift* spectra

Obs ID	$N_{\rm H}{}^a$	Γ^b	χ^2/d.o.f.	$\log(f_{\rm X})^c$	Total counts^d	θ^e
00032188001	$0.11^{+0.11}_{-0.09}$	$1.46^{+0.23}_{-0.21}$	29.16/41	-10.80	481	9.81
00032188004	$0.06^{+0.48}_{-0.06}$	$1.73^{+0.62}_{-0.33}$	8.33/12	-10.98	171	9.24
00032188005	$0.20^{+0.31}_{-0.20}$	$1.48^{+0.51}_{-0.45}$	16.08/13	-10.99	183	9.36
00032188006	$0.92^{+0.51}_{-0.41}$	$2.31^{+0.66}_{-0.57}$	11.20/13	-11.07	183	9.54
00032188007	$0.23^{+0.39}_{-0.23}$	$1.56^{+0.52}_{-0.44}$	6.45/14	-10.93	188	9.73
00032188008	< 0.40	$1.54^{+0.49}_{-0.23}$	19.99/15	-10.86	206	9.17
00032188009	< 0.39	$1.22^{+0.52}_{-0.23}$	12.42/13	-10.89	174	9.62
00032188010	$0.34^{+0.24}_{-0.19}$	$1.76^{+0.49}_{-0.43}$	5.78/16	-10.98	209	9.94
00032188011	$0.06^{+0.38}_{-0.06}$	$1.35^{+0.53}_{-0.32}$	4.61/11	-10.97	155	9.07
00032188012	$0.35^{+0.38}_{-0.30}$	$1.73^{+0.55}_{-0.48}$	10.94/12	-10.97	167	10.09
00032188013	$0.21^{+0.28}_{-0.21}$	$1.46^{+0.49}_{-0.44}$	9.88/14	-10.89	194	8.54
00032188014	$0.61^{+0.47}_{-0.38}$	$2.08^{+0.57}_{-0.49}$	11.69/15	-11.05	195	8.33
00032188015	$0.21^{+0.28}_{-0.21}$	$1.74^{+0.49}_{-0.43}$	16.58/14	-11.02	190	8.89
00032188018	0.30^{*}	1.6^{*}	2.93/6	-10.91	87	10.89
00032188021	$0.56^{+0.38}_{-0.31}$	$1.91^{+0.61}_{-0.53}$	14.21/12	-11.00	171	9.17
00032188022	$0.15^{+0.20}_{-0.15}$	$1.40^{+0.38}_{-0.34}$	11.10/18	-10.88	228	8.20
00032188023	$0.58^{+0.32}_{-0.25}$	$1.84^{+0.40}_{-0.36}$	12.03/22	-10.80	273	10.09
00032188024	$0.28^{+0.21}_{-0.16}$	$1.52^{+0.30}_{-0.27}$	28.71/27	-10.75	333	9.58
00032188025	$0.85^{+0.43}_{-0.33}$	$2.12^{+0.43}_{-0.37}$	20.71/20	-10.83	245	9.49
00032188027	$0.33^{+0.44}_{-0.32}$	$1.77^{+0.68}_{-0.58}$	5.35/9	-11.05	140	9.73
00032188028	$0.46^{+0.37}_{-0.30}$	$1.87^{+0.50}_{-0.44}$	15.10/17	-11.01	216	9.27

Table A.1 – *continued*

Obs ID	$N_{\rm H}{}^a$	Γ^b	χ^2/d.o.f.	$\log(f_{\rm X})^c$	Total counts^d	θ^e
00032188030	$0.07^{+0.25}_{-0.07}$	$1.72^{+0.45}_{-0.30}$	13.34/17	-10.98	220	8.59
00032188031	< 0.43	$1.43^{+0.75}_{-0.30}$	11.22/11	-10.94	156	10.34
00032188032	$0.32^{+0.29}_{-0.23}$	$1.52^{+0.39}_{-0.35}$	26.59/27	-10.61	333	10.76
00032188033	$0.24^{+0.21}_{-0.17}$	$1.28^{+0.29}_{-0.27}$	31.10/24	-10.64	298	8.98
00032188034	$0.34^{+0.29}_{-0.22}$	$1.51^{+0.37}_{-0.33}$	29.91/27	-10.72	325	9.57
00032188035	$0.48^{+0.36}_{-0.28}$	$1.63^{+0.36}_{-0.32}$	18.73/24	-10.72	290	8.43
00032188036	$0.21^{+0.21}_{-0.14}$	$1.53^{+0.32}_{-0.28}$	18.13/25	-10.71	295	9.37
00032188039	$0.20^{+0.22}_{-0.18}$	$1.37^{+0.34}_{-0.32}$	20.03/26	-10.71	324	7.96
00032188041	0.30^*	1.6^*	2.75/6	-10.79	84	8.14
00032188042	$0.26^{+0.24}_{-0.19}$	$1.30^{+0.35}_{-0.31}$	27.84/26	-10.68	319	9.45
00032188043	$0.29^{+0.30}_{-0.25}$	$1.69^{+0.42}_{-0.37}$	14.30/18	-10.75	226	7.88
00032188044	$0.28^{+0.39}_{-0.28}$	$1.46^{+0.44}_{-0.40}$	10.29/14	-10.71	188	7.70
00032188045	$0.52^{+0.24}_{-0.20}$	$2.02^{+0.38}_{-0.34}$	19.73/25	-10.83	314	5.63
00032188046	$0.32^{+0.25}_{-0.21}$	$1.95^{+0.48}_{-0.42}$	19.99/21	-10.88	275	8.78
00032188047	$0.42^{+0.26}_{-0.19}$	$1.80^{+0.34}_{-0.29}$	25.22/27	-10.82	329	8.13
00032188048	$0.42^{+0.34}_{-0.28}$	$1.55^{+0.41}_{-0.38}$	14.29/23	-10.74	297	8.20
00032188049	$0.24^{+0.27}_{-0.19}$	$1.68^{+0.53}_{-0.46}$	5.12/11	-10.80	149	8.82
00032188050	$0.65^{+0.46}_{-0.33}$	$2.26^{+0.57}_{-0.48}$	17.68/15	-10.91	192	10.30
00032188051	$0.32^{+0.35}_{-0.27}$	$1.64^{+0.38}_{-0.34}$	15.17/22	-10.80	268	7.96
00032188053	$0.39^{+0.32}_{-0.24}$	$1.62^{+0.35}_{-0.31}$	26.09/23	-10.80	280	7.91
00032188054	$0.39^{+0.33}_{-0.26}$	$1.86^{+0.40}_{-0.36}$	18.68/20	-10.85	247	9.44
00032188055	$0.58^{+0.35}_{-0.27}$	$2.15^{+0.43}_{-0.37}$	20.03/20	-10.91	257	7.85
00032188058	$0.43^{+0.24}_{-0.20}$	$2.04^{+0.38}_{-0.34}$	17.93/21	-10.91	261	8.99
00032188061	$0.36^{+0.26}_{-0.21}$	$1.47^{+0.34}_{-0.31}$	22.38/24	-10.73	295	9.41

Table A.1 – *continued*

Obs ID	$N_{\rm H}{}^a$	Γ^b	χ^2/d.o.f.	$\log(f_{\rm X})^c$	Total counts^d	θ^e
00032188063	$0.15^{+0.21}_{-0.15}$	$1.41^{+0.33}_{-0.30}$	37.59/30	-10.71	368	10.05
00032188064	$0.25^{+0.36}_{-0.25}$	$1.74^{+0.44}_{-0.39}$	19.26/19	-10.84	241	9.30
00032188065	$0.18^{+0.20}_{-0.15}$	$1.31^{+0.30}_{-0.27}$	28.41/27	-10.65	324	9.77
00032188066	$0.34^{+0.31}_{-0.26}$	$1.65^{+0.46}_{-0.40}$	9.27/14	-10.99	190	9.97
00032188067	$0.35^{+0.21}_{-0.17}$	$1.84^{+0.35}_{-0.31}$	24.02/26	-10.85	317	9.56
00032188069	$0.14^{+0.33}_{-0.14}$	$1.56^{+0.48}_{-0.38}$	18.79/15	-11.00	200	9.31
00032188070	< 0.32	$1.28^{+0.19}_{-0.19}$	23.46/21	-10.79	253	9.27
00032188072	$0.67^{+0.43}_{-0.33}$	$1.94^{+0.44}_{-0.39}$	14.12/16	-10.96	210	9.78
00032188074	$0.06^{+0.38}_{-0.06}$	$1.31^{+0.49}_{-0.29}$	8.05/13	-10.87	180	10.92
00032188075	$0.60^{+0.91}_{-0.60}$	$2.22^{+1.12}_{-0.83}$	11.75/8	-11.18	131	10.94
00032188080	$0.51^{+0.32}_{-0.26}$	$1.84^{+0.36}_{-0.32}$	29.69/26	-10.77	320	9.54
00032188081	$0.53^{+0.32}_{-0.24}$	$1.52^{+0.34}_{-0.31}$	15.32/25	-10.71	302	8.86
00032188082	$0.33^{+0.38}_{-0.28}$	$1.56^{+0.46}_{-0.41}$	16.65/17	-10.83	225	9.86
00032188085	0.30^*	1.6^*	6.52/6	-11.20	90	9.16
00032188086	< 0.28	$1.20^{+0.36}_{-0.19}$	20.31/22	-10.66	275	11.00
00032188087	0.30^*	1.6^*	8.00/7	-10.75	96	9.64
00032188089	$0.33^{+0.26}_{-0.20}$	$1.65^{+0.33}_{-0.30}$	21.81/25	-10.75	304	9.47
00032188091	$0.40^{+0.63}_{-0.40}$	$1.71^{+0.70}_{-0.58}$	8.19/10	-11.10	142	9.52
00032188093	$0.89^{+0.81}_{-0.64}$	$1.87^{+1.07}_{-0.89}$	4.34/6	-11.10	104	10.77
00032188096	$0.38^{+0.29}_{-0.23}$	$1.74^{+0.40}_{-0.36}$	35.72/21	-10.79	263	10.83
00032188097	$0.53^{+0.72}_{-0.53}$	$1.95^{+0.86}_{-0.73}$	3.00/10	-11.03	149	10.49
00032188101	$0.40^{+0.41}_{-0.30}$	$1.69^{+0.46}_{-0.39}$	19.17/20	-10.78	244	9.60
00032188102	$0.29^{+0.28}_{-0.22}$	$1.60^{+0.32}_{-0.29}$	22.63/23	-10.78	279	9.65
00032188103	$0.43^{+0.51}_{-0.41}$	$1.40^{+0.64}_{-0.57}$	3.23/11	-10.85	164	10.72

Table A.1 – *continued*

Obs ID	$N_{\rm H}{}^a$	Γ^b	χ^2/d.o.f.	$\log(f_{\rm X})^c$	Total counts^d	θ^e
00032188105	$0.34^{+0.33}_{-0.27}$	$1.90^{+0.57}_{-0.48}$	8.90/14	-11.02	186	10.48
00032188109	$0.11^{+0.89}_{-0.11}$	$1.21^{+1.01}_{-0.50}$	3.85/5	-11.05	101	10.55
00032188110	$0.07^{+0.44}_{-0.07}$	$1.29^{+0.49}_{-0.29}$	7.07/11	-11.01	154	9.79
00032188111	$0.01^{+0.53}_{-0.01}$	$1.29^{+0.58}_{-0.29}$	5.38/8	-11.05	122	10.40
00032188113	$0.22^{+0.26}_{-0.19}$	$1.53^{+0.40}_{-0.35}$	18.93/18	-10.97	223	10.37
00032188114	$0.32^{+0.29}_{-0.22}$	$1.66^{+0.38}_{-0.33}$	21.29/24	-10.86	293	10.89
00032188116	$0.10^{+0.68}_{-0.10}$	$1.54^{+0.75}_{-0.53}$	3.53/8	-11.09	127	8.82
00032188117	< 0.36	$1.15^{+0.51}_{-0.38}$	7.00/6	-11.08	104	10.76
00032188119	< 0.20	$1.35^{+0.40}_{-0.27}$	10.64/10	-11.03	146	10.64
00032188121	$0.23^{+0.29}_{-0.23}$	$1.75^{+0.57}_{-0.48}$	14.46/14	-11.09	188	9.52
00032188122	$0.17^{+0.38}_{-0.17}$	$1.52^{+0.69}_{-0.51}$	9.79/10	-11.09	145	9.08
00032188124	$0.19^{+0.41}_{-0.19}$	$1.48^{+0.51}_{-0.41}$	19.84/14	-10.96	194	9.36
00032188125	< 0.38	$1.30^{+0.46}_{-0.29}$	19.05/8	-11.04	119	10.28
00032188126	< 0.24	$1.13^{+0.36}_{-0.24}$	6.13/13	-10.93	183	10.88
00032188127	$0.26^{+0.51}_{-0.26}$	$1.55^{+0.62}_{-0.49}$	3.13/8	-11.09	121	10.17
00032188128	$0.24^{+0.47}_{-0.24}$	$1.65^{+0.96}_{-0.75}$	3.22/6	-11.11	107	11.01
00032188130	$0.06^{+0.40}_{-0.06}$	$1.47^{+0.60}_{-0.34}$	17.49/12	-11.01	168	10.88
00032188131	< 0.40	$1.30^{+0.56}_{-0.30}$	5.96/9	-10.98	140	10.13
00032188132	$0.13^{+0.36}_{-0.13}$	$1.65^{+0.53}_{-0.39}$	8.53/11	-11.04	158	10.85
00032188136	$0.75^{+0.56}_{-0.47}$	$2.39^{+0.75}_{-0.64}$	10.95/15	-10.99	208	10.65
00032188137	< 0.26	$1.33^{+0.43}_{-0.25}$	3.46/10	-11.05	146	10.77
00032188138	$0.02^{+0.38}_{-0.02}$	$1.28^{+0.54}_{-0.30}$	11.89/9	-11.06	132	10.28
00032188139	$0.59^{+0.44}_{-0.36}$	$2.10^{+0.61}_{-0.53}$	6.62/13	-11.06	176	9.57
00032188140	$0.26^{+0.41}_{-0.26}$	$1.81^{+0.68}_{-0.57}$	2.28/10	-11.11	147	10.82

Table A.1 – *continued*

Obs ID	$N_{\rm H}{}^a$	Γ^b	χ^2/d.o.f.	$\log(f_{\rm X})^c$	Total counts^d	θ^e
00032188141	< 0.43	$1.61^{+0.69}_{-0.32}$	8.43/8	-11.12	130	9.97
00032188144	0.30^*	1.6^*	1.86/3	-10.88	51	8.45
00032188148	$0.41^{+0.27}_{-0.22}$	$1.70^{+0.32}_{-0.28}$	20.81/26	-10.74	309	8.36
00032188150	$0.19^{+0.36}_{-0.19}$	$1.50^{+0.43}_{-0.37}$	27.17/15	-10.78	204	8.18
00032188151	$0.24^{+0.22}_{-0.18}$	$1.74^{+0.29}_{-0.27}$	35.60/31	-10.82	366	6.20
00032188152	$0.10^{+0.38}_{-0.10}$	$1.24^{+0.50}_{-0.33}$	20.59/16	-10.75	210	10.09
00032188154	$0.55^{+0.25}_{-0.20}$	$1.79^{+0.35}_{-0.32}$	14.20/26	-10.71	313	7.99
00032188155	$0.37^{+0.33}_{-0.27}$	$1.51^{+0.40}_{-0.36}$	22.48/24	-10.71	290	8.61
00032188156	$0.22^{+0.33}_{-0.22}$	$1.76^{+0.50}_{-0.44}$	13.20/15	-10.93	199	10.79
00032188157	$0.28^{+0.28}_{-0.22}$	$1.68^{+0.39}_{-0.35}$	10.72/18	-10.87	223	10.08
00032188158	$0.47^{+0.32}_{-0.26}$	$1.70^{+0.45}_{-0.41}$	13.61/19	-10.88	242	9.47
00032188160	$0.26^{+0.23}_{-0.19}$	$1.41^{+0.30}_{-0.28}$	38.15/34	-10.69	402	8.08
00032188161	$0.27^{+0.21}_{-0.15}$	$1.59^{+0.30}_{-0.26}$	25.11/24	-10.81	286	8.44
00032188162	$0.23^{+0.28}_{-0.23}$	$1.48^{+0.43}_{-0.38}$	21.47/22	-10.77	279	9.18
00032188163	$0.65^{+0.39}_{-0.31}$	$1.86^{+0.53}_{-0.47}$	19.42/21	-10.77	272	9.47
00032188164	$0.26^{+0.37}_{-0.26}$	$1.65^{+0.38}_{-0.34}$	17.61/21	-10.77	265	10.44
00032188165	$0.52^{+0.23}_{-0.19}$	$1.89^{+0.34}_{-0.30}$	28.68/32	-10.77	387	8.79
00032188167	$0.45^{+0.29}_{-0.23}$	$1.71^{+0.35}_{-0.32}$	13.09/22	-10.76	272	9.27
00032188168	$0.11^{+0.28}_{-0.11}$	$1.35^{+0.38}_{-0.30}$	29.83/21	-10.74	263	9.98
00032188169	$0.31^{+0.27}_{-0.20}$	$1.75^{+0.41}_{-0.36}$	15.87/20	-10.86	244	8.00
00032188171	$0.07^{+0.45}_{-0.07}$	$1.46^{+0.63}_{-0.36}$	9.65/9	-11.08	141	9.68
00032188176	< 0.68	$1.28^{+0.77}_{-0.31}$	3.90/6	-11.20	102	9.65
00032188177	< 0.24	$1.00^{+0.37}_{-0.32}$	16.58/10	-10.96	148	9.42
00032188178	< 0.44	$1.20^{+0.61}_{-0.39}$	10.49/6	-11.08	110	10.59

Table A.1 – *continued*

Obs ID	$N_{\rm H}{}^a$	Γ^b	χ^2/d.o.f.	$\log(f_{\rm X})^c$	Total counts^d	θ^e
00032188180	$0.60^{+0.72}_{-0.59}$	$2.03^{+0.84}_{-0.71}$	5.01/8	-11.11	134	7.68
00032188182	$0.30^{+0.33}_{-0.25}$	$1.30^{+0.40}_{-0.36}$	12.42/21	-10.66	266	9.85
00032188183	$0.07^{+0.26}_{-0.07}$	$1.22^{+0.40}_{-0.28}$	13.33/20	-10.67	253	10.99
00032188188	$0.42^{+0.55}_{-0.42}$	$1.70^{+0.57}_{-0.51}$	7.60/11	-10.83	162	9.68
00032188189	$0.17^{+0.32}_{-0.17}$	$1.46^{+0.40}_{-0.34}$	16.04/17	-10.76	217	9.06
00032188190	$0.43^{+0.51}_{-0.33}$	$1.51^{+0.47}_{-0.39}$	19.87/20	-10.79	248	10.71
00032188191	$0.63^{+0.37}_{-0.29}$	$1.99^{+0.40}_{-0.36}$	16.77/19	-10.90	242	9.37
00032188192	$0.82^{+0.51}_{-0.36}$	$1.87^{+0.46}_{-0.40}$	21.63/24	-10.83	299	9.81
00032188193	0.30^{*}	1.6^{*}	2.29/4	-10.70	65	10.24
00032188194	$0.52^{+0.40}_{-0.32}$	$1.65^{+0.45}_{-0.41}$	25.75/20	-10.81	251	9.95
00032188198	$0.74^{+1.12}_{-0.74}$	$1.95^{+1.04}_{-0.87}$	7.93/6	-10.83	113	10.26
00032188199	$0.11^{+0.21}_{-0.11}$	$1.44^{+0.31}_{-0.27}$	18.78/28	-10.69	342	8.38
00032188200	$0.74^{+0.42}_{-0.33}$	$2.00^{+0.41}_{-0.36}$	19.07/21	-10.79	257	9.78
00032188201	$0.24^{+0.25}_{-0.19}$	$1.36^{+0.32}_{-0.29}$	43.98/33	-10.68	396	10.08
00032188202	$0.38^{+0.37}_{-0.28}$	$1.59^{+0.53}_{-0.47}$	11.84/14	-10.88	194	10.10
00032188203	$0.75^{+0.80}_{-0.61}$	$1.80^{+0.92}_{-0.79}$	1.89/6	-10.98	107	8.28
00032188204	$0.56^{+0.29}_{-0.23}$	$1.93^{+0.39}_{-0.35}$	19.12/25	-10.80	313	8.12
00032188206	$0.05^{+0.29}_{-0.05}$	$1.26^{+0.48}_{-0.29}$	14.15/17	-10.68	229	9.43
00032188207	$0.13^{+0.42}_{-0.13}$	$1.19^{+0.52}_{-0.36}$	18.47/16	-10.77	218	8.74
00032188208	$0.66^{+0.37}_{-0.27}$	$2.09^{+0.40}_{-0.35}$	28.33/22	-10.83	273	9.61
00032188209	$0.46^{+0.73}_{-0.46}$	$1.43^{+0.90}_{-0.76}$	7.59/7	-10.65	117	9.36
00032188210	$0.24^{+0.31}_{-0.24}$	$1.76^{+0.42}_{-0.38}$	20.54/25	-10.80	305	10.06
00032188211	$0.39^{+0.25}_{-0.21}$	$1.71^{+0.38}_{-0.34}$	20.66/21	-10.83	259	9.50
00032188212	$0.33^{+0.35}_{-0.25}$	$1.67^{+0.44}_{-0.38}$	19.05/20	-10.82	262	9.79

Table A.1 – *continued*

Obs ID	$N_{\rm H}{}^a$	Γ^b	χ^2/d.o.f.	$\log(f_{\rm X})^c$	Total counts^d	θ^e
00032188213	$0.19^{+0.26}_{-0.19}$	$1.47^{+0.37}_{-0.34}$	22.55/20	-10.81	250	9.57
00032188215	$0.08^{+0.68}_{-0.08}$	$1.10^{+1.27}_{-0.60}$	3.30/6	-10.62	111	8.59
00032188216	$0.43^{+0.50}_{-0.35}$	$1.61^{+0.50}_{-0.43}$	14.60/16	-10.77	211	8.70
00032188217	$0.33^{+0.23}_{-0.18}$	$1.83^{+0.33}_{-0.29}$	20.56/23	-10.94	280	9.77
00032188218	$0.15^{+0.20}_{-0.15}$	$1.67^{+0.37}_{-0.33}$	13.81/19	-10.87	241	10.56
00032188219	$0.50^{+0.29}_{-0.23}$	$1.62^{+0.33}_{-0.30}$	20.28/27	-10.76	321	8.91
00032188223	$0.43^{+0.39}_{-0.32}$	$1.95^{+0.50}_{-0.44}$	13.75/17	-10.99	223	9.00
00032188224	$0.46^{+0.41}_{-0.33}$	$1.85^{+0.50}_{-0.44}$	11.31/15	-10.96	198	8.95
00032188226	$0.20^{+0.36}_{-0.20}$	$1.74^{+0.58}_{-0.49}$	16.37/11	-11.20	158	9.40
00032188227	$0.08^{+0.50}_{-0.08}$	$1.58^{+0.73}_{-0.41}$	6.23/8	-11.13	128	9.91
00032188228	$0.24^{+0.32}_{-0.24}$	$1.63^{+0.46}_{-0.41}$	8.84/15	-11.03	195	8.97
00032188231	< 0.34	$1.32^{+0.52}_{-0.26}$	4.04/10	-11.05	145	9.29
00032188232	< 0.36	$1.33^{+0.57}_{-0.35}$	15.59/9	-11.07	143	9.63
00032188233	< 0.53	$1.22^{+0.62}_{-0.34}$	11.54/7	-11.07	119	9.68
00032188234	$0.07^{+0.31}_{-0.07}$	$1.31^{+0.43}_{-0.28}$	10.92/17	-10.95	221	8.48
00032188235	$0.23^{+0.28}_{-0.23}$	$1.63^{+0.44}_{-0.39}$	10.85/18	-10.95	230	8.89
00032188237	$0.42^{+0.34}_{-0.27}$	$1.57^{+0.40}_{-0.36}$	20.64/22	-10.77	270	9.17
00032188238	$0.40^{+0.45}_{-0.31}$	$1.85^{+0.57}_{-0.48}$	15.97/14	-11.07	187	9.60
00032188239	$0.44^{+0.48}_{-0.37}$	$1.81^{+0.59}_{-0.52}$	6.57/10	-11.04	143	9.02
00032188240	< 0.48	$1.20^{+0.58}_{-0.29}$	11.50/8	-11.07	122	10.78
00032188241	$0.05^{+0.38}_{-0.05}$	$1.62^{+0.58}_{-0.32}$	7.64/13	-10.94	176	8.81
00032188243	< 0.3	$1.77^{+0.60}_{-0.30}$	4.53/9	-11.05	143	10.95
00032188244	< 0.32	$1.24^{+0.49}_{-0.25}$	18.94/12	-11.02	164	9.04
00032188246	$1.46^{+1.57}_{-0.91}$	$3.46^{+1.62}_{-1.14}$	6.06/6	-11.07	109	10.63

Table A.1 – *continued*

Obs ID	$N_{\rm H}{}^a$	Γ^b	χ^2/d.o.f.	$\log(f_{\rm X})^c$	Total counts^d	θ^e
00032188247	$0.24^{+0.22}_{-0.17}$	$1.45^{+0.33}_{-0.30}$	26.79/24	-10.81	294	9.76
00032188248	$0.34^{+0.30}_{-0.24}$	$1.52^{+0.48}_{-0.43}$	13.16/16	-10.86	204	10.77
00032188252	$0.20^{+0.44}_{-0.20}$	$1.67^{+0.60}_{-0.48}$	15.99/11	-11.06	158	10.95
00032519002	$0.25^{+0.26}_{-0.22}$	$1.56^{+0.34}_{-0.31}$	28.21/27	-10.77	336	1.64
00032519003	$0.51^{+0.26}_{-0.21}$	$2.46^{+0.52}_{-0.45}$	24.58/23	-11.02	286	3.86
00032519004	$0.31^{+0.10}_{-0.09}$	$1.78^{+0.17}_{-0.16}$	75.04/73	-10.89	871	2.39
00032519005	$0.42^{+0.33}_{-0.28}$	$1.62^{+0.46}_{-0.42}$	11.65/19	-10.73	243	2.62
00032519006	$0.09^{+0.28}_{-0.09}$	$1.45^{+0.43}_{-0.32}$	13.11/18	-11.03	230	1.66
00032519007	$0.19^{+0.25}_{-0.18}$	$1.63^{+0.38}_{-0.34}$	15.17/17	-11.13	219	1.15
00032519008	$0.10^{+0.21}_{-0.10}$	$1.32^{+0.48}_{-0.39}$	23.99/19	-11.01	245	1.55
00032519009	$0.39^{+0.31}_{-0.25}$	$1.76^{+0.38}_{-0.34}$	7.62/18	-11.10	230	0.99
00032519010	$0.12^{+0.33}_{-0.12}$	$1.45^{+0.45}_{-0.34}$	23.79/17	-11.08	225	2.70
00032519012	$0.36^{+0.42}_{-0.34}$	$2.02^{+0.76}_{-0.62}$	7.47/8	-11.40	131	0.85
00032519013	$0.26^{+0.31}_{-0.25}$	$1.86^{+0.49}_{-0.43}$	10.22/13	-11.25	175	2.73
00032519014	< 0.22	$1.39^{+0.43}_{-0.22}$	19.23/18	-11.03	231	2.17
00032519015	$0.09^{+0.10}_{-0.09}$	$1.33^{+0.21}_{-0.20}$	34.57/48	-11.16	560	0.67
00032519016	$0.18^{+0.25}_{-0.18}$	$1.63^{+0.37}_{-0.33}$	28.23/28	-11.15	336	1.64
00032519017	$0.27^{+0.11}_{-0.09}$	$1.84^{+0.24}_{-0.22}$	56.02/43	-11.29	519	1.86
00032519018	$0.19^{+0.09}_{-0.08}$	$1.59^{+0.19}_{-0.18}$	37.91/56	-11.12	660	0.76
00032519020	$0.51^{+0.32}_{-0.26}$	$1.93^{+0.45}_{-0.39}$	8.14/19	-10.98	236	0.77
00032519021	$0.21^{+0.09}_{-0.07}$	$1.53^{+0.14}_{-0.13}$	94.08/86	-10.78	1050	1.51
00032519022	$0.25^{+0.20}_{-0.15}$	$1.62^{+0.30}_{-0.27}$	29.30/36	-10.79	431	0.77
00032519023	$0.26^{+0.09}_{-0.07}$	$1.52^{+0.13}_{-0.13}$	104.56/96	-10.76	1144	0.96
00032519024	$0.34^{+0.17}_{-0.13}$	$1.46^{+0.19}_{-0.18}$	48.82/58	-10.77	673	0.96

Table A.1 – *continued*

Obs ID	$N_{\rm H}{}^a$	Γ^b	χ^2/d.o.f.	$\log(f_{\rm X})^c$	Total counts^d	θ^e
00032519025	$0.26^{+0.19}_{-0.15}$	$1.48^{+0.24}_{-0.22}$	40.16/45	-10.73	523	3.48
00032519026	$0.34^{+0.25}_{-0.19}$	$1.64^{+0.29}_{-0.25}$	40.07/40	-10.77	473	3.89
00032519027	$0.32^{+0.17}_{-0.13}$	$1.66^{+0.28}_{-0.25}$	43.08/37	-10.79	435	3.03
00032519028	$0.90^{+0.45}_{-0.31}$	$2.56^{+0.44}_{-0.36}$	41.16/30	-10.94	361	3.07
00032519029	$0.51^{+0.28}_{-0.22}$	$1.85^{+0.31}_{-0.28}$	24.94/31	-10.79	369	0.96
00032519030	$0.15^{+0.20}_{-0.15}$	$1.43^{+0.31}_{-0.28}$	26.63/32	-10.77	382	2.68
00032519031	$0.38^{+0.20}_{-0.16}$	$1.84^{+0.27}_{-0.24}$	29.24/40	-10.85	468	2.27
00032519032	$0.43^{+0.34}_{-0.25}$	$1.63^{+0.35}_{-0.31}$	21.01/23	-10.70	292	4.67
00032519033	$0.44^{+0.21}_{-0.16}$	$1.72^{+0.23}_{-0.21}$	49.35/45	-10.74	516	3.88
00032519034	$0.32^{+0.19}_{-0.16}$	$1.81^{+0.27}_{-0.25}$	38.67/41	-10.83	492	2.91
00032519035	$0.58^{+0.50}_{-0.40}$	$1.76^{+0.55}_{-0.49}$	18.55/16	-11.06	211	0.62
00032519036	$0.37^{+0.51}_{-0.37}$	$1.82^{+0.58}_{-0.50}$	13.40/14	-10.84	185	1.08
00032519037	$0.29^{+0.21}_{-0.16}$	$1.77^{+0.31}_{-0.28}$	21.00/32	-10.85	386	2.99
00032519038	$0.25^{+0.38}_{-0.25}$	$1.69^{+0.56}_{-0.48}$	13.80/11	-10.84	154	3.59
00032519039	$0.06^{+0.25}_{-0.06}$	$1.53^{+0.33}_{-0.23}$	34.39/26	-10.87	329	1.05
00032519040	$0.38^{+0.18}_{-0.14}$	$1.72^{+0.25}_{-0.22}$	38.77/43	-10.77	514	2.09
00032519041	$0.26^{+0.46}_{-0.26}$	$1.61^{+0.58}_{-0.49}$	10.60/12	-11.20	167	0.82
00032519083	< 0.34	$1.39^{+0.55}_{-0.25}$	13.51/13	-11.05	177	3.47
00032519084	$0.02^{+0.13}_{-0.02}$	$1.44^{+0.23}_{-0.16}$	29.51/32	-11.25	385	1.30
00032519085	0.30^*	1.6^*	4.19/7	-11.05	91	0.36
00033286004	0.30^*	1.6^*	3.40/8	-11.15	97	10.32
00033286006	0.30^*	1.6^*	13.35/8	-11.22	96	9.73
00033286007	$0.25^{+0.58}_{-0.25}$	$1.64^{+0.67}_{-0.52}$	9.34/8	-11.23	125	9.46
00033286008	$0.07^{+0.53}_{-0.07}$	$1.41^{+0.63}_{-0.35}$	4.73/7	-11.16	112	10.02

Table A.1 – *continued*

Obs ID	$N_{\rm H}{}^a$	Γ^b	χ^2/d.o.f.	$\log(f_{\rm X})^c$	Total counts^d	θ^e
00033286009	0.30*	1.6*	2.25/6	-11.24	82	8.28
00033286010	< 0.36	$1.25^{+0.36}_{-0.34}$	2.47/7	-11.11	114	8.34
00033286011	< 0.42	$1.12^{+0.45}_{-0.43}$	1.44/5	-11.09	100	8.30
00033286014	0.30*	1.6*	4.86/6	-11.25	90	9.08
00033286017	0.30*	1.6*	6.32/6	-11.26	88	11.00
00033286021	0.30*	1.6*	2.60/4	-11.33	65	9.01
00033286023	< 0.20	$1.20^{+0.31}_{-0.30}$	6.06/7	-11.11	110	9.65
00033286024	0.30*	1.6*	2.28/4	-11.33	61	9.88
00033286028	0.30*	1.6*	4.70/7	-11.16	98	10.49
00033286031	< 0.16	$1.35^{+0.50}_{-0.45}$	11.02/6	-11.21	101	9.34
00033286034	< 0.14	$1.55^{+0.40}_{-0.34}$	11.70/9	-11.25	145	10.30
00033286036	< 0.72	$1.10^{+0.83}_{-0.41}$	14.97/6	-11.11	104	10.47
00033286037	0.30*	1.6*	8.18/7	-11.24	90	9.98
00035335001	$0.11^{+0.04}_{-0.04}$	$1.46^{+0.11}_{-0.10}$	131.66/129	-11.17	1611	1.52
00035335002	$0.10^{+0.10}_{-0.08}$	$1.57^{+0.24}_{-0.22}$	44.38/39	-11.21	460	1.99
00035335003	0.30*	1.6*	0.91/3	-11.08	51	1.85
00035335004	$0.24^{+0.03}_{-0.03}$	$1.71^{+0.06}_{-0.05}$	379.26/342	-10.85	6127	1.66
00035335005	$0.24^{+0.04}_{-0.04}$	$1.77^{+0.08}_{-0.08}$	204.32/211	-10.94	2919	3.44
00035335006	$0.13^{+0.11}_{-0.09}$	$1.52^{+0.25}_{-0.22}$	22.42/28	-10.93	318	2.37
00035335007	$0.16^{+0.18}_{-0.16}$	$1.55^{+0.29}_{-0.26}$	28.34/31	-11.07	381	1.26
00035335009	$0.12^{+0.05}_{-0.04}$	$1.57^{+0.13}_{-0.12}$	113.93/101	-11.18	1201	1.44
00080427001	$0.18^{+0.15}_{-0.12}$	$1.65^{+0.28}_{-0.25}$	29.71/30	-11.08	354	0.51
00080427002	$0.29^{+0.13}_{-0.10}$	$1.58^{+0.18}_{-0.17}$	53.28/67	-10.77	780	1.22
00080711001	$0.14^{+0.18}_{-0.14}$	$1.44^{+0.30}_{-0.27}$	34.43/31	-11.05	373	2.92

Table A.1 – *continued*

Obs ID	$N_{\rm H}{}^a$	Γ^b	χ^2/d.o.f.	$\log(f_{\rm X})^c$	Total counts^d	θ^e
00090008001	$0.50^{+0.26}_{-0.20}$	$1.96^{+0.30}_{-0.27}$	54.26/39	-10.93	453	0.74
00090008002	$0.26^{+0.19}_{-0.15}$	$1.64^{+0.29}_{-0.26}$	27.25/31	-10.98	376	0.60
00090008003	$0.13^{+0.14}_{-0.11}$	$1.57^{+0.22}_{-0.20}$	33.05/34	-10.99	401	1.58
00090008004	$0.24^{+0.24}_{-0.19}$	$1.44^{+0.36}_{-0.33}$	17.45/23	-11.06	283	1.69
00090008005	$0.38^{+0.25}_{-0.17}$	$2.04^{+0.36}_{-0.30}$	45.04/29	-11.12	361	0.73
00090008007	$0.31^{+0.11}_{-0.09}$	$1.68^{+0.17}_{-0.16}$	39.88/70	-10.91	838	0.96
00090008008	$0.17^{+0.09}_{-0.08}$	$1.54^{+0.16}_{-0.15}$	64.44/69	-10.89	794	0.64
00090008009	$0.24^{+0.12}_{-0.10}$	$1.61^{+0.18}_{-0.17}$	55.30/60	-10.94	702	0.71
00090008010	$0.17^{+0.11}_{-0.09}$	$1.55^{+0.18}_{-0.17}$	50.49/56	-10.93	648	0.66
00090008011	$0.18^{+0.11}_{-0.09}$	$1.65^{+0.22}_{-0.20}$	34.57/46	-11.06	532	0.21
00090008012	< 0.37	$1.25^{+0.48}_{-0.24}$	4.94/12	-11.16	166	0.27
00090008013	< 0.33	$1.43^{+0.61}_{-0.32}$	4.51/7	-11.40	116	0.75
00090008014	$0.05^{+0.21}_{-0.05}$	$1.46^{+0.44}_{-0.29}$	9.99/14	-11.15	183	0.95
00090008015	$0.06^{+0.20}_{-0.06}$	$1.40^{+0.38}_{-0.28}$	17.61/18	-11.08	226	2.65
00090008016	$0.05^{+0.19}_{-0.05}$	$1.37^{+0.31}_{-0.23}$	15.68/19	-11.07	236	1.67
00090008017	$0.16^{+0.27}_{-0.16}$	$1.51^{+0.41}_{-0.36}$	11.11/14	-11.23	186	0.32
00090008018	$0.05^{+0.22}_{-0.05}$	$1.52^{+0.32}_{-0.23}$	18.25/21	-11.24	258	1.30
00090008019	$0.15^{+0.21}_{-0.15}$	$1.33^{+0.32}_{-0.29}$	22.70/26	-11.03	324	0.47
00090008020	$0.19^{+0.12}_{-0.10}$	$1.56^{+0.22}_{-0.20}$	61.65/53	-11.01	632	2.02
00090008021	$0.24^{+0.15}_{-0.11}$	$1.66^{+0.27}_{-0.24}$	37.94/37	-11.03	435	1.47
00090008022	$0.26^{+0.12}_{-0.10}$	$1.71^{+0.25}_{-0.23}$	40.01/45	-11.04	538	2.13
00090008023	$0.21^{+0.12}_{-0.10}$	$1.44^{+0.23}_{-0.21}$	29.70/41	-10.92	470	1.86
00090008024	$0.14^{+0.14}_{-0.12}$	$1.61^{+0.26}_{-0.23}$	30.39/35	-11.03	423	2.70
00090008025	$0.17^{+0.14}_{-0.12}$	$1.61^{+0.27}_{-0.25}$	18.43/31	-11.08	370	1.34

Table A.1 – *continued*

Obs ID	$N_{\rm H}{}^a$	Γ^b	χ^2/d.o.f.	$\log(f_{\rm X})^c$	Total counts^d	θ^e
00090008026	< 0.24	$1.17^{+0.31}_{-0.19}$	19.29/19	-11.13	235	2.59
00090008028	$0.02^{+0.28}_{-0.02}$	$1.44^{+0.52}_{-0.28}$	12.67/13	-11.33	182	1.12
00090008029	0.30^*	1.6^*	1.58/4	-11.05	70	0.45
00090008030	$0.03^{+0.23}_{-0.03}$	$1.38^{+0.42}_{-0.25}$	13.47/18	-11.07	237	1.88
00090008031	$0.26^{+0.18}_{-0.14}$	$1.77^{+0.32}_{-0.28}$	30.25/27	-11.19	321	2.07
00090008032	$0.13^{+0.18}_{-0.13}$	$1.59^{+0.29}_{-0.26}$	15.71/26	-11.14	314	1.00
00090008033	$0.26^{+0.21}_{-0.17}$	$1.74^{+0.35}_{-0.31}$	29.31/25	-11.12	304	0.68
00090008034	$0.15^{+0.28}_{-0.15}$	$1.68^{+0.44}_{-0.37}$	16.84/15	-11.25	205	0.62
00090008035	$0.24^{+0.08}_{-0.07}$	$1.47^{+0.13}_{-0.12}$	97.63/101	-10.81	1219	1.24
00090008036	$0.24^{+0.17}_{-0.14}$	$1.91^{+0.31}_{-0.27}$	24.94/27	-11.09	320	2.31
00090008037	$0.25^{+0.19}_{-0.14}$	$1.60^{+0.24}_{-0.22}$	43.91/40	-10.87	474	2.43
00090008038	$0.14^{+0.21}_{-0.14}$	$1.64^{+0.38}_{-0.34}$	9.63/22	-11.06	270	4.84
00090008039	$0.22^{+0.17}_{-0.13}$	$1.71^{+0.27}_{-0.25}$	36.98/28	-11.08	328	2.82
00090008040	$0.27^{+0.15}_{-0.12}$	$1.67^{+0.24}_{-0.22}$	33.76/43	-10.95	512	0.68
00090008041	$0.24^{+0.16}_{-0.13}$	$1.79^{+0.30}_{-0.27}$	16.70/25	-11.14	308	1.21
00090008042	$0.43^{+0.63}_{-0.43}$	$1.71^{+0.70}_{-0.61}$	10.76/11	-10.92	155	1.88
00090008043	$0.15^{+0.14}_{-0.12}$	$1.69^{+0.28}_{-0.25}$	29.97/34	-11.10	406	1.88
00090008044	$0.17^{+0.16}_{-0.13}$	$1.62^{+0.31}_{-0.28}$	24.70/27	-11.18	324	1.88
00090008045	$0.09^{+0.20}_{-0.09}$	$1.46^{+0.36}_{-0.29}$	19.41/20	-11.11	252	2.23
00090008046	< 0.19	$1.38^{+0.35}_{-0.21}$	15.00/16	-11.14	214	2.35
00090008047	$0.04^{+0.16}_{-0.04}$	$1.40^{+0.33}_{-0.24}$	49.07/25	-11.18	313	2.35
00090008048	$0.09^{+0.21}_{-0.09}$	$1.67^{+0.42}_{-0.33}$	24.40/19	-11.19	240	1.72
00090008049	$0.14^{+0.15}_{-0.12}$	$1.48^{+0.28}_{-0.25}$	18.77/29	-11.01	341	2.39
00090008050	$0.09^{+0.24}_{-0.09}$	$1.47^{+0.39}_{-0.30}$	16.30/17	-11.10	218	2.15

Table A.1 – *continued*

Obs ID	$N_{\rm H}{}^a$	Γ^b	χ^2/d.o.f.	$\log(f_{\rm X})^c$	Total counts^d	θ^e
00090008052	$0.33^{+0.21}_{-0.17}$	$2.12^{+0.39}_{-0.34}$	16.00/23	-11.23	286	2.35
00090008054	$0.11^{+0.13}_{-0.11}$	$1.69^{+0.29}_{-0.26}$	28.03/32	-11.12	389	2.09
00090008055	$0.14^{+0.24}_{-0.14}$	$1.75^{+0.43}_{-0.36}$	12.70/19	-11.13	246	2.42
00090008056	$0.15^{+0.18}_{-0.15}$	$1.65^{+0.33}_{-0.29}$	39.24/31	-11.07	378	2.89
00090008057	$0.20^{+0.19}_{-0.15}$	$1.81^{+0.38}_{-0.33}$	17.27/21	-11.13	266	2.17
00090008058	$0.20^{+0.52}_{-0.20}$	$1.81^{+0.82}_{-0.57}$	4.31/8	-11.11	128	3.65
00090008059	$0.19^{+0.17}_{-0.14}$	$1.64^{+0.28}_{-0.25}$	23.89/32	-11.04	380	3.37
00090008060	$0.13^{+0.13}_{-0.11}$	$1.73^{+0.26}_{-0.23}$	21.68/34	-11.01	401	3.09
00090008061	$0.21^{+0.15}_{-0.12}$	$1.69^{+0.25}_{-0.23}$	24.66/39	-11.06	472	3.70
00090008062	$0.20^{+0.20}_{-0.17}$	$1.82^{+0.30}_{-0.27}$	14.57/27	-10.99	334	2.94
00090008063	$0.25^{+0.16}_{-0.13}$	$1.95^{+0.27}_{-0.24}$	49.08/36	-11.07	424	2.89
00090008064	$0.17^{+0.22}_{-0.17}$	$1.54^{+0.32}_{-0.28}$	23.56/23	-11.07	279	1.85
00090008065	$0.03^{+0.26}_{-0.03}$	$1.25^{+0.40}_{-0.25}$	12.56/12	-11.21	162	2.09
00090008066	< 0.16	$1.41^{+0.34}_{-0.26}$	12.67/11	-11.24	156	0.80
00090008067	0.30^*	1.6^*	6.49/3	-11.24	59	3.22
00090008068	< 0.32	$1.45^{+0.35}_{-0.33}$	2.46/7	-11.29	117	2.75
00090008069	< 0.40	$1.25^{+0.53}_{-0.28}$	3.55/7	-11.18	114	0.61
00090008070	$0.36^{+0.60}_{-0.36}$	$1.87^{+0.83}_{-0.69}$	3.47/6	-11.36	111	2.21
00090008071	< 0.32	$1.01^{+0.36}_{-0.35}$	5.09/9	-11.14	139	2.50
00090008072	0.30^*	1.6^*	1.82/3	-11.15	50	2.55
00090008073	0.30^*	1.6^*	7.48/6	-11.31	88	1.66
00090008074	0.30^*	1.6^*	14.12/7	-11.36	92	2.59
00090008076	0.30^*	1.6^*	12.27/6	-11.39	87	3.16
00090008077	$0.13^{+0.42}_{-0.13}$	$1.62^{+0.83}_{-0.52}$	14.10/9	-11.34	143	0.77

Table A.1 – *continued*

Obs ID	$N_{\rm H}{}^a$	Γ^b	χ^2/d.o.f.	$\log(f_{\rm X})^c$	Total counts^d	θ^e
00090008078	0.30^*	1.6^*	6.51/6	-11.36	87	2.74
00090008079	< 0.47	$1.04^{+0.59}_{-0.34}$	7.21/7	-11.03	115	3.77
00090008081	< 0.48	$1.62^{+0.56}_{-0.33}$	6.99/8	-11.28	126	1.87
00090008082	$0.17^{+0.14}_{-0.12}$	$1.72^{+0.29}_{-0.26}$	41.86/30	-11.34	363	1.56
00090079001	$0.15^{+0.27}_{-0.15}$	$1.44^{+0.42}_{-0.36}$	10.89/16	-11.07	211	8.75
00090079002	$0.07^{+0.23}_{-0.07}$	$1.48^{+0.38}_{-0.29}$	17.53/15	-11.17	201	9.20
00090079003	$0.13^{+0.34}_{-0.13}$	$1.45^{+0.49}_{-0.37}$	11.26/14	-11.14	187	9.36
00090079004	$0.01^{+0.59}_{-0.01}$	$1.08^{+0.94}_{-0.38}$	6.71/6	-11.17	104	9.93
00090079005	$0.10^{+0.22}_{-0.10}$	$1.53^{+0.39}_{-0.32}$	12.58/19	-11.24	253	8.57
00090079006	$0.14^{+0.20}_{-0.14}$	$1.54^{+0.43}_{-0.37}$	8.70/13	-11.29	169	8.29
00090079007	0.30^*	1.6^*	16.86/7	-11.32	94	8.96
00090079008	0.30^*	1.6^*	10.06/7	-11.28	95	9.37
00090079009	$0.19^{+0.39}_{-0.19}$	$1.62^{+0.58}_{-0.47}$	5.22/10	-11.31	152	9.06
00090079010	< 0.18	$1.07^{+0.45}_{-0.27}$	10.25/11	-11.20	157	9.64
00090079011	0.30^*	1.6^*	4.96/5	-11.35	73	8.66
00090079012	0.30^*	1.6^*	5.53/6	-11.32	84	8.65
00090079013	0.30^*	1.6^*	6.24/7	-11.27	91	9.53
00090079014	0.30^*	1.6^*	7.24/7	-11.33	96	6.72
00090079015	0.30^*	1.6^*	4.00/4	-11.38	61	6.79
00090079016	0.30^*	1.6^*	2.66/7	-11.30	90	9.02
00090079017	0.30^*	1.6^*	9.19/6	-11.27	83	7.01
00090079018	0.30^*	1.6^*	10.00/6	-11.35	83	6.01
00090079019	< 0.34	$1.18^{+0.49}_{-0.34}$	5.89/6	-11.20	107	6.12
00090079020	$0.05^{+0.50}_{-0.05}$	$1.15^{+0.70}_{-0.38}$	8.07/7	-11.18	118	6.37

Table A.1 – *continued*

Obs ID	$N_{\rm H}{}^a$	Γ^b	χ^2/d.o.f.	$\log(f_{\rm X})^c$	Total counts^d	θ^e
00090079021	0.30^*	1.6^*	11.25/6	-11.36	93	8.91
00090079022	< 0.31	$1.54^{+0.56}_{-0.26}$	11.73/13	-11.19	182	10.85
00090079023	0.30^*	1.6^*	5.07/7	-11.28	95	9.60
00090079024	< 0.19	$1.06^{+0.47}_{-0.44}$	7.61/7	-11.19	119	7.72
00090079025	0.30^*	1.6^*	1.85/4	-11.30	61	8.29
00090079026	$0.14^{+0.38}_{-0.14}$	$1.65^{+0.51}_{-0.38}$	7.32/11	-11.31	152	9.73
00090079027	$0.61^{+0.76}_{-0.52}$	$2.33^{+0.89}_{-0.73}$	7.65/6	-11.43	105	8.15
00090079028	0.30^*	1.6^*	3.65/4	-11.41	68	7.56
00090079029	0.30^*	1.6^*	7.56/7	-11.31	91	7.61
00090079030	$0.61^{+1.21}_{-0.61}$	$1.44^{+1.37}_{-1.03}$	4.01/5	-11.17	101	6.92
00090079031	$0.23^{+0.28}_{-0.23}$	$1.60^{+0.54}_{-0.47}$	6.81/11	-11.37	154	7.21
00090079032	0.30^*	1.6^*	7.09/6	-11.28	90	6.68
00090079033	0.30^*	1.6^*	10.98/7	-11.21	93	8.14
00090079036	$0.17^{+0.39}_{-0.17}$	$1.26^{+0.47}_{-0.38}$	12.03/13	-11.13	175	8.89
00090079037	0.30^*	1.6^*	4.78/7	-11.18	91	7.79
00090079038	0.30^*	1.6^*	1.93/4	-11.34	67	7.26
00090079039	$0.01^{+0.40}_{-0.01}$	$1.11^{+0.60}_{-0.29}$	6.63/10	-11.01	150	9.40
00090079040	0.30^*	1.6^*	8.79/6	-11.29	89	7.17
00090079041	0.30^*	1.6^*	13.99/7	-11.35	95	8.33
00090079044	< 0.57	$0.97^{+0.52}_{-0.28}$	4.91/9	-11.04	134	7.46
00090079045	$0.10^{+0.22}_{-0.10}$	$1.11^{+0.36}_{-0.30}$	9.03/21	-11.05	267	7.74
00090079047	$0.18^{+0.60}_{-0.18}$	$1.46^{+0.72}_{-0.48}$	3.65/7	-11.23	117	6.82
00090079048	0.30^*	1.6^*	1.90/7	-11.22	97	6.08
00090079049	< 0.29	$1.28^{+0.46}_{-0.23}$	12.67/15	-11.14	201	8.09

Table A.1 – *continued*

Obs ID	$N_{\rm H}{}^a$	Γ^b	χ^2/d.o.f.	$\log(f_{\rm X})^c$	Total counts^d	θ^e
00090079050	0.30*	1.6*	3.88/6	-11.31	85	6.92
00090079051	0.30*	1.6*	3.18/7	-11.24	94	7.86
00090079052	0.30*	1.6*	7.19/6	-11.34	81	8.50
00090079053	$0.21^{+0.50}_{-0.21}$	$1.40^{+0.64}_{-0.50}$	5.54/7	-11.24	122	7.80
00090079054	$0.05^{+0.37}_{-0.05}$	$0.86^{+0.48}_{-0.29}$	13.48/13	-11.00	174	7.98
00090079055	< 0.40	$1.25^{+0.50}_{-0.27}$	7.51/8	-11.12	119	7.25
00090079056	< 0.57	$1.46^{+0.79}_{-0.33}$	11.02/7	-11.28	114	7.55
00090079057	$0.09^{+0.36}_{-0.09}$	$1.52^{+0.62}_{-0.39}$	18.92/12	-11.23	170	6.92
00090079058	$0.13^{+0.40}_{-0.13}$	$1.53^{+0.56}_{-0.40}$	7.42/10	-11.20	143	8.00
00090079059	0.30*	1.6*	1.37/3	-11.19	58	6.66
00090079060	< 0.26	$1.54^{+0.47}_{-0.31}$	7.06/10	-11.12	146	6.36
00090079062	0.30*	1.6*	2.11/3	-11.29	53	7.13
00090079063	0.30*	1.6*	4.33/7	-11.16	96	6.66
00090079064	$0.03^{+0.53}_{-0.03}$	$1.34^{+0.78}_{-0.34}$	6.22/8	-11.16	124	8.49
00090079065	< 0.53	$1.44^{+0.61}_{-0.31}$	7.51/6	-11.20	101	8.17
00090079066	< 0.16	$1.08^{+0.34}_{-0.31}$	9.75/8	-11.08	124	8.53
00090079067	$0.29^{+0.51}_{-0.29}$	$1.47^{+0.62}_{-0.53}$	8.99/7	-11.29	113	7.94
00090079068	< 0.32	$0.88^{+0.44}_{-0.43}$	3.72/6	-11.09	107	7.63
00090079069	$0.08^{+0.64}_{-0.08}$	$1.43^{+0.70}_{-0.39}$	7.57/6	-11.24	103	6.85
00090079070	< 0.32	$1.34^{+0.65}_{-0.36}$	9.39/7	-11.20	119	6.86
00090079071	$0.05^{+0.49}_{-0.05}$	$1.55^{+0.68}_{-0.35}$	3.92/7	-11.16	115	7.96
00090079072	$0.28^{+0.58}_{-0.28}$	$1.87^{+0.71}_{-0.56}$	6.18/8	-11.22	121	7.23
00090079073	< 0.37	$1.35^{+0.71}_{-0.36}$	7.05/7	-11.13	121	7.05
00090079074	< 0.47	$0.95^{+0.70}_{-0.35}$	8.81/7	-11.01	113	7.99

Table A.1 – *continued*

Obs ID	$N_{\rm H}{}^a$	Γ^b	χ^2/d.o.f.	$\log(f_{\rm X})^c$	Total counts^d	θ^e
00090079075	< 0.32	$1.70^{+0.42}_{-0.39}$	8.91/6	-11.29	107	7.77
00090079076	$0.21^{+0.34}_{-0.21}$	$1.56^{+0.60}_{-0.50}$	7.23/10	-11.09	149	9.37
00090079077	$0.19^{+0.42}_{-0.19}$	$1.42^{+0.60}_{-0.47}$	10.52/11	-11.18	157	7.49
00090079078	$0.23^{+0.35}_{-0.23}$	$1.47^{+0.58}_{-0.50}$	18.03/12	-11.08	162	8.55
00090079079	$0.47^{+0.68}_{-0.47}$	$1.57^{+0.91}_{-0.77}$	8.95/8	-11.12	126	7.17
00090079080	$0.28^{+0.17}_{-0.15}$	$1.78^{+0.27}_{-0.25}$	35.30/34	-11.02	408	7.05
00090079081	$0.19^{+0.44}_{-0.19}$	$1.51^{+0.58}_{-0.43}$	13.68/11	-11.09	154	7.63
00090079082	$0.03^{+0.29}_{-0.03}$	$1.31^{+0.39}_{-0.23}$	4.75/15	-11.03	197	7.59
00090079083	$0.21^{+0.39}_{-0.21}$	$1.41^{+0.80}_{-0.62}$	12.12/10	-10.99	152	9.58
00090079084	$0.22^{+0.30}_{-0.22}$	$1.56^{+0.45}_{-0.40}$	13.66/17	-11.03	222	9.78
00090079085	$0.03^{+0.26}_{-0.03}$	$1.31^{+0.39}_{-0.23}$	21.96/17	-11.01	223	6.74
00090079086	$0.47^{+0.51}_{-0.39}$	$1.85^{+0.62}_{-0.55}$	11.84/14	-10.96	196	7.95
00090079087	$0.41^{+0.52}_{-0.41}$	$1.70^{+0.63}_{-0.56}$	19.95/14	-11.00	192	8.23
00090079088	$0.29^{+0.21}_{-0.17}$	$1.61^{+0.31}_{-0.28}$	21.64/31	-10.75	375	7.98
00090079090	$0.25^{+0.40}_{-0.25}$	$1.67^{+0.56}_{-0.48}$	9.07/12	-10.98	159	8.66
00090079091	$0.10^{+0.23}_{-0.10}$	$1.51^{+0.52}_{-0.41}$	7.36/11	-10.94	164	8.13
00090079092	$0.33^{+0.27}_{-0.20}$	$1.76^{+0.40}_{-0.35}$	13.30/21	-10.90	266	8.36
00090079093	$0.25^{+0.18}_{-0.14}$	$1.33^{+0.29}_{-0.27}$	22.41/31	-10.65	384	8.18
00090079094	$0.03^{+0.21}_{-0.03}$	$1.14^{+0.27}_{-0.18}$	28.12/29	-10.68	358	7.66
00090079095	$0.15^{+0.24}_{-0.15}$	$1.35^{+0.35}_{-0.32}$	25.04/24	-10.71	293	8.24
00090079096	$0.24^{+0.33}_{-0.24}$	$1.67^{+0.42}_{-0.37}$	14.39/19	-10.90	238	8.27
00090079097	$0.25^{+0.20}_{-0.16}$	$1.83^{+0.34}_{-0.30}$	24.92/24	-10.87	298	8.22
00090079098	$0.65^{+0.36}_{-0.29}$	$2.09^{+0.45}_{-0.40}$	22.30/22	-10.85	277	9.55
00090079099	$0.24^{+0.26}_{-0.18}$	$1.45^{+0.36}_{-0.32}$	22.34/23	-10.81	292	9.42

Table A.1 – *continued*

Obs ID	$N_{\rm H}{}^a$	Γ^b	χ^2/d.o.f.	$\log(f_{\rm X})^c$	Total counts^d	θ^e
00090079100	$0.31^{+0.21}_{-0.16}$	$1.74^{+0.32}_{-0.29}$	18.34/27	-10.80	322	8.21
00090079101	$0.49^{+0.35}_{-0.24}$	$1.96^{+0.36}_{-0.31}$	23.47/23	-10.89	280	8.28
00090079102	$0.50^{+0.25}_{-0.20}$	$1.99^{+0.38}_{-0.34}$	20.41/25	-10.87	323	9.07
00090079103	$0.31^{+0.19}_{-0.16}$	$1.60^{+0.29}_{-0.26}$	18.10/29	-10.81	342	9.08
00090989001	$0.28^{+0.19}_{-0.15}$	$1.80^{+0.37}_{-0.32}$	26.91/26	-10.87	327	7.54
00090989002	$0.51^{+0.28}_{-0.20}$	$1.81^{+0.29}_{-0.25}$	35.42/32	-10.84	376	7.35
00090989003	$0.25^{+0.18}_{-0.15}$	$1.52^{+0.30}_{-0.27}$	32.51/34	-10.85	396	10.45
00090989005	$0.15^{+0.19}_{-0.15}$	$1.64^{+0.35}_{-0.32}$	18.40/25	-10.84	314	9.30
00090989006	$0.80^{+0.72}_{-0.50}$	$2.49^{+0.71}_{-0.58}$	7.59/9	-10.98	134	7.56
00090989007	$0.33^{+0.17}_{-0.14}$	$1.70^{+0.26}_{-0.24}$	28.95/35	-10.73	410	7.72
00090989008	$0.37^{+0.36}_{-0.29}$	$1.97^{+0.51}_{-0.43}$	12.27/13	-11.18	174	7.10
00090989009	$0.03^{+0.44}_{-0.03}$	$0.97^{+0.65}_{-0.34}$	15.16/8	-11.14	122	8.27
00090989010	$0.25^{+0.29}_{-0.23}$	$1.67^{+0.50}_{-0.44}$	13.14/14	-11.06	192	8.98
00090989011	$0.33^{+0.28}_{-0.23}$	$2.07^{+0.44}_{-0.38}$	15.49/15	-11.23	203	7.10
00090989012	$0.22^{+0.22}_{-0.17}$	$1.44^{+0.31}_{-0.28}$	36.85/32	-10.76	378	7.01
00090989014	$0.30^{+0.24}_{-0.18}$	$1.63^{+0.34}_{-0.30}$	18.84/26	-10.79	324	7.90
00090989015	$0.65^{+0.25}_{-0.20}$	$2.53^{+0.36}_{-0.31}$	30.37/27	-10.96	333	7.23
00090989016	$0.31^{+0.21}_{-0.16}$	$1.70^{+0.32}_{-0.29}$	27.39/26	-10.86	312	8.55
00090993001	$0.28^{+0.17}_{-0.14}$	$1.48^{+0.26}_{-0.24}$	27.36/35	-10.75	424	9.46
00090993002	$0.21^{+0.34}_{-0.21}$	$1.52^{+0.45}_{-0.39}$	18.15/20	-10.92	254	8.82
00090993003	$0.26^{+0.38}_{-0.26}$	$1.63^{+0.44}_{-0.40}$	9.41/15	-10.91	201	9.78
00090993004	$0.38^{+0.44}_{-0.35}$	$2.00^{+0.70}_{-0.61}$	18.55/13	-11.07	188	8.97
00090993005	< 0.14	$1.09^{+0.29}_{-0.24}$	12.45/15	-10.88	200	9.08
00090993006	$0.29^{+0.30}_{-0.22}$	$1.71^{+0.41}_{-0.36}$	17.80/20	-11.04	251	8.79

Table A.1 – *continued*

Obs ID	$N_{\rm H}{}^a$	Γ^b	χ^2/d.o.f.	$\log(f_{\rm X})^c$	Total counts^d	θ^e
00090993007	$0.30^{+0.56}_{-0.30}$	$1.85^{+0.79}_{-0.63}$	8.72/11	-11.09	160	9.50
00090993008	$0.41^{+0.45}_{-0.34}$	$1.41^{+0.48}_{-0.43}$	15.13/13	-10.94	177	8.90
00090993009	< 0.32	$1.57^{+0.26}_{-0.25}$	7.29/12	-11.09	161	9.07
00090993010	$0.36^{+0.43}_{-0.34}$	$1.76^{+0.54}_{-0.47}$	6.60/13	-11.01	175	9.41
00090993011	$0.01^{+0.29}_{-0.01}$	$1.76^{+0.65}_{-0.28}$	17.30/13	-11.05	176	9.56
00090993012	$0.41^{+0.52}_{-0.39}$	$1.88^{+0.60}_{-0.53}$	13.22/11	-11.12	158	8.63
00090993013	$0.23^{+0.56}_{-0.23}$	$1.51^{+0.69}_{-0.52}$	6.51/9	-11.02	141	9.09
00090993014	$0.04^{+0.44}_{-0.04}$	$1.42^{+0.64}_{-0.34}$	10.99/10	-11.10	152	9.48
00090993015	$0.05^{+0.32}_{-0.05}$	$1.29^{+0.63}_{-0.36}$	10.87/9	-11.02	138	10.54
00090993016	$0.28^{+0.37}_{-0.28}$	$1.96^{+0.62}_{-0.53}$	9.54/12	-11.17	167	9.87
00090993017	$0.19^{+0.38}_{-0.19}$	$1.61^{+0.61}_{-0.49}$	8.06/11	-11.13	164	8.80
00090993018	0.30^*	1.6^*	4.58/6	-11.13	78	10.67
00090993019	< 0.32	$1.61^{+0.50}_{-0.42}$	10.45/7	-11.21	111	8.92
00090993020	$0.32^{+0.29}_{-0.23}$	$1.73^{+0.46}_{-0.40}$	6.41/13	-11.10	173	8.69
00090993022	< 0.34	$1.47^{+0.33}_{-0.31}$	6.68/9	-11.13	139	9.42
00090993023	$0.02^{+0.43}_{-0.02}$	$1.11^{+0.53}_{-0.27}$	8.10/10	-11.03	146	10.12
00090993024	$0.14^{+0.36}_{-0.14}$	$1.88^{+0.61}_{-0.44}$	19.06/12	-11.22	163	8.47
00090993025	$0.18^{+0.33}_{-0.18}$	$1.69^{+0.48}_{-0.40}$	4.39/16	-11.03	206	8.91
00090993026	$0.17^{+0.38}_{-0.17}$	$1.37^{+0.51}_{-0.39}$	14.70/14	-11.03	186	8.18
00090993027	$0.20^{+0.49}_{-0.20}$	$1.54^{+0.64}_{-0.48}$	13.42/11	-11.05	160	9.49
00090993028	$0.23^{+0.32}_{-0.23}$	$1.71^{+0.52}_{-0.46}$	7.46/16	-11.00	213	8.32
00090993029	$0.27^{+0.36}_{-0.27}$	$1.90^{+0.65}_{-0.55}$	17.34/14	-11.08	197	10.20
00090993030	$0.27^{+0.34}_{-0.27}$	$1.96^{+0.48}_{-0.42}$	16.19/16	-11.09	204	8.61
00090993031	$0.22^{+0.43}_{-0.22}$	$1.84^{+0.52}_{-0.41}$	15.84/14	-11.13	185	8.11

Table A.1 – *continued*

Obs ID	$N_{\rm H}{}^a$	Γ^b	χ^2/d.o.f.	$\log(f_{\rm X})^c$	Total counts^d	θ^e
00090993032	< 0.32	$1.29^{+0.30}_{-0.29}$	16.78/13	-11.00	185	9.01
00090993033	$0.10^{+0.38}_{-0.10}$	$1.25^{+0.54}_{-0.36}$	11.95/13	-10.98	180	8.02
00090993034	$0.37^{+0.32}_{-0.26}$	$2.12^{+0.57}_{-0.49}$	5.50/15	-11.16	199	8.71
00090993035	$0.22^{+0.43}_{-0.22}$	$1.60^{+0.54}_{-0.45}$	12.00/11	-11.13	158	8.99
00090993036	$0.24^{+0.33}_{-0.24}$	$1.58^{+0.44}_{-0.39}$	10.97/15	-11.05	199	5.77
00090993037	$0.16^{+0.39}_{-0.16}$	$1.43^{+0.61}_{-0.45}$	8.57/11	-11.04	159	9.01
00090993038	0.30^*	1.6^*	10.44/3	-11.23	56	10.31
00090993039	$0.14^{+0.38}_{-0.14}$	$1.81^{+0.52}_{-0.38}$	8.90/12	-11.15	175	8.83
00090993040	$0.05^{+0.27}_{-0.05}$	$1.37^{+0.40}_{-0.25}$	14.15/16	-11.00	209	8.74
00090993041	$0.20^{+0.37}_{-0.20}$	$1.37^{+0.43}_{-0.37}$	12.64/14	-11.02	187	8.71
00090993042	$0.36^{+0.39}_{-0.32}$	$1.78^{+0.55}_{-0.47}$	10.99/13	-11.05	177	10.93
00090993043	$0.05^{+0.33}_{-0.05}$	$1.41^{+0.62}_{-0.35}$	15.52/12	-11.05	167	9.74
00090993044	$0.40^{+0.49}_{-0.37}$	$1.84^{+0.58}_{-0.48}$	15.47/13	-11.15	178	9.16
00090993046	< 0.26	$1.02^{+0.39}_{-0.27}$	15.23/11	-10.96	159	10.65
00090993047	< 0.32	$0.91^{+0.32}_{-0.32}$	19.48/11	-10.91	159	10.30
00090993048	< 0.47	$1.23^{+0.57}_{-0.26}$	7.95/9	-11.05	133	9.94
00090993049	$0.20^{+0.43}_{-0.20}$	$1.86^{+0.67}_{-0.50}$	2.12/8	-11.19	126	10.61
00090993050	< 0.35	$1.25^{+0.53}_{-0.33}$	10.58/8	-11.05	124	10.47
00090993051	< 0.28	$1.12^{+0.43}_{-0.27}$	8.62/10	-11.05	147	9.23
00090993052	$0.06^{+0.59}_{-0.06}$	$1.29^{+0.82}_{-0.41}$	2.70/7	-11.10	118	7.62
00090993053	< 0.21	$1.32^{+0.36}_{-0.27}$	11.96/9	-11.12	136	8.32
00090993054	$0.14^{+0.41}_{-0.14}$	$1.39^{+0.68}_{-0.47}$	11.67/9	-11.14	134	8.26
00090993055	$0.03^{+0.24}_{-0.03}$	$1.52^{+0.58}_{-0.33}$	5.01/8	-11.17	119	8.83
00090993056	< 0.37	$1.25^{+0.63}_{-0.34}$	2.63/6	-11.12	108	8.81

Table A.1 – *continued*

Obs ID	$N_{\rm H}{}^a$	Γ^b	χ^2/d.o.f.	$\log(f_{\rm X})^c$	Total counts^d	θ^e
00090993057	< 0.21	$1.23^{+0.47}_{-0.39}$	8.04/8	-11.06	129	7.83
00090993058	< 0.00	$1.08^{+0.35}_{-0.35}$	7.03/7	-11.07	118	7.97
00090993059	$0.11^{+0.32}_{-0.11}$	$1.17^{+0.57}_{-0.42}$	4.93/10	-10.91	146	9.13
00090993060	< 0.55	$1.15^{+0.52}_{-0.27}$	9.94/8	-11.09	122	7.62
00090993061	$0.27^{+0.56}_{-0.27}$	$1.91^{+0.83}_{-0.61}$	4.92/6	-11.32	102	8.67
00090993062	$0.01^{+0.49}_{-0.01}$	$1.27^{+0.68}_{-0.31}$	4.78/8	-11.10	132	8.32
00090993063	< 0.49	$1.43^{+0.76}_{-0.36}$	7.35/6	-11.22	110	9.92
00090993064	$0.58^{+0.81}_{-0.57}$	$1.70^{+0.74}_{-0.63}$	4.21/7	-11.25	116	8.50
00090993065	< 0.32	$1.05^{+0.34}_{-0.34}$	13.60/9	-11.07	134	8.99
00090993066	$0.07^{+0.28}_{-0.07}$	$1.41^{+0.53}_{-0.35}$	4.54/9	-11.12	138	9.66
00090993067	$0.34^{+0.36}_{-0.30}$	$1.96^{+0.62}_{-0.52}$	11.10/12	-11.16	173	9.79
00090993069	0.30^*	1.6^*	7.58/7	-11.17	93	9.94
00090993070	< 0.21	$1.20^{+0.38}_{-0.33}$	9.81/8	-11.08	124	9.55
00090993071	< 0.22	$1.21^{+0.36}_{-0.24}$	10.57/13	-11.07	173	9.48
00090993072	$0.42^{+0.48}_{-0.39}$	$1.73^{+0.61}_{-0.54}$	12.69/12	-11.23	170	9.61
00090993074	$0.27^{+0.40}_{-0.27}$	$1.44^{+0.54}_{-0.49}$	5.94/11	-11.05	159	9.68
00090993075	$0.16^{+0.73}_{-0.16}$	$1.29^{+1.02}_{-0.55}$	5.61/6	-11.10	103	10.52
00259527001	$0.15^{+0.15}_{-0.12}$	$1.50^{+0.24}_{-0.22}$	30.09/40	-10.88	466	7.50

Note. [a]Absorption column external to our Galaxy ($\times$ 10^{22} cm^{-2}). [b]Power-law photon index. [c]Logarithm of observed flux in the 0.3-10 keV band (erg cm^{-2} s^{-1}). [d]Total spectral counts in the 0.3-10 keV energy band. [e]The off-axis angle of the source from the *Swift* XRT detector aim point. [*]The parameter is frozen during the spectral fit.

Appendix B

A catalogue of point sources detected in the LIRG sample

Here we present the catalogue of all X-ray point source detections in the *Chandra* observations of our sample of 17 LIRGs. For convenience we have divided the sources into two tables: the ULX catalogue (sources with $L_X \geq 10^{39}$ erg s^{-1}; Table B.1); and the catalogue of less luminous X-ray point sources (Table B.2).

Table B.1: ULX candidates

RA	Dec	Host galaxy	Net counts	Flux	Luminosity	Notes
(1)	(2)	(3)	(4)	(5)	(6)	(7)
00 09 53	+ 25 55 48	NGC 23	$6.62^{+3.78}_{-2.58}$	$0.27^{+0.16}_{-0.11}$	$1.20^{+0.68}_{-0.47}$	
00 09 53	+ 25 55 39	NGC 23	$10.66^{+4.43}_{-3.26}$	$0.44^{+0.18}_{-0.13}$	$1.93^{+0.80}_{-0.59}$	
02 09 38	– 10 08 47	NGC 838	$10.27^{+4.43}_{-3.26}$	$0.58^{+0.25}_{-0.19}$	$1.80^{+0.78}_{-0.57}$	
02 09 39	– 10 08 44	NGC 838	$11.83^{+4.57}_{-3.41}$	$0.67^{+0.26}_{-0.19}$	$2.08^{+0.80}_{-0.60}$	
02 42 38	– 00 01 18	NGC 1068	$385.72^{+20.72}_{-19.69}$	$6.44^{+0.35}_{-0.33}$	$1.46^{+0.08}_{-0.07}$	
02 42 39	– 00 00 55	NGC 1068	$1370.25^{+38.09}_{-37.08}$	$22.87^{+0.64}_{-0.62}$	5.17 ± 0.14	1
02 42 40	– 00 01 01	NGC 1068	$487.09^{+23.84}_{-22.81}$	$8.13^{+0.40}_{-0.38}$	1.84 ± 0.09	
03 33 32	– 36 08 09	NGC 1365	$68.79^{+9.35}_{-8.28}$	$4.02^{+0.55}_{-0.48}$	$1.57^{+0.21}_{-0.19}$	

Table B.1 – *continued*

RA	Dec	Host galaxy	Net counts	Flux	Luminosity	Notes
(1)	(2)	(3)	(4)	(5)	(6)	(7)
03 33 34	– 36 11 03	NGC 1365	$123.75^{+12.17}_{-11.12}$	$7.24^{+0.71}_{-0.65}$	$2.82^{+0.28}_{-0.25}$	
03 33 35	– 36 09 37	NGC 1365	$204.89^{+15.34}_{-14.30}$	$11.99^{+0.90}_{-0.84}$	$4.66^{+0.35}_{-0.33}$	
03 33 38	– 36 09 35	NGC 1365	$111.89^{+11.62}_{-10.57}$	$6.55^{+0.68}_{-0.62}$	$2.55^{+0.26}_{-0.24}$	
03 33 40	– 36 07 27	NGC 1365	$68.83^{+9.35}_{-8.28}$	$4.03^{+0.55}_{-0.48}$	$1.57^{+0.21}_{-0.19}$	
03 33 50	– 36 10 26	NGC 1365	$32.88^{+6.81}_{-5.71}$	$2.80^{+0.58}_{-0.49}$	$1.09^{+0.23}_{-0.19}$	
10 22 20	+ 21 34 02	NGC 3221	$16.61^{+5.21}_{-4.08}$	$0.69^{+0.22}_{-0.17}$	$2.91^{+0.91}_{-0.71}$	
10 22 20	+ 21 33 29	NGC 3221	$14.82^{+4.97}_{-3.83}$	$0.61^{+0.21}_{-0.16}$	$2.60^{+0.87}_{-0.67}$	
10 22 20	+ 21 34 50	NGC 3221	$16.74^{+5.21}_{-4.08}$	$0.69^{+0.22}_{-0.17}$	$2.93^{+0.91}_{-0.71}$	
10 22 20	+ 21 34 05	NGC 3221	$6.63^{+3.78}_{-2.58}$	$0.27^{+0.16}_{-0.11}$	$1.16^{+0.66}_{-0.45}$	
10 22 21	+ 21 33 36	NGC 3221	$14.73^{+4.97}_{-3.83}$	$0.61^{+0.21}_{-0.16}$	$2.58^{+0.87}_{-0.67}$	
10 22 22	+ 21 33 25	NGC 3221	$14.87^{+4.97}_{-3.83}$	$0.62^{+0.21}_{-0.16}$	$2.61^{+0.87}_{-0.67}$	
11 28 27	+ 58 34 07	Arp 299	$16.81^{+5.21}_{-4.08}$	$0.80^{+0.25}_{-0.19}$	$2.22^{+0.69}_{-0.54}$	
11 28 31	+ 58 33 45	Arp 299	$62.30^{+9.84}_{-8.77}$	$2.96^{+0.47}_{-0.42}$	$8.24^{+1.30}_{-1.16}$	
11 28 31	+ 58 33 27	Arp 299	$12.03^{+4.71}_{-3.56}$	$0.57^{+0.22}_{-0.17}$	$1.59^{+0.62}_{-0.47}$	
11 28 32	+ 58 33 18	Arp 299	$48.52^{+8.05}_{-6.97}$	$2.30^{+0.38}_{-0.33}$	$6.42^{+1.06}_{-0.92}$	
11 28 33	+ 58 33 37	Arp 299	$28.32^{+6.55}_{-5.45}$	$1.35^{+0.31}_{-0.26}$	$3.74^{+0.87}_{-0.72}$	2
11 28 33	+ 58 34 03	Arp 299	$32.87^{+6.90}_{-5.80}$	$1.56^{+0.33}_{-0.28}$	$4.34^{+0.91}_{-0.77}$	
11 28 34	+ 58 33 41	Arp 299	$28.02^{+6.55}_{-5.45}$	$1.33^{+0.31}_{-0.26}$	$3.70^{+0.87}_{-0.72}$	
11 28 37	+ 58 33 41	Arp 299	$10.84^{+4.43}_{-3.26}$	$0.51^{+0.21}_{-0.15}$	$1.43^{+0.59}_{-0.43}$	
12 14 10	+ 54 31 27	NGC 4194	$25.27^{+6.56}_{-5.46}$	$0.56^{+0.15}_{-0.12}$	$1.11^{+0.29}_{-0.24}$	
13 25 43	– 29 50 06	NGC 5135	$12.57^{+4.71}_{-3.55}$	$0.40^{+0.15}_{-0.11}$	$1.35^{+0.51}_{-0.38}$	
13 25 45	– 29 50 04	NGC 5135	$31.36^{+6.81}_{-5.72}$	$1.01^{+0.22}_{-0.18}$	$3.37^{+0.73}_{-0.62}$	
13 25 45	– 29 50 14	NGC 5135	$20.53^{+5.66}_{-4.54}$	$0.66^{+0.18}_{-0.15}$	$2.21^{+0.61}_{-0.49}$	
13 25 45	– 29 50 12	NGC 5135	$9.64^{+4.28}_{-3.10}$	$0.31^{+0.14}_{-0.10}$	$1.04^{+0.46}_{-0.33}$	
13 25 45	– 29 50 07	NGC 5135	$13.69^{+4.84}_{-3.69}$	$0.44^{+0.16}_{-0.12}$	$1.47^{+0.52}_{-0.40}$	
13 25 48	– 29 49 48	NGC 5135	$27.77^{+6.36}_{-5.26}$	$0.89^{+0.20}_{-0.17}$	$2.99^{+0.68}_{-0.57}$	
13 58 38	+ 37 25 33	NGC 5395	$7.70^{+3.96}_{-2.76}$	$0.39^{+0.20}_{-0.14}$	$1.35^{+0.69}_{-0.48}$	
13 58 38	+ 37 24 41	NGC 5395	$8.80^{+4.12}_{-2.94}$	$0.44^{+0.21}_{-0.15}$	$1.54^{+0.72}_{-0.51}$	

Table B.1 – *continued*

RA	Dec	Host galaxy	Net counts	Flux	Luminosity	Notes
(1)	(2)	(3)	(4)	(5)	(6)	(7)
13 58 39	+ 37 25 32	NGC 5395	$13.68^{+4.84}_{-3.69}$	$0.69^{+0.24}_{-0.19}$	$2.40^{+0.85}_{-0.65}$	
13 58 40	+ 37 26 28	NGC 5395	$6.87^{+3.78}_{-2.58}$	$0.34^{+0.19}_{-0.13}$	$1.20^{+0.66}_{-0.45}$	
14 30 11	+ 31 13 00	NGC 5653	$7.54^{+3.96}_{-2.76}$	$0.36^{+0.19}_{-0.13}$	$1.32^{+0.69}_{-0.48}$	
22 16 08	– 36 50 56	IC 5179	$13.61^{+4.84}_{-3.69}$	$0.89^{+0.32}_{-0.24}$	$2.38^{+0.85}_{-0.65}$	
22 16 08	– 36 50 19	IC 5179	$7.85^{+3.96}_{-2.76}$	$0.52^{+0.26}_{-0.18}$	$1.37^{+0.69}_{-0.48}$	
22 16 10	– 36 50 40	IC 5179	$14.30^{+4.97}_{-3.83}$	$0.94^{+0.33}_{-0.25}$	$2.51^{+0.87}_{-0.67}$	
22 16 10	– 36 50 34	IC 5179	$6.43^{+3.78}_{-2.58}$	$0.42^{+0.25}_{-0.17}$	$1.13^{+0.66}_{-0.45}$	
22 16 10	– 36 50 20	IC 5179	$36.62^{+7.14}_{-6.05}$	$2.41^{+0.47}_{-0.40}$	$6.42^{+1.25}_{-1.06}$	
22 16 10	– 36 50 24	IC 5179	$6.57^{+3.78}_{-2.58}$	$0.43^{+0.25}_{-0.17}$	$1.15^{+0.66}_{-0.45}$	
22 16 12	– 36 50 24	IC 5179	$12.83^{+4.71}_{-3.55}$	$0.84^{+0.31}_{-0.23}$	$2.25^{+0.83}_{-0.62}$	
22 16 12	– 36 50 09	IC 5179	$19.81^{+5.56}_{-4.43}$	$1.30^{+0.36}_{-0.29}$	$3.47^{+0.97}_{-0.78}$	
23 16 14	– 42 35 02	NGC 7552	$50.89^{+8.19}_{-7.12}$	$7.87^{+1.27}_{-1.10}$	$4.37^{+0.70}_{-0.61}$	
23 16 16	– 42 35 18	NGC 7552	$11.94^{+4.57}_{-3.41}$	$1.85^{+0.71}_{-0.53}$	$1.03^{+0.39}_{-0.29}$	
23 51 22	+ 20 06 39	NGC 7771	$28.82^{+6.45}_{-5.35}$	$1.35^{+0.30}_{-0.25}$	$5.44^{+1.22}_{-1.01}$	
23 51 24	+ 20 06 38	NGC 7771	$9.67^{+4.28}_{-3.10}$	$0.45^{+0.20}_{-0.15}$	$1.82^{+0.81}_{-0.59}$	
23 51 24	+ 20 06 43	NGC 7771	$18.68^{+5.44}_{-4.32}$	$0.88^{+0.26}_{-0.20}$	$3.53^{+1.03}_{-0.81}$	
23 51 28	+ 20 06 52	NGC 7771	$34.72^{+6.98}_{-5.89}$	$1.63^{+0.33}_{-0.28}$	$6.55^{+1.32}_{-1.11}$	

Notes. The candidate ULX detections, ordered by right ascension (RA). Column 1 and 2: right ascension and declination, at epoch J2000, respectively. Column 3: host galaxy. Column 4: net photon counts. Column 5: source flux (10^{-14} erg cm^{-1} s^{-1}). Column 6: source luminosity, assuming the source is at the distance of the host galaxy (10^{39} erg s^{-1}). Columns 4 – 6 are all quoted from data in the 0.3–10 keV energy band. Column 7: additional notes for the ULXs: (1) CXOU J024238.9-000055 (Smith & Wilson, 2003); (2) This ULX is coincident with a radio source detection. This may be related to the ULX; it may be an unrelated radio supernova in the host galaxy; or it might be a background AGN (Ulvestad 2009; Neff et al. 2004; Huang et al. 1990).

Table B.2: Less luminous X-ray point sources

RA	Dec	Host galaxy	Net counts	Flux	Luminosity	Notes
(1)	(2)	(3)	(4)	(5)	(6)	(7)
00 09 53	+ 25 54 55	NGC 23	$3.78^{+3.18}_{-1.91}$	$0.16^{+0.13}_{-0.08}$	$0.68^{+0.57}_{-0.34}$	
00 09 55	+ 25 55 25	NGC 23	$5.29^{+3.60}_{-2.38}$	$0.22^{+0.15}_{-0.10}$	$0.96^{+0.65}_{-0.43}$	
02 09 39	– 10 08 38	NGC 838	$4.73^{+3.40}_{-2.15}$	$0.27^{+0.19}_{-0.12}$	$0.83^{+0.60}_{-0.38}$	
02 42 33	– 00 01 05	NGC 1068	$58.24^{+8.73}_{-7.66}$	$0.97^{+0.15}_{-0.13}$	0.22 ± 0.03	
02 42 33	– 00 01 30	NGC 1068	$4.35^{+3.40}_{-2.15}$	$0.07^{+0.06}_{-0.04}$	0.02 ± 0.01	
02 42 37	+ 00 00 13	NGC 1068	$10.25^{+4.43}_{-3.26}$	$0.17^{+0.07}_{-0.05}$	$0.04^{+0.02}_{-0.01}$	
02 42 37	– 00 00 28	NGC 1068	$12.05^{+4.71}_{-3.56}$	$0.20^{+0.08}_{-0.06}$	$0.05^{+0.02}_{-0.01}$	
02 42 37	– 00 01 09	NGC 1068	$38.92^{+7.38}_{-6.30}$	$0.65^{+0.12}_{-0.11}$	$0.15^{+0.03}_{-0.02}$	
02 42 37	– 00 00 19	NGC 1068	$8.06^{+4.12}_{-2.94}$	$0.13^{+0.07}_{-0.05}$	$0.03^{+0.02}_{-0.01}$	
02 42 38	– 00 00 29	NGC 1068	$49.79^{+8.19}_{-7.12}$	$0.83^{+0.14}_{-0.12}$	0.19 ± 0.03	
02 42 38	– 00 01 43	NGC 1068	$29.50^{+6.64}_{-5.54}$	$0.49^{+0.11}_{-0.09}$	$0.11^{+0.03}_{-0.02}$	
02 42 38	– 00 01 37	NGC 1068	$8.59^{+4.58}_{-3.42}$	$0.14^{+0.08}_{-0.06}$	$0.03^{+0.02}_{-0.01}$	
02 42 39	– 00 00 50	NGC 1068	$34.66^{+7.56}_{-6.47}$	$0.58^{+0.13}_{-0.11}$	$0.13^{+0.03}_{-0.02}$	
02 42 39	– 00 00 52	NGC 1068	$23.56^{+6.77}_{-5.67}$	$0.39^{+0.11}_{-0.09}$	$0.09^{+0.03}_{-0.02}$	
02 42 39	– 00 01 23	NGC 1068	$36.77^{+7.55}_{-6.47}$	$0.61^{+0.13}_{-0.11}$	$0.14^{+0.03}_{-0.02}$	
02 42 39	– 00 00 57	NGC 1068	$38.83^{+8.03}_{-6.95}$	$0.65^{+0.13}_{-0.12}$	0.15 ± 0.03	
02 42 39	– 00 01 31	NGC 1068	$12.27^{+5.10}_{-3.97}$	$0.20^{+0.09}_{-0.07}$	$0.05^{+0.02}_{-0.01}$	
02 42 39	– 00 00 35	NGC 1068	$70.92^{+9.77}_{-8.70}$	$1.18^{+0.16}_{-0.15}$	$0.27^{+0.04}_{-0.03}$	
02 42 39	– 00 01 04	NGC 1068	$57.03^{+8.93}_{-7.86}$	$0.95^{+0.15}_{-0.13}$	0.22 ± 0.03	
02 42 40	– 00 00 28	NGC 1068	$183.48^{+14.67}_{-13.63}$	$3.06^{+0.24}_{-0.23}$	$0.69^{+0.06}_{-0.05}$	
02 42 40	– 00 00 38	NGC 1068	$57.47^{+12.80}_{-11.76}$	$0.96^{+0.21}_{-0.20}$	$0.22^{+0.05}_{-0.04}$	
02 42 41	– 00 00 37	NGC 1068	$174.24^{+17.01}_{-15.98}$	$2.91^{+0.28}_{-0.27}$	0.66 ± 0.06	
02 42 41	– 00 01 32	NGC 1068	$24.69^{+6.27}_{-5.16}$	$0.41^{+0.10}_{-0.09}$	0.09 ± 0.02	
02 42 41	– 00 00 60	NGC 1068	$100.64^{+11.75}_{-10.70}$	$1.68^{+0.20}_{-0.18}$	0.38 ± 0.04	
02 42 41	– 00 01 44	NGC 1068	$32.82^{+6.90}_{-5.80}$	$0.55^{+0.12}_{-0.10}$	$0.12^{+0.03}_{-0.02}$	

Table B.2 – *continued*

RA	Dec	Host galaxy	Net counts	Flux	Luminosity	Notes
(1)	(2)	(3)	(4)	(5)	(6)	(7)
02 42 41	− 00 01 25	NGC 1068	$35.90^{+7.31}_{-6.22}$	$0.60^{+0.12}_{-0.10}$	$0.14^{+0.03}_{-0.02}$	
02 42 41	− 00 02 15	NGC 1068	$33.45^{+6.90}_{-5.80}$	$0.56^{+0.12}_{-0.10}$	$0.13^{+0.03}_{-0.02}$	
02 42 41	− 00 02 53	NGC 1068	$8.36^{+4.12}_{-2.94}$	$0.14^{+0.07}_{-0.05}$	$0.03^{+0.02}_{-0.01}$	
02 42 42	− 00 01 22	NGC 1068	$7.72^{+4.28}_{-3.11}$	$0.13^{+0.07}_{-0.05}$	$0.03^{+0.02}_{-0.01}$	
02 42 42	− 00 01 09	NGC 1068	$14.50^{+5.34}_{-4.21}$	$0.24^{+0.09}_{-0.07}$	0.05 ± 0.02	
02 42 42	+ 00 00 02	NGC 1068	$29.16^{+6.73}_{-5.63}$	$0.49^{+0.11}_{-0.09}$	$0.11^{+0.03}_{-0.02}$	
02 42 43	− 00 00 52	NGC 1068	$18.12^{+5.67}_{-4.55}$	$0.30^{+0.09}_{-0.08}$	0.07 ± 0.02	
02 42 43	− 00 00 48	NGC 1068	$19.87^{+5.88}_{-4.76}$	$0.33^{+0.10}_{-0.08}$	0.08 ± 0.02	
02 42 43	+ 00 00 23	NGC 1068	$10.92^{+4.71}_{-3.56}$	$0.18^{+0.08}_{-0.06}$	$0.04^{+0.02}_{-0.01}$	
02 42 43	− 00 00 04	NGC 1068	$10.62^{+5.59}_{-4.47}$	$0.18^{+0.09}_{-0.07}$	0.04 ± 0.02	
02 42 43	− 00 02 45	NGC 1068	$60.48^{+8.86}_{-7.79}$	$1.01^{+0.15}_{-0.13}$	0.23 ± 0.03	
02 42 43	− 00 01 40	NGC 1068	$110.24^{+11.57}_{-10.52}$	$1.84^{+0.19}_{-0.18}$	0.42 ± 0.04	
02 42 44	− 00 00 35	NGC 1068	$95.72^{+10.94}_{-9.88}$	$1.60^{+0.18}_{-0.16}$	0.36 ± 0.04	
02 42 45	− 00 00 10	NGC 1068	$61.82^{+8.98}_{-7.91}$	$1.03^{+0.15}_{-0.13}$	0.23 ± 0.03	
02 42 45	− 00 01 27	NGC 1068	$7.33^{+3.96}_{-2.76}$	$0.12^{+0.07}_{-0.05}$	0.03 ± 0.01	
02 42 45	− 00 02 19	NGC 1068	$51.43^{+8.26}_{-7.19}$	$0.86^{+0.14}_{-0.12}$	0.19 ± 0.03	
02 42 46	− 00 00 30	NGC 1068	$29.05^{+6.55}_{-5.45}$	$0.49^{+0.11}_{-0.09}$	0.11 ± 0.02	
02 42 46	+ 00 00 06	NGC 1068	$17.92^{+5.44}_{-4.32}$	$0.30^{+0.09}_{-0.07}$	0.07 ± 0.02	
02 42 47	− 00 01 13	NGC 1068	$6.29^{+3.78}_{-2.58}$	$0.11^{+0.06}_{-0.04}$	0.02 ± 0.01	
02 42 47	+ 00 00 28	NGC 1068	$167.85^{+14.03}_{-12.99}$	$2.80^{+0.23}_{-0.22}$	0.63 ± 0.05	
03 33 21	− 36 08 15	NGC 1365	$21.48^{+5.77}_{-4.65}$	$1.26^{+0.34}_{-0.27}$	$0.49^{+0.13}_{-0.11}$	
03 33 23	− 36 07 53	NGC 1365	$38.58^{+7.31}_{-6.22}$	$2.26^{+0.43}_{-0.36}$	$0.88^{+0.17}_{-0.14}$	
03 33 24	− 36 10 50	NGC 1365	$7.42^{+3.96}_{-2.76}$	$0.43^{+0.23}_{-0.16}$	$0.17^{+0.09}_{-0.06}$	
03 33 26	− 36 08 38	NGC 1365	$21.74^{+5.77}_{-4.65}$	$1.27^{+0.34}_{-0.27}$	$0.49^{+0.13}_{-0.11}$	
03 33 26	− 36 08 50	NGC 1365	$22.78^{+5.87}_{-4.76}$	$1.33^{+0.34}_{-0.28}$	$0.52^{+0.13}_{-0.11}$	
03 33 27	− 36 08 14	NGC 1365	$11.76^{+4.57}_{-3.41}$	$0.69^{+0.27}_{-0.20}$	$0.27^{+0.10}_{-0.08}$	
03 33 30	− 36 07 56	NGC 1365	$7.77^{+3.96}_{-2.76}$	$0.45^{+0.23}_{-0.16}$	$0.18^{+0.09}_{-0.06}$	
03 33 30	− 36 08 30	NGC 1365	$35.75^{+7.06}_{-5.97}$	$2.09^{+0.41}_{-0.35}$	$0.81^{+0.16}_{-0.14}$	

Table B.2 – *continued*

RA	Dec	Host galaxy	Net counts	Flux	Luminosity	Notes
(1)	(2)	(3)	(4)	(5)	(6)	(7)
03 33 30	– 36 08 21	NGC 1365	$10.73^{+4.43}_{-3.26}$	$0.63^{+0.26}_{-0.19}$	$0.24^{+0.10}_{-0.07}$	
03 33 31	– 36 11 06	NGC 1365	$7.71^{+3.96}_{-2.76}$	$0.45^{+0.23}_{-0.16}$	$0.18^{+0.09}_{-0.06}$	
03 33 31	– 36 08 08	NGC 1365	$11.78^{+4.57}_{-3.41}$	$0.69^{+0.27}_{-0.20}$	$0.27^{+0.10}_{-0.08}$	
03 33 32	– 36 06 43	NGC 1365	$42.65^{+7.61}_{-6.53}$	$2.50^{+0.45}_{-0.38}$	$0.97^{+0.17}_{-0.15}$	
03 33 32	– 36 09 03	NGC 1365	$19.87^{+5.56}_{-4.43}$	$1.16^{+0.32}_{-0.26}$	$0.45^{+0.13}_{-0.10}$	
03 33 33	– 36 07 15	NGC 1365	$4.81^{+3.40}_{-2.15}$	$0.28^{+0.20}_{-0.13}$	$0.11^{+0.08}_{-0.05}$	
03 33 36	– 36 08 21	NGC 1365	$25.57^{+6.56}_{-5.46}$	$1.50^{+0.38}_{-0.32}$	$0.58^{+0.15}_{-0.12}$	
03 33 36	– 36 05 57	NGC 1365	$4.62^{+3.40}_{-2.15}$	$0.27^{+0.20}_{-0.13}$	$0.11^{+0.08}_{-0.05}$	
03 33 36	– 36 09 58	NGC 1365	$8.91^{+4.12}_{-2.94}$	$0.52^{+0.24}_{-0.17}$	$0.20^{+0.09}_{-0.07}$	
03 33 37	– 36 10 26	NGC 1365	$17.80^{+5.33}_{-4.20}$	$1.04^{+0.31}_{-0.25}$	$0.40^{+0.12}_{-0.10}$	
03 33 39	– 36 08 01	NGC 1365	$4.80^{+3.40}_{-2.15}$	$0.28^{+0.20}_{-0.13}$	$0.11^{+0.08}_{-0.05}$	
03 33 39	– 36 05 24	NGC 1365	$13.43^{+4.84}_{-3.69}$	$0.79^{+0.28}_{-0.22}$	$0.31^{+0.11}_{-0.08}$	
03 33 39	– 36 10 02	NGC 1365	$20.82^{+5.66}_{-4.54}$	$1.22^{+0.33}_{-0.27}$	$0.47^{+0.13}_{-0.10}$	
03 33 40	– 36 10 37	NGC 1365	$31.85^{+6.72}_{-5.62}$	$1.86^{+0.39}_{-0.33}$	$0.72^{+0.15}_{-0.13}$	
03 33 42	– 36 08 19	NGC 1365	$4.87^{+3.40}_{-2.15}$	$0.29^{+0.20}_{-0.13}$	$0.11^{+0.08}_{-0.05}$	
03 33 42	- 36 07 41	NGC 1365	$18.79^{+5.44}_{-4.32}$	$1.10^{+0.32}_{-0.25}$	$0.43^{+0.12}_{-0.10}$	
11 28 34	+ 58 33 24	Arp 299	$6.41^{+3.78}_{-2.58}$	$0.30^{+0.18}_{-0.12}$	$0.85^{+0.50}_{-0.34}$	
12 14 09	+ 54 31 45	NGC 4194	$13.84^{+4.97}_{-3.83}$	$0.31^{+0.11}_{-0.09}$	$0.61^{+0.22}_{-0.17}$	
12 14 10	+ 54 31 42	NGC 4194	$11.61^{+4.57}_{-3.41}$	$0.26^{+0.10}_{-0.08}$	$0.51^{+0.20}_{-0.15}$	
12 14 13	+ 54 31 29	NGC 4194	$5.59^{+3.60}_{-2.38}$	$0.14^{+0.08}_{-0.06}$	$0.27^{+0.17}_{-0.15}$	
12 26 54	– 00 52 54	NGC 4418	$7.78^{+3.96}_{-2.76}$	$0.31^{+0.16}_{-0.11}$	$0.38^{+0.20}_{-0.14}$	
13 25 44	– 29 49 33	NGC 5135	$7.67^{+3.96}_{-2.76}$	$0.25^{+0.13}_{-0.09}$	$0.82^{+0.43}_{-0.30}$	
13 58 40	+ 37 24 45	NGC 5395	$2.86^{+2.94}_{-1.63}$	$0.14^{+0.15}_{-0.08}$	$0.50^{+0.51}_{-0.29}$	
14 30 10	+ 31 12 33	NGC 5653	$4.80^{+3.40}_{-2.15}$	$0.23^{+0.16}_{-0.10}$	$0.84^{+0.60}_{-0.38}$	
23 16 08	– 42 34 36	NGC 7552	$3.93^{+3.18}_{-1.91}$	$0.61^{+0.49}_{-0.30}$	$0.34^{+0.27}_{-0.16}$	
23 16 10	– 42 35 08	NGC 7552	$3.92^{+3.18}_{-1.91}$	$0.61^{+0.49}_{-0.30}$	$0.34^{+0.27}_{-0.16}$	
23 16 11	– 42 34 43	NGC 7552	$8.82^{+4.12}_{-2.94}$	$1.36^{+0.64}_{-0.45}$	$0.76^{+0.35}_{-0.25}$	
23 16 14	– 42 35 40	NGC 7552	$10.95^{+4.43}_{-3.26}$	$1.69^{+0.68}_{-0.50}$	$0.94^{+0.38}_{-0.28}$	

Table B.2 – *continued*

RA	Dec	Host galaxy	Net counts	Flux	Luminosity	Notes
(1)	(2)	(3)	(4)	(5)	(6)	(7)
23 16 17	– 42 35 00	NGC 7552	$7.93^{+3.96}_{-2.76}$	$1.23^{+0.61}_{-0.43}$	$0.68^{+0.34}_{-0.24}$	
23 51 24	+ 20 06 19	NGC 7771	$2.81^{+2.94}_{-1.63}$	$0.13^{+0.14}_{-0.08}$	$0.53^{+0.55}_{-0.31}$	
23 51 26	+ 20 06 47	NGC 7771	$4.62^{+3.40}_{-2.15}$	$0.22^{+0.16}_{-0.10}$	$0.87^{+0.64}_{-0.41}$	
23 51 26	+ 20 06 55	NGC 7771	$3.64^{+3.18}_{-1.91}$	$0.17^{+0.15}_{-0.09}$	$0.69^{+0.60}_{-0.36}$	
23 51 27	+ 20 06 31	NGC 7771	$4.79^{+3.40}_{-2.15}$	$0.23^{+0.16}_{-0.10}$	$0.90^{+0.64}_{-0.41}$	

Notes. The columns are as per Table B.1

Bibliography

Abramowicz M. A., Czerny B., Lasota J. P., Szuszkiewicz E., 1988, ApJ, 332, 646

Avni Y., 1976, ApJ, 210, 642

Bachetti M., et al., 2013, ApJ, 778, 163

Bachetti M., et al., 2014, Nature, 514, 202

Bai J. M., Lee M. G., 2001, ApJ, 558, L19

Ballo L., Braito V., Della Ceca R., Maraschi L., Tavecchio F., Dadina M., 2004, ApJ, 600, 634

Bassani L., Dadina M., Maiolino R., Salvati M., Risaliti G., Della Ceca R., Matt G., Zamorani G., 1999, ApJS, 121, 473

Basu-Zych A. R., Lehmer B. D., Hornschemeier A. E., Bouwens R. J., Fragos T., Oesch P. A., Belczynski K., Brandt W. N., Kalogera V., Luo B., Miller N., Mullaney J. R., Tzanavaris P., Xue Y., Zezas A., 2013a, ApJ, 762, 45

Basu-Zych A. R., Lehmer B. D., Hornschemeier A. E., Gonçalves T. S., Fragos T., Heckman T. M., Overzier R. A., Ptak A. F., Schiminovich D., 2013b, ApJ, 774, 152

Bauer F. E., et al., 2014, ArXiv e-prints

Bautz M. W., Mushotzky R., Fabian A. C., Yamashita K., Gendreau K. C., Arnaud K. A., Crew G. B., Tawara Y., 1994, PASJ, 46, L131

Bedregal A. G., Colina L., Alonso-Herrero A., Arribas S., 2009, ApJ, 698, 1852

Belczynski K., Bulik T., Fryer C. L., Ruiter A., Valsecchi F., Vink J. S., Hurley J. R., 2010, ApJ, 714, 1217

Belloni T. M., 2010, in Belloni T., ed., Lecture Notes in Physics, Berlin Springer Verlag Vol. 794 of Lecture Notes in Physics, Berlin Springer Verlag, States and Transitions in Black Hole Binaries. p. 53

Berghea C. T., Dudik R. P., Tincher J., Winter L. M., 2013, ApJ, 776, 100

Berghea C. T., Weaver K. A., Colbert E. J. M., Roberts T. P., 2008, ApJ, 687, 471

Bolton C. T., 1972, Nature, 235, 271

Bowyer S., Byram E. T., Chubb T. A., Friedman H., 1964, Nature, 201, 1307

Bowyer S., Byram E. T., Chubb T. A., Friedman H., 1965, Science, 147, 394

Brenneman L. W., Reynolds C. S., 2006, ApJ, 652, 1028

Broos P., Townsley L., Getman K., Bauer F., 2012, Astrophysics Source Code Library, p. 3001

Broos P. S., Townsley L. K., Feigelson E. D., Getman K. V., Bauer F. E., Garmire G. P., 2010, ApJ, 714, 1582

Brorby M., Kaaret P., Prestwich A., 2014, MNRAS, 441, 2346

Burnight T. R., 1949, Phys. Rev., 76, 165

Byram E. T., Chubb T. A., Friedman H., 1966, Science, 152, 66

Caballero-García M. D., Fabian A. C., 2010, MNRAS, 402, 2559

Calzetti D., et al., 2007, ApJ, 666, 870

Calzetti D., Wu S.-Y., Hong S., Kennicutt R. C., Lee J. C., Dale D. A., Engelbracht C. W., van Zee L., Draine B. T., Hao C.-N. e. a., 2010, ApJ, 714, 1256

Cash W., 1979, ApJ, 228, 939

Clark G. W., 1965, Phys. Rev. Lett., 14, 91

Clemens M. S., Scaife A., Vega O., Bressan A., 2010, MNRAS, 405, 887

Colbert E. J. M., Heckman T. M., Ptak A. F., Strickland D. K., Weaver K. A., 2004, ApJ, 602, 231

Colbert E. J. M., Mushotzky R. F., 1999, ApJ, 519, 89

Colbert E. J. M., Ptak A. F., 2002, ApJS, 143, 25

Cooke B. A., Pounds K. A., 1971, Nature Physical Science, 229, 144

Corbel S., Tomsick J. A., Kaaret P., 2006, ApJ, 636, 971

de Vaucouleurs G., de Vaucouleurs A., Corwin Jr. H. G., Buta R. J., Paturel G., Fouqué P., 1991, Third Reference Catalogue of Bright Galaxies. Volume I: Explanations and references. Volume II: Data for galaxies between 0^h and 12^h. Volume III: Data for galaxies between 12^h and 24^h.

Dewangan G. C., Griffiths R. E., Rao A. R., 2006, ApJ, 641, L125

Dewangan G. C., Jithesh V., Misra R., Ravikumar C. D., 2013, ApJ, 771, L37

Dickey J. M., Lockman F. J., 1990, ARA&A, 28, 215

Dolan J. F., 1970, AJ, 75, 223

Done C., 2010, ArXiv e-prints

Done C., Gierliński M., Kubota A., 2007, A&A Rev., 15, 1

Eisenhauer F., et al., 2005, ApJ, 628, 246

Fabbiano G., 1988, ApJ, 325, 544

Fabbiano G., 1989, ARA&A, 27, 87

Fabbiano G., 2006, ARA&A, 44, 323

Fabbiano G., Zezas A., Murray S. S., 2001, ApJ, 554, 1035

Fabian A. C., 2012, ARA&A, 50, 455

Fabian A. C., Shioya Y., Iwasawa K., Nandra K., Crawford C., Johnstone R., Kunieda H., McMahon R., Makishima K., Murayama T., Ohashi T., Tanaka Y., Taniguchi Y., Terashima Y., 1994, ApJ, 436, L51

Fabian A. C., Zoghbi A., Ross R. R., Uttley P., Gallo L. C., Brandt W. N., Blustin A. J., Boller T., Caballero-Garcia M. D., Larsson J., Miller J. M., Miniutti G., Ponti G., Reis R. C., Reynolds C. S., Tanaka Y., Young A. J., 2009, Nature, 459, 540

Fabrika S., 2004, Astrophysics and Space Physics Reviews, 12, 1

Farrell S. A., Webb N. A., Barret D., Godet O., Rodrigues J. M., 2009, Nature, 460, 73

Fender R., 2006, Jets from X-ray binaries. pp 381–419

Feng H., Kaaret P., 2007, ApJ, 668, 941

Feng H., Kaaret P., 2009, ApJ, 696, 1712

Feng H., Soria R., 2011, New A Rev., 55, 166

Forman W., Jones C., Cominsky L., Julien P., Murray S., Peters G., Tananbaum H., Giacconi R., 1978, ApJS, 38, 357

Fragos T., Lehmer B., Tremmel M., Tzanavaris P., Basu-Zych A., Belczynski K., Hornschemeier A., Jenkins L., Kalogera V., Ptak A., Zezas A., 2013a, ApJ, 764, 41

Fragos T., Lehmer B. D., Naoz S., Zezas A., Basu-Zych A., 2013b, ApJ, 776, L31

Franceschini A., Braito V., Persic M., Della Ceca R., Bassani L., Cappi M., Malaguti P., Palumbo G. G. C., Risaliti G., Salvati M., Severgnini P., 2003, MNRAS, 343, 1181

Frank J., King A., Raine D. J., 2002, Accretion Power in Astrophysics: Third Edition

Friedman H., Byram E. T., 1967, Science, 158, 257

Gao Y., Wang Q. D., Appleton P. N., Lucas R. A., 2003, ApJ, 596, L171

Gebhardt K., Rich R. M., Ho L. C., 2005, ApJ, 634, 1093

Genzel R., Lutz D., Sturm E., Egami E., Kunze D., Moorwood A. F. M., Rigopoulou D., Spoon H. W. W., Sternberg A., Tacconi-Garman L. E., Tacconi L., Thatte N., 1998, ApJ, 498, 579

Georgakakis A., Nandra K., Laird E. S., Aird J., Trichas M., 2008, MNRAS, 388, 1205

Giacconi R., et al., 1979, ApJ, 230, 540

Giacconi R., Gursky H., Kellogg E., Schreier E., Tananbaum H., 1971b, ApJ, 167, L67

Giacconi R., Gursky H., Paolini F. R., Rossi B. B., 1962, Physical Review Letters, 9, 439

Giacconi R., Kellogg E., Gorenstein P., Gursky H., Tananbaum H., 1971a, ApJ, 165, L27

Gilfanov M., 2010, in Belloni T., ed., Lecture Notes in Physics, Berlin Springer Verlag Vol. 794 of Lecture Notes in Physics, Berlin Springer Verlag, X-Ray Emission from Black-Hole Binaries. p. 17

Gladstone J. C., Copperwheat C., Heinke C. O., Roberts T. P., Cartwright T. F., Levan A. J., Goad M. R., 2013, ApJS, 206, 14

Gladstone J. C., Roberts T. P., 2009, MNRAS, 397, 124

Gladstone J. C., Roberts T. P., Done C., 2009, MNRAS, 397, 1836

Goad M. R., Roberts T. P., Reeves J. N., Uttley P., 2006, MNRAS, 365, 191

Goldader J. D., Joseph R. D., Doyon R., Sanders D. B., 1997, ApJ, 474, 104

Gonçalves A. C., Soria R., 2006, MNRAS, 371, 673

González-Alfonso E., et al., 2012, A&A, 541, A4

González-Martín O., Masegosa J., Márquez I., Guerrero M. A., Dultzin-Hacyan D., 2006, A&A, 460, 45

González-Martín O., Papadakis I., Reig P., Zezas A., 2011, A&A, 526, A132

Gou L., McClintock J. E., Liu J., Narayan R., Steiner J. F., Remillard R. A., Orosz J. A., Davis S. W., Ebisawa K., Schlegel E. M., 2009, ApJ, 701, 1076

Grier C. J., Mathur S., Ghosh H., Ferrarese L., 2011, ApJ, 731, 60

Grimm H.-J., Gilfanov M., Sunyaev R., 2003, MNRAS, 339, 793

Grisé F., Kaaret P., Feng H., Kajava J. J. E., Farrell S. A., 2010, ApJ, 724, L148

Grisé F., Kaaret P., Pakull M. W., Motch C., 2011, ApJ, 734, 23

Grisé F., Pakull M. W., Soria R., Motch C., Smith I. A., Ryder S. D., Böttcher M., 2008, A&A, 486, 151

Guainazzi M., Mihara T., Otani C., Matsuoka M., 1996, PASJ, 48, 781

Gültekin K., Cackett E. M., Miller J. M., Di Matteo T., Markoff S., Richstone D. O., 2009, ApJ, 706, 404

Güver T., Özel F., 2009, MNRAS, 400, 2050

Harnden Jr. F. R., Branduardi G., Gorenstein P., Grindlay J., Rosner R., Topka K., Elvis M., Pye J. P., Vaiana G. S., 1979, ApJ, 234, L51

Harrison F. A., et al., 2013, ApJ, 770, 103

Heil L. M., Vaughan S., Roberts T. P., 2009, MNRAS, 397, 1061

Horiuchi S., Beacom J. F., Kochanek C. S., Prieto J. L., Stanek K. Z., Thompson T. A., 2011, ApJ, 738, 154

Huang Z. P., Condon J. J., Yin Q. F., Thuan T. X., 1990, IAU Circ., 4988, 1

Hui Y., Krolik J. H., 2008, ApJ, 679, 1405

Huo Z. Y., Xia X. Y., Xue S. J., Mao S., Deng Z. G., 2004, ApJ, 611, 208

Jenkins L. P., Roberts T. P., Ward M. J., Zezas A., 2004, MNRAS, 352, 1335

Jenkins L. P., Roberts T. P., Ward M. J., Zezas A., 2005, MNRAS, 357, 109

Johnson H. L., Morgan W. W., 1953, ApJ, 117, 313

Kaaret P., Alonso-Herrero A., 2008, ApJ, 682, 1020

Kaaret P., Feng H., 2009, ApJ, 702, 1679

Kaaret P., Feng H., Wong D. S., Tao L., 2010, ApJ, 714, L167

Kajava J. J. E., Poutanen J., 2009, MNRAS, 398, 1450

Kajava J. J. E., Poutanen J., Farrell S. A., Grisé F., Kaaret P., 2012, MNRAS, 422, 990

Kawashima T., Ohsuga K., Mineshige S., Yoshida T., Heinzeller D., Matsumoto R., 2012, ApJ, 752, 18

Kewley L. J., Ellison S. L., 2008, ApJ, 681, 1183

King A. R., 2004, MNRAS, 347, L18

King A. R., 2009, MNRAS, 393, L41

King A. R., Davies M. B., Ward M. J., Fabbiano G., Elvis M., 2001, ApJ, 552, L109

Komossa S., Schulz H., 1998, A&A, 339, 345

Kong A. K. H., Yang Y. J., Yen T.-C., Feng H., Kaaret P., 2010, ApJ, 722, 1816

Kroupa P., 2001, MNRAS, 322, 231

La Parola V., Peres G., Fabbiano G., Kim D. W., Bocchino F., 2001, ApJ, 556, 47

Lehmer B. D., Alexander D. M., Bauer F. E., Brandt W. N., Goulding A. D., Jenkins L. P., Ptak A., Roberts T. P., 2010, ApJ, 724, 559

Lehmer B. D., Wik D. R., Hornschemeier A. E., Ptak A., Antoniou V., Argo M. K., Bechtol K., Boggs S., Christensen F. E., Craig W. W., Hailey C. J., Harrison F. A., Krivonos R., Leyder J.-C., Maccarone T. J., Stern D., Venters T., Zezas A., Zhang W. W., 2013, ApJ, 771, 134

Lewin W. H. G., van Paradijs J., Taam R. E., 1993, Space Sci. Rev., 62, 223

Li L.-X., Zimmerman E. R., Narayan R., McClintock J. E., 2005, ApJS, 157, 335

Linden T., Kalogera V., Sepinsky J. F., Prestwich A., Zezas A., Gallagher J. S., 2010, ApJ, 725, 1984

Lira P., Ward M., Zezas A., Alonso-Herrero A., Ueno S., 2002, MNRAS, 330, 259

Liu J., McClintock J. E., Narayan R., Davis S. W., Orosz J. A., 2010, ApJ, 719, L109

Liu J.-F., Bregman J. N., 2005, ApJS, 157, 59

Liu J.-F., Bregman J. N., Bai Y., Justham S., Crowther P., 2013, Nature, 503, 500

Long K. S., Helfand D. J., Grabelsky D. A., 1981, ApJ, 248, 925

Luangtip W., Roberts T. P., Mineo S., Lehmer B. D., Alexander D. M., Jackson F. E., Goulding A. D., Fischer J. L., 2015, MNRAS, 446, 470

Lumb D. H., Schartel N., Jansen F. A., 2012, ArXiv e-prints

Madau P., Rees M. J., 2001, ApJ, 551, L27

Magorrian J., Tremaine S., Richstone D., Bender R., Bower G., Dressler A., Faber S. M., Gebhardt K., Green R., Grillmair C., Kormendy J., Lauer T., 1998, AJ, 115, 2285

Maiolino R., Comastri A., Gilli R., Nagar N. M., Bianchi S., Böker T., Colbert E., Krabbe A., Marconi A., Matt G., Salvati M., 2003, MNRAS, 344, L59

Mapelli M., Bressan A., 2013, MNRAS, 430, 3120

Mapelli M., Ripamonti E., Zampieri L., Colpi M., 2011, Astronomische Nachrichten, 332, 414

Marlowe H., et al., 2014, MNRAS, 444, 642

Matt G., Guainazzi M., Frontera F., Bassani L., Brandt W. N., Fabian A. C., Fiore F., Haardt F., Iwasawa K., Maiolino R., Malaguti G., Marconi A., Matteuzzi A., Molendi S., Perola G. C., Piraino S., Piro L., 1997, A&A, 325, L13

Mattila S., Dahlen T., Efstathiou A., Kankare E., Melinder J., Alonso-Herrero A., Pérez-Torres M. Á., Ryder S., Väisänen P., Östlin G., 2012, ApJ, 756, 111

McClintock J. E., Shafee R., Narayan R., Remillard R. A., Davis S. W., Li L.-X., 2006, ApJ, 652, 518

Mezcua M., Roberts T. P., Lobanov A. P., Sutton A. D., 2015, MNRAS, 448, 1893

Middleton M. J., et al., 2013, Nature, 493, 187

Middleton M. J., Heil L., Pintore F., Walton D. J., Roberts T. P., 2015, MNRAS, 447, 3243

Middleton M. J., Roberts T. P., Done C., Jackson F. E., 2011a, MNRAS, 411, 644

Middleton M. J., Sutton A. D., Roberts T. P., 2011b, MNRAS, 417, 464

Middleton M. J., Walton D. J., Roberts T. P., Heil L., 2014, MNRAS, 438, L51

Miller J. M., Fabbiano G., Miller M. C., Fabian A. C., 2003, ApJ, 585, L37

Miller J. M., Fabian A. C., Miller M. C., 2004a, ApJ, 607, 931

Miller J. M., Fabian A. C., Miller M. C., 2004b, ApJ, 614, L117

Miller J. M., Walton D. J., King A. L., Reynolds M. T., Fabian A. C., Miller M. C., Reis R. C., 2013, ApJ, 776, L36

Mineo S., Gilfanov M., Sunyaev R., 2012a, MNRAS, 419, 2095

Mineo S., Gilfanov M., Sunyaev R., 2012b, MNRAS, 426, 1870

Mineo S., Rappaport S., Steinhorn B., Levine A., Gilfanov M., Pooley D., 2013, ApJ, 771, 133

Mirabel I. F., Sanders D. B., 1988, ApJ, 335, 104

Mitsuda K., et al., 1984, PASJ, 36, 741

Mitsuda K., et al., 2007, PASJ, 59, 1

Mizuno T., Miyawaki R., Ebisawa K., Kubota A., Miyamoto M., Winter L., Ueda Y., Isobe N., Makishima K., Ngc 1313 Team 2007, Progress of Theoretical Physics Supplement, 169, 229

Mizuno T., Ohnishi T., Kubota A., Makishima K., Tashiro M., 1999, PASJ, 51, 663

Motch C., Pakull M. W., Soria R., Grisé F., Pietrzyński G., 2014, Nature, 514, 198

Moustakas J., Kennicutt Jr. R. C., Tremonti C. A., Dale D. A., Smith J.-D. T., Calzetti D., 2010, ApJS, 190, 233

Mullaney J. R., Alexander D. M., Goulding A. D., Hickox R. C., 2011, MNRAS, 414, 1082

Murdin P. G., 1976, NASA Special Publication, 389, 425

Narayan R., Yi I., 1995, ApJ, 452, 710

Neff S. G., Ulvestad J. S., Teng S. H., 2004, ApJ, 611, 186

Nelemans G., Voss R., Nielsen M. T. B., Roelofs G., 2010, MNRAS, 405, L71

Nousek J. A., Baluta C. J., Corbet R. H. D., Mukai K., Osborne J. P., Ishida M., 1994, ApJ, 436, L19

Oda M., Gorenstein P., Gursky H., Kellogg E., Schreier E., Tananbaum H., Giacconi R., 1971, ApJ, 166, L1

Ohsuga K., 2007, ApJ, 659, 205

Ohsuga K., Mineshige S., 2011, ApJ, 736, 2

Okada K., Dotani T., Makishima K., Mitsuda K., Mihara T., 1998, PASJ, 50, 25

Peterson K. C., Gallagher S. C., Hornschemeier A. E., Muno M. P., Bullard E. C., 2006, AJ, 131, 133

Petrucci P. O., 2008, Mem. Soc. Astron. Italiana, 79, 118

Pietsch W., Roberts T. P., Sako M., Freyberg M. J., Read A. M., Borozdin K. N., Branduardi-Raymont G., Cappi M., Ehle M., Ferrando P., Kahn S. M., Ponman T. J., Ptak A., Shirey R. E., Ward M., 2001, A&A, 365, L174

Pintore F., Zampieri L., 2012, MNRAS, 420, 1107

Pintore F., Zampieri L., Wolter A., Belloni T., 2014, MNRAS, 439, 3461

Plotkin R. M., Gallo E., Miller B. P., Baldassare V. F., Treu T., Woo J.-H., 2014, ApJ, 780, 6

Pounds K., 2002, Philosophical Transactions of the Royal Society of London A: Mathematical, Physical and Engineering Sciences, 360, 1905

Poutanen J., Lipunova G., Fabrika S., Butkevich A. G., Abolmasov P., 2007, MNRAS, 377, 1187

Pravdo S. H., Day C. S. R., Angelini L., Harmon B. A., Yoshida A., Saraswat P., 1995, ApJ, 454, 872

Prestwich A. H., Tsantaki M., Zezas A., Jackson F., Roberts T. P., Foltz R., Linden T., Kalogera V., 2013, ApJ, 769, 92

Ptak A., Colbert E., van der Marel R. P., Roye E., Heckman T., Towne B., 2006, ApJS, 166, 154

Relaño M., Lisenfeld U., Pérez-González P. G., Vílchez J. M., Battaner E., 2007, ApJ, 667, L141

Remillard R. A., McClintock J. E., 2006, ARA&A, 44, 49

Risaliti G., Elvis M., Fabbiano G., Baldi A., Zezas A., 2005, ApJ, 623, L93

Roberts T. P., Gladstone J. C., Goulding A. D., Swinbank A. M., Ward M. J., Goad M. R., Levan A. J., 2011, Astronomische Nachrichten, 332, 398

Roberts T. P., Warwick R. S., 2000, MNRAS, 315, 98

Roberts T. P., Warwick R. S., Ward M. J., Goad M. R., Jenkins L. P., 2005, MNRAS, 357, 1363

Sanders D. B., Mazzarella J. M., Kim D.-C., Surace J. A., Soifer B. T., 2003, AJ, 126, 1607

Sanders D. B., Mirabel I. F., 1996, ARA&A, 34, 749

Sazonov S. Y., Lutovinov A. A., Krivonos R. A., 2014, Astronomy Letters, 40, 65

Schmoll S., Miller J. M., Volonteri M., Cackett E., Reynolds C. S., Fabian A. C., Brenneman L. W., Miniutti G., Gallo L. C., 2009, ApJ, 703, 2171

Shakura N. I., Sunyaev R. A., 1973, A&A, 24, 337

Shipman H. L., 1975, Astrophys. Lett., 16, 9

Smith B. J., Swartz D. A., Miller O., Burleson J. A., Nowak M. A., Struck C., 2012, AJ, 143, 144

Smith D. A., Wilson A. S., 2003, ApJ, 591, 138

Snowden S. L., Freyberg M. J., Plucinsky P. P., Schmitt J. H. M. M., Truemper J., Voges W., Edgar R. J., McCammon D., Sanders W. T., 1995, ApJ, 454, 643

Soria R., Baldi A., Risaliti G., Fabbiano G., King A., La Parola V., Zezas A., 2007, MNRAS, 379, 1313

Steiner J. F., Narayan R., McClintock J. E., Ebisawa K., 2009, PASP, 121, 1279

Stobbart A.-M., Roberts T. P., Wilms J., 2006, MNRAS, 368, 397

Strateva I. V., Komossa S., 2009, ApJ, 692, 443

Sutton A. D., Done C., Roberts T. P., 2014, MNRAS, 444, 2415

Sutton A. D., Roberts T. P., Gladstone J. C., Farrell S. A., Reilly E., Goad M. R., Gehrels N., 2013a, MNRAS, 434, 1702

Sutton A. D., Roberts T. P., Middleton M. J., 2013b, MNRAS, 435, 1758

Sutton A. D., Roberts T. P., Walton D. J., Gladstone J. C., Scott A. E., 2012, MNRAS, 423, 1154

Swartz D. A., Ghosh K. K., Tennant A. F., Wu K., 2004, ApJS, 154, 519

Swartz D. A., Soria R., Tennant A. F., 2008, ApJ, 684, 282

Swartz D. A., Soria R., Tennant A. F., Yukita M., 2011, ApJ, 741, 49

Swartz D. A., Tennant A. F., Soria R., 2009, ApJ, 703, 159

Tagliaferri G., et al., 2004, in Flanagan K. A., Siegmund O. H. W., eds, X-Ray and Gamma-Ray Instrumentation for Astronomy XIII Vol. 5165 of Society of Photo-Optical Instrumentation Engineers (SPIE) Conference Series, Swift XRT effective area measured at the Panter end-to-end tests. pp 241–250

Takagi T., Arimoto N., Vansevičius V., 1999, ApJ, 523, 107

Takeuchi S., Ohsuga K., Mineshige S., 2013, PASJ, 65, 88

Tanaka Y., Inoue H., Holt S. S., 1994, PASJ, 46, L37

Tananbaum H., Gursky H., Kellogg E. M., Levinson R., Schreier E., Giacconi R., 1972, ApJ, 174, L143

Tauris T. M., van den Heuvel E. P. J., 2006, Formation and evolution of compact stellar X-ray sources. pp 623–665

Tawa N., Hayashida K., Nagai M., Nakamoto H., Tsunemi H., Yamaguchi H., Ishisaki Y., Miller E. D., Mizuno T., Dotani T., Ozaki M., Katayama H., 2008, PASJ, 60, 11

Titarchuk L., 1994, ApJ, 434, 570

Truemper J., 1982, Advances in Space Research, 2, 241

Ulvestad J. S., 2009, AJ, 138, 1529

Vega O., Clemens M. S., Bressan A., Granato G. L., Silva L., Panuzzo P., 2008, A&A, 484, 631

Vierdayanti K., Done C., Roberts T. P., Mineshige S., 2010, MNRAS, 403, 1206

Vierdayanti K., Mineshige S., Ebisawa K., Kawaguchi T., 2006, PASJ, 58, 915

Vierdayanti K., Sadowski A., Mineshige S., Bursa M., 2013, MNRAS, 436, 71

Voges W., et al., 1999, A&A, 349, 389

Voges W., et al., 2000, VizieR Online Data Catalog, 9029, 0

Volonteri M., 2010, A&A Rev., 18, 279

Voss R., Gilfanov M., 2006, A&A, 447, 71

Vrtilek S. D., Mihara T., Primini F. A., Kahabka P., Marshall H., Agerer F., Charles P. A., Cheng F. H., Dennerl K., La Dous C., Hu E. M., Rutten R., Serlemitsos P., Soong Y., Stull J., Truemper J., Voges W., Wagner R. M., Wilson R., 1994, ApJ, 436, L9

Wald R. M., 1984, General Relativity. The University of Chicago Press

Walton D. J., et al., 2013b, ApJ, 779, 148

Walton D. J., et al., 2014, ApJ, 793, 21

Walton D. J., et al., 2015, ApJ, 806, 65

Walton D. J., Miller J. M., Harrison F. A., Fabian A. C., Roberts T. P., Middleton M. J., Reis R. C., 2013a, ApJ, 773, L9

Walton D. J., Miller J. M., Reis R. C., Fabian A. C., 2012, MNRAS, 426, 473

Walton D. J., Roberts T. P., Mateos S., Heard V., 2011, MNRAS, 416, 1844

Wang J., Fabbiano G., Elvis M., Risaliti G., Mazzarella J. M., Howell J. H., Lord S., 2009, ApJ, 694, 718

Wang Q. D., Yao Y., Fukui W., Zhang S. N., Williams R., 2004, ApJ, 609, 113

Watarai K.-y., Fukue J., Takeuchi M., Mineshige S., 2000, PASJ, 52, 133

Webster B. L., Murdin P., 1972, Nature, 235, 37

White N. E., Nagase F., Parmar A. N., 1995, X-ray Binaries, pp 1–57

Wilms J., Allen A., McCray R., 2000, ApJ, 542, 914

Windhorst R. A., Burstein D., Mathis D. F., Neuschaefer L. W., Bertola F., Buson L. M., Koo D. C., Matthews K., Barthel P. D., Chambers K. C., 1991, ApJ, 380, 362

Winter L. M., Mushotzky R. F., Reynolds C. S., 2006, ApJ, 649, 730

Winter L. M., Mushotzky R. F., Reynolds C. S., 2007, ApJ, 655, 163

Wood K. S., Meekins J. F., Yentis D. J., Smathers H. W., McNutt D. P., Bleach R. D., Friedman H., Byram E. T., Chubb T. A., Meidav M., 1984, ApJS, 56, 507

Yamaguchi H., Nakajima H., Koyama K., Tsuru T. G., Matsumoto H., Tawa N., Tsunemi H., Hayashida K., Torii K., Namiki M., Katayama H., Dotani T., Ozaki M., Murakami H., Miller E., 2006, in Society of Photo-Optical Instrumentation Engineers (SPIE) Conference Series Vol. 6266 of Society of Photo-Optical Instrumentation Engineers (SPIE) Conference Series, The background properties of Suzaku/XIS

Yoshida T., Ebisawa K., Matsushita K., Tsujimoto M., Kawaguchi T., 2010, ApJ, 722, 760

Zampieri L., Roberts T. P., 2009, MNRAS, 400, 677

Zaritsky D., Kennicutt Jr. R. C., Huchra J. P., 1994, ApJ, 420, 87

Zezas A., Ward M. J., Murray S. S., 2003, ApJ, 594, L31

Zombeck M. V., 1990, Handbook of the Space Astronomy and Astrophysics, 2nd, edn. Cambridge University Press, Worcester